2020

PROBABILISTIC APPROACH TO WATER, SEDIMENT, AND NUTRIENT CONNECTIVITY FOR ADVANCING WATERSHED MODELLING

David Tyler Mahoney
University of Kentucky, david.tyler.mahoney@gmail.com
Author ORCID Identifier:
https://orcid.org/0000-0003-0523-508X
Digital Object Identifier: https://doi.org/10.13023/etd.2020.271

STUDENT AGREEMENT:

I represent that my thesis or dissertation and abstract are my original work. Proper attribution has been given to all outside sources. I understand that I am solely responsible for obtaining any needed copyright permissions. I have obtained needed written permission statement(s) from the owner(s) of each third-party copyrighted matter to be included in my work, allowing electronic distribution (if such use is not permitted by the fair use doctrine) which will be submitted to UKnowledge as Additional File.

I hereby grant to The University of Kentucky and its agents the irrevocable, non-exclusive, and royalty-free license to archive and make accessible my work in whole or in part in all forms of media, now or hereafter known. I agree that the document mentioned above may be made available immediately for worldwide access unless an embargo applies.

I retain all other ownership rights to the copyright of my work. I also retain the right to use in future works (such as articles or books) all or part of my work. I understand that I am free to register the copyright to my work.

REVIEW, APPROVAL AND ACCEPTANCE

The document mentioned above has been reviewed and accepted by the student's advisor, on behalf of the advisory committee, and by the Director of Graduate Studies (DGS), on behalf of the program; we verify that this is the final, approved version of the student's thesis including all changes required by the advisory committee. The undersigned agree to abide by the statements above.

David Tyler Mahoney, Student

Dr. James F. Fox, Major Professor

Dr. Tim Taylor, Director of Graduate Studies

PROBABILISTIC APPROACH TO WATER, SEDIMENT, AND NUTRIENT CONNECTIVITY FOR ADVANCING WATERSHED MODELLING

DISSERTATION

A dissertation submitted in partial fulfillment of the
requirements for the degree of Doctor of Philosophy in the
College of Engineering at the University of Kentucky

By

David Tyler Mahoney

Lexington, Kentucky

Director: Dr. James F. Fox, Professor of Civil Engineering

Lexington, Kentucky

2020

ABSTRACT OF DISSERTATION

PROBABILISTIC APPROACH TO WATER, SEDIMENT, AND NUTRIENT CONNECTIVITY FOR ADVANCING WATERSHED MODELLING

The goal of this dissertation is to represent the spatial and temporal domains of water, sediment, and nutrient flux and pathways within fluvial and watershed settings. To complete this goal, we integrate connectivity theory into watershed model structures to simulate water, sediment, and nutrient movement at the fundamental unit they occur. Fluvial-based sediment and nutrient flux is an important driver of global sediment and nutrient budgets, and the quantification of which serves as an ongoing challenge to limnologists, engineers, and watershed managers. Watershed models have been richly developed over the past century, but are currently restrained by problems related to omission of physical transport and detachment processes as well ambiguous representation of active non-point sources and their transport pathways. To overcome limitations such as these, geomorphologists introduced connectivity theory, which has garnered popularity from watershed managers and modelers due perhaps to its ability to explain the non-linearity of system response and explicitly detail non-point sources, sinks, and transport pathways. Connectivity is defined herein as, "the integrated transfer of material from source to sink facilitated by the continuum of material generation, loss, and transport in three dimensions and through time." Connectivity theory has matured such that we now have a holistic view of phenomena controlling connectivity, however, the connectivity community has not yet adopted a unified conceptual framework with the goal of connectivity quantification. Existing connectivity models have varying approaches to quantify connectivity such as: (1) index-based connectivity assessments; (2) effective catchment area estimation; and (3) network-based connectivity simulations. While these models often adequately represent the structural connections of landscape elements, few frameworks are able to represent the variability of connectivity from dynamic hydrologic forcings. We argue that explicit coupling of watershed models with a unified connectivity framework will help to improve the basis of watershed modelling in physics while avoiding problems that current watershed models possess: namely due to spatial and temporal lumping and empirical estimations of non-point source generation and fate. This dissertation seeks to fulfill this objective through of six studies that advance formulation of the tenets of connectivity including the magnitude, extent, timing, and continuity of connectivity with respect to water, sediment, and nutrients.

Keywords: connectivity, sediment, hydrology, watershed model, water quality

Tyler Mahoney
Student Signature

05/15/2020
Date

PROBABILISTIC APPROACH TO WATER, SEDIMENT, AND NUTRIENT CONNECTIVITY FOR ADVANCING WATERSHED MODELLING

By

David Tyler Mahoney

Dr. James F. Fox
Director of Thesis

Dr. Tim Taylor
Director of Graduate Studies

05/15/2020
Date

ACKNOWLEDGEMENTS

I would like to acknowledge a number of individuals who have contributed to this research and my personal growth as a student, including the members of this dissertation committee, my fellow graduate students, undergraduate researcher collaborators, and faculty in the Civil Engineering Department at the University of Kentucky. First, I would like to acknowledge Dr. James Fox, the director of this PhD thesis, for his gentle guidance, patience, and positive encouragement throughout my time as a PhD student. I attribute my accomplishments as a researcher to his mentorship, and strive to follow in his footsteps as a scientist and instructor. I would like to acknowledge Dr. Scott Yost, my undergraduate research advisor, who introduced me to water resources research and mentored me throughout my undergraduate and graduate degrees. I extend my thanks to other members of this dissertation committee, including Dr. Ed Wang, Dr. Bill Ford, and outside examiner Dr. Rebecca Freeman for their insight and mentorship. I would especially like to thank my graduate student collaborators, who not only inspired this research, but supported me in the field, laboratory, and office in both technical matters and as very good friends. I would especially like to thank Evan Clare, Erika Hernandez, Nabil Al-Aamery, Admin Husic, Steven Hoagland, and many others with whom it has been a pleasure to collaborate. I would like to thank the hard-working group of undergraduate researchers who assisted with preparation of this dissertation and the faculty of the Civil Engineering department for their support.

Ultimately, this research would not have been possible without the love, support, and encouragement of the connected network of family members and friends for whom this dissertation is dedicated. First, I would like to acknowledge my fiancée, Jamie Harrison, for her love, kindness, and unwavering support during the dissertation process, for which I will always be grateful. I would like to thank my parents and brother, David, Karen, and Chase Mahoney for their support and inspiration. I would also like to thank Jamie’s family for their love and support over the past three years.

TABLE OF CONTENTS

LIST OF TABLES

TABLE OF FIGURES

Chapter	Innovative Method	Conclusions	Dataset
1	Spatially explicit sediment connectivity simulations in the watershed uplands.	Coupling connectivity and watershed modeling improves the spatial representation of upland sediment transport in gently rolling watersheds. Disconnectivity dominates in the low-gradient system.	High-resolution geospatial data, TSS samples
2	Coupling of connectivity theory with instream sediment modeling and the equilibrium sediment exchange process.	Coupled sediment fingerprinting and connectivity numerical simulations elucidate the roll of the equilibrium sediment exchange process in low-gradient stream networks.	Same as Ch. 1; stable C and N isotopes
3	Explicit representation and conceptualization of the connected timing in the watershed uplands.	Spatial connectivity is dependent on both structural and functional process. The timing of connectivity is dependent on only structural processes.	Same as Ch. 1
4	Application of connected timing and instream sediment routing.	Inclusion of hysteresis in model evaluation improved sediment model simulations. Sensitive connected pathways control sediment yield in the low-gradient system.	High-resolution turbidity and TSS data
5	Coupling of connectivity theory and RUSLE erosion modeling in mountainous catchments with reclaimed mineland.	Coupling of connectivity and RUSLE simulations shows promise to improve sediment calculations in steep watersheds. Sediment connectivity is greater in reclaimed mineland than forest land.	TSS and sediment fingerprinting data
6	Formulation of instream probability of connectivity and continuity for bedrock controlled low-gradient stream networks.	Coupled connectivity and continuity models shows instream erosion and deposition are discontinuous processes in low gradient streams. Bedrock barriers control stream morphology.	Same as Ch. 4

Chapter 1. Watershed erosion modeling using the probability of sediment connectivity in a gently rolling system

Adapted per my Elsevier publishing rights from Mahoney, D.T., Fox, J.F. and Al Aamery, N., 2018. Watershed erosion modeling using the probability of sediment connectivity in a gently rolling system. Journal of Hydrology, 561, 862-883.

1.0 ABSTRACT

Sediment connectivity has been shown in recent years to elucidate the role of the watershed configuration in controlling sedimnet transport. However, we find no studies develop a watershed erosion modeling framework based on sediment connectivity and few, if any, studies have quantified sediment connectivity for gently rolling systems. We develop a new predictive sediment connectivity model that relies on the intersecting probabilities for sediment supply, detachment, transport, and buffers to sediment transport, which is integrated in a watershed erosion model framework. The model predicts sediment flux temporally and spatially across the watershed using field reconnaissance results, high-resolution 1.5 meter by 1.5 meter digital elevation models, a hydrologic model, and shear-based erosion formulae. Model results validate the capability of the model to predict erosion pathways causing sediment connectivity. More notably, disconnectivity dominates the gently rolling watershed across all morphologic levels of the uplands, including, microtopography from low energy undulating surfaces across the landscape, swales and gullies only active in the highest events, karst sinkholes that disconnect drainage areas, and floodplains that de-couple the hillslopes from the stream corridor. Results show that sediment connectivity is predicted for about 2% or more the watershed's area 37 days of the year, with the remaining days showing very little or no connectivity. Only 12.8 ± 0.7% of the gently rolling watershed shows sediment connectivity on the wettest day of the study year. Results also highlight the importance of urban/suburban sediment pathways in gently rolling watersheds, and dynamic and longitudinal distributions of sediment connectivity might be further investigated in future work. We suggest the method herein provides the modeler with an added tool to account for sediment transport criteria and has the potential to reduce computational costs in watershed erosion modeling.

1.1 INTRODUCTION

Watershed erosion modeling aims to simulate sediment flux in a basin to discern impacts of sediment loss on landscape practices and sediment impacts on stream biology, reservoir water supply, and water quality (Morris and Fan, 1998; USEPA, 2004). However, quantifying watershed erosion has proven precarious due to spatially diverse landscapes that can buffer and disconnect sediment pathways (Fryirs, 2013). We argue sediment connectivity theory provides a meaningful concept to elucidate the role of the watershed configuration and advance watershed erosion modeling, especially in light of now often available high-resolution digital elevation models. Our motivation was to develop a probability-based theory of sediment connectivity that may be integrated within continuous-based watershed erosion simulations. We apply our modeling framework with the intent to gain knowledge of sediment disconnectivity in gently rolling terrains, which are understudied.

Currently, there is a need to advance watershed erosion models within the water resources community. Substantial advancement of watershed erosion modeling over the past four decades results from the intensive field data collection systems and experimental watersheds of the 1970s and 1980s, the coupled hydrologic formulae advancement of the 1980s, and the computational and geospatial data advancements of the 1990s and 2000s (Walling, 1983; Merritt et al., 2003; Mahoney, 2017). Researchers and practitioners now have watershed erosion modeling platforms that are often freely available and can be readily applied. However, current watershed models often do not explicitly account for the three-dimensional spatial complexity of the landscape and its dynamic nature when predicting erosion and routing of sediment. The advanced ability of our current computational environment allows parameterization of watershed erosion models that shifts the physical-based functions within the models away from the inputs and parameters for which the equations were originally designed. Often, the governing erosion formulae providing the basis of the watershed model is one, or a few, assumed erosion processes (e.g., plot scale sheet flow). Extrapolating these processes to the watershed scale produces an empirically parameterized model, assuming sufficient verification data, in which the modeler produces a posterior solution space that may not reflect the sediment detachment

and transport occurring across the uplands. In this case, the modeler neglects the three dimensional and temporally dynamic landscape.

Presently, we detail a promising approach to help overcome spatial complexity limitations and advance watershed erosion modeling by coupling erosion formulae with an investigation of watershed morphology and connectivity using high-resolution spatial data. We argue the time is ripe to advance watershed erosion modeling by improving its spatiotemporal context for several reasons. Highly resolved topographic and landscape feature datasets are now often freely available, making incorporation of such data into watershed platforms feasible. Also, geomorphologic field-based and geospatial-based investigation have been highly advanced in recent years to focus on the topic of 'sediment connectivity.' Sediment connectivity is now recognized to be a major control on sediment budgets (Fryirs et al., 2007), but has seldom taken precedence in quantitative sediment transport models (Ambroise, 2004; De Vente et al., 2005; Heckmann and Schwanghart, 2013).

Sediment connectivity is a contemporary term that we define similarly to Bracken et al. (2015) as the integrated detachment and transport of sediment from source to sink between geomorphic zones of a watershed. While the term is contemporary, we recognize general concern for how erosion zones are connected to the stream channel (i.e., sediment delivery) has been studied for the past 60 years (e.g., Maner and Barnes, 1953; Glymph, 1954; Schumm, 1954), if not earlier. The contemporary definition of sediment connectivity has evolved from several bodies of sediment transport and geomorphologic literature. One body of literature is research focused on the sediment delivery ratio, which was developed in the 1950s and 60s by Maner and Barnes (1953), Roehl (1962), and studied extensively thereafter. A second body of literature is the work by Schumm (1977) and researchers thereafter, which conceptually compartmentalizes zones of the watershed by their respective dominance of sediment production, transfer, and deposition. This work led to numerous studies assessing sediment source-to-channel delivery at various scales (e.g., Ferguson, 1981; Roberts and Church, 1986; Knighton, 1989; Brunsden, 1993; Harvey, 1996; Machaelides and Wainwright, 2002). The third body of literature is general connectivity theory, which is defined as the transfer of matter between two landscape compartments or throughout an entire system (Chorley and Kennedy, 1971). General

connectivity theory was further developed by ecologists (e.g., Taylor et al., 1993 and Pringle, 2003) until adopted by geomorphologists to describe the hydrologic connection of geomorphologic compartments.

The contemporary idea of sediment connectivity focused herein has evolved by synthesizing the above literature bodies. Contemporary sediment connectivity aims to identify the watershed's configuration and its role within the sediment continuum including the stores and sinks of sediment, the pathways of sediment detachment and transport, and the morphologic features disconnecting the pathways of sediment transport during hydrologic events (Fryirs et al., 2007; Jain and Tandon, 2010) to work towards solving the 'sediment delivery problem' (Walling, 1983). Contemporary sediment connectivity gained popularity in the early- and mid-2000s through conceptual work from researchers such as Hooke (2003), Brierley et al. (2006), Fryirs et al. (2007), Bracken and Croke (2007) and Bracken et al. (2015), and has been extended to morphological budgeting (Croke et al., 2013) and morphometric analysis (Marchamalo et al., 2016). Current application of sediment connectivity includes index-based, empirical, and process-based analyses (e.g. Borselli et al., 2008; Messenzehl et al., 2014; Liu and Fu, 2016; Masselink et al., 2016; Heckmann and Schwanghart, 2013). Sediment connectivity is implicit within empirical models such as the sediment delivery ratio, but as identified by many researchers (e.g., Walling, 1983; Bracken and Croke, 2007; Fryirs, 2013), these historic sediment models lack integration of the complex physical processes governing sediment erosion, transport, and deposition due to spatial and temporal lumping.

We suggest sediment connectivity's emphasis on the watershed's configuration provides a meaningful descriptive and topologic concept for integrating within watershed erosion modeling. Numerous features of sediment connectivity, including its emphasis on field assessment and geospatial modeling, are attractive for advancing watershed erosion modeling. Field assessment of the watershed's morphology provides the foundation of sediment connectivity theory and allows identification of features that may disconnect sediment pathways lacking inclusion in watershed modeling frameworks. For example, field assessments identify sediment transport buffers such as long flat floodplains that laterally disconnect hillslopes to the stream corridor (Fryirs, 2013). Spatially explicit modeling of the watershed *via* sediment connectivity models has the potential to reflect the

actual three-dimensional landscape to elucidate zones of active erosion and concentrated pathways of sediment transport (Cavalli et al., 2013). Thereafter, researchers may apply erosion formulae typical of watershed models to active erosion zones and active contributing area of the watershed (Ambroise, 2004), rather than extrapolating and calibrating formulae beyond their physical-basis across the entire landscape.

We commend the pioneering and recent efforts of scientists to advance the theory and application of sediment connectivity (e.g., Fryirs et al., 2007; Borselli et al., 2008; Cavalli et al., 2013; Fryirs, 2013; Bracken et al., 2015; Souza et al., 2016), which in turn provides a promising basis for improving watershed erosion models. However, we highlight several features of sediment connectivity theory requiring further development to allow integration with continuous-based watershed erosion model simulations. First, previous sediment connectivity modeling has focused on one or a few factors controlling sediment transport in a watershed such as Fryirs et al., (2007) who focused on sediment "dis"connectivity and Borselli et al., (2008), who focused on upstream and downstream sediment transport. A recent perspective article emphasizes the need to consider the many hydrologic and non-hydrologic factors controlling sediment connectivity across a watershed (Bracken et al., 2015). Therefore, our approach aims to extend sediment connectivity theory by developing a probabilistic framework that accounts for hydrologic and non-hydrologic supply, detachment, transport, and disconnectivity features. Second, sediment connectivity is dynamic by its nature and varies temporally, yet most models of sediment connectivity are static, emphasizing physical-connections in the landscape and do not capture dynamic features such as varying soil moisture conditions (Ambroise, 2004; Lexartza-Artza and Wainwright, 2009; Fryirs, 2013). Therefore, our approach aims to couple hydrologic connectivity within their watershed modeling framework to help elucidate the dynamic nature of sediment connectivity. Third, we remind the reader that sediment connectivity alone does not provide erosive flux prediction (Bracken et al., 2015), and therefore we couple their sediment connectivity theory with erosive formulae within the watershed modeling framework.

As a second contribution, we advance knowledge of sediment disconnectivity for 'gently rolling' watersheds. Most slopes of our study watershed are 'gentle' or 'undulating' although the steeper sections of complex hillslopes are classified as 'rolling'

in our system (Sims et al., 1968, pp. 58; USDA, 2017 pp. 44). To highlight this idea, we use the term *gently rolling watershed*, which has been used previously concerning watersheds with similar terrain where fine sediment deposition occurs (e.g., Morris and Fan, 1998) and used extensively to describe our study region (McGrain, 1983 and citations thereafter). The upland morphology of gently rolling watersheds includes relatively stable land surfaces and ephemeral pathways (Jarrit and Lawrence, 2007; Ford and Fox, 2014). Mild gradients and fertile soils of gently rolling watersheds foster agricultural and suburban land uses, which in turn further stabilizes the morphology of the sediment pathways and floodplains. Previous studies investigating sediment disconnectivity emphasize moderate and steep gradient systems (e.g., Fryirs et al., 2007; Borselli et al., 2008), and gently rolling watersheds have been understudied.

The objective of the present research was twofold and includes (i) developing a watershed erosion model grounded in probability theory for sediment connectivity and (ii) investigating sediment connectivity and erosion within a gently rolling watershed. We present a probabilistic-based development of sediment connectivity that is general to the governing factors controlling sediment transport but can be tailored and parameterized for a watershed-specific configuration. We include the concept of dynamic connectivity of sediment transport by integrating hydrologic connectivity within a continuous-based model simulation. We use probability theory to develop a predictive model reliant upon the intersecting probabilities for sediment supply, detachment, transport, and the absence of buffers. The model predicts sediment flux temporally and spatially across the watershed using high-resolution geospatial data, field reconnaissance, external modeling of hydrologic connectivity, and erosion formulae. We apply the model to a gently rolling watershed to gain knowledge of sediment disconnectivity. The primary contribution herein is a watershed erosion model that includes sediment connectivity and disconnectivity results for a gently rolling watershed.

1.2 MODELING FRAMEWORK AND FORMULATION

The watershed erosion modeling framework includes geospatial, field assessment and meteorological inputs that lead to three stages of model simulation to produce spatially and temporally explicit sediment connectivity and flux outputs (see Figure 1). High-

resolution geospatial data reflect the actual three-dimensional landscape of the watershed. Inputs from field assessment identify features that may connect and disconnect sediment pathways across the watershed. Continuous precipitation and weather data provide information leading to the dynamic nature of the watershed's connectivity.

The first stage of modeling assists with simulating dynamic connectivity by integrating hydrologic connectivity within a continuous-based model simulation. For this stage, we prescribe use of an off-the-shelf hydrologic model providing continuous simulation of soil moisture conditions and runoff depth across the watershed.

The second stage of modeling simulates the probability of sediment connectivity (see Figure 2) to estimate pathways and buffers impacting the delivery of sediment from the uplands to the stream corridor, as a precursor to erosion rates and routing in stage three. We express the intersecting probabilities of sediment supply, detachment, transport, and the absence of buffers to produce the probability of sediment connectivity. In Figure 2, we specify the union of both hydrologic and non-hydrologic processes. Mathematically, we express the probability of sediment connectivity, $P(C)$, as

$$P(C) = P(S) \cap P(D_H \cup D_{NH}) \cap P(T_H \cup T_{NH}) \cap \{1 - P(B)\} \ , \quad (1)$$

where S denotes supply, D_H is hydrologic detachment, D_{NH} is non-hydrologic detachment, T_H is hydrologic transport, T_{NH} is non-hydrologic transport, and B is buffers. The intersections and unions of probabilities *via* their multiplicative and summation definitions becomes

$$P(C) = \{P(S)\} \times \{P(D_H) + P(D_{NH}) - P(D_H)P(D_{NH})\} \times \{P(T_H) + P(T_{NH}) - P(T_H)P(T_{NH})\} \times \{1 - P(B)\}. \quad (2)$$

The probability of sediment connectivity can be calculated when each process-associated probability is known or can be estimated. In the present study, we take a Boolean approach to Equation (2) by modeling each geospatial grid cell represented across the landscape as having a probability of zero or one, and then integration provides the watershed's net probability of sediment connectivity. We keep Equation (2) as general for the moment highlighting that future work could adopt a fuzzy or Bayesian approach to the probabilities of each spatial cell.

Several features of Equation (2) require some elaboration as to their background and justification. First, we adopt a probabilistic definition of sediment connectivity

because we recognize the stochastic nature of sediment transport across a heterogeneous landscape. Probability theory has long been a suitable approach to the sediment transport problem given the non-uniformity of sediment size distributions, the stochastic nature of turbulence, and the heterogeneity of landscapes (see examples of such studies in Table 1). Concerning sediment connectivity, the probability approach is attractive because of its multiplicative ability to account for the many processes required for transport. Our approach reflects the ideas of Borselli et al. (2008), who defines the probability of connectivity as the probability that the landscape can transport sediment laterally and longitudinally in the fluvial network. Second, the probability of sediment connectivity model reflects the necessity for co-occurrence of sediment supply, detachment, and transport conditions, as these processes are well known to potentially limit transport (Leopold et al., 1964). Third, the model accepts the dynamic nature of the sediment transport controls (e.g., Jencso et al., 2009) and thus couples with the stage one modeling. Fourth, we include both non-hydrologic connectivity, i.e., connectivity caused by non-fluvial processes, and hydrologic connectivity given the recent realization of non-hydrologic prevalence (eolian transport, landslides) in some systems at some time scales (see theory by Bracken et al., 2015). Fifth, we explicitly include the concept of disconnectivity *via* morphologic features and anthropogenic obstacles given the recent realization that buffers can create sediment disconnectivity (Fryirs et al., 2007; Fryirs, 2013).

The probability model in Equation (2) may be applied for an entire watershed by using spatially explicit information across the landscape and thus reflects a distributed watershed modeling framework. The output may be used to map erosion prone features and disconnected regions. The output has specific utility in watershed erosion modeling because the probability of sediment connectivity for a hydrologic event is distributed spatially and can be integrated to estimate the active watershed area for sediment transport.

The third stage of modeling simulates erosion formulae for connected features and is tailored to the specific erosion processes known to exist in a watershed. Parameterization of the erosion formulae will vary depending on the timescale of intent, the spatial scale reflecting the connected feature, and the dominant sediment transport processes distributed across the upland landscape (e.g., mass wasting, fluvial erosion, eolian transport). Outputs

include both distributed soil loss and net sediment transport results. We intend that the model may be verified *via* practical qualitative data of erosional features as well as quantitative data such that the model may be useful as a predictive tool in watershed studies.

1.3 MODELING APPLICATION

We apply the modeling framework to a gently rolling watershed in Kentucky USA. We parameterize the probability of sediment connectivity for fluvial erosion processes given the study site conditions. We keep in mind a prevalence of agricultural practices potentially promoting unconsolidated and low vegetation cover soil surface, at least at some times of the year in some portions of the watershed.

1.3.1 Study Site:

We applied the model to the Upper South Elkhorn watershed (65.1 km^2), located in the Inner Bluegrass physiographic region of Kentucky USA (see Figure 3). The watershed has mixed land uses, consisting of primarily agricultural lands (55%) and urban areas (45%) (Fry et al., 2011). The watershed was chosen for model application because (i) past studies conducted in the watershed provide data results for calibration of modeling (Davis, 2008; Fox et al., 2010; Russo, 2009; Ford, 2011; Russo and Fox, 2012; Ford, 2014); (ii) on-going data collection is conducted by the University of Kentucky and the United States Geological Survey (USGS); and (iii) the proximity of the watershed to the University of Kentucky.

Headwaters of the South Elkhorn Creek originate in southwestern Lexington, Kentucky, within urban areas and the middle and lower watershed extends into agricultural pastureland. Gently rolling hills and relatively mild slopes characterize the land surface. The stream channel is bedrock-controlled with fine sediment deposits. Silt loams primarily make up the South Elkhorn watershed's soil cover. Upland erosion occurs primarily through rill erosion and ephemeral gully erosion, while diffusional erosion processes (i.e., sheet and interrill erosion) are a minor contribution to the overall sediment flux (Gumbert, 2017; Smallwood, 2017). Livestock and construction sites in the uplands exacerbate the detachment rates of sediment particles through the removal of protective vegetation and

exposure to fluvial shear stresses (Evans, 2017). The Upper South Elkhorn watershed is also characterized by long, flat floodplains adjacent to the stream network. Air temperature ranges between, on average, 0.5°C in January to 24.5°C in July. The average yearly rainfall for this region is 1148 mm. The climate is classified as humid subtropical (Ulack et al., 1998).

The Inner Bluegrass Region of Kentucky USA is well-recognized as exhibiting terrain with high karst potential (Thrailkill, 1974; Thrailkill et al., 1991; Phillips, 2015), with the land surface showing depressions and sinkholes leading to springsheds. Based on analyses of geospatial data files and results published by Taylor and Nelson (2008) and the Kentucky Geological Survey (KGS, 2017), the sub-region of the South Elkhorn Watershed is immature karst terrain (e.g., termed channel-rich/karst-poor, Phillips et al., 2004) relative to neighboring and nearby watersheds in the Inner Bluegrass. For example, the karst-impacted drainage area of the South Elkhorn Watershed is very low (~13% of the watershed drainage area, see Table 2) relative to other watersheds in the Inner Bluegrass Region (e.g., nearby watersheds show karst-impacted drainage areas ranging from 26 to 99%, see Table 2). The result is highly consistent with past morphologic research in the Inner Bluegrass karst region where the landscape is organized into discrete local zones dominated by either karst or fluvial features, to the near-exclusion of the other (Phillips et al., 2004). Dye traces performed in the South Elkhorn Watershed have shown that existing sinkhole to spring flow pathways follow the same general pathways as topographic flowlines (Currens et al., 2002). Therefore, we assume sediment pirated by sinkholes likely does not leave the watershed's topographic boundary. Nevertheless, we realized the potential importance of the karst sinkhole to impart sediment disconnectivity. Hence, we explicitly include the role of the karst terrain in watershed sediment connectivity modeling.

1.3.2 Field Assessment, Geospatial Data and Hydrologic Data:

A field assessment and geospatial analyses method was designed and carried out to identify sediment processes (e.g., sheet, rill, and gully erosion, instream sediment storage, channel morphology) and sediment disconnectivity. The field method combined published methods to visually assess sediment in watersheds and streams, including region-specific methods (NRCS, 2009; Rosgen, 2001; USEPA, 1999; Fryirs et al., 2007; Third Rock

Consultants, 2016). Geospatial analyses of high-resolution digital elevation models (DEMs) and orthophotos complimented the field work and were used to map karst sinkholes in the basin.

Before field visits, we created maps in *ArcGIS* (version 10.4.1) showing the stream corridor, surrounding land cover, and tributaries. We discretized reaches into sub-reaches and spatially identified features for field inspection.

In the field, we assessed connectivity of streambanks and floodplains, the streambed, upland hillslopes, and tributaries. We observed the density of vegetation surrounding the stream, the structure of the banks, and human infrastructure potentially influencing sediment transport. We estimated channel bathymetry, morphology, and the type and depth of sediment stored in the streambed. We assessed hillslope conditions through identification of the type of land use, evidence of historic upland erosion, and upland human interferences that may accelerate sediment transport *via* visual observations from within the stream network coupled with orthophotograph assessment. We walked tributaries and noted bank angles, heights, bed material, erosional hotspots, and upstream land cover. We geolocated photographs of (dis)connectivity within the watershed including check dams, bedrock outcrops, point bars, depositional zones, armoring zones, connected hillslopes, floodplains, in-stream features (riffles, runs, and pools) as well as upland features (human or livestock interference). To assess long-term connectivity, we coupled this method with the following procedures: (1) we inferred evidence of strongly connected sediment transport pathways in the field by mapping erosion scars, ephemeral gullies, and concentrated flow pathways with evidence of erosion; (2) we coupled the field disconnectivity assessment with GIS analyses to observe larger and more prominent landscape features that might also influence the connectivity, such as floodplains and karst sinkholes; (3) we used general knowledge of the system gathered from field visits and data collection the past three years of study from researchers at the University of Kentucky; and (4) we compared landscape features, land use, and erosion pathways visually using multiple sets of orthophotos from varying years, especially in regards to parameterizing the probability of non-hydrologic detachment component of the model.

After completing each site visit, we post-processed reach information on a geospatial database using a weighting and averaging technique to score qualitatively

several watershed sedimentation parameters including erosion, deposition, and lateral and longitudinal disconnectivity. Conglomerate scores led to the development of hotspot maps. In particular, the presence of buffers such as floodplains, sinkholes, farm dams, and terraces within sub-reaches qualitatively determined lateral disconnectivity. We recognized the potential for subjectivity in the field assessment, and thus multiple researchers individually scored each parameter of the sub-reaches and the average of the researchers' scores was used to create the conglomerate hotspot maps for the major parameters assessed.

One main utility of the field assessment and geospatial analyses was to understand disconnectivity from floodplains and karst sinkholes. The land surface upstream of floodplain buffers was assumed disconnected from the stream network and thus not contributing to sediment flux at the watershed outlet. Approximately 5,200 points simulated the extent of the delineated buffer features. Using *ArcHydro*, which is a set of data models that delineate and characterize watersheds in ArcMap (Maidment, 2002), and specifically the *Batch watershed delineation* tool, we determined the upstream contributing area of each point to delineate disconnected land. Another feature of potential sediment disconnectivity was water and sediment transport to karst sinkholes. Karst sinkholes are depressions leading to active or legacy (i.e., clogged) holes in the ground surface caused by cover collapse resulting from chemical dissolution of carbonate rock (Taylor, 1992). In the South Elkhorn, sinkhole drainage area can vary from a few square meters to as large as five hectares, where the former is from a relatively new cover collapse and the latter from successive dissolution and collapse leading to depression in the land surface. During rainfall events, runoff and eroded sediment can transport in the depressions and either deposit or enter the karst subsurface. We quantified the extent of the sinkhole drainage area in our study basin using published files from the USGS and the Kentucky Geological Survey (Currens et al., 2002; Taylor and Nelson, 2008; Zhu et al., 2014; KGS, 2017). Currens et al. (2002) as well as references cited therein performed extensive study of the karst features in the basin and surrounding watersheds over the course of a 25 year period. Sinkhole occurrence, drainage areas, and flow pathways were mapped in a geospatial data file using dye trace studies, water-level data and inference, geologic structure, the existence of significant sinkhole and spring features, and delineation methods (Currens et al., 2002; Taylor and Nelson, 2008; Zhu et al., 2014). The karst geospatial data served to highlight

the percent coverage of sinkholes and their pathways, and then we coupled the spatially explicit data with sediment connectivity modeling, as discussed later.

Additional hydrologic and geospatial data served as model inputs. A land cover map was coupled with soil survey data, as determined by the United States Department of Agriculture (USDA), and the Natural Resources Conservation Service (NRCS). A high-resolution DEM created by the Kentucky Aerial Photography and Elevation Data Program in 2014 (KYAPED, 2014) was used to predict the probability of connectivity at 1.5 meters by 1.5 meters. Practicality of using the high resolution DEM is a function of its availability and computational processing time. The high resolution DEMs are freely available for the entire state of Kentucky USA, where the study is performed. Simulation of the probability of connectivity model using a 1.5 m DEM for a 62 km^2 watershed for one year took 28 hours on a desktop PC (Intel® Core™ i7-6700 CPU at 3.40 GHz; 64-bit operating system, x64-based processor). The computational time will increase with watershed scale, but the time could be offset with the use of parallel computing. A USGS gage located near the watershed provided discharge data from October 1, 2017, until the present. Turbidity and total suspended solids data were collected intermittently in the watershed since 2005. The National Oceanic and Atmospheric Administration (NOAA) maintains a precipitation and temperature monitoring station at the Lexington Bluegrass Airport located centrally in the watershed.

1.3.3 Hydrologic Modeling:

We utilize an off-the-shelf hydrologic model deemed suitable for the study watershed to simulate the hydrologic connectivity. The Soil and Water Assessment Tool (SWAT) was developed (Arnold et al., 1998; Neitsch et al., 2011; SWAT 2012) to simulate the physical processes of water movement from different land uses and management practices at various watershed scales. We chose this model due to its past successful application in the central Kentucky USA region (Palanisamy and Workman, 2014; Al-Aamery et al., 2016) and its wide popularity.

Equation (3) represents the water balance equation used by SWAT to simulate the hydrologic cycle and is presented as:

$$SW_t = SW_0 + \sum_{i=1}^{t}(R_{day} - Q_{surface} - E_a - w_{seep} - Q_{gw}) \quad (3)$$

where $SW_t$is the final soil water content on day t (mm of water); SW_0 is the initial soil water content on day i (mm of water); R_{day} is the amount of precipitation on day i (mm of water); $Q_{surface}$ is the amount of surface runoff on day i (mm of water); E_a is the amount of evapotranspiration on day i (mm of water); w_{seep} is the amount of lateral flow (interflow) on day i (mm of water); and Q_{gw} is the amount of (return flow) on day i (mm of water). Hydrologic response units (HRUs) group landscapes with similar land uses, soil types, and slopes. SWAT outputs runoff, soil water content, and many other parameters for each HRU at the indicated time step. To simulate hydrologic connectivity, each of the 62 HRUs modeled within the Upper South Elkhorn were spatially mapped in ArcMap and model results were assigned as attributes. Output parameters from SWAT used in the probability of connectivity model include daily runoff and daily curve number for each HRU. Daily runoff for each HRU is determined using the NRCS Curve Number method (NRCS, 1972), which is shown in Equation (4) as

$$Q_{surface} = \frac{(R_{day} - I_a)^2}{(R_{day} - I_a + S)} \quad (4)$$

where $Q_{surface}$ is the accumulative surface runoff or rainfall excess on a day (mm of water), R_{day} is the depth of the rain on a day (mm of water), S is the retention parameter (mm of water), I_a is the initial abstraction on a day (mm of water) and is generally estimated as $0.2S$, the retention parameter (S) varies spatially due to changes in soil, land cover, and surface slope and temporally due to changes in soil water content. This parameter is explained as the following

$$S = 25.4\left(\frac{1000}{CN} - 10\right) \quad (5)$$

where CN is the curve number.

Semi-automatic calibration was adopted to calibrate the SWAT model for our watershed (Al-Aamery et al., 2016) on a daily basis. The focus of this paper investigates sediment mobility at the event time scale because sediment connectivity is a dynamic processes (Ambroise, 2004; Lexartza-Artza and Wainwright, 2009; Fryirs, 2013) and because of the event-based "pulses" of sediment transport that are important at the watershed scale (Fryirs, 2013). The Sequential Uncertainty Fitting SUFI2 of SWAT-CUP (Abbaspour et al., 2007) was used to perform the calibration, sensitivity analysis and

uncertainty of our results. The statistical metrics selected for this study to assess the simulated versus the observed streamflow were the coefficient of determination R^2, percent bias (*PBIAS%*), Nash-Sutcliff Efficiency (*NSE*) and the ratio of the root mean square error to the standard deviation of measured data (*RSR*) (Moriasi et al., 2007). The degree of uncertainty of the calibrated model was assessed using the P-factor and R-factor (SWAT, 2012). The parameters chosen for model evaluation were selected based on what was reported in previous studies (Arnold et al., 2012). Two years (2004-2005) of the SWAT simulation were treated as a warm-up period. The model evaluation was consistent with methods and results in Al-Aamery et al. (2016). Model simulation from 2006 to 2010 served as the calibration phase while 2011 to 2013 served as the validation phase. Results from the model evaluation (see Table 3) showed the hydrologic model performed very well. Based on hydrologic model evaluation criteria outlined in Moriasi et al. (2007), the monthly time step model performance is considered satisfactory if the NS>0.5, RSR<0.7, and PBIAS<±25%; our simulation met all criteria in both calibration and validation. Model performance on daily time steps is expected to be poorer than the criteria set for monthly time steps, somewhat relaxing the mentioned thresholds (Moriasi et al., 2007, Engel et al., 2007). In the present case, the daily simulation meets the monthly threshold criteria further highlighting the very good performance of the model.

1.3.4 Probability of Sediment Connectivity Modeling:

We parameterized the individual probabilities in Equation (2) as a set of discrete, piecewise distributions to represent small regions, or geospatial cells, of the watershed. The six probabilities were estimated for each geospatial cell, and the discretized results were later integrated to provide continuous distribution functions applicable to the entire watershed.

A simple piecewise function predicts the probability of sediment supply for a geospatial cell n as

$$P_i(S) = \begin{cases} 1, & \text{if sediment is present within the cell} \\ 0, & \text{if sediment is absent within the cell} \end{cases} \quad (6)$$

where *i* is an index representing a geospatial cell. We parameterized equation (6) through observations, both from field visits and remote sensing, of the occurrence of a sediment

surface that might be eroded. We consider erodible surfaces to be any pervious surface. Impervious surfaces were digitized using aerial imagery provided by the USDA National Agriculture Imagery Program (NAIP) in 2010. The digitization of the probability of sediment supply was converted into a raster with resolution of 1.5 meters by 1.5 meters.

We express the probability of hydrologic detachment using an excessive shear stress approach as

$$P_{ij}(D_H) = \begin{cases} 1, & \text{if } \tau_{f\,ij} - \tau_{cr\,i} > 0 \\ 0, & \text{if } \tau_{f\,ij} - \tau_{cr\,i} \leq 0 \end{cases} \quad (7)$$

where *j* is an index representing a time step. The probability of hydrologic detachment was a temporally varying probability because the runoff depth changes with time as function of the distribution of precipitation and soil conditions. Equation (7) evaluates the shear stress of the fluid in the geospatial cell, τ_f, with respect to the critical shear stress. The shear stress of the fluid was approximated *via* the fluid momentum equation considering one-dimensional uniform flow (see Jain, 2001, pp. 58). The runoff depth of the geospatial cell for a given time step was estimated from the hydrologic model, the energy gradient was assumed the landscape slope determined in *ArcMap*. The critical shear stress of the sediment to resist erosion was parameterized by considering the soil characteristics and land management characteristics controlling the binding of particles into aggregates (Tisdall and Oades, 1982; Alberts et al., 1995; Foster et al., 1995; Lal, 1999). Critical shear stress was predicted using the empirical critical shear stress equation for rangeland soil (Alberts et al., 1995) as a function of texture, organic matter and soil bulk density, which were available in the soil geospatial layers from the USDA.

The probability of non-hydrologic detachment considers the presence of natural or anthropogenic disturbance agents, other than fluvial processes, that might initiate sediment detachment as

$$P_i(D_{NH}) = \begin{cases} 1, & \text{if a disturbance agent exists} \\ 0, & \text{if a disturbance agent is not present} \end{cases} \quad (8)$$

Equation (8) is not dependent on watershed scale. However, thorough field or remote sensing observations of non-hydrologic disturbances that detach sediment from the soil surface must be identified to parameterize the probability of non-hydrologic detachment. Examples include livestock that trample and dislodge soil particles and mechanized

detachment that might occur during construction. Farms with livestock nearby the stream corridor and construction sites were digitized in *ArcMap* and assumed to detach sediment.

Other non-hydrologic disturbances such as tillage, vehicle traffic, and mass wasting were not included in the analyses, which is a potential limitation of the study. However, we assumed tillage, vehicle traffic and mass wasting to be of small importance to sediment transport in this watershed for following reasons. Regarding tillage, almost all of the agriculture in the watershed is hay pasture, and cultivated crops account for less than 3% of the land cover (see Figure 3). Of the existing cultivated crops, most of the row crops are grown with no-till, and the farming industry protects the cropland from erosion (Smallwood, 2017). Dirt roads and skidding trails have been shown to increase connectivity in forest regions (López-Vicente et al., 2017). In the present study, we do not expect roadways to cause sediment mobilization, other than water accumulation in ditches from roadway runoff. Based on our field assessment, there are no commonly used dirt roads in the watershed. Some gravel roads exist, but these are highly compacted. The agriculture lands had paved or gravel roads attributed to the profitable and optical equine industry. The agriculture of the basin is well-established pasture to serve the 3-billion-dollar equine industry in the Bluegrass, and the horse farms generally do a good job of maintaining their pastureland resource (ESR, 2013; Smallwood, 2017). The watershed falls within the low landslide incidence (less than 1.5% of the area involved) in the United States (Radbruch-Hall et al., 1982). We found no evidence of mass wasting in the basin during field assessments, which is consistent with the gently rolling topography.

We parameterize the probability for upstream hydrologic transport with the following piecewise function as

$$P_{ij}\left(T_{H-up}\right) = \begin{cases} 1, & \text{if } S_{ac\,i} - S_{cr\,ij} > 0 \\ 0, & \text{if } S_{ac\,i} - S_{cr\,ij} \leq 0 \end{cases} \tag{9}$$

where S_{ac} indicates the slope of geospatial cell i and is assumed equal to the energy gradient and S_{cr} represents the critical slope required to initiate ephemeral gully incision of geospatial cell i (Montgomery and Dietrich 1994; Vandaele et al., 1996; Torri and Poesen, 2014). Equation (9) compares the actual slope (S_{ac}) with the critical slope (S_{cr}) to estimate the probability of upstream hydrologic transport. When S_{ac} of the land surface in the geospatial cell is greater than the S_{cr}, the probability is one for that individual cell. We

parameterized S_{ac} using gradient analyses of a DEM. We parameterize S_{cr} using the equation of Vandaele (1993) as

$$S_{cr\,i} = a_i A_i^{-b} \tag{10}$$

where a is a coefficient representative of the local climate and land use and soil characteristics of geospatial cell i, A is the upstream drainage area of geospatial cell i, and b is an exponent. The theory reflects the concept that the upstream drainage area may be a surrogate for the volume of concentrated surface runoff with sufficient magnitude and duration to sustain erosion (Vandaele, 1993). Torri and Poesen (2014) empirically derived a critical slope-upstream drainage area relationship for geospatial cells after extensively reviewing data collected by many researchers from 1983 to 2011 across six continents, and the relationship between critical slope and the upslope area was included here as

$$S_{cr\,i\,j} = 0.73 c_i e^{1.3RFC_i}\left(0.00124 S_{0.05\,ij} - 0.37\right) A_i^{-0.38} \tag{11}$$

where $S_{0.05}$ represents the maximum potential loss to runoff as determined from the NRCS Curve Number (CN) method for a geospatial cell at a particular time step, RFC is the rock fragment cover of the soil, which affects the infiltration rate of runoff, and c represents other sources of the variation of the coefficient a from Equation (10) in geospatial cell i not accounted for by the CN approximation. Data from Torri and Poesen's (2014) study included numerous landscape features, ranging from rills to large ephemeral gullies. We included this equation in the model since these landscape features are known to facilitate sediment transport in the study basin. The CN method is assumed appropriate because runoff initiates in the silt loam soils, and the system as a whole is fluvial dominated. Sinkhole drainage areas cover 13% of the drainage basin, but the sinkhole flow pathways align well with the dendritic stream network. When runoff occurs, water is routed through sinkholes, to the shallow subsurface, and out springheads connecting to the stream. The CN method models the effect that vegetation, land use, and soil type have on runoff abstraction. Initial abstraction was predicted using the empirical equation developed by Hawkins et al. (2009) as

$$S_{0.05} = 0.819\left(25.4\left[\frac{1000}{CN_{ij}} - 10\right]^{1.15}\right) \tag{12}$$

where CN_{ij} represents the Curve Number of cell i at time step j. The daily curve number output for individual HRUs via the SWAT hydrologic model represents CN_{ij}.

We parameterized the probability for downstream hydrologic transport as

$$P_i(T_{H-dwn}) = \begin{cases} 1, \text{ if } S_i - \frac{\sum S_{up}}{N} > 0 \\ 0, \text{ if } S_i - \frac{\sum S_{up}}{N} \leq 0 \end{cases} \quad (13)$$

where S_i, representative of the slope in a particular geospatial cell, was found by applying the *Slope* tool in ArcMap to the Upper South Elkhorn DEM. N is representative of the number of upstream cells flowing into cell *i,* determined *via* the *Flow Accumulation* tool, which estimates the number of cells flowing into a downstream cell. $\sum S_{up}$ is the sum of the slopes of each cell upstream of cell *i*. This is determined by weighting the flow accumulation raster by the slope raster. In this manner, the fluid energy to transport sediment in cell *i* is compared to the incoming fluid energy. The probability of downstream hydrologic transport parameterization reflects the static connectivity of the watershed when surrogating slope for the energy gradient of the fluid. Note disconnected cells downstream of connected cells do not necessarily cause deposition. Rather, we imply that disconnected cells downstream of connected cells simply do not have the capacity to pick up more sediment that is contributable to the stream network. We believe this is reasonable considering very low gradient features causing deposition are explicitly included in the probability of buffers equation and the realization that fine sediments, once entrained, can take hours, or even days to settle (Jin and Romkens, 2001; Jin et al., 2002; Le Bissonnais et al., 2004; Owens et al., 2007; Liu et al., 2008; Rienzi et al., 2018).

The probability of non-hydrologic transport represents processes such as eolian transport and land sliding. However, the present application focuses on a fluvial-dominated system only; thus non-hydrologic transport was not parameterized.

We parameterize the probability of buffer disconnectivity as

$$P_i(B) = \begin{cases} 1, \text{ if a buffer exists} \\ 0, \text{ if a buffer does not exist} \end{cases} . \quad (14)$$

We identified features causing sediment disconnectivity *via* observations in the field assessment. If features did exist, the entire upstream region of the watershed that was disconnected was parameterized with $P(B) = 1$. However, we had uncertainty regarding the ability of karst sinkhole features to cause a net disconnectivity and act as buffers of lateral transport (i.e., $P(B)$=1) within the basin. Sinkhole drainage areas are expected to pirate transported sediment or sediment may deposit in the surface depression itself

similarly to the fallout of sediment transported from hillslopes to floodplains. Uncertainty of the disconnectivity occurs because pirated sediment may resurface at springheads and therefore the sediment may reconnect back to the fluvial network. Recent studies in the Inner Bluegrass have mixed results regarding springhead sediment production. For example, we analyzed karst spring sediment productivity from data reported in recent journal papers for the Inner Bluegrass (Reed et al., 2010; Husic et al. 2017a,b). Husic et al. (2017b) showed the Royal Spring to produce an order of magnitude lower sediment concentration than surface streams during hydrologic events of various magnitude. Reed et al. (2010) showed two springs in the region produced sediment concentrations on the same order of magnitude as surface streams, albeit they collected data from rather substantial hydrologic events with 4 to 6 cm of rainfall. In the South Elkhorn, the sinkhole drainage area is small (13% of the drainage area) relative to surrounding basins (see Table 2) but springhead sediment production may not be negligible. Therefore, we perform disconnectivity analyses and propagate the analyses through the probability of connectivity modeling by considering the sinkhole drainages as disconnected and separately analyzed the watershed considering the sinkholes as connected. The analyses provides upper and lower level uncertainty bounds on our results.

1.3.5 Surface Erosion Modeling:

The probability of sediment connectivity model provides the spatially explicit erosion features and the active contributing area for sediment transport in any time step. The erosion model simulates sediment yield at the watershed outlet by integrating the daily volume of eroded sediment from the active contributing area predicted by the probability of connectivity model at the specified time step. Yearly sediment yield is predicted by integrating the daily sediment yield. Daily sediment yield was predicted as

$$S_y = \epsilon \rho_s t l w \quad (15)$$

where S_y is the sediment yielded at the watershed outlet from the active contributing area (tonnes), ϵ is the erosion rate (m/s) as predicted by the Partheniades (1965) equation, ρ_s is the bulk density of the sediment (kg/m^3), t is the amount of time sediment is contributed from the active contributing area (s), l is the length of the eroding rill or ephemeral gully (m), and w is the width of the eroding rill or ephemeral gully (m). We assume the erosion

rate is proportional to shear stress in excess of the critical shear stress of the eroding surface, as predicted by Partheniades (1965), as

$$\epsilon = k_d * (\tau_f - \tau_{cr}) \quad (16)$$

where ϵ is the erosion rate of the soil (m/s), k_d is the erodibility coefficient (m^3/N-s), τ_{cr} is the critical shear stress of the eroding surface (Pa), and τ_f is the effective shear stress (Pa) of the accumulated flow on the eroding surface. The effective shear stress of the accumulated flow on the eroding surface was approximated *via* the fluid momentum equation considering one-dimensional uniform flow of runoff and runoff depth was approximated using the Darcy-Weisbach approach (e.g., Jain, 2001). The inputs to the erosion model including the critical shear stress of the eroding surface, bathymetries, channel lengths, relative roughness of the channel, bulk density of the eroded sediment, storm length, the time sediment is produced from an eroding channel, and an erodibility coefficient are shown in Table 4.

We specified several parameters using literature-derived methods. Time of concentration was used as a surrogate for storm length when surface erosion was occurring. We applied three methods to estimate the storm length including the watershed lag method (Mockus, 1961), the velocity method (NRCS, 2010), and the Kirpich equation (Wanielista et al., 1997). Average rill and gully width was empirically parameterized using the equation developed by Nachtergaele et al., (2002). Erodibility, k_d, and critical shear stress, τ_{cr}, of the eroding soil were parameterized *via* typical literature values (Alberts et al., 1995; Hanson and Simon, 2001). We applied the friction factor following the Colebrook-White equation. The relative roughness ranged between 10% and 20% of the flow depth.

To estimate the net erosion rate of the connected cells, cells were lumped into three discrete fractions based on upstream contributing area. A flow accumulation raster within the GIS model was multiplied with the probability of sediment connectivity raster to estimate the upstream contributing area for each cell. We chose size fractions iteratively such that several orders of magnitude of upstream contributing area were represented. The average slope of the connected cells was estimated using the most connected day of the first study year. The accumulated flow rate was determined for each cell by multiplying the average upstream contributing area times the runoff depth at the particular time step, and then dividing by a representative storm length.

We performed data assimilation to reduce propagation of error from the water model to the sediment model. As mentioned, the hydrologic model performed very well (see Table 3). However, even when a hydrologic model performs very well, differences between point observation and point simulation of the model results will still occur. We did not want to propagate these differences through the sediment transport model, so we performed data assimilation for days when the predicted average flow rate differed by more than 30% of the actual average daily flow rate (Mahoney, 2017). In turn, the sediment model could better reflect the actual runoff of the individual day and reduce propagation of error to the sediment formula.

We calibrated and validated the erosion model by comparing the prediction of daily sediment flux to sediment flux estimated *via* measurements at the watershed outlet. Sediment flux estimates were completed by Russo and Fox (2012) using automated sampling and the Einstein approach (1950). The model was iteratively calibrated so the predicted daily sediment flux matched as closely as possible with the observed sediment flux. Three hydrologic events were used to calibrate the model and two hydrologic events were used for validation (Mahoney, 2017). Calibration parameters that were adjusted included the erodibility coefficient, k_d, the critical shear stress of the eroding surface τ_{cr}, the relative roughness of the channel surface $\frac{\epsilon}{D}$, the length of storm, and the contribution time of sediment from the eroding surface. The coefficient of determination and the Nash-Sutcliff coefficient were optimized during calibration. Thereafter, annual sediment yield was compared with results from Russo (2009) for additional verification.

1.4 RESULTS

1.4.1 Evaluating Model Sensitivity:

We investigated how each probability in Equation (1) captured well-known erosion mechanisms to validate the probability of connectivity model was working well. Our validation was confirmed as shown in Figure 4 where the individual probabilities predict disconnectivity from impervious surfaces with no sediment supply, low gradient surfaces with limited shear, surfaces towards the top of a slope length with limited flow accumulation, and surfaces upstream of buffers.

We next investigated the sensitivity of the individual probabilities to the results. Integration showed the probability of upstream transport exhibited the most control on the probability of connectivity, and this was true of both moderate and high rainfall events simulated throughout the model run (see Figure 5). Differences in the results for moderate and high rainfall events show the dynamic nature of the probabilities of detachment and upstream transport, given their dependence on hydrologic connectivity. The probabilities of downstream transport, buffer disconnectivity, and supply are shown in Figure 5 to be static given their dependence on the topography, morphologic features, and human-associated land cover. The dominant control of upstream transport in the present study qualitatively agrees with the high success of the Borselli et al. (2008) model founded on upstream transport. Nevertheless, the results in Figure 5 show the importance of the other individual probabilities we included in our sediment connectivity model.

Our sensitivity analysis (Figure 6) next focused on evaluating parameters in the model affecting the sediment connectivity including the critical shear stress and sediment transport coefficients, and results suggest our model parameterization is robust for the conditions of our application. The critical shear stress of sediment to resist detachment showed a lack of sensitivity until reaching a value of approximately 15 Pa (Figure 6a), and critical shear stress parameterization beyond this threshold could reduce the sediment connectivity by as much as 100%. The high critical shear stresses reflect surface conditions more akin to vegetated channels and consolidated, stabilized bank soil conditions (Millar and Quick, 1998). The 15 Pa threshold is considerably higher than the critical shear stress expected for agricultural surface erosion processes (Alberts et al., 1995), and we do not expect such high critical shear stress conditions across the soils of the present study. The *b* exponent represents the flow condition to initiate erosion also showed a lack of sensitivity until reaching very low values for the exponent of approximately 0.2. The very low threshold for sensitivity reflects conditions of viscous, laminar flow conditions. Results show that such laminar conditions would double sediment connectivity in the watershed, and these conditions reflect the dominance of pure sheet flow or perhaps pseudo-laminar flows with extremely high sediment concentrations. Nevertheless, we do not expect these conditions in the concentrated turbulent flow pathways to occur in the present study (Montgomery and Dietrich, 1994; Vandaele et al., 1996; Torri and Poesen, 2014). The *c*

factor represents additional fluid and sediment pathways in the landscape that are not captured by the surface transport formula, and previous research emphasized the ability of the *c* factor to reflect piping. Torri and Poesen (2014) suggest a range of 0.1 to 0.4 reflects pronounced piping. Results show that a *c* factor in this range would nearly double sediment connectivity estimated from the model, although the South Elkhorn soils do not experience piping given the lack of soil texture variation vertically in the soil column (Fox et al., 2006). The South Elkhorn does have immature karst and 13% of the drainage area is sinkhole controlled. Rather than adjusting the *c* factor to try and account for the karst, we accounted for sinkholes within the probability of buffers term (see below for additional discussion of karst sinkholes).

We next investigated the sensitivity of geospatial resolution upon the results. DEM resolution showed a substantial impact on the results. The 9 m by 9 m DEM estimated the probability of sediment connectivity to be nearly two times greater than the 1.5 m by 1.5 m DEM for the most highly connected days of the year (Figure 6b). The sensitivity of the DEMs was a noteworthy result, and, on average, the deviation between the 1.5 m by 1.5 m and 9 m by 9 m DEM was 80%. The low-resolution DEM always estimated greater connectivity.

We carried forward the higher resolution, 1.5 m by 1.5 m, DEM when estimating sediment connectivity for several reasons. The higher resolution DEM better reflects the microtopography of the landscape and its ability, or lack thereof, to accumulate water, which agrees with recent sentiment by Cavalli et al. (2013) that higher resolution DEMs better reflect the actual landscape in connectivity studies. Visually, broad regions of connectivity and disconnectivity agree with one another for both the 1.5 m by 1.5 m and 9 m by 9 m DEMs (see Figure 6c). However, results show the 1.5 m by 1.5 m DEM better captures the microtopography including steeper gradient swales where water accumulates before entering the stream while the 9 m by 9 m DEM masks across leads and ridges in the topography and treats entire sub-regions of the land surface as connected. Also, locally flat surfaces recognizable within the 1.5 m by 1.5 m DEM were masked in 9 m by 9 m DEM and further increased the connectivity estimate. We inspected the results and found delineation of the landscape contributing area was one mathematical reason for higher connectivity estimates from the low-resolution DEM. As the upstream contributing area

increases so too does the accumulated runoff to transport sediment in the ephemeral pathways of the uplands reflected *via* the probability of upstream transport. The lower resolution 9 m by 9 m DEM masks across locally flat surfaces in upstream geospatial scales and in turn increases the contributing area and the probability of connectivity.

We considered the sensitivity of karst sinkholes upon connectivity results. Sinkholes intercept approximately 13% of the watershed's drainage and are distributed throughout the landscape (see Figure 7). We realized the potential importance of the sinkholes to impart sediment disconnectivity due to buffering lateral transport (i.e., $P(B)=1$) because sinkhole drainage areas may pirate transported sediment or sediment may deposit within the surface depression. At the same time, pirated sediment may resurface at springheads and reconnect back to the fluvial network (i.e., $P(B)=0$). This consideration was also deemed possible because dye traces showed that sinkhole pathways are consistent with the dendritic surface network in this watershed (see insert in Figure 7). We considered a net disconnectivity versus net connectivity effect of the sinkhole drainage areas and found that the uncertainty from the karst features had a rather small effect on results. For example, the probability of connectivity varied from 12.1% to 13.5% on a wet day of the simulation period when including the karst uncertainty. The result is commensurate with the 13% coverage of sinkhole drainage in the South Elkhorn. At the same time, the results highlight the potential of karst sinkholes to cause sediment disconnectivity from microtopography. We include this uncertainty component by accounting for the range of results throughout the remainder of the paper.

Generally, predicted and observed daily sediment flux values showed good agreement when comparing data and modeling results (Figure 8a). Assimilation of hydrologic data during calibration and validation reduced the propagation of error from the hydrologic model to the watershed erosion model, and we found substantial differences in daily sediment flux when comparing assimilated and non-assimilated model runs (Figure 8b). However, data assimilation did not affect net sediment yield results at the end of the simulation period. The results highlight the effectiveness of our data assimilation procedure for calibration purposes on an event-based daily to multi-day basis but also the annual prediction capabilities of the watershed erosion model for times when data assimilation is not possible. Annual sediment yield for the watershed ($3{,}300 \pm 140$ t y^{-1})

was 2% more than annual sediment yield estimated for the upland contribution reported in Russo and Fox (2012) for the same period, which provides further verification of the modeling results. Sensitivity analysis of parameters calibrated in the watershed erosion model showed the importance of the erodibility coefficient (Figure 8c), which varies widely in the literature (e.g., review in Hanson and Simon, 2001). The time of concentration also showed moderate sensitivity upon sediment flux while the impact of the friction coefficient and critical shear stress of sediment to resist erosion was marginal upon the sediment yield results.

1.4.2 Watershed Scale Results:

The probability of sediment connectivity is shown throughout the year in Figure 9 and reached a maximum value of 12.8 ± 0.7%, on March 12 (day 72 of the study year) when high rainfall fell on wet soils. The results imply 12.8 ± 0.7% of the watershed's surface had the potential to erode sediment on March 12. The mean sediment connectivity for the 104 days with some connectivity was 2.26 ± 0.1% and the standard deviation was 3.5 ± 0.15%. Sediment connectivity ranged from 0 to 1.5% for 67 of the 104 days and ranged from 1.7% to 13% for remaining 37 days (Figure 10a). The beta distribution best fit the dynamic connectivity results. The beta distribution is a logical choice for representation of the dynamic probability given the beta distribution is continuous but bounded by 0 and 1, and therefore is suitable for representing the behavior of probabilities.

Results showed that the probability of sediment connectivity alone was not a good predictor of sediment flux. We highlight this idea in Figure 10b, where temporal results are different for the probability of sediment connectivity and sediment flux. Obviously, sediment flux occurs only when some sediment connectivity exists; but sediment connectivity by itself does not predict sediment flux, as recently noted by Bracken et al. (2015).

Modeling results estimate that sediment connectivity was spatially distributed across the watershed and that the northern region of the South Elkhorn Watershed exhibits the highest sediment connectivity. We attribute the spatially distributed results to a shift in the soil conditions in this region of the watershed. Engineering properties of the soils shift from being dominated by moderately drained soils (i.e., NRCS hydrologic soil group

B) in the southern and central regions of the watershed to dominated by poorly and very poorly drained soils (i.e., NRCS hydrologic groups C and D) in the northern region of the watershed. The NRCS attributes the shift in the engineering properties to the decrease in percent sand and increase in percent fine clay in the northern region of the watershed (NRCS, 2009). Sediment connectivity is slightly higher in the central-eastern region of the watershed relative to the central-western and southern regions. The result reflects the higher contribution of urban and suburban land uses in the central-eastern region, which in turn produce impervious surfaces, higher estimated runoff, and therefore higher values for the probability of hydrologic detachment and probability of upstream hydrologic transport.

We also assessed longitudinal variability of sediment connectivity by investigating the probability of sediment connectivity from catchment (~1 km^2) to mid-sized watershed scales (~60 km^2). Longitudinal variability results included a weak increase in the probability of sediment connectivity with scale (Figure 10c), and the variance of sediment connectivity was highest at the smaller scale. The longitudinal variability of sediment connectivity reflects competing processes operating at different scales in a watershed configuration (Phillips, 2003; Borselli et al., 2008; Fryirs, 2013). Researchers suggest relatively steep landscape gradients promote sediment connectivity at smaller scales such as hillslope and small catchment scales (Fryirs et al., 2007). On the other hand, as the watershed scale increases, fluid accumulation has the potential to increase fluid shear stress and produce hydrologic connectivity for conveying sediment (Borselli et al., 2008). The weak power function result tends to suggest the latter process, i.e., flow accumulation, for the South Elkhorn, which we attribute to the dominance of erosion in concentrated flow pathways as opposed to sheet erosion processes.

1.4.3 Features of Connectivity and Disconnectivity:

Unsurprisingly, sediment connectivity was high for the ephemeral network, steep slopes in newly constructed areas, ditches adjacent to roadways, and hillslopes adjacent to the stream (see Figure 11). In turn, erosion-prone landscape features showed sediment flux from these sources, and the watershed erosion model results provided a spatially explicit estimate of erosion rates (see Figure 12). The results further validated that our model was working well because past research has suggested that erosion dominates from rill erosion,

ephemeral gully erosion, and concentrated flow pathways in the watershed (Gumbert, 2017; Smallwood, 2017), and livestock and construction sites have been suggested to show increased detachment rates (Evans, 2017).

More surprisingly, sediment disconnectivity was dominated by microtopography across the gently rolling landscape. The greatest control on disconnectivity was the probability of upstream transport (Figure 5), and upon further inspection of results from the high-resolution DEM, we found that the disconnectivity occurs because undulating land surfaces produces local low to zero gradient surfaces, i.e., flat slopes. The microtopography from the undulations causes small-sources of disconnectivity because runoff loses its energy in small depressions. Our field visits during storm events justified the geospatial model results. We found that even during intense rainfall events when runoff and flow accumulation were pronounced in ditches and swales, there was little to no runoff or sediment transport across pastureland surfaces and rather pooling within microtopographic depressions. The microtopography identified with the high-resolution DEM is noteworthy given the watershed itself was not flat (i.e., average hillslope gradient was 7%).

The potential of karst microtopography to impart disconnectivity is also noteworthy. Sinkhole microtopography may pirate transported sediment or cause fallout within depressions similarly to floodplain deposition, thus increasing lateral disconnectivity. While sinkhole impact was relatively small in this basin, sinkhole microtopography could potentially act as the dominant in neighboring basins in this region (see Table 2) as well as other regions with karst morphology.

Other recent studies corroborate the importance of microtopography upon sediment connectivity. Phillips et al., (2017) shows that microtopography associated with pits from tree uprooting and local surface armoring of rock fragments can disconnect erosion processes in an old-growth forest. Lopez et al. (2017) shows that a high-resolution DEM is useful to reveal how microtopography impacts hydrological connectivity for roads and skidding trails in forest catchments. The usefulness of high-resolution DEMs is encouraging for sediment connectivity studies.

The floodplains are another disconnecting feature, yet the floodplains did not dominate disconnectivity as perhaps sometimes assumed. Based on our field assessment

while walking the stream corridor, we initially presumed such a dominant behavior for the Upper South Elkhorn Watershed due to the prevalence of floodplains with flat gradients adjacent to the stream network. However, after completing the spatially explicit modeling, we found that floodplains buffered only 5% of the catchment. We recognized that the net effect of floodplains causes disconnectivity beyond the 5% measure due to the extension of low gradient surfaces forcing deposition of sediment from adjacent hillslopes draining to the floodplains. Nevertheless, the net effect of the floodplains was only 35% disconnectivity, which was low relative to the probabilities of detachment, upstream transport, and downstream transport (i.e., 55 to 90% disconnectivity during hydrologic events, see example in Figure 5b).

1.5 DISCUSSION

1.5.1 Spatially explicit and computational advancement of watershed erosion modeling:

Our results show the efficacy of the probability of sediment connectivity approach to advance watershed erosion modeling for several reasons. First, results show that the approach accounts for spatial variability across the landscape by coupling the probability of sediment connectivity with the high-resolution digital elevation model (DEM). The high-resolution DEM helps resolve specific erosion features and sources, such as sediment connectivity around roadside ditches and disconnectivity from flat land surface gradients. In general, advantages of the 1.5 meter by 1.5 meter DEM suggest the researcher acquire the highest resolution DEM possible, which tends to agree with sentiment in the literature (Cavalli et al., 2013). However, some qualification is needed, and we suggest an upper limit is conceivable based on the underlying fluid mechanics assumptions. For example, calculations of both the probability of detachment and the probability of transport assume the landscape gradient equals the energy gradient of the fluid. These simplified representations assume the fluid mechanics in a geospatial cell may be treated as uniform flow. The assumption is reasonable, albeit a recognized practical simplification, when the flow depth across the landscape is on the order of a few centimeters while the streamwise length scale is two orders of magnitude greater. The assumption may break down and require further investigation as to its sensitivity as the DEM resolution increases to a

resolution of a few centimeters—a resolution that is no longer out of the question as technology continues to improve. In this case, the flow depth of runoff would be on the same order of magnitude as the resolution of the streamwise length scale, and individual large roughness elements act as hydraulic controls indicuing non-uniformity to the flow. The landscape gradient in the profile of the hydraulic controls will be more extreme than the energy gradient of the flow. For example, an adverse landscape gradient has the potential to predict disconnectivity when the decelerating flow still has sufficient fluid shear stress to detach sediment. We point out that applying a very high, few centimeter resolution DEM in the probability of sediment connectivity does not negate the multiplicative theoretical basis for intersecting probabilities. However, researchers might consider parameterizing the flow as non-uniform across the landscape for such a high-resolution application.

Second, our results show that the watershed erosion model structure accounts for supply, shear, and transport criteria of sediment transport. Coupling sediment connectivity in watershed erosion models is a new area of research, and we suggest the approach provides the modeler with an added tool to account for sediment transport criteria *via* permutations of erosion formulae and connectivity principles. We highlight our model application as one such permutation. The model approach considers sediment supply limitations in a spatially explicit manner by calculating the probability of sediment supply using geospatial analyses. The approach considers transport limitations explicitly by calculating upstream and downstream probabilities of transport at each cell (see Figure 4) and by identifying buffer discontinuities using field reconnaissance. With supply and transport accounted, we emphasized the shear limitation when coupling to the surface erosion formulae. We maximized the advantages of the spatially explicit datasets and the quantitative hydraulic formulae when considering shear, supply and transport limitations for the specific conditions of our system. We expect researchers may find many other permutations of erosion formulae and connectivity principles in future modeling of watershed erosion.

Third, we highlight that reducing the cost of computational hydrology is another attractive feature of a connectivity-based watershed erosion model. In the present application, the watershed modeling included calculations for 3×10^{10} space-time

combinations. The probability of sediment connectivity subroutine added explicit formulae to the watershed erosion model, and a geospatial modeling software performed calculations requiring several hours to run on a desktop PC. Considering all space-time combinations in the watershed modeling, only 0.7% of the combinations contained connectivity. Therefore, the model carried forward only 2×10^8 space-time combinations in the hydraulic and sediment transport formulae and removed 2.98×10^{10} space-time calculations. Hydraulic calculations are often computationally intensive requiring solution of implicit formulae at each space-time step. Computational sediment transport is even more demanding as higher dimensional formulae (e.g., see above discussion of flow non-uniformities) and as researchers implement advanced routing methods. Thus, we suggest the inclusion of the connectivity-based watershed erosion model may have a net reduction in overall computational complexity. Further, the connectivity-based watershed erosion model provides the flexibility to include advanced computational complexity. Simulation of the breach of a buffer within the watershed configuration (e.g., see descriptions in Bracken et al., 2015) allows calling up sophisticated hydraulic and sediment subroutines that could simulate such spatiotemporal feedback and connectivity between sediment sources and sinks.

1.5.2 Extending our view of sediment disconnectivity and connectivity:

The newly quantified features of the gently rolling watershed complement existing knowledge and extend our view of disconnectivity. Our results agree with the concept that the gently rolling watershed morphology includes relatively stable land surfaces, ephemeral flow pathways, and the presence of decoupled floodplains (Jarrit and Lawrence, 2007; Ford and Fox, 2014) that can lead to trapping of as much as 90% of mobilized sediments in disconnected land surfaces (Meade et al., 1990; Hupp, 2000; Walling et al., 2006). Our results reflect this idea and show spatial disconnectivity on the order of 90% on the wettest day of the year. Microtopography across the landscape dominates disconnectivity because local low to zero gradient surfaces cause the ponding of runoff and sediment deposition in the undulating landscape. Our result is corroborated by past studies where sediment erosion from diffusive processes on land surfaces of the uplands only travel a spatial scale of several meters or less (Roering et al., 1999) as well as by recent results

highlighting the influence of microtopography in forest catchments (Lopez et al., 2017; Phillips et al., 2017). Karst microtopography and the ability of sinkholes to pirate transported sediment and cause lateral disconnectivity is also noteworthy for the gently rolling watershed. The ephemeral network represents the most connected morphology of the uplands; however, disconnectivity persists through much of the ephemeral network even during high magnitude events. Floodplains cause lateral disconnectivity due to their potential to break connectivity between the ephemeral network and main channel, which is consistent with the work of others (Goudie, 2004; Florsheim et al., 2006; Kronvang et al., 2007; Jaeger et al., 2017).

Only about 10% of the uplands showed lateral sediment connectivity with the stream for the gently rolling watershed, which contrasts steeper gradient systems where connectivity results are much higher, e.g., Fryirs et al., (2007). Fryirs et al., (2007) predicted the active contributing area for four landscape units in the upper Hunter catchment in Australia, which have relatively high elevation, deep dissection, and a rugged, hilly landscape. Nearly 50% of the catchment was connected for a moderate storm event, which contrasts greatly with our gently rolling results of 10% connectivity for one of the most hydrologically intensive days of the year. We caution fine scale quantitative comparisons of papers given the modeling approaches applied and DEM resolution applied. Nevertheless, we mention the vast differences in connectivity that cast gently rolling watersheds as event-resilient, disconnected systems.

Regarding sediment connectivity, one potentially interesting result is the net importance of ditches and roadside gullies in the urban regions. The urban regions showed net higher connectivity than surrounding agricultural regions. The importance of roadways to induce erosion and sediment connectivity has been discussed previously for mountainous catchments (Latocha, 2014), and urban sprawl, i.e., urbanization, has been well understood to induce gully formation and channeling processes (Trimble, 1993). However, few papers to our knowledge have reported the net importance of roadway ditches and gullies in well-established urban environments. More generally, these ephemeral networks of urban and suburban regions may exhibit more sediment connectivity than agricultural regions in gently rolling systems, given the presence of a higher concentration of impervious surfaces and the well-defined drainage network

promiting flow accumulation. The exception would likely be poorly managed watersheds where agricultural best management practices have yet to be adopted.

1.6 CONCLUSIONS

Model evaluation results verify the capability of the probability of sediment connectivity to be integrated within watershed erosion modeling. We highlight the potential usefulness of the approach. The modeling approach accounts for the spatial variability of sediment connectivity across the landscape, and high-resolution DEMs were able to predict erosion features impacting sediment connectivity and disconnectivity. We suggest this approach provides the modeler with an added tool to account for sediment transport criteria given that each of the individual sediment probabilities exhibit some importance and coupling with erosion formulae provides sediment flux estimates. We also highlight the potential ability of the approach to reduce the cost of computational hydrology as modeling tools rely more-and-more on high-resolution prediction.

In the gently rolling watershed, results show that sediment connectivity occurs within ephemeral pathways across the uplands, but disconnectivity dominates the watershed configuration both spatially and temporally. All morphologic levels of the uplands exhibit disconnecting features including microtopography causing low energy undulating surfaces, karst sinkholes disconnecting drainage areas, and floodplains that de-couple the hillslopes from the stream corridor. Only 12.8 ± 0.7% of the gently rolling watershed shows sediment connectivity on the wettest day of the year. Spatially, results highlight the importance of sediment connectivity in urban and suburban pathways given the well-defined channel network and influence of impervious surfaces. Dynamic and longitudinal results suggest the beta distribution and power function, respectively, might be further investigated for their ability to reflect the gently rolling watershed's connectivity more generally.

1.7 ACKNOWLEDGEMENTS

We thank an anonymous reviewer for comments that helped us to improve greatly the quality of the work. We gratefully acknowledge the financial support of this research under National Science Foundation Award 163288.

Table 1.1 Probability theory in sediment transport studies.

Sediment Transport Topics that Adopt Probability Theory	Examples of Published Studies
Incipient motion and entrainment	Gessler, 1970; Grass, 1970; He and Han, 1982; Torri et al., 1990; Hsu and Holly, 1992; Cheng and Chiew, 1998; Lisle et al., 1998; Papanicolaou et al., 2002; Wu and Chou, 2003
Sediment deposition and residence time	Dietrich et al., 1982; Celik and Rodi, 1988; Lumborg, 2004; Malmon et al., 2003; Pan and Huang, 2010
Erosion modeling inputs and parameters	Wright and Webster, 1991; Govindaraju and Kavvas, 1992; Lewis et al., 1994; Quinton, 1997; Lisle et al., 1998; Haschenburger, 1999; Govindaraju, 1998; Foster and Fell, 2000; Baban and Yusof, 2001; Robichaud et al., 2007
Sediment export and flux	Burns, 1979; Verhoff et al., 1979; Tazioli, 1981; Mehagan et al., 1991; Borselli et al., 2008

Table 1.2. Karst sinkhole drainage of the South Elkhorn and other neighboring Inner Bluegrass watersheds.

*HUC 14 Watershed	Watershed Area (km^2)	Sinkhole Drainage Area (km^2)	Percent Karst
Upper South Elkhorn Watershed	65.1	8.3	12.8%
Cane Run Watershed	118.0	75.2	63.8%
Sinking Creek Watershed	18.7	18.5	98.9%
Steels Run Watershed	18.2	4.8	26.3%
Lee Branch	61.4	27.3	44.5%

*HUC 14 delineations are consistent with the revised USGS Watershed Boundary Dataset and the Hydrologic Unit Code (HUC) 14 description is consistent with Seaber et al. (1987).

Table 1.3. Statistical metrics for calibration and validation of the hydrologic model.

Optimization Gage	Total Flow Calibration (For the period 1/1/2006-12/31/2010)				Total Flow Validation (For the period 1/1/2011-12/31/2013)			
	R^2	RSR	PBIAS%	NS	R^2	RSR	PBIAS%	NS
USGS-03289000	0.61	0.66	18.43	0.56	0.76	0.56	5.5	0.69

Table 1.4 Erosion model inputs and parameters.

Parameter	Description	Value	Units
A_1	Contributing Area, Bin 1	116	m^2
A_3	Contributing Area, Bin 2	951	m^2
A_3	Contributing Area, Bin 3	34,079	m^2
τ_{cr}	Critical Shear Stress	3.5	Pa
S_1	Longitudinal Slope, Bin 1	0.16	m/m
S_2	Longitudinal Slope, Bin 2	0.13	m/m
S_3	Longitudinal Slope, Bin 3	0.12	m/m
w_1	Channel Width, Bin 1	0.088	m
w_2	Channel Width, Bin 2	0.13	m
w_3	Channel Width, Bin 3	0.44	m
ε/D	Relative Roughness	0.1	Unitless
F	Darcy-Weisbach Friction Factor	0.102	Unitless
ρ_d	Bulk Density of Eroded Sediment	1,400	kg/m^3
t_1	Storm Length, Erosion Time Bin 1	0.0833	hr
t_2	Storm Length, Erosion Time Bin 2	0.25	hr
t_3	Storm Length, Erosion Time Bin 3	0.5	hr
k_d	Erodibility Coefficient	0.0055	$cm^3/N\text{-}s$
L_1	Channel Length, Bin 1	Varies daily	m
L_2	Channel Length, Bin 2	Varies daily	m
L_3	Channel Length, Bin 3	Varies daily	m
ρ_w	Density of Fluid	1,000	kg/m^3

Figure 1.1. Watershed erosion modeling framework.

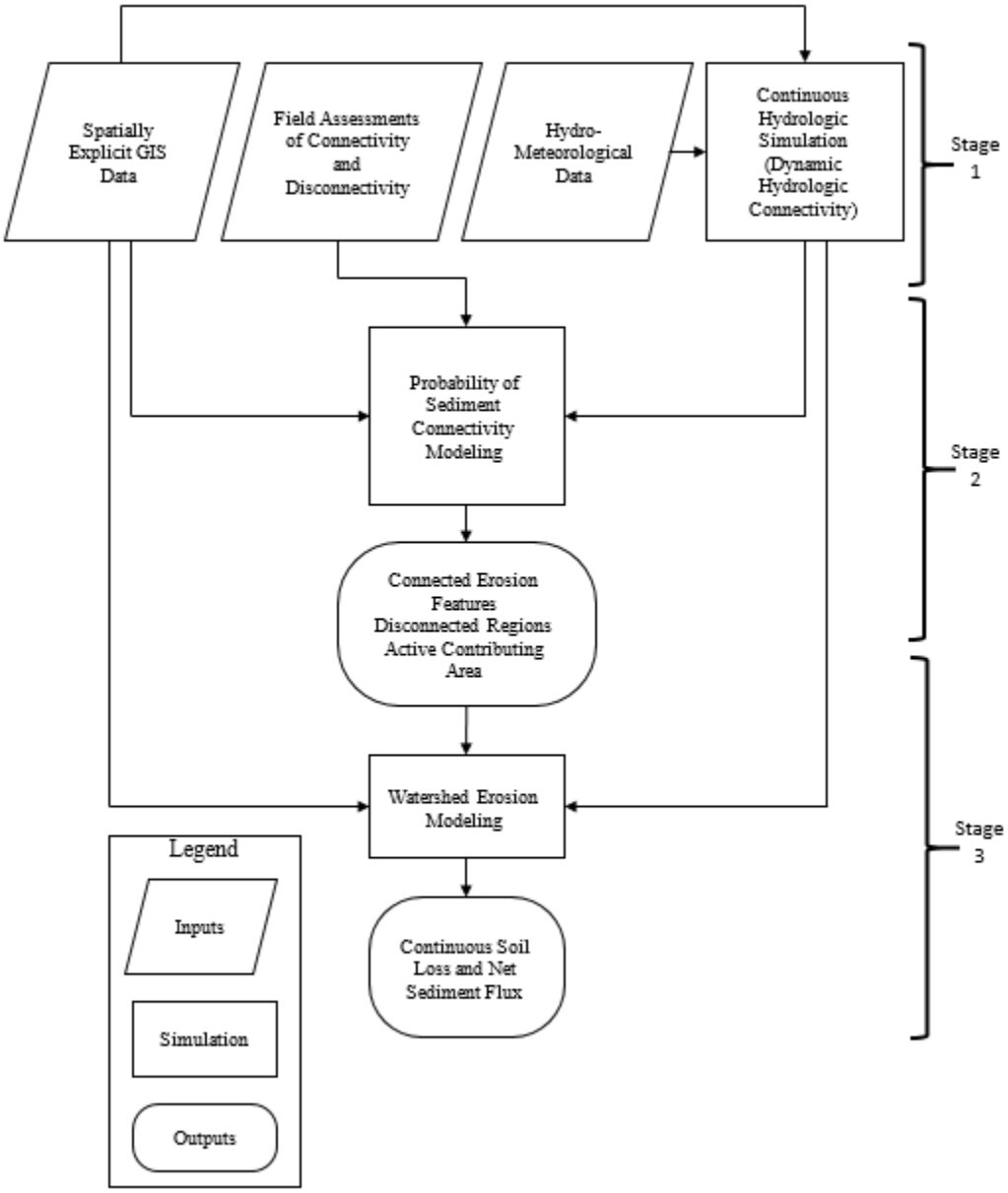

Figure 1.2. Probability-based model of sediment connectivity.

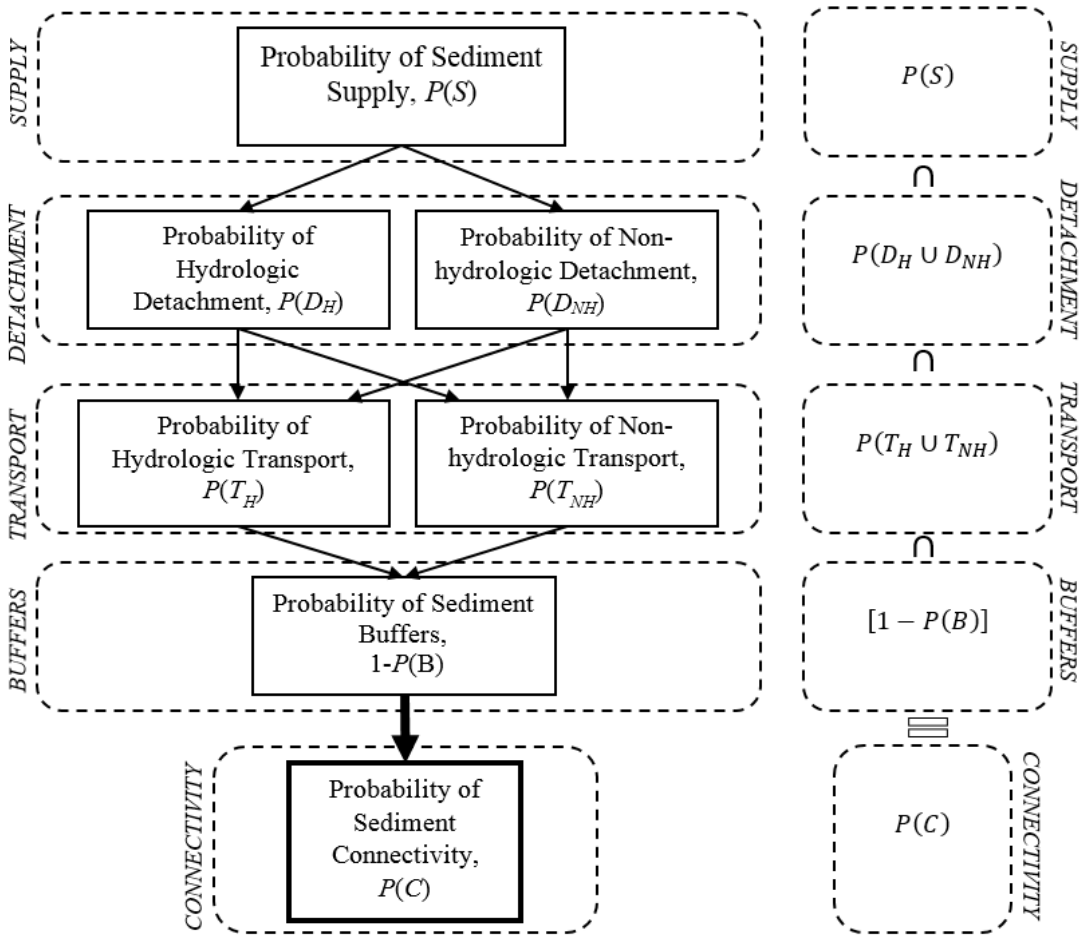

Figure 1.3. Study watershed location within the Kentucky River Basin, USA and land use**.**

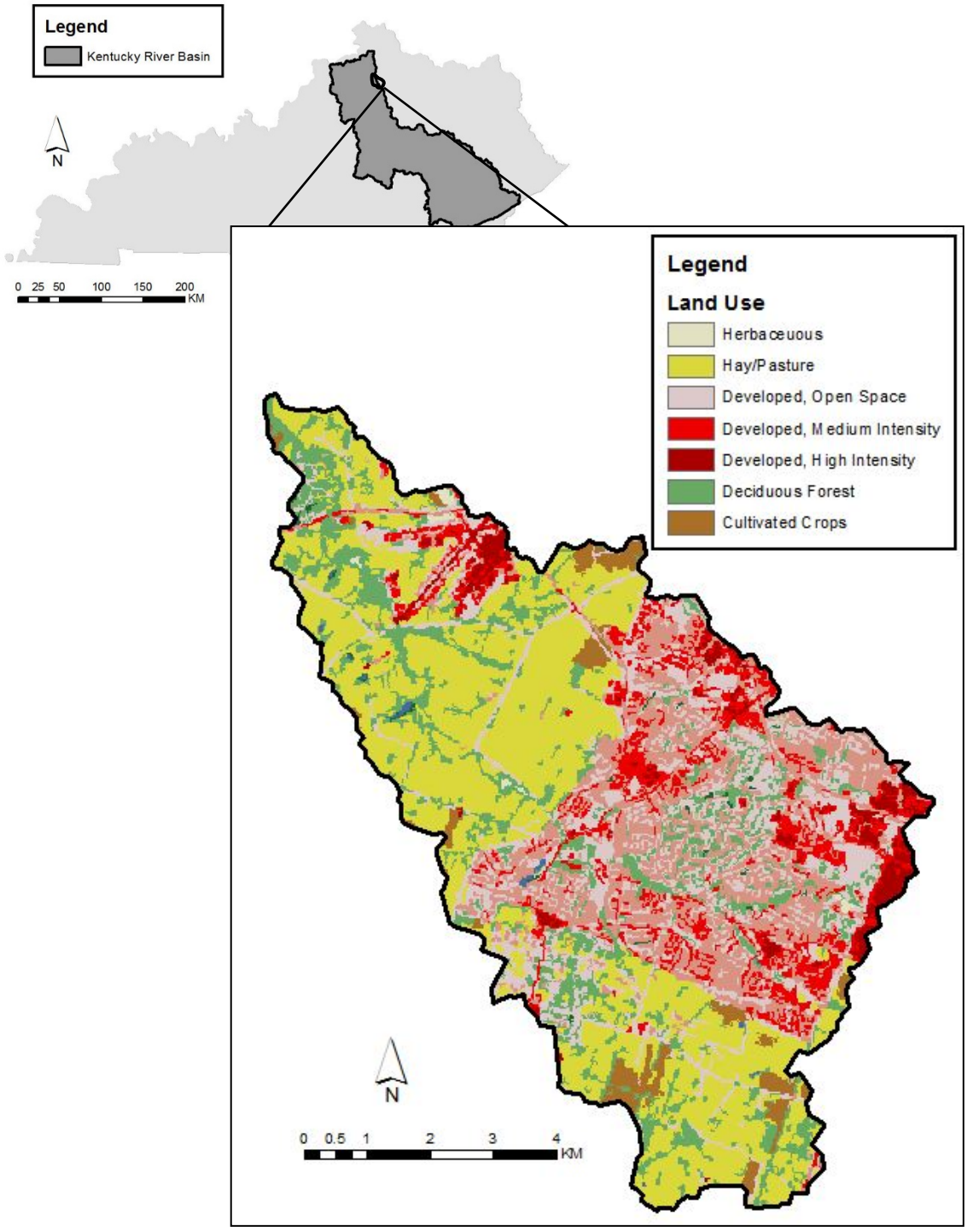

Figure 1.4. Sediment erosion processes exemplified within probability of connectivity results.

(a) Probability of sediment supply

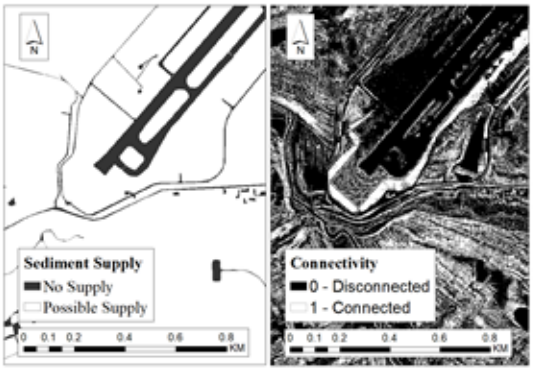

(b) Probability of sediment detachment

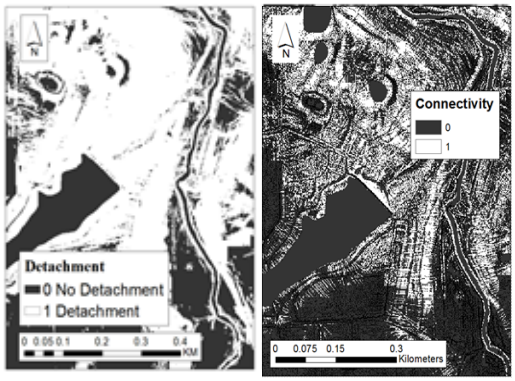

(c) Probability of downstream transport

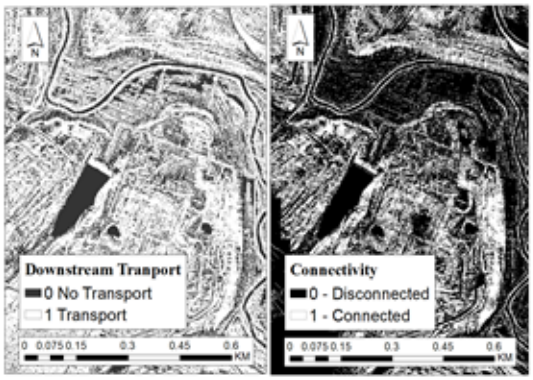

(d) Probability of upstream transport

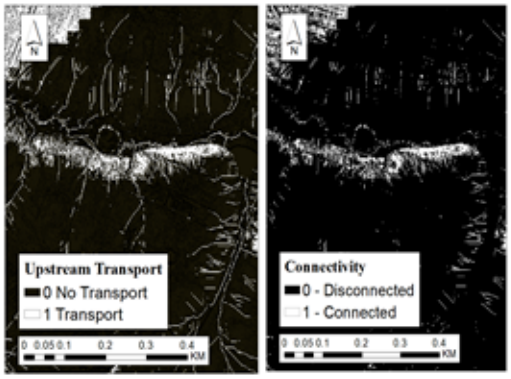

(e) Probability of buffers

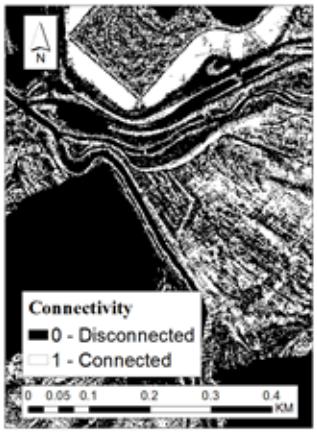

Figure 1.5. Results of examples of net impact of individual probabilities upon the probability of sediment connectivity incorporating karst buffers. (a) Individual probabilities of connectivity for Day 72 within the simulation period. (b) Individual probabilities of connectivity for Day 138 within the simulation period.

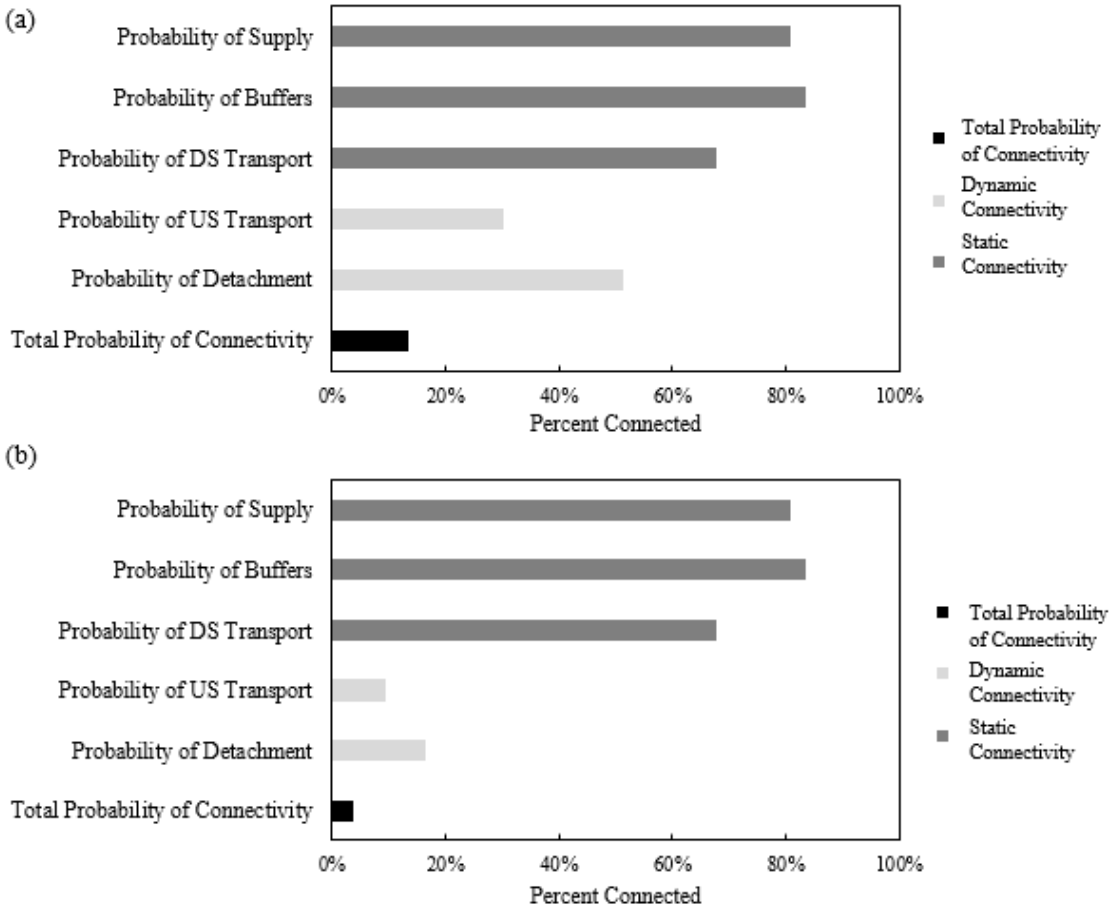

Figure 1.6. Sensitivity analysis for the probability of sediment connectivity. (a) Sensitivity of individual parameters. (b) Sensitivity of geospatial resolution. (c) Comparison of the 1.5 m by 1.5 m DEM and the 9 m by 9 m DEM.

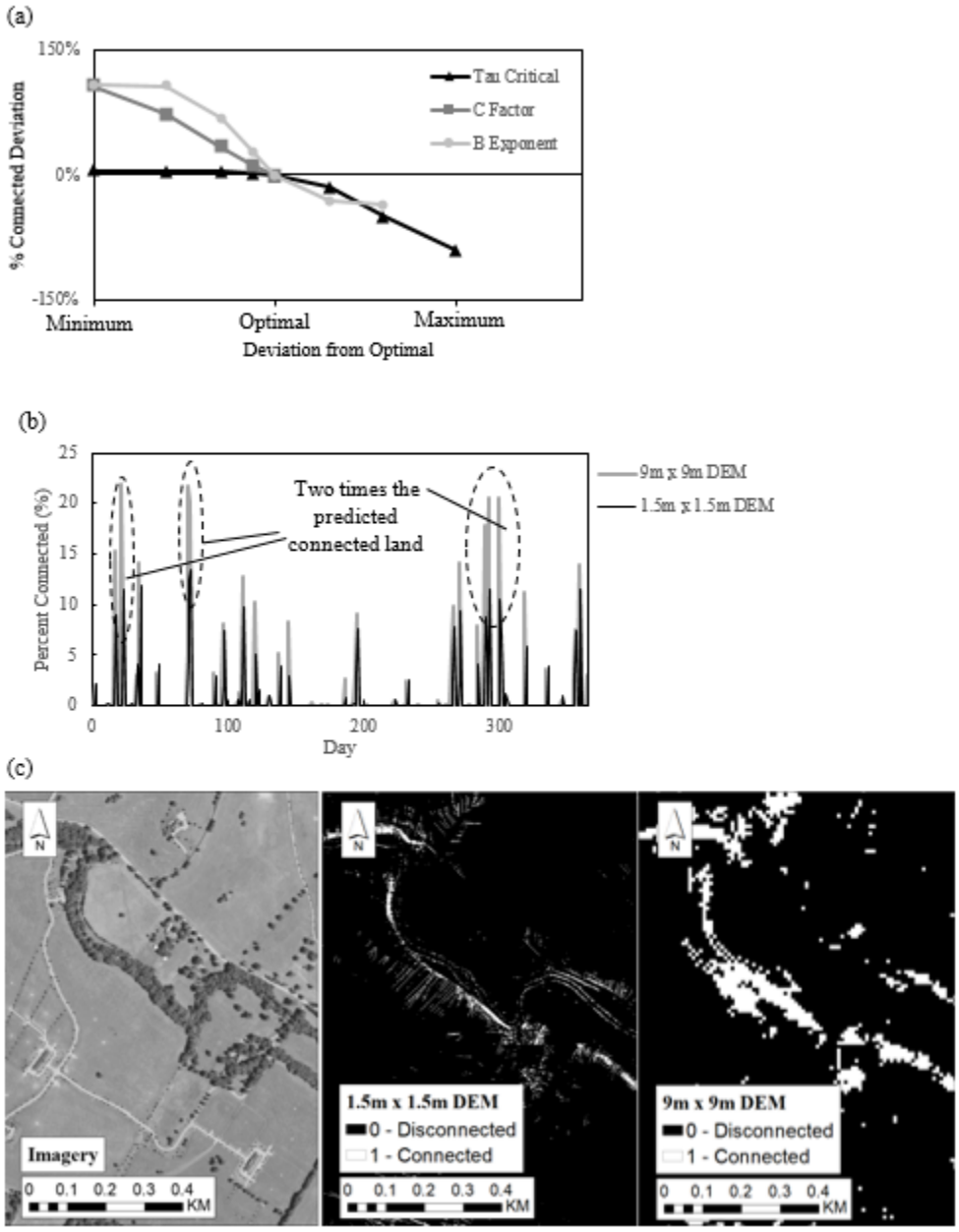

Figure 1.7. Sinkhole map for the Upper South Elkhorn. Karst features drain 13% of the watershed area. The insert illustrates dye trace flow pathways performed by the Kentucky Geological Survey. Dye traces show that sinkhole pathways are consistent with the dendritic surface network, which emphasizes the fluvial dominance of this particular system. The South Elkhorn's immature karst is consistent with the findings of Phillips et al. (2004) for the Inner Bluegrass.

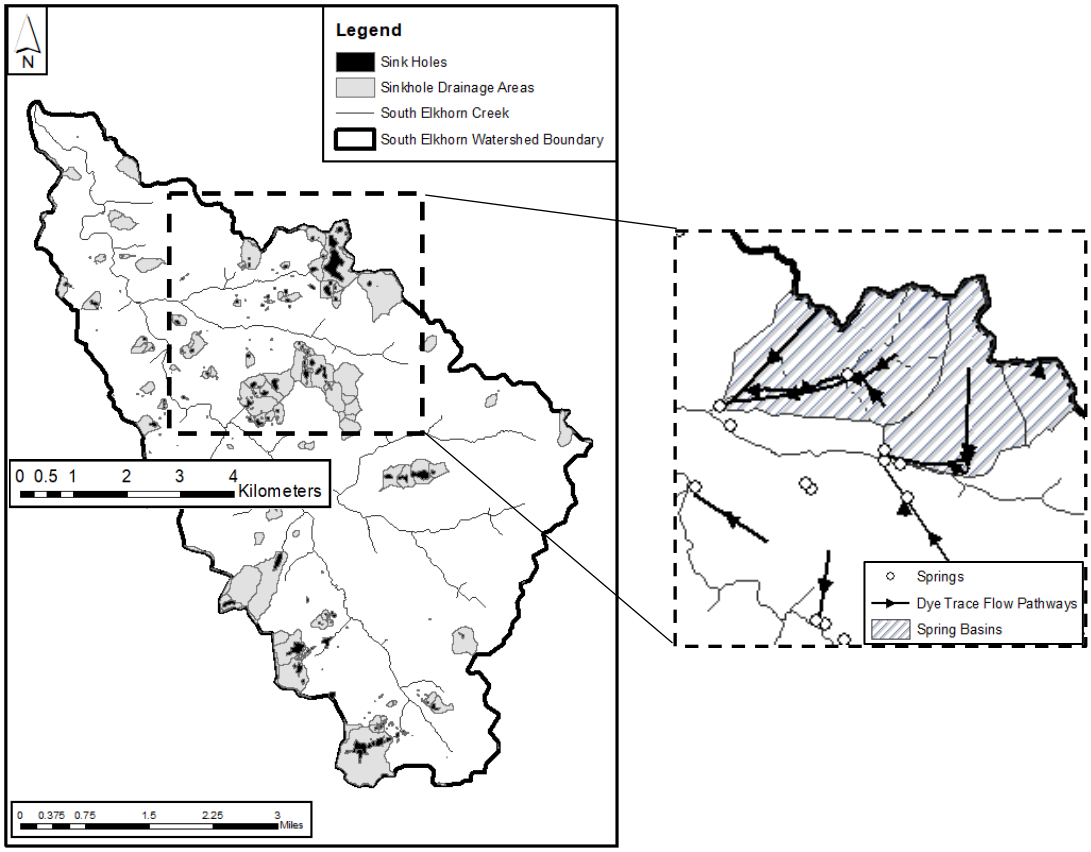

Figure 1.8. Evaluation of the watershed erosion model results; R^2 = 0.95. (a) Predicted and observed sediment flux for specified days of the study period reflecting the upper limit where karst is assumed to be connected. (b) Sediment flux estimated with non-assimilated and assimilated streamflow data not accounting for the influence of karst. (c) Sensitivity analysis of parameters in the sediment transport model.

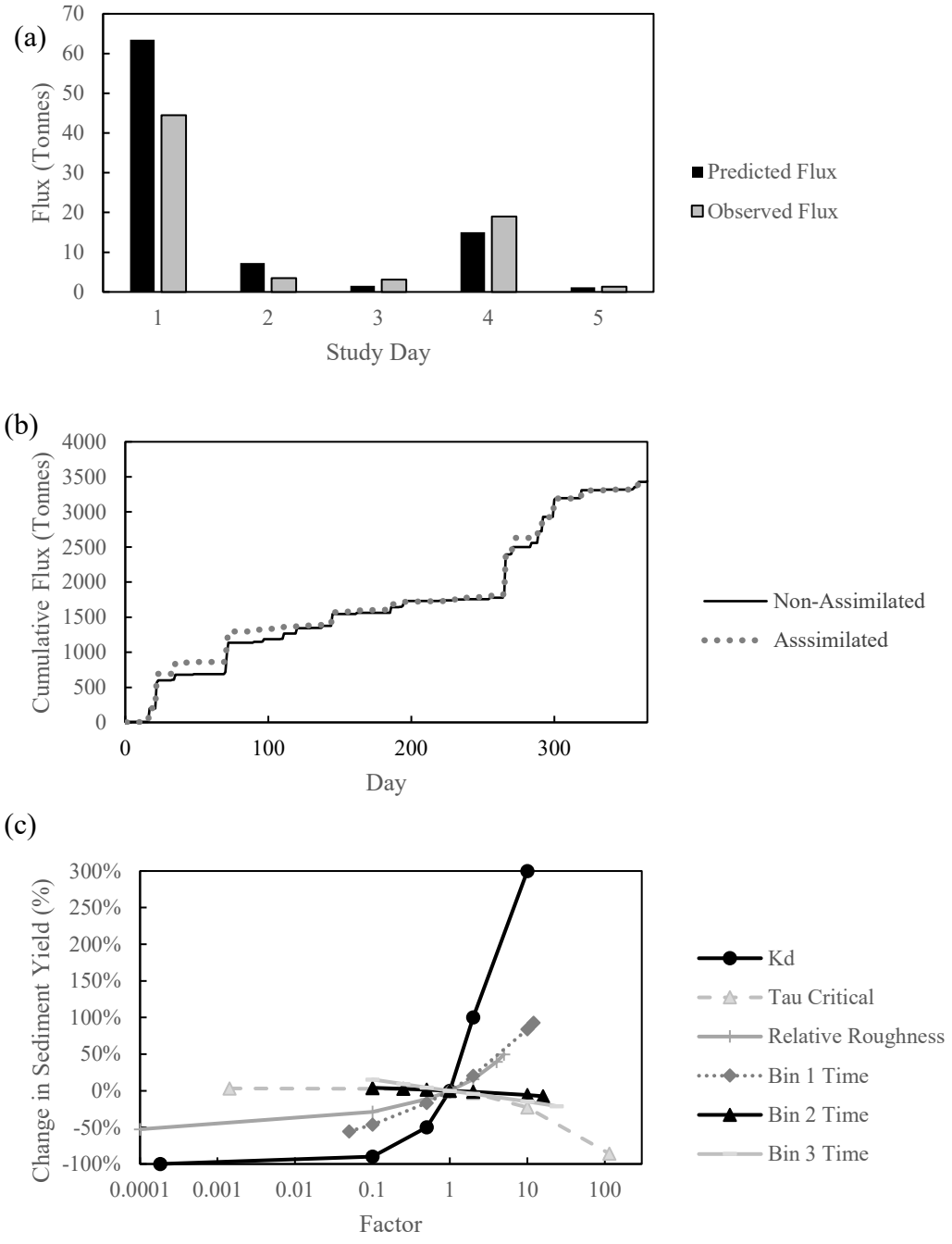

Figure 1.9. Probability of sediment connectivity results for the South Elkhorn Watershed. (a) Probability of sediment connectivity results throughout one year reflecting the influence of karst. (b) Probability of sediment connectivity for March 12, 2006 (day 72).

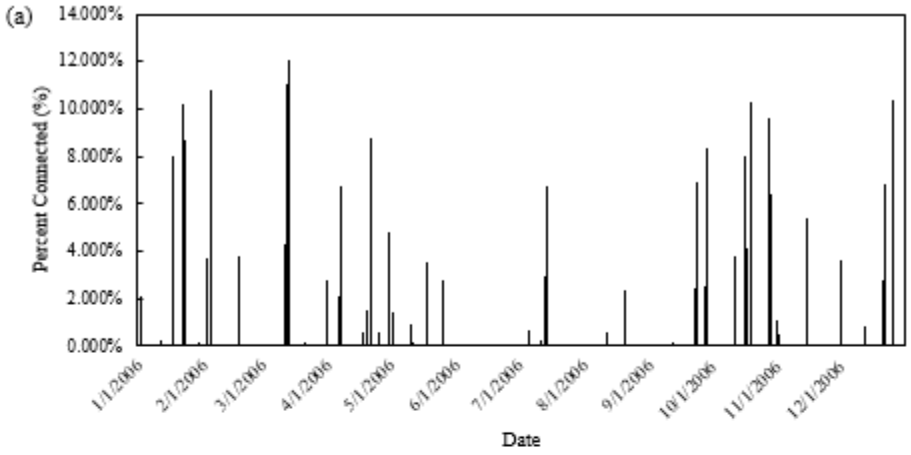

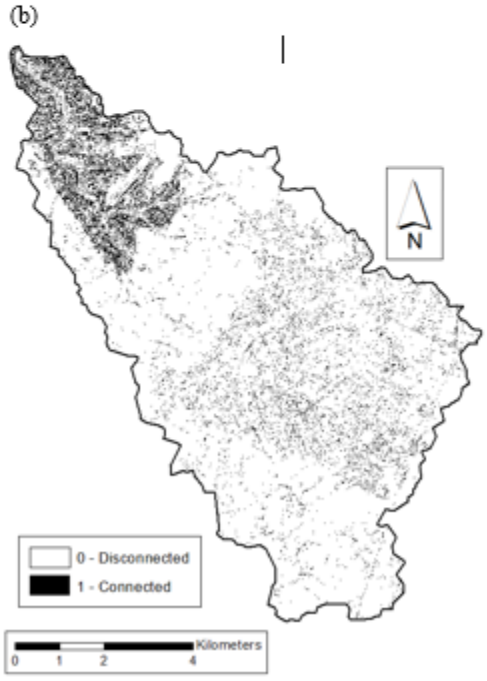

Figure 1.10. (a) Frequency distribution for the probability of sediment connectivity (connected days only) accounting for influence of karst. (b) Results of percent connected versus sediment flux accounting for influence of karst. (c) Probability of sediment connectivity versus catchment area.

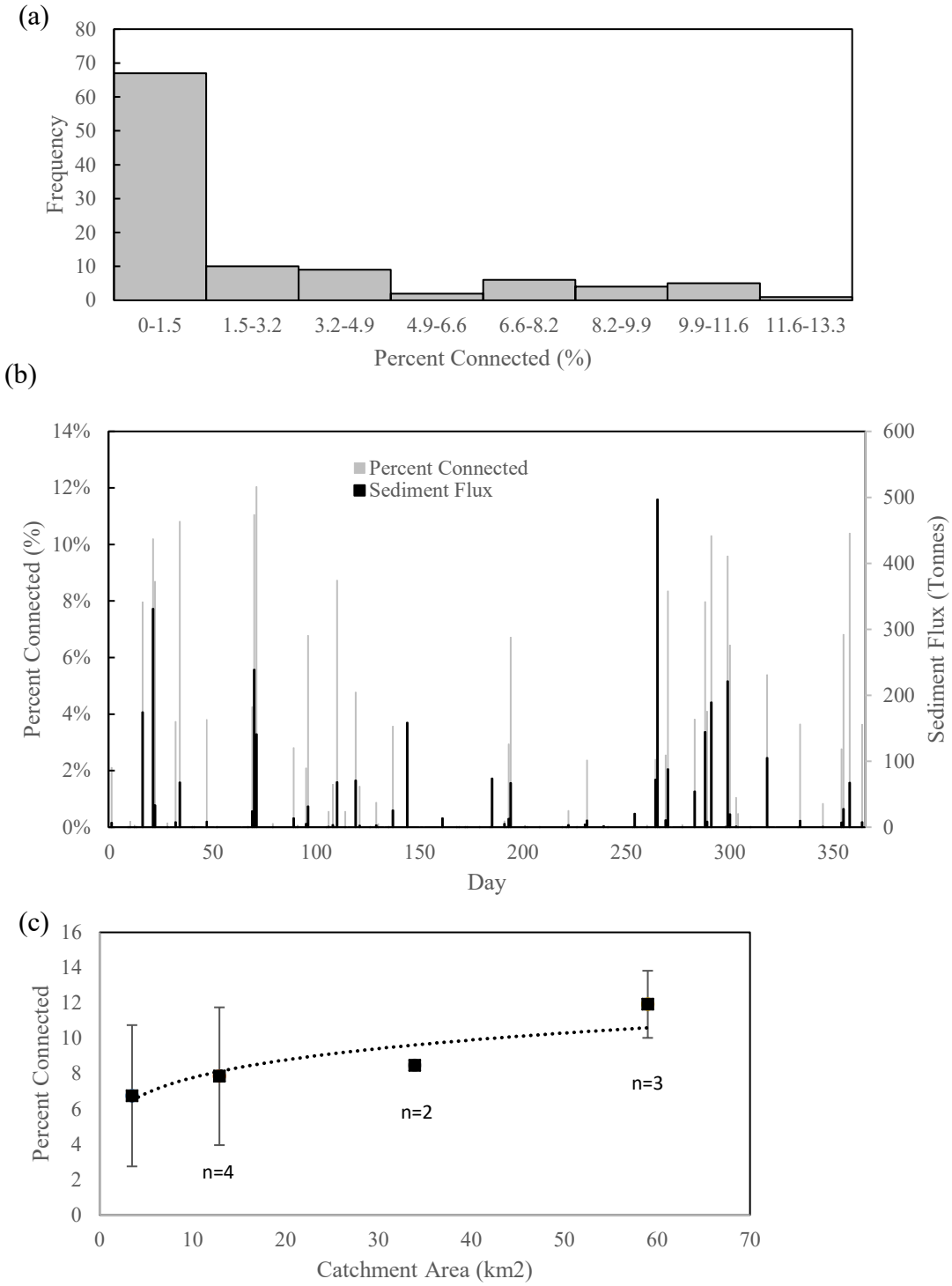

Figure 1.11. Evaluation of the probability of sediment connectivity results by inspecting landscape features.

(a) Steep slopes in urban/newly constructed developments exhibiting connectivity

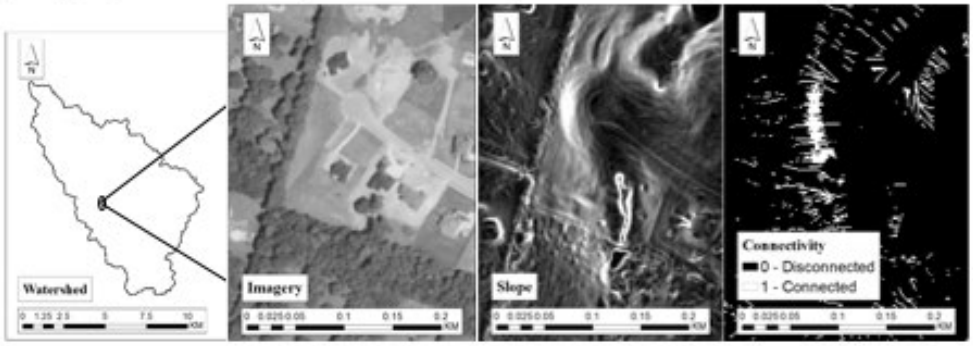

(b) Water accumulation from roadways exhibiting connectivity

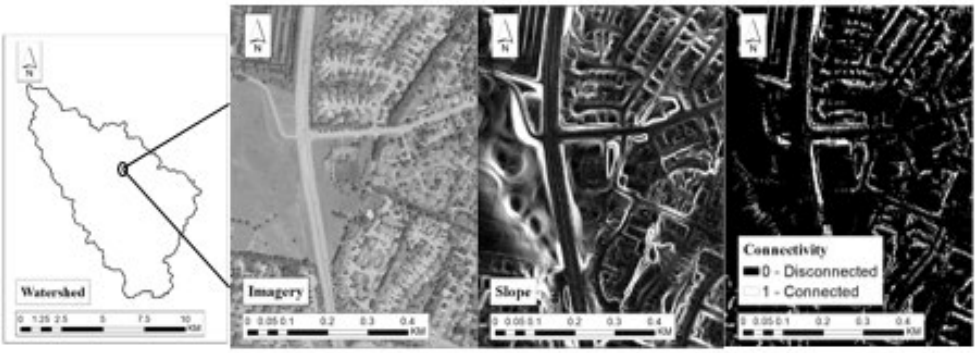

(c) Agricultural concentrated flow pathways exhibiting connectivity

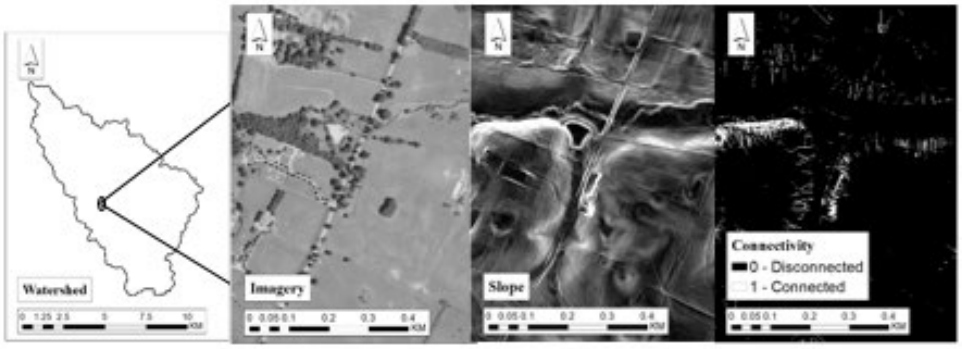

Figure 1.12. Connected areas and the erosion rates for connected cells for a road network on day 72 of 2006.

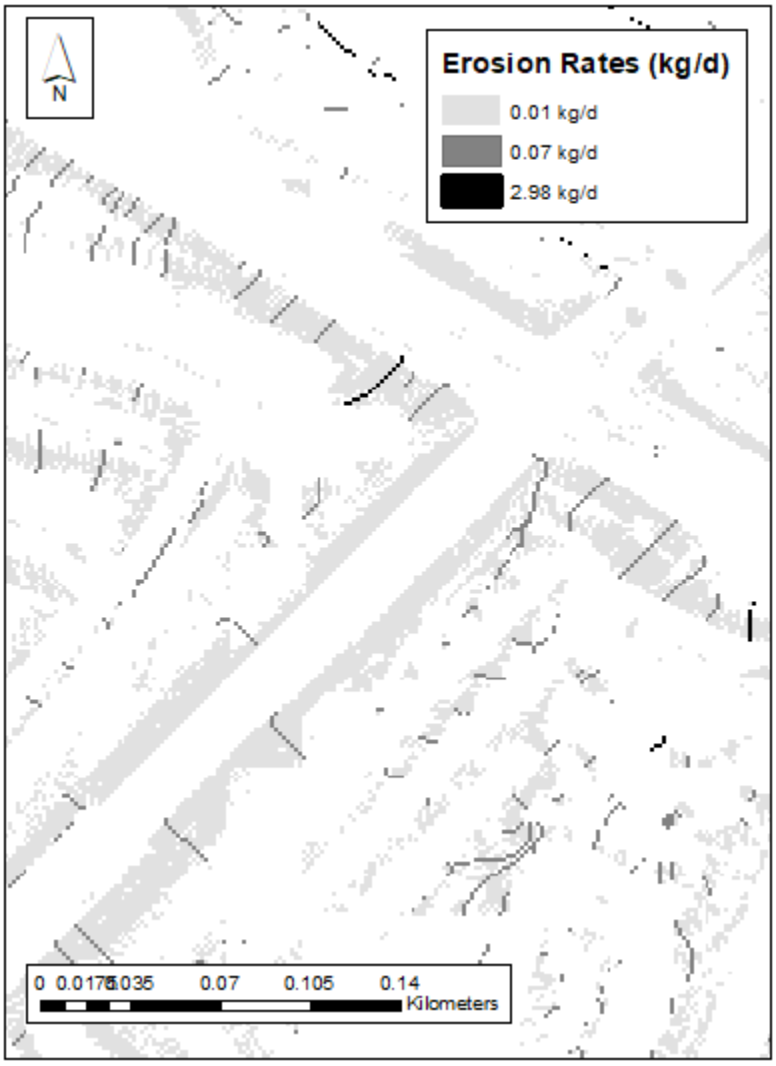

Chapter 2. Equilibrium sediment exchange in the earth's critical zone: evidence from sediment fingerprinting with stable isotopes and watershed modelling

Adapted per my Springer publishing rights from Mahoney, et al., 2019. Equilibrium sediment exchange in the earth's critical zone: evidence from sediment fingerprinting with stable isotopes and watershed modeling. Journal of Soils and Sediments, 19(9), 3332-3356.

2.0 ABSTRACT

Purpose: The equilibrium sediment exchange process is defined as instantaneous deposition of suspended sediment to the streambed countered by equal erosion of sediment from the streambed. Equilibrium exchange has rarely been included in sediment transport studies but is needed when the sediment continuum is used to investigate the earth's critical zone.

Materials and methods: Numerical modelling in the watershed uplands and stream corridor simulate sediment yield and sediment source partitioning for the Upper South Elkhorn watershed in Kentucky, USA. We simulate equilibrium exchange when upland-derived sediment simultaneously deposits to the streambed while streambed sediments erode. Sediment fingerprinting with stable carbon isotopes allowed constraint of the process in a gently rolling watershed.

Results and discussion: Carbon isotopes work well to partition upland sediment versus streambed sediment because sediment deposited in the streambed accrues a unique autotrophic, i.e., algal, fingerprint. Stable nitrogen isotopes do not work well to partition the sources in this study because the nitrogen isotope fingerprint of algae falls in the middle of the nitrogen isotope fingerprint of upland sediment. The source of sediment depends on flow intensity for the gently rolling watershed. Streambed sediments dominate the fluvial load for low and moderate events, while upland sediments become increasingly important during high flows and extreme events. We used sediment fingerprinting results to calibrate the equilibrium sediment exchange rate in the watershed sediment transport model.

Conclusions: Our sediment fingerprinting and modelling evidence suggest equilibrium sediment exchange is a substantial process occurring in the system studied. The process does not change the sediment load or streambed sediment storage but does impact the quality of sediment residing in the streambed. Therefore, we suggest equilibrium sediment exchange should be considered when the sediment continuum is used to investigate the

critical zone. We conclude the paper by outlining future research priorities for coupling sediment fingerprinting with watershed modelling.

2.1 INTRODUCTION

A deep understanding of sediment continuum dynamics provides a valuable framework in which to evaluate the streambed as part of the critical zone's response to human impacts. Scientists are now well aware that the sediment continuum in a stream and watershed system is more akin to discontinuities in sediment mobilization and sustained transport than continuity or linearity (e.g., Phillips 2003; Fryirs 2013). The current sediment paradigm is best framed by considering a range of morphologic features across both the landscape surface and stream corridor that are connected or disconnected as a function of non-hydrologic and hydrologic thresholds (e.g., Bracken et al. 2015). We suggest more emphasis on the streambed and a process termed 'equilibrium sediment exchange' should be considered when the critical zone is evaluated with the sediment continuum. Equilibrium sediment exchange is the process of instantaneous deposition of upland-derived suspended sediment to the streambed countered by equal erosion of in-stream sediment from the streambed (Husic et al. 2017). The process does not change the suspended sediment load or the stored mass of sediment in the streambed reflecting equilibrium sediment continuity (e.g., Chang 1998). Equilibrium sediment exchange occurs because low momentum zones of sweeping coherent fluid episodically deposit sediment to the streambed while fluid ejections episodically re-suspend bed sediment to the water column (Cellino and Lemmin 2004; Husic et al. 2017). The equilibrium sediment exchange process of simultaneous deposition and erosion are known to exist (Cellino and Lemmin 2004; Winterwerp and van Kesteren 2004) but are rarely included in fluvial sediment transport models (Husic et al. 2017).

Sediment fingerprinting using organic tracers provides a potential tool to estimate the contribution of sediment from upland-derived and instream-derived streambed sediment, and in turn, assist with parameterizing equilibrium sediment exchange during watershed sediment transport modelling. Our literature review (see Table 1) suggests few studies have used sediment fingerprinting with organic tracers to partition upland-derived versus streambed-derived sediments, albeit we recognize several studies have considered the streambed source. Organic tracers are expected to partition upland and streambed

sediments for the scenario when upland sediment deposits to the streambed and then accrues a unique fingerprint from the autotrophy of the streambed. Therefore, the success of the approach will be conditional on a biogeochemically active streambed, an accrued organic tracer signature that is unique, and the presence of instream fluvial storage in the streambed. Another consideration is the streambed may be continuously evolving due to physical and biogeochemical processes. Thus, we might expect the organic tracer fingerprint to be non-stationary (Fox et al. 2010; Ford et al. 2015a,b), which needs to be accounted for during critical zone simulation.

Sediment fingerprinting may partition upland and instream sediments, however, we realize that sediment fingerprinting alone cannot provide answers such as the time-varying nature of erosion and deposition rates, equilibrium sediment exchange rates, and continuous sediment flux from a watershed. Coupling sediment fingerprinting with watershed modelling provides a useful composite tool for estimating sediment process rates and serves as a potentially new class of sediment transport studies. In the present study, we couple sediment fingerprinting with an upland sediment transport model that estimates sediment connectivity in a spatially explicit manner (Mahoney et al. 2018) and an instream sediment transport model explicitly accounting for benthic sediment stores including both consolidated legacy sediments and the surficial fine grained laminae (Russo and Fox 2012). We were motivated to investigate how sediment fingerprinting of upland and instream sediments could be useful for calibrating the equilibrium sediment exchange process.

The overall goal of this paper was to investigate equilibrium sediment exchange using sediment fingerprinting and watershed sediment transport modelling. Specific objectives were to: (1) test and, if applicable, use sediment fingerprinting with stable carbon and nitrogen isotopes to partition upland sediment versus streambed sediment; (2) couple sediment fingerprinting with watershed sediment transport modelling and use sediment fingerprinting to calibrate the equilibrium sediment exchange process; and (3) investigate the role the equilibrium sediment exchange process plays when applying the sediment continuum to study the earth's critical zone.

2.2 THEORETICAL DEVELOPMENT

Figure 1 outlines the sediment transport processes in a gently rolling watershed framing the basis of our theoretical development. The upland morphology of gently rolling watersheds includes relatively stable land surfaces and ephemeral sediment pathways (e.g., swales, gullies, roadside ditches) (Jarritt and Lawrence 2007; Ford 2011; Ford and Fox 2014; Mahoney et al. 2018). Mild hillslopes and fertile soils support agricultural and urban/suburban land uses, which further stabilize upland sediment pathways and floodplains (Mahoney et al. 2018). Low gradient to near zero gradient micro-topography of gently rolling landscapes can stifle sediment transport (Mahoney et al. 2018), and the floodplains can disconnect entire hillslopes from downstream sediment transport (Fryirs et al. 2007a,b; Mahoney et al. 2018). Sediment delivered from the uplands to the stream corridor during hydrologic events often fallout to temporarily stored streambed deposits because the sediment transport carrying capacity cannot sustain the upland sediment inputs (Russo 2009).

In the stream network, streambed storage of fluvial sediment can include consolidated legacy sediments as well as a biologically active, unconsolidated layer known as the surficial fine grained laminae (or SFGL, Droppo and Stone 1994; Droppo and Amos 2001). The agricultural land use of gently rolling systems produces dissolved nutrient loading to the stream that supports autotrophy, such as benthic algae growth in and above the SFGL (Ford and Fox 2017). The SFGL is a sediment layer on the order of a few millimeters to centimeter thick, is fluffy and neutrally buoyant with high water content, and has inter particle–inter floc pores where biological processes are persistent (Droppo and Stone 1994; Droppo and Amos 2001). The SFGL can accumulate organic matter, and the flora and fauna of the SFGL has been reviewed previously (see Russo and Fox 2012, and references therein), and includes autotrophic algae, fungi, macrophytes, benthic macroinvertebrates (e.g., crayfish, aquatic worms), biofilm development via the live bodies of microorganisms and their excretions, and heterotrophic bacteria responsible for carbon turnover and nitrogen mineralization. Taken together, these biological processes of the SFGL have the potential to impact sediment transport through binding and decomposition mechanisms while at the same time provide a unique organic fingerprint for sediment fingerprinting analyses.

As mentioned in the introduction, we consider equilibrium sediment exchange between the water column and streambed. Equilibrium sediment exchange is the process of instantaneous deposition of suspended sediment to the streambed countered by equal erosion of sediment from the streambed (Husic et al. 2017). Past findings allowed us to adopt equilibrium sediment exchange driven by the turbulent bursting phenomena (Cellino and Lemmin 2004). The sweeping motions of turbulent bursts permit fine sediments to arrive near bed deposits, allowing deposition. The ejection motion re-suspends bed sediments in the water column. The downwelling-upwelling motion of turbulent bursting provides a conceptual model for representing the sediment exchange process, even during equilibrium conditions where zero change of suspended load in the water column occurs. We consider the total mass of sediment transferred during equilibrium exchange, S_x, as a function of sediment transport during bursting as follows:

$$S_x = fn[\text{suspended sediment availability, bed sediment availability, bursting, duration of the process}]. \quad (1)$$

The components of Equation (1) realize equilibrium exchange is not less simple than sediment transport prediction itself. Nevertheless, we may begin to substitute likely governing variables controlling the components of Equation (1) as:

$$S_x = fn\left[\{\overline{\overline{C_s}}, V_w, z^*, d_{ss}, \sigma_{ss}\}, \{d_{ss}, \sigma_{ss}, d_{bs}, \sigma_{bs}, (\tau_{burst} - \tau_{cr})\}, \{S_B, T_B^{-1}, k_s, H\}, \{t_d\}\right]. \quad (2)$$

The first group of variables reflects the availability of suspended sediment in the water column to exchange with the bed including the double-averaged suspended sediment concentration ($\overline{\overline{C_s}}$), the volume of water in the channel (V_w), the distribution of suspended sediment in the vertical via the Rouse number (z^*), and properties of the suspended sediment particle size distribution (d_{ss}, σ_{ss}). Bed sediment availability for exchange may be represented with a bed sediment supply threshold (d_{ss}, σ_{ss}), particle size distribution of the bed (d_{bs}, σ_{bs}), and excess shear to allow transport during bursting ($\tau_{burst} - \tau_{cr}$). Bursting action to cause exchange may reflect the energy of turbulent bursting (S_B), the time scale of bursting called the bursting period (T_B^{-1}), and the distribution of bursting in the water column as a function of the roughness height of the streambed (k_s) and the flow depth (H). Finally, the duration (t_d) of equilibrium exchange is included, which reflects that our interest is not in the exchange from a single burst but rather the cumulative impact

on streambed and suspended sediment over some period (e.g., hour, hydrologic event, year).

Our theoretical development in Equations (1) and (2) does not provide a predictive model of equilibrium exchange but does provide variables for consideration in systems where it exists and may vary through space and time. The gently rolling watershed is argued to provide such conditions given the high suspended sediment loads during hydrologic events, pronounced fluvial storage, and ubiquitous nature of turbulent bursting. As will be shown, we use sediment fingerprinting to empirically calibrate the equilibrium exchange process. We then consider the factors in Equations (1) and (2) in our discussion of governing processes in the basin. Sediment fingerprinting is useful in calibrating S_x because it partitions suspended sediment arriving from the uplands with streambed sediments.

2.3 STUDY SITE AND MATERIALS

The study site was the gently rolling Upper South Elkhorn watershed in the Inner Bluegrass Region of Kentucky, USA (see Figure 2). The Upper South Elkhorn watershed (61.8 km^2) fits in the 'gently rolling' classification previously described due to generally low gradient hillslopes with interspersed 'rolling' surfaces with increased slope (Sims et al. 1968; McGrain 1983). Bedrock outcrops located throughout the stream network control longitudinal stream morphology and create instream deposits of fine sediment. We selected this watershed to investigate the ability of sediment fingerprinting and modelling to elucidate equilibrium exchange because: (i) low gradient watersheds such as the Upper South Elkhorn foster life-sustaining ecosystem processes throughout earth's critical zone; (ii) anthropogenic disturbance to the critical zone is often pervasive in low gradient watersheds due to their adeptness for sustaining life; (iii) scientists recognize the importance of low gradient watersheds in global nutrient and sediment budgets (e.g., Fox et al. 2010; Ford and Fox 2014); and (iv) we have extensive materials associated with historical and on-going data collection conducted by the University of Kentucky, USGS, and Lexington-Fayette County Urban Government including raw and de-trended data, information, and resources published in our group's previous journal papers.

Materials used herein from previous assessments included establishing an upper and lower catchment and field assessment to gain background knowledge of the system (Mahoney 2017; Mahoney et al. 2018). Two different long-term sediment data collection sites have been established in South Elkhorn Creek (see Figure 2), and the locations nearly divide the watershed in half. The upper catchment above Site 1 is dominated by urban land uses (60% urban, 40% agricultural, Fox et al. 2010) and the lower catchment between Site 1 and Site 2 is primarily agricultural (28% urban, 72% agricultural, Fox et al. 2010). The entire Upper South Elkhorn watershed is predominantly agricultural land use (44% urban, 55% agricultural, Mahoney et al. 2018). Upland field reconnaissance has shown suburban grass lots and agricultural pastureland dominate upland land cover. Geospatial analyses of sediment connectivity in the uplands have shown upland sediments are primarily derived from gullies, swales, and roadside ditches (Mahoney et al. 2018). Instream field assessments have shown pronounced storage of fluvial sediment throughout South Elkhorn Creek, and estimated streambed storage exceeds the annual sediment yield (Russo 2009; Mahoney 2017; Mahoney et al. 2018).

Materials for this study also included a collection of published stable isotope data of soils, sediments, and algae. Nearly a decade of stable isotope measurements of transported sediments collected from Sites 1 and 2 in Figure 2 were published for the system (Ford 2014; Ford et al. 2015b). We collected the transported sediments approximately weekly using sediment traps (Phillips et al. 2000) and performed stable carbon and nitrogen isotope analyses and elemental analyses for all sediment after pre-processing and wet sieving to retain the less than 53-micron size fraction of sediments (Fox et al. 2010; Ford et al. 2015b). Ford et al. (2015b) performed time-series analyses of the data streams including removal of the biological-associated mean trends with empirical mode decomposition analyses. The decomposition analyses accounted for the non-stationary mean in the present study. Stable isotope results of sediment sources have also been published, including stable carbon and nitrogen isotope measurements of streambed sediments, algae, and of grassland and agricultural soils from different particle size classes (see Figure 2 for instream sediment sample locations; Davis 2008; Campbell et al. 2009; Fox et al. 2010; Ford et al. 2015b). Multiple years of sediment particle size distribution

results for the study stream were performed using microscopy of fluvial sediments and are shown in Figure 3 (from Fox et al. 2014).

Materials also included previously published and calibrated numerical models established for upland sediment transport, instream transport, and streambed storage for the Upper South Elkhorn watershed. A sediment connectivity and upland erosion model simulates transport thresholds and rates, respectively for the Upper South Elkhorn (Mahoney et al. 2018). A sediment transport and streambed evolution model developed for the stream corridor considers upland sediment supply to the stream corridor, bank processes, surficial fine grained laminae processes, and fate of deeper bed sediments (Russo and Fox 2012).

2.4 METHODS

2.4.1 Sediment fingerprinting of upland sediment versus streambed sediment:

We characterized sediment sources in the watershed as originating from the uplands or the temporarily stored streambed deposits. The rather coarse characterization lumps together several sub-sources, as we will discuss, but this characterization was needed to investigate the equilibrium exchange process. For the scale considered (32.8 km^2 and 61.8 km^2), the upland sediment source classification lumps together all sediment classified as 'not bed sediments' including surface soil from both agricultural and suburban/urban land uses as well as sediment eroded from subsurface soils of gully and swale pathways. Surface and subsurface soils eroded from streambanks are also included in the upland sediment classification, which is not necessarily typical. However, streambanks make up less than 1% of the sediment load in this watershed (Russo and Fox 2012). The temporarily stored streambed deposits lump together the surficial fine grained laminae (SFGL) at the surface of the streambed and deeper legacy sediments. However, in this system, the SFGL contribution dominates the instream sediment production due to its high supply and low critical shear stress (Russo and Fox 2012).

We apply stable carbon and nitrogen isotopes of sediment as potentially unique tracers for partitioning upland sediments versus streambed sediments. Stable carbon and nitrogen isotopes are reported using delta notation as $\delta^{13}C$ and $\delta^{15}N$ to indicate depletion (-

) or enrichment (+) of the heavy (higher-mass) stable isotopes (^{13}C and ^{15}N) compared to the lighter mass stable isotopes (^{12}C and ^{14}N) and can be defined as

$$\delta X\ (in\ ‰) = \left(\frac{R_{sample}}{R_{std}} - 1\right) * 10^3, \quad (3)$$

where R_{sample} is the isotope ratio (^{13}C /^{12}C or ^{15}N /^{14}N) of the sample and R_{std} is the isotope ratio of the standard (Vienna Pee Dee Belemnite, VPDB, and atmospheric nitrogen, respectively). Stable carbon and nitrogen isotope measurements of transported and source sediments were previously collected (Davis 2008; Campbell et al. 2009; Fox et al. 2010; Ford et al. 2015b), as mentioned in the materials section.

Representing $\delta^{13}C$ and $\delta^{15}N$ of the sediment sources and sinks in the fingerprinting method required proper selection of samples to construct the distributions (Davis and Fox 2009) and consideration of source stationarity (Fox et al. 2010). We represented the upland sediment source with $\delta^{13}C$ and $\delta^{15}N$ measurements of surface and subsurface soils (Campbell et al. 2009; Fox et al. 2010). We considered $\delta^{13}C$ and $\delta^{15}N$ of the less than 53-micron fraction of the soil since this was the sediment particle size class we investigated. We assume $\delta^{13}C$ and $\delta^{15}N$ of upland sediment were stationary. Fox (2006) found a lack of seasonal or annual change for the less than 53-micron size fraction of upland soil, which agrees with the relatively long turnover time of finer sized, more recalcitrant organic matter fractions of the soil (Cambardella and Elliott 1992). While disturbances likely existed throughout the uplands, we feel an assumption of stationarity is reasonable given that grass cover and silt loam dominated the land cover and soils, respectively, in both agriculture and suburban regions. We represented the streambed sediment with $\delta^{13}C$ and $\delta^{15}N$ measurements of sediment collected via the Lambert and Walling (1988) method during low flow periods (Q_{pk2}<2.8 $m^3\ s^{-1}$, where Q_{pk2} is the peak water discharge at location two during the sediment collection period) when only instream sediment was transported. We verified this method by comparing low flow sample results with streambed sediments collected during the same period and found only 0.2‰ difference or less.

We assumed the streambed isotope values are non-stationary given mean trends found in the published isotope data of streambed and transported sediments (Davis 2008; Fox et al. 2010; Ford et al. 2015b). We subtracted the mean trend using empirical mode decomposition to account for the non-stationarity (Ford et al. 2015b). After decomposition, $\delta^{13}C$ and $\delta^{15}N$ of transported sediment included 189 and 232 measurements at Sites 1 and

2, respectively, collected over a range of low, moderate and extreme hydrologic events. Based on flow dependence of the dataset and previous study of sediment transport in the watershed (Russo and Fox 2012; Mahoney et al. 2018), we divided the datasets in four flow regimes including low flow events (Q_{pk2}<2.8 m^3 s^{-1}), moderate events (2.8 m^3 s^{-1}<Q_{pk2}<12.2 m^3 s^{-1}), high flow events (12.2 m^3 s^{-1}<Q_{pk2}<24.4 m^3 s^{-1}), and extreme hydrologic events (Q_{pk2}>24.4 m^3 s^{-1}). We adjusted these flow regimes by a factor of 0.53 from the lower catchment (presented above) to the upper catchment using the area weighted method. We performed source allocation via un-mixing for each flow regime and individual hydrologic events corresponding to each sediment trap sample.

We estimated source allocation using an un-mixing model analysis specific to $\delta^{13}C$ and $\delta^{15}N$ (Fox and Martin 2015). The $\delta^{13}C$ and $\delta^{15}N$ signatures of sediment indicate the fingerprint of 'sediment carbon' and 'sediment nitrogen', respectively, rather than the fingerprint of the total sediment. Therefore, the carbon and nitrogen concentration of sediment corrected the source allocation in the un-mixing model. The elemental concentrations were measured with a coupled elemental analyzer during stable isotope ratio mass spectroscopy, which is a typical analytical setup in the laboratory, and therefore the added data needs did not place an undue burden on the researcher. Our correction was analogous to organic matter and particle size corrections included in the traditional model of Collins et al. (1997) and widely cited thereafter, albeit only carbon and nitrogen concentration corrections were needed for un-mixing with $\delta^{13}C$ and $\delta^{15}N$ because the concentration changes of soil are highly correlated with particle size shifts (e.g., Cambardella and Elliot 1992; Campbell et al. 2009). Fox and Martin (2015) extensively described the un-mixing model formulation and only the primary governing formulae are included here. Un-mixing simulation with $\delta^{13}C$ and $\delta^{15}N$ were performed as:

$$\delta^{13}C_T = \sum_{i=1}^{n} \alpha_i \delta^{13}C_i X_{C,i}, \quad (4)$$

$$\delta^{15}N_T = \sum_{i=1}^{n} \beta_i \delta^{15}N_i X_{C,i} \frac{ER_{N,i}}{ER_{C,i}} \frac{(N/C)_i}{(N/C)_T}, \text{ and} \quad (5)$$

$$P_i = \frac{X_{C,i}\left(\frac{TOC_T}{ER_{C,i}TOC_i}\right)}{\sum_{i=1}^{n}\left(X_{C,i}\frac{TOC_T}{ER_{C,i}TOC_i}\right)}, \quad (6)$$

where T and i indicate transported and source i, respectively; α and β indicate functions for nonconservative $\delta^{13}C$ and $\delta^{15}N$ during transport; ER_N and ER_C is the enrichment ratios; N/C

is the nitrogen to carbon atomic ratio of sediment; X_C is the carbon mass fraction; and TOC is the organic carbon concentration of sediment. Equations (4), (5) and (6) were solved together with constraints of unity for summation of both sediment carbon fractions and summation of sediment fractions. We corrected for the shifts in sediment carbon and sediment nitrogen from the sediment sources to sinks using the above equations. We treat the nonconservative functions and enrichment ratios as zero given the source to sink transport is less than one-day transit time. We also performed a Monte Carlo robust analysis to account for uncertainty. Isotope tracer distributions were assumed normal, and parameterized via data mean and variance estimates. Each realization of the Monte Carlo simulation was solved via a random number generator to draw from the tracer distributions. We performed a sensitivity analysis of the ensemble size, and we found 10^5 realizations produced stable results for the ensemble first and second order moments. Therefore, we used 10^5 realizations for each ensemble solved.

2.4.2 Numerical modelling of the equilibrium sediment exchange

Numerical modelling of the equilibrium sediment exchange required coupling an existing upland erosion model (Mahoney et al. 2018) with an existing instream sediment transport model (Russo and Fox 2012) and sediment fingerprinting. As outlined in Mahoney et al. (2018), we used sediment connectivity theory in conjunction with probability theory to model upland sediment transport pathways in the watershed (Borselli et al. 2008; Bracken et al. 2015). We predicted upland sediment delivery to the stream network by coupling the active contributing area predicted from the probability of connectivity model with a threshold based erosion model. Next, the continuity equation modelled instream sediment transport from various upland and instream sediment sources (Russo and Fox 2012), and a new feature of the instream model was added herein to simulate equilibrium sediment exchange calibrated using sediment fingerprinting. The mentioned references described the original model formulations, and the model application is described briefly below. The new methods described here include: inclusion of the equilibrium exchange process in the instream sediment continuity equation; refined calibration and global sensitivity analysis of the coupled model with both upland and

instream components; and the calibration of the equilibrium exchange process using sediment fingerprinting.

The probability of connectivity model provided spatially explicit results for the sediment active contributing area in the watershed uplands. Ambroise (2004) defined the active contributing area as the portion of a catchment that actively transports sediment to the stream network at a particular time step. The model simulated connectivity at a given time step using hydrologic modelling results from the Soil and Water Assessment Tool (SWAT; see Al Aamery et al. (2016) for model validation), a high-resolution (2.5 m) DEM, soil critical shear stress, orthophotographs, and morphologic data collected from field reconnaissance and remote sensing (Mahoney et al. 2018). We used SWAT to model hydrologic scenarios given its ability to simulate the processes of overland runoff and subsurface antecedent moisture (Arnold et al. 1998; Neitsch et al. 2011). The probability of sediment connectivity model represented the intersection of several threshold-based probability equations to simulate various upland sediment transport processes. Equations used to model the upland probability of sediment connectivity model have been included in Supplementary Material I (see also Mahoney et al. 2018 for additional background). Simulation of the probability of connectivity model for the Upper South Elkhorn watershed took place using ArcMap (version 10.4) on a desktop PC (Intel® Core™ i7-6700 CPU at 3.40 GHz; 64-bit operating system, x64-based processor) over the course of approximately 112 hours for the 4-year simulation period.

We applied the upland erosion model to active contributing cells from the probability of connectivity model and simulated sediment flux from the uplands by integrating the volume of eroded upland sediment at a particular time step. Upland sediment flux was simulated as a function of the sediment erosion rate, as predicted by the Partheniades (1965) equation, the soil bulk density, and the bathymetry of the sediment transport pathways, as predicted by the probability of connectivity model. We allocated connected cells to the upper or lower catchment based on their geospatial location in the watershed, and the upland erosion model was individually applied to the discretized cells to determine the total upland sediment flux from the upper and lower catchment at a given time step. Equations used in the upland erosion model have been included in the section Supplementary Material I.

Inputs and parameter ranges used in the upland erosion model (see Table 2) included channel bathymetry, geospatial data, hydrologic data, sediment routing information, and soil properties. We specify several parameter ranges using literature-derived methods. Time of concentration surrogated the storm length when surface erosion occurred (Mahoney et al. 2018). Literature values defined soil parameter ranges for critical shear stress, relative roughness, and the erodibility coefficient (e.g., Alberts et al. 1995; Hanson and Simon 2001). We estimated sediment bulk density using Russo and Fox (2012). We empirically replicated the width of connected rills and ephemeral gullies using equations developed by Nachtergaele et al. (2002). Finally, we parameterized the longitudinal slope and contributing area of connected cells with geospatial analyses in *ArcMap* v10.4. The channel length for the bins depended on the daily results from the probability of connectivity model.

The instream sediment model simulated sediment transport from five potential sources in the stream network by estimating erosion and deposition in a reach during a particular time step (Russo and Fox 2012). Sediment sources included the SFGL biofilm, SFGL sediment component, streambed, streambanks, and upland sediments. The model accounted for sediment erosion and deposition from each source and estimated the total contribution of each source to the total sediment yield at a given time step. Erosion and deposition were functions of the transport capacity of the fluid, which we predicted using the stream's available energy to transport sediment (Julien and Simons 1985). The SFGL layer lies atop bed sediments and has a relatively lesser critical shear stress compared to bed sediments (Droppo and Stone 1994). Thus, we assumed the SFGL preferentially erodes before deeper bed sediments. Sediment flux predicted from the upland erosion model served as the supply of upland suspended sediment in the instream sediment transport model. To account for equilibrium erosion and deposition resultant of turbulent bursts and sweeps occurring simultaneously in a reach, we updated the sediment continuity equation of Russo and Fox (2012) herein to include the equilibrium sediment exchange process as:

$$SS_i^j = SS_{i-1}^j + \sum_{k=1}^{N} E_{i\ k}^j - D_i^j + \left(Q_{ss\ in_i}^j + Q_{ss\ up_i}^j - Q_{ss\ out_i}^j\right) * \Delta t, \quad (7)$$

$$S_{bed_i}^j = S_{bed_{i-1}}^j + D_{bed_i}^j - E_{bed_i}^j, \quad (8)$$

$$SS_{i+\frac{1}{2}}^j = SS_i^j - Exf * SS_i^j + Exf * S_{bed_i}^j * \left[\frac{SS_i^j}{S_{bed_i}^j}\right], \quad (9)$$

$$S^{j}_{bed_{i+\frac{1}{2}}} = S^{j}_{bed_i} - Exf * S^{j}_{bed_i} * \left[\frac{SS^{j}_{i}}{S^{j}_{bed_i}}\right] + Exf * SS^{j}_{i}, \quad (10)$$

where *Exf* is the sediment exchange factor, (*j*) represents the stream-reach, (*i*) represents the time step, (*k*) represents the sediment source, *N* represents the number of sediment sources, *SS* is the mass of sediment (kg), *E* is erosion (kg), *D* is deposition (kg), $Q_{ss\ in}$ is the sediment flow rate in the reach (kg s^{-1}), $Q_{ss\ up}$ is the sediment flow rate in the reach from the uplands (kg s^{-1}), $Q_{ss\ out}$ is the sediment flow rate out of the reach (kg s^{-1}), and S_{bed} is the mass of bed sediments (kg). Equations utilized in the instream sediment transport model have been included in Supplementary Material II. Supplementary Material III defines all parameters used in the modelling.

Table 3 shows the inputs and parameter ranges for the instream sediment transport model. We defined several initial ranges using literature values. Literature suggests the SFGL is neutrally buoyant and this is reflected by the SFGL density (Stone and Droppo 1994; Droppo and Amos 2001). The development time, maximum depth, and the generation rate of the SFGL biofilm and sediment were parameterized from Stone and Droppo (1994) and Droppo and Amos (2001). The ranges for the transport capacity coefficients were empirical and we optimized these during model calibration (Dou 1974; Ahmadi et al. 2006; Yan et al. 2008; Guy et al. 2009; Madej et al. 2009). We determined the shear stress coefficient for unsteady flow by the boundary shear stress distribution for a trapezoidal channel (Chang 1988). Previous research assisted in parameterization of the critical shear stress coefficients and erodibility of the instream sediment sources (Droppo and Amos 2001; Hanson and Simon 2001; Sanford and Maa 2001; Simon and Thomas 2002). We estimated the mean settling velocity of suspended material based on particle size and shape for sediments in the Inner Bluegrass Region of Kentucky, USA, as described in Fox et al. (2014). The sediment routing and flood wave coefficients were based on the travel time between the two study points and flood routing theory (e.g., Gupta 2016). Field reconnaissance and remote sensing helped estimate the channel bathymetry. We parameterized the longitudinal channel slope with longitudinal profiles and GIS analyses of high-resolution (1.5 m) digital elevation models (KYAPED 2014).

Calibration and validation data included total suspended solids samples collected approximately every two hours over the course of 32 storm events from 2007 until 2010

using a Teledyne ISCO automated sampler. Of the 32 sampled storm events, we deemed 18 storms suitable for use in calibration and validation based on the quality of the data. For example, we removed storms with little to no sediment transport from the calibration and validation process because they may bias evaluation statistics. Other qualitative calibration data included orthophotographs and visual reconnaissance of sediment transport pathways collected during field assessment.

Model evaluation consisted of a three-stage calibration and validation process and a global sensitivity and uncertainty analysis (Figure 4). Stage one calibrated the upland probability of sediment connectivity model. Upon running the model, we visually compared simulated sediment transport pathways to known sediment transport pathways identified during field reconnaissance and from orthophotographs. If the predicted sediment transport pathways were unacceptable, then we iteratively adjusted parameters from the probability of connectivity model until calibration was acceptable.

Stage two calibrated the upland erosion and instream sediment transport models. We used fifteen storms from 2007 to 2009 in model calibration and three storms in 2010 for model validation. Three objective functions evaluated the model's performance including: (1) the Nash Sutcliffe statistic of the simulated sediment flux and observed sediment flux for the fifteen calibration storm events; (2) equilibrium of the streambed such that net aggradation and net degradation were nearly zero over the four-year simulation period; and (3) long-term equilibrium of upland sediment flux and sediment flux from the watershed outlet. Sediment transport parameters in the upland erosion and instream sediment models were automatically adjusted until each of the criteria was fulfilled. We included simulations fulfilling the three evaluation criteria with parameters in mutually permissible ranges based on the literature in the solution space. We performed quasi-random, low discrepancy Sobol sequencing to generate 10,000 sets of the 20 parameters in the coupled models. The 10,000 sets stabilized the results of the global sensitivity analysis and sediment yield. The global sensitivity analysis was performed by determining the sensitivity indices (Joe and Kuo 2003; Saltelli et al. 2008).

Stage three calibrated the model's partitioning of sediment sources to the sediment fingerprinting results collected over the simulation period. We adjusted the equilibrium exchange factor shown in Equations (9) and (10) such that modelled sediment source

partitioning from the sediment transport model matched the partitioned results from sediment fingerprinting. Four different exchange factors were used in both the upper catchment and lower catchment to represent adjustment of the equilibrium sediment exchange process across flow regimes.

2.5 RESULTS AND DISCUSSION

2.5.1 Sediment fingerprinting of upland sediment versus streambed sediment

We found $\delta^{13}C$ was able to discriminate the upland and instream sediment sources while $\delta^{15}N$ was unable to discriminate between the two sources. The $\delta^{13}C$ value of upland and instream sources was significantly different (p-value<0.001). The reason $\delta^{13}C$ worked well is because of the isotope signature differences for organic matter in the upland and instream sediments. Upland organic matter in this study site is from C3 plants, including northern grasses and to a lesser degree deciduous trees, with $\delta^{13}C$ from -27 to -28‰ (Campbell et al. 2009). During litter and root decomposition to soil carbon, isotopic enrichment of ^{13}C occurs for the more recalcitrant organic matter product (Nadelhoffer and Fry 1988). The $\delta^{13}C$ values of soils in the Bluegrass Region agree with the enrichment and show an increase in the value of $\delta^{13}C$ for surface soils, finer sized sediment carbon pools, and with depth in soil (Campbell et al. 2009). Subsurface soils show $\delta^{13}C$ values as low as -23.9‰ (Davis, 2008). The streambed sediments acquire a $\delta^{13}C$ value that is distinct from the upland soil. Streambed sediments accrue stabilized benthic algae as the algae decompose (Ford et al. 2017). $\delta^{13}C$ of algae is -37.8(±5.5)‰ in South Elkhorn Creek (Ford et al. 2015b). Therefore, $\delta^{13}C$ of streambed sediment (temporal mean, -27.3‰) establishes a sediment fingerprint that is less than $\delta^{13}C$ of upland sediment (mean, -25.9‰).

We were unable to differentiate upland and instream sediment sources using $\delta^{15}N$ because the isotope distributions of upland and instream sediments were overlapping. The $\delta^{15}N$ value of the near-surface soil nitrogen with northern grasses is 2.5‰ in this region (Campbell et al. 2009). During soil organic nitrogen mineralization, isotopic enrichment increases the $\delta^{15}N$ of the organic N substrate, and enrichment is on the order of two times that of carbon isotope enrichment (Nadelhoffer and Fry 1988). The isotope enrichment during mineralization is in agreement with data from our watershed and subsurface soils have $\delta^{15}N$ on average equal to 6.9‰ (Davis 2008; Fox et al. 2010). Therefore, our upland

sediment δ^{15}N value ranges from approximately 2 to 7‰. Similarly to the carbon isotopes, streambed sediments accrue the δ^{15}N of autotrophs. δ^{15}N of algae is 4.95(±1.6)‰ in the South Elkhorn Creek (Ford et al. 2015b). δ^{15}N of algae falls in between the range of upland surface soil and upland subsurface soil. Therefore, the accrual of stabilized benthic algae in streambed sediments caused δ^{15}N to be an ineffective fingerprint for separating upland and streambed sediments.

The distribution of δ^{13}C of transported sediment fell between the upland and instream source end-members, and δ^{13}C of transported sediment showed dependence on peak water discharge for the stream during the period when the sediment trap collected the sediment (see Figure 5). We normalized the hydrologic events presented on the x-axis in Figures 5 and 6 by dividing the observed peak flowrate (Q_p) by the mean flowrate (Q_{pm}) observed while collecting all of the sediment samples. We validated the relation of bulk instream flow intensity parameters to sediment transport by separating streamflow into baseflow and runoff using hydrograph separation techniques (e.g., Hooghoudt et al. 1940; Arnold et al. 1995; Arnold et al. 1999; Neitsch et al. 2000). Hydrograph separation results showed a consistent increase in the volume of upland runoff produced during hydrologic events of increasing magnitude (see Supplementary Material IV, Figure I). The results suggested the increased runoff and peak flow produced a greater contribution of upland sediments to the total load, which is reflected in the increased δ^{13}C signatures observed in Figures 5 and 6. The hydrograph separation results suggest Figures 5 and 6 capture the nature of upland runoff and sediment entering the stream network relatively well. However, we recognize one improvement to this work would be quantitative hydrograph separation, as such represented in the research of Gourdin et al. (2015), to validate and better couple water and sediment sources in the instream model. The stable carbon isotope data suggested a dominance of streambed sediment origin during smaller hydrologic events and an increasing contribution of upland sediment as the magnitude of peak discharge increases. The δ^{13}C value of transported sediment was significantly dependent on peak water discharge during an event at both sites (p-value<0.001 for the regression slope). However, the results in Figure 5 suggest even during the most extreme events the contribution of upland and instream sediment sources is on the same order of magnitude. The results generally agree with our previous work in the watershed. We have found

substantial loading of upland sediments occurs only during moderate to extreme rainfall events for the gently rolling system (Mahoney et al. 2018). Also, the importance of temporarily stored bed sediments has been suggested across all flow regimes (Russo and Fox 2012). These results agree well with other researchers (e.g., Dalzell et al. 2005; Walling 2005; Fox and Papanicolaou 2007; McCarney-Castle et al. 2017) who also found a significant contribution of distal sediments to total sediment loadings during moderate and high events. For example, Dalzell et al. (2005) used stable carbon isotopes to show a prominence of terrestrial organic carbon in overall organic carbon export during high magnitude hydrologic events. Fox and Papanicolaou (2007) predicted nearly 60% of the eroded soil contributing to the total suspended sediment load during a moderate hydrologic event had upland (proximal) origins.

We carried out the sediment fingerprinting analyses with the stable carbon isotope tracer while accounting for changes in organic matter content of the sources in transported sediments. On average, the upper catchment showed nearly equal percent of sediment originating from the uplands and streambed (see Figure 6). The lower catchment only showed equal contribution from both upland and instream sources during the 12 most extreme events over the years where we collected samples. For the other hydrologic events, the lower catchment was dominated by approximately three-fourths streambed sediments and one-fourth upland derived sediments. One main reason attributed to differences in source percentages in the upper and lower catchments is the relative supply of sediment sources. The surface area supplying upland sediment approximately doubles from the upper catchment to lower catchment. However, the surface area supplying streambed sediments is approximately four times greater in the lower catchment compared to the upper catchment.

Uncertainty bounds on the source contributions are high for the sediment fingerprinting results (see Figure 6), with standard error on the order of 35%, and several reasons explain the high uncertainty. First, we were very conservative in our estimates of uncertainty surrounding $\delta^{13}C$ of sediment sources. We used the standard error of $\delta^{13}C$ surrounding source data to define uncertainty bounds, however, the watershed system averages sources distributions to some degree during erosion and transport (Fox and Papanicolaou 2008a). For example, for moderate and extreme hydrologic events only 4

out of 294 data (1.3%) of transported sediment $\delta^{13}C$ values fell outside the $\delta^{13}C$ source distribution space defined in Figure 5. Second, uncertainty in the results of Figure 6 reflects temporal variability in episodic sediment transport for the 294 hydrologic events samples, as opposed to uncertainty associated with the tracer error in sediment fingerprinting modelling. Episodic variability exists as a spatially explicit sediment source may be pronounced due to rainfall variability or disturbances. The temporal variability of individual hydrologic events is reflected in Figure 7. Similarly to Figure 6, the event results show the upland contribution is higher during larger hydrologic events, the streambed is a greater contributor overall, and the streambed is a greater contributor of sediment in the lower catchment relative to the upper catchment. At the same time, the event-to-event variability of upland versus streambed contributions is sometimes substantial in the results of Figure 7, even when inspecting results from nearly equal peak flow conditions. Results highlight the episodic variability of sediment transport in the basin when considering many hydrologic events. In summary, the mean source contributions in Figure 6 capture temporal variability of processes and are very conservative concerning error placed on tracer error at the source. Therefore, we have more confidence in the mean values then perhaps reflected by the error bars because they represent variability of hydrologic events as opposed to error introduced from sampling and analyses.

As one discussion point, the reader is reminded of the non-stationary assumption of the streambed sediment source, which is differentiated from the term "non-conservative" where the former reflects the changing tracer signature of the source at the source while the latter reflects the changing of the tracer signature during transport from source to sink. The biology of the streambed continuously evolves due to physical and biogeochemical processes, and in turn, the organic tracer fingerprint was non-stationary (Fox et al. 2010; Fox and Martin 2015). We needed to subtract the non-stationary mean $\delta^{13}C$ using the empirical mode decomposition results of Ford et al. (2015b). Our application and results herein are in the context of previous studies where the non-stationary signature of stable carbon and nitrogen isotopes should be considered during sediment fingerprinting. Fox et al. (2010) used numerical modelling of the stable nitrogen isotopes of benthic sediments to show seasonality of the tracer in the context of sediment fingerprinting. Fox and Martin (2015) showed the stable carbon and nitrogen fingerprint of sediment from forest sediments

exhibited non-stationarity in a two-year period following drastic forest disturbance from ice storms and tree tip-over. Results highlight that a non-stationary tracer signature of the streambed sediment source needs to be considered when stable isotopes are used in sediment fingerprinting.

2.5.2 Numerical modelling of the equilibrium sediment exchange:

Calibration and validation of the coupled upland and instream sediment transport model showed, in general, the model captured well both sediment leaving the upper catchment and lower catchment (see Figure 8). Optimum parameters from model calibration are reported in Table 4. The Nash Sutcliff parameter of the model solution space was 0.37, which shows acceptable performance of the model (Moriasi et al. 2007). Sediment yield from the watershed was 2180 ± 330 t km^{-2} yr^{-1}, which was similar to previous estimates for the basin (Russo and Fox 2012; Mahoney et al. 2018). Global sensitivity analysis of the coupled model showed the erodibility coefficient in the upland model was the most sensitive parameter to sediment flux from the outlet followed by the instream sediment transport carrying capacity of the flow. The erodibility coefficient directly impacts the fluvial erosion rate in upland gullies, swales, and ditches while the transport capacity estimate dictates when a model reach will erode or deposit sediment in a given time step. The sensitivity highlights the importance of both upland and instream processes to sediment transport prediction.

The contribution of sediment originating from upland sediments and streambed sediments was sensitive to the equilibrium sediment exchange process, and we found a significant improvement in model results when including the equilibrium exchange process versus model runs when the equilibrium exchange was excluded (see Figure 9). Inclusion of the equilibrium exchange was needed to replicate results of the sediment fingerprinting. In this manner, the sediment fingerprinting results provided independent information to assist with investigating sediment transport.

As a discussion point, the efficacy of the sediment fingerprinting results to constrain the sediment exchange process provides an example of an emerging class of sediment transport studies coupling sediment fingerprinting and sediment transport modelling. Sediment fingerprinting and sediment transport modelling have advanced in parallel in

recent years. Sediment fingerprinting has progressed from a research tool to an accepted method with usefulness in watershed management applications (Mukundan et al. 2012). Sediment transport models have been developed for various applications the past three decades with off-the-shelf tools available to the modeler and various sediment processes considered (Papanicolaou et al. 2008). While these advancements have been in parallel, they have also been somewhat independent, and it appears the time is ripe for greater coupling of these tools. For example, most instream sediment transport models do not account for soil contributions from the uplands (Papanicolaou et al. 2008), yet sediment fingerprinting can readily provide this information to the modeler. The example in this study serves as one step towards meeting this goal. Another recent study showed sediment fingerprinting was useful for calibrating watershed sediment transport model parameters, including the transport capacity coefficient, sediment delivery ratio for reclaimed mining soils, and stream bank erosion parameters (Fox and Martin 2015). We suggest the community might welcome additional studies under this theme as we expect many different permutations of the modelling and fingerprinting coupling are possible.

Sediment transport results show the equilibrium exchange process transfers sediment on the same order of magnitude as erosion and deposition fluxes in both the upper and lower catchments over the four-year simulation period (see Figures 10 and 11). The results illustrate the process as significant. Calibration of the equilibrium process was data-driven via the fingerprinting results (see Figure 9) However, some comparison of the results and consideration of the parameters in Equations (1) and (2) is worthwhile. The empirically fit exchange factor decreased in value as the peak discharge of the hydrologic event increased for the first three flow regimes, but then increased in value for the fourth flow regime for the upper catchment (Figure 9, Table 4). The first three flow regimes, in general, could be classified as net streambed erosion events, while the most extreme events of the fourth flow regime deposited high amounts of sediment to the streambed, i.e., net deposition events in the upper catchment. The exchange factor decreased in value as the peak discharge of the hydrologic event increased for all four events in the lower catchment (Figure 9, Table 4). One explanation for the inverse relationship between the exchange coefficient and discharge during erosion events is an increase in the bursting period and a smaller contribution of the overall flow depth experiencing exchange. The bursting period

is proportional to the flow depth (Nezu and Nakagawa 1993), and the flow depth would be inversely related to exchange in Equation (2). We might also expect a smaller proportion of suspended particles to be impacted by bursting as the flow depth increases, albeit the connectivity of macroturbulence to near-bed bursting adds uncertainty to this process (Stewart and Fox 2015). During the most extreme events of the fourth flow regime, deposition of suspended sediment from the uplands to the streambed dominates transport in the stream. The extreme events have been found to cause a net increase in streambed storage (Ford et al. 2015a). However, our fingerprinting results suggest the extreme events also have a pronounced contribution of streambed sediment, and the equilibrium exchange coefficient reflected the process.

Several other factors in Equations (1) and (2) are also worthy of discussion. Bed sediment availability is directly accounted for when including the surface area of the streambed sediments in the lower and upper catchments, although we assume similarity of particle size distributions during exchange. The assumption is justified based on the highly similar estimates of particle size parameters across flow regimes and over time for the study stream (Fox et al. 2014), which suggests a similar particle size distribution regardless of the source distributions or extent of exchange. We suggest shear threshold also has little impact on bed sediment availability in this study, given the presence of the loosely held and near buoyant surficial fine grained laminae across much of the streambed (Russo and Fox 2012; Mahoney 2017). While we marginalize these impacts in our system, other watersheds may show dependence of equilibrium exchange on particle size distribution changes and shear thresholds.

The duration of the process in Equation (2) is particularly noteworthy for discussion. The duration of the equilibrium exchange process reflects the sediment transport time step in model simulation. Erosion and deposition were mutually exclusive in a model time step, and therefore we might expect the exchange coefficient to decrease as the model resolution is increased. The coefficient is therefore expected to be dependent on model resolution. One surmised numerical modelling attempt to account for the equilibrium sediment exchange processes would be to simulate sediment transport at the timescale of turbulent bursting when the exchange process is occurring. However, this sub-second/centimeter scale coherent process controlling fluid momentum and sediment

exchange directed from and to the streambed can only be resolved using direct numerical simulation (DNS) modelling, which is impractical for watershed sediment transport modelling (Papanicolaou et al. 2008). Additionally, the efficiency of a burst to subsequently fallout and pick up sediment is unknown and requires experimentation. Therefore, physically and explicitly representing the bursting-driven equilibrium sediment exchange in a watershed scale model is not practical at this time. We use data-driven results from sediment fingerprinting to help calibrate the equilibrium sediment exchange simulated in our modelling, and we hope the work here might be built on to develop other semi-theoretical approaches.

Finally, equilibrium sediment exchange impacts the quality of sediment in the streambed and sediment transported from the watershed. This concept is reflected in the sediment fingerprinting data and results in Figures 5 and 6. In this watershed, sediment originating from the uplands is more recalcitrant in nature with lower overall carbon content as compared to the labile autochthonous carbon accrued in streambed sediments (Ford et al. 2017). The evolving streambed and sediment load include a changing matrix of inert and labile sediment carbon as a function of upland and instream processes. To this end, equilibrium sediment exchange should be considered when the sediment continuum is used to investigate the evolving critical zone.

2.6 CONCLUSIONS

This research provided new coupling of sediment fingerprinting and watershed modelling methods to elucidate the role of the equilibrium sediment exchange process. Our results suggest equilibrium sediment exchange is a substantial process occurring in the system studied. The process does not change the sediment load or streambed sediment storage but does impact the quality of sediment residing in the streambed. Therefore, we suggest equilibrium sediment exchange should be considered when the sediment continuum is used to investigate the critical zone.

Coupling sediment fingerprinting with watershed modelling is a new area of research deserving substantial development. We outline future research priorities for coupling the methods as follows:

1. Improved coupling of sediment fingerprinting time scales with watershed modelling time scales is needed. Sediment fingerprinting results typically have high variance on a daily basis due to the episodic nature of erosion and the distribution of tracer signatures across a basin. Watershed modelling results are typically specified for daily or sub-daily time steps and results are more representative of the mean behavior of the watershed during the period. Probabilistic approaches might be advanced for better comparisons between the different time scales.
2. Improved sediment tracking and allocation of sediment provenance and sediment history is needed in watershed modelling. For example, the residence time of deposited sediments and their origin before deposition is rarely accounted in fluvial watershed modelling. This lack of information makes a direct comparison of provenance with sediment fingerprinting results cumbersome. Lagrangian methods and better source fractionalization methods coupled with watershed modelling tools might help overcome this limitation.
3. Improved accounting of spatially explicit erosion prone sources is needed in watershed modelling. Sediment fingerprinting relies on field collection of sediments from erosion-prone surfaces identified in the field via erosion scars and deteriorated morphology. These connected sediment transport pathways often are not spatially explicit in watershed modelling, which hinders coupling of the methods. Sediment connectivity theory serves as one method to inform sediment transport models and design sampling regimes for sediment fingerprinting to improve the coupling of the methods. This advancement will require additional research focused on in-stream connectivity theory given this topic is under-developed in the modelling community.
4. Improved development of physically-based formulae for source exchange processes, such as equilibrium sediment exchange, is needed. For example, this present research offered potential governing variables controlling equilibrium exchange, but a predictive model of equilibrium exchange has not yet been developed. Modelling formula accounting for source exchange processes both

in the uplands and stream corridor will facilitate better coupling with sediment fingerprinting results.

5. Improved nonconservative tracer simulation *via* watershed modelling is needed to assist with tracer representation in fingerprinting. Watershed modelling efforts can increasingly quantify both physical and biogeochemical changes of sediment properties, and utilization of these sub-routines to assist with sediment fingerprinting is expected to be fruitful.
6. Improved optimization strategies for coupling sediment transport modelling and sediment fingerprinting results are needed. For example, if sediment fingerprinting is simultaneously simulated in sediment transport modeling, sediment sources may be better partitioned during modeling. Optimization of sediment fingerprinting and watershed modeling using iterative feedback loops and multi-step calibration methods serve as one approach. Data assimilation methods applied similarly to tracer-transport models of the atmospheric science community serve as another approach.

2.7 ACKNOWLEDGEMENTS

We thank the two anonymous reviewers, the submission editor, and the Editor-In-Chief for comments that greatly improved the quality of this paper. We gratefully acknowledge the financial support of this research under National Science Foundation Award 163288. We thank LIF Creative (www.lif-creative.com) for illustration and graphic design assistance.

2.8 SUPPLEMENTARY MATERIAL I: EQUATIONS OF THE PROBABILITY OF CONNECTIVITY AND UPLAND EROSION MODELS

$$P(C) = P(S) \cap P(D_H \cup D_{NH}) \cap P(T_H \cup T_{NH}) \cap \{1 - P(B)\} \quad \text{(A.1)}$$

$$P(C) = \{P(S)\} \times \{P(D_H) + P(D_{NH}) - P(D_H)P(D_{NH})\} \times \{P(T_H) + P(T_{NH}) - P(T_H)P(T_{NH})\} \times \{1 - P(B)\} \quad \text{(A.2)}$$

$$SW_t = SW_0 + \sum_{i=1}^{t}(R_{day} - Q_{surface} - E_a - w_{seep} - Q_{gw}) \quad \text{(A.3)}$$

$$Q_{surface} = \frac{(R_{day} - I_a)^2}{(R_{day} - I_a + S)} \quad \text{(A.4)}$$

$$S = 25.4\left(\frac{1000}{CN} - 10\right) \quad \text{(A.5)}$$

$$P_i(S) = \begin{cases} 1, & \text{if sediment is present in the cell} \\ 0, & \text{if sediment is absent in the cell} \end{cases} \quad \text{(A.6)}$$

$$P_{ij}(D_H) = \begin{cases} 1, & \text{if } \tau_{f\,ij} - \tau_{cr\,i} > 0 \\ 0, & \text{if } \tau_{f\,ij} - \tau_{cr\,i} \leq 0 \end{cases} \quad \text{(A.7)}$$

$$P_i(D_{NH}) = \begin{cases} 1, & \text{if a disturbance agent exists} \\ 0, & \text{if a disturbance agent is not present} \end{cases} \quad \text{(A.8)}$$

$$P_{ij}(T_{H-up}) = \begin{cases} 1, & \text{if } S_{ac\,i} - S_{cr\,ij} > 0 \\ 0, & \text{if } S_{ac\,i} - S_{cr\,ij} \leq 0 \end{cases} \quad \text{(A.9)}$$

$$S_{cr\,i} = a_i A_i^{-b} \quad \text{(A.10)}$$

$$S_{cr\,i\,j} = 0.73 c_i e^{1.3RFC_i}\left(0.00124 S_{0.05\,ij} - 0.37\right) A_i^{-0.38} \quad \text{(A.11)}$$

$$S_{0.05} = 0.819\left(25.4\left[\frac{1000}{CN_{ij}} - 10\right]^{1.15}\right) \quad \text{(A.12)}$$

$$P_i(T_{H-dwn}) = \begin{cases} 1, & \text{if } S_i - \frac{\sum S_{up}}{N} > 0 \\ 0, & \text{if } S_i - \frac{\sum S_{up}}{N} \leq 0 \end{cases} \quad \text{(A.13)}$$

$$P_i(B) = \begin{cases} 1, & \text{if a buffer exists} \\ 0, & \text{if a buffer does not exist} \end{cases} \quad \text{(A.14)}$$

$$S_y = \epsilon \rho_s t l w \quad \text{(A.15)}$$

$$\epsilon = k_d * \left(\tau_f - \tau_{cr}\right) \quad \text{(A.16)}$$

2.9 SUPPLEMENTARY MATERIAL II: EQUATIONS OF THE INSTREAM SEDIMENT TRANSPORT MODEL

$$Q_i^j = \frac{1}{n_j}\frac{(A_i^j)^{5/3}}{(P_i^j)^{2/3}}(S_j)^{1/2} \quad \text{(B.1)}$$

$$B_i^j = B_{i-1}^j + Ed_i^j \quad \text{(B.2)}$$

$$SS_i^j = SS_{i-1}^j + \sum_{k=1}^{N} {E_i}^j{}_{(k)} - D_i^j + {Qssin_i}^j\,\Delta t - {Qssout_i}^j\,\Delta t \quad \text{(B.3)}$$

$$Tc_i^j = C_{Tc}\,({\tau_f}_i^j)^{1.5}\,L_{reach_j}\,\Delta t \quad \text{(B.4)}$$

$$Tc_i^j > SS_{i-1}^j, \quad \text{(B.5)}$$

$$Tc_i^j < SS_{i-1}^j \quad \text{(B.6)}$$

$${Tc_{(k)}}_i^j = {Tc_{(k-1)}}_i^j - {E_{(k)}}_i^j \quad \text{(B.7)}$$

$${E_{(k)}}_i^j = \min[a_{(k)}\left({\tau_f}_i^j - {\tau_{cr}}_{(k)}{}_i^j\right)^b {SA_{(k)}}_i^j\,\Delta t, {Tc_{(k)}}_i^j, {S_{(k)}}_i^j] \quad \text{(B.8)}$$

$${\tau_f}_i^j = C_{\tau(1)}(\rho g R_i^j S_j + C_{\tau(2)}\rho\left(\frac{u_i^j - u_{i-1}^j}{\Delta t}\right)R_i^j) \quad \text{(B.9)}$$

$$C_{\tau(bed)} = 4.05 * 10^{-6}\left(\frac{B_i^j}{H_i^j}\right)^6 + 2.1201 * 10^{-4}\left(\frac{B_i^j}{H_i^j}\right)^5 - 4.37492 * 10^{-3}\left(\frac{B_i^j}{H_i^j}\right)^4 +$$
$$0.04505583\left(\frac{B_i^j}{H_i^j}\right)^3 - 0.241185\left(\frac{B_i^j}{H_i^j}\right)^2 + 0.58925899\left(\frac{B_i^j}{H_i^j}\right)^1 + 1.00975426$$

$$if\ C_{\tau(bed)} > 1.5, then\ C_{\tau(bed)} = 1.5 \quad \text{(B.10)}$$

$$C_{\tau(bank)} = 2.4825 * 10^{-3}\left(\frac{B_i^j}{H_i^j}\right)^2 - 0.0773109\left(\frac{B_i^j}{H_i^j}\right)^1 + 1.6$$

$$if\ C_{\tau(bank)} > 1.5, then\ C_{\tau(bank)} = 1.5 \quad \text{(B.11)}$$

$$E_{SFGL_i}^{\ j} = \min[a_{SFGL}\left(\tau_{f_i}^{\ j} - \tau_{cr_{SFGL_i}}^{\ j}\right)^b SA_{SFGL_i}^{\ j}\,\Delta t, Tc_{SFGL_i}^{\ j}, S_{SFGL_i}^{\ j}] \quad \text{(B.12)}$$

$$S_{SFGL_i}^{\ j} = S_{SFGL\,sediment_i}^{\ j} - S_{SFGL\,biology_i}^{\ j} \quad \text{(B.13)}$$

$$S_{SFGL\,sediment_i}^{\ j} = \min[\left(S_{SFGL\,sediment_{i-1}}^{\ j} - E_{SFGL\,sediment_i}^{\ j} + D_{SFGL\,sediment_i}^{\ j}\right), S_{SFGL\,sediment\ max}] \quad \text{(B.14)}$$

$$S_{SFGL\,biology_i}^{\ j} = \min[\left(S_{SFGL\,biology_{i-1}}^{\ j} - E_{SFGL\,biology_i}^{\ j} + D_{SFGL\,biology_i}^{\ j} + G_{SFGL\,sediment}\right), S_{SFGL\,biology\ max}] \quad \text{(B.15)}$$

$$E_{Bed_i}^{\ j} = \min[a_{Bed}\left(\tau_{f_i}^{\ j} - \tau_{cr_{Bed_i}}^{\ j}\right)^b SA_{Bed_i}^{\ j}\,\Delta t, Tc_{Bed_i}^{\ j}, S_{Bed_i}^{\ j}] \quad \text{(B.16)}$$

$$S_{bed_i}^{\ j} = S_{bed_{i-1}}^{\ j} + D_{bed_{i-1}}^{\ j} - E_{bed_{i-1}}^{\ j} \quad \text{(B.17)}$$

$$E_{Bank_i}^{\ j} = \min[a_{Bank}\left(\tau_{f_i}^{\ j} - \tau_{cr_{Bank_i}}^{\ j}\right)^b SA_{Bank_i}^{\ j}\,\Delta t, Tc_{Bank_i}^{\ j}] \quad \text{(B.18)}$$

$$D_i^j = \frac{\omega_s\,\Delta t}{K_{p_i}^{\ j} H_i^j}\,(SS_{i-1}^j - Tc_i^j) \quad \text{(B.19)}$$

$$K_{p_i}^{\ j} = 0.5\,e^{-0.98\,z^{*j}_i} \quad \text{(B.20)}$$

$$z^{*j}_i = \frac{ws}{K\,U_{*_i}^{\ j}} \quad \text{(B.21)}$$

$$U_{*_i}^{\ j} = \left(g\,H_i^j\,S_j\right)^{0.5} \quad \text{(B.22)}$$

$$P_{Upland_i}^{\ j} = \frac{(Qssup_i^j + Qssup_i^{j-1}) * \Delta t}{\sum_{k=1}^{N}(E_{i\,(k)}^{\ j} + E_i^{j-1}{}_{(k)})} * (1 - Exf) \quad \text{(B.23)}$$

$$P_{Bed_i}^{\ j} = 1 - P_{Upland_i}^{\ j} \quad \text{(B.24)}$$

$$SS_{i+\frac{1}{2}}^j = SS_i^j - Exf * SS_i^j + Exf * S_{bed_i}^j * \left[\frac{SS_i^j}{S_{bed_i}^j}\right] \quad \text{(B.25)}$$

$$S_{bed_{i+\frac{1}{2}}}^j = S_{bed_i}^j + Exf * S_{bed_i}^j * \left[\frac{SS_i^j}{S_{bed_i}^j}\right] - Exf * SS_i^j \quad \text{(B.26)}$$

2.10 SUPPLEMENTARY MATERIAL III: LIST OF SYMBOLS

$P(C)$	=	probability of sediment connectivity
$P(S)$	=	probability of sediment supply
$P(D_H)$	=	probability of hydrologic detachment
$P(D_{NH})$	=	probability of nonhydrologic detachment
$P(T_H)$	=	probability of hydrologic transport
$P(T_{NH})$	=	probability of nonhydrologic transport
$P(B)$	=	probability of buffers
SW_t	=	final soil water content
SW_0	=	initial soil water content
R_{day}	=	amount of precipitation
$Q_{surface}$	=	amount of surface runoff
E_a	=	amount of evapotranspiration
w_{seep}	=	amount of lateral flow
Q_{gw}	=	amount of return flow

S	=	retention parameter
I_a	=	initial abstraction
CN	=	curve number
$\tau_{f\,ij}$	=	fluid shear stress at cell *i* during time step *j*
$\tau_{cr\,i}$	=	critical shear stress of the eroding surface in cell *i*
S_{ac}	=	slope of geospatial cell *i*
S_{cr}	=	critical slope required to initiate ephemeral gully incision of cell *i*
a	=	local climate and land use and soil characteristics of geospatial cell *i*,
A	=	upstream drainage area of geospatial cell *i*
b	=	an exponent
$S_{0.05}$	=	maximum potential loss to runoff
RFC	=	rock fragment cover of the soil
c	=	other sources of the variation of the coefficient *a*
S_i	=	slope in a particular geospatial cell
N	=	number of upstream cells flowing in cell *i*
$\sum S_{up}$	=	sum of the slopes of each cell upstream of cell *i*
S_y	=	sediment yielded at the watershed outlet from the active contributing area
ϵ	=	erosion rate as predicted by the Partheniades (1965) equation
ρ_s	=	bulk density of the sediment
t	=	amount of time sediment is contributed from the active contributing area
l	=	length of the eroding rill or ephemeral gully
w	=	width of the eroding rill or ephemeral gully
ϵ	=	erosion rate of the soil
k_d	=	erodibility coefficient
τ_{cr}	=	upland critical shear stress of the eroding surface
τ_f	=	effective shear stressof the accumulated flow on the eroding surface
A_1	=	contributing area, bin 1
A_2	=	contributing area, bin 2
A_3	=	contributing area, bin 3
S_1	=	longitudinal slope, bin 1
S_2	=	longitudinal slope, bin 2
S_3	=	longitudinal slope, bin 3
w_1	=	channel width, bin 1
w_2	=	channel width, bin 2
w_3	=	channel width, bin 3
ε/D	=	upland relative roughness
t_1	=	storm length, erosion time bin 1
t_2	=	storm length, erosion time bin 2
t_3	=	storm length, erosion time bin 3
L_1	=	channel length, bin 1
L_2	=	channel length, bin 2
L_3	=	channel length, bin 3
ρ_w	=	density of fluid

$\rho bank$ = density of bank sediment
ρ_{SFGL} = density of SFGL sediment
P_i^j = wetted peremeter
B_i^j = channel width
Ed_i^j = erosion/deposition from/to the banks
Exf = sediment exchange factor
j = a particular stream-reach
i = a particular time step
k = the sediment source
N = number of sediment sources
SS = mass of sediment
E = erosion
D = deposition
$Q_{ss\ in}$ = sediment flow rate in the reach
$Q_{ss\ up}$ = sediment flow rate in the reach from the uplands
$Q_{ss\ out}$ = sediment flow rate out of the reach
S_{bed} = mass of bed sediments
Δt = the time step
T_c = transport capacity
C_{Tc} = transport capacity coefficient
L_{reach} = length of the spatial step
k = a particular sediment source
a_k = erodibility of the source
SA = surface area of the sediment source
S = supply of a sediment source
$C_{\tau(1)}$ = coefficient accounting for the difference between bed and banks erosion
H = flow depth
R = hydraulic radius
u = flow velocity
S_{SFGL} = supply to the SFGL layer
$S_{SFGL\ sediment}$ = supply to the SFGL sediment layer
$S_{SFGL\ biology}$ = supply to the SFGL biofilm layer
S_{bed} = supply to the bed layer
z^* = rouse number
U_* = friction velocity
P_{Upland} = percent of exported sediment from the uplands
P_{Bed} = percent of exported sediment from the bed
$C_{\tau(2)}$ = shear stress coefficient for unsteady flow
$C_{tc(low)}$ = transport capacity coefficient for low flows
$C_{tc(high)}$ = transport capacity coefficient for high flows
ω_s = mean settling velocity of suspended material
κ = von Karmen coefficient
$D_{SFGL,\ max}$ = maximum depth of SFGL
t_d = development time of the SFGL layer

$G_{SFGL,\ Bio}$ = generation rate of SFGL biofilm
$\tau_{cr(sfgl)}$ = critical shear of the SFGL source
$\tau_{cr(bed)}$ = critical shear of the bed source
$\tau_{cr(bank)}$ = critical shear of the bank source
$a_{(sfgl)}$ = erodibility of the SFGL source
$a_{(bed)}$ = erodibility of the bed source
$a_{(bank)}$ = erodibility of bank source
k_{ss} = sediment routing coefficient
k_s = flood wave coefficient
N_{reach} = number of reaches in the stream segment
Θ = bank sideslope
B_{upper} = channel bottom width, upper catchment
B_{lower} = channel bottom width, lower catchment
n_{upper} = manning's coefficient, upper catchment
n_{lower} = manning's coefficient, lower catchment
S_{upper} = channel slope, upper catchment
S_{lower} = channel slope, lower catchment
$L_{reach,\ upper}$ = channel length, upper catchment
$L_{reach,\ lower}$ = channel length, lower catchment
$H_{bank,\ upper}$ = bankfull depth, upper catchment
$H_{bank,\ lower}$ = bankfull depth, lower catchment
$Q_{boundary,\ upper}$ = boundary flow, upper catchment
$Q_{boundary,\ lower}$ = boundary flow, upper catchment
K_p = settling depth coefficient
$Exf_{Upper,\ Regime\ 1}$ = upper catchment exchange factor, flow regime 1
$Exf_{Upper,\ Regime\ 2}$ = upper catchment exchange factor, flow regime 2
$Exf_{Upper,\ Regime\ 3}$ = upper catchment exchange factor, flow regime 3
$Exf_{Upper,\ Regime\ 4}$ = upper catchment exchange factor, flow regime 4
$Exf_{Lower,\ Regime\ 1}$ = lower catchment exchange factor, flow regime 1
$Exf_{Lower,\ Regime\ 2}$ = lower catchment exchange factor, flow regime 2
$Exf_{Lower,\ Regime\ 3}$ = lower catchment exchange factor, flow regime 3
$Exf_{Lower,\ Regime\ 4}$ = lower catchment exchange factor, flow regime 4
Q_p = hydrograph peak when each sediment sample was collected
Q_{pm} = mean peak when considering all transported sediment data
$\delta^{13}C\text{-}\delta^{13}C_m$ = stable carbon isotope value subtracted by mean stable carbon isotope value

Table 2.1. Review of organic tracers applied in sediment fingerprinting studies.

Study	Watershed (km^2)	Sediment Sources	Organic Tracers
Studies considering distal/upland sources with different land uses and vegetative cover			
Papanicolaou et al. 2003	600	Winter wheat agriculture and conifer forest silt loam soil	$\delta^{13}C$, $\delta^{15}N$, C/N
Bellanger et al. 2004	25**	Experimental coffee, maize, and bare plots	$\delta^{13}C$, $\delta^{15}N$, TOC, TN, C/N
*Minella et al. 2004**	1.3, 0.57	Cultivated areas, pastures, unpaved roads	TOC, TN, TP
Dalzell et al. 2005	850	Corn, soybean, tall fescue	$\delta^{13}C$, DOC
*Gibbs 2008**	117	Pastures, forested areas	$\delta^{13}C$
Jacinthe et al. 2009	Unspecified	Corn, soy bean, rye rotation, plowed continuous corn, no-till continuous corn	$\delta^{13}C$
*Kouhpeima et al. 2010**	1.0, 5.4	Gullies, surface materials from various soil formations	TOC, TON, TOP
*Nazari Samani et al. 2011**	Unspecified	Gully side wall, dry farming and rangeland	OC, N, C/N
Studies considering distal/upland sources as well as streambanks or floodplains			
Walling et al. 1993	46	Pastures, cultivated agriculture Streambanks	TOC, TN
*Walling and Woodward 1995**	276	Cultivated areas, pastures Streambanks	TOC, TON, TOP
*Collins et al. 1997**	46, 8.7	Pastures, cultivated areas, woodland Streambanks	TOC, TON, TOP
*Walling et al. 1999**	3315	Woodland topsoil, uncultivated topsoil, cultivated topsoil Streambanks	TOC, TON, TOP
*Russell et al. 2001**	2 (~4 km^2)	Field drains, pastures, arable land, hopyards Streambanks	TOC, TN, TP
*Walling et al. 2001**	63	Cultivated areas, bush grazing, gullies Streambanks	TOC, TON
Gomez et al. 2003	1580	Weathered bedrock from gullies, soil and regolith on hillslopes Floodplains	$\delta^{13}C$, C/N
*Walling 2005 (via Nicholls 2001; unpublished dissertation)**	258	Woodland topsoil, pastures, cultivated topsoil Streambanks	TOC, TON
Fox and Papanicolaou 2007	0.71	Agricultural hillslopes Floodplains	$\delta^{13}C$, $\delta^{15}N$, C/N
Fox and Papanicolaou 2008a	15	Logging in conifer forest, hay pastures, winter wheat and peas agriculture Winter wheat-floodplains	$\delta^{15}N$, C/N
Fox and Papanicolaou 2008b	600	Winter wheat-uplands, hay pastures, conifer forest, agricultural conservation reserve-uplands Winter wheat-floodplains, agricultural conservation reserve-floodplains	TOC, TON, TOP, $\delta^{15}N$
*Rhoton et al. 2008**	150	Fan remnants, hillslopes, mountain slopes, alluvial fans Floodplains	$\delta^{13}C$, $\delta^{15}N$, C/N, TOC, TN
Fox 2009	4 (~2 km^2)	Surface coal mining, forested areas, reclaimed grassland, geogenic organic matter Streambanks	$\delta^{13}C$, $\delta^{15}N$, TOC, TN
*Gellis et al. 2009**	109-156	Construction sites, ditches, agricultural topsoil, forested areas Streambanks and floodplains	$\delta^{13}C$, $\delta^{15}N$, TOC, TN
*Mukundan et al. 2010**	182	Croplands, pastures, forested areas, unpaved roads, construction sites Streambanks and floodplains	$\delta^{15}N$

Table 2.1 (Continued). Review of organic tracers applied in sediment fingerprinting studies.

Study	Watershed (km^2)	Sediment Sources	Organic Tracers
*Mukundan et al. 2011**	182	Croplands, pastures, forested areas, unpaved roads, construction sites Streambanks	TOC, TN
*Blake et al. 2012**	1.45	Maize agriculture, winter wheat agriculture, pastures, wooded areas Streambanks	$\delta^{13}C$
Jung et al. 2012	60	Forested areas, cultivated fields Streambanks	$\delta^{13}C$, $\delta^{15}N$, TOC
*Hancock and Revill 2013**	3860	Cultivated areas, forested areas, pastures, subsoils Streambanks	$\delta^{13}C$
*Slimane et al. 2013**	2.63	Cropland topsoils, grasslands, scrublands, gullies Streambanks	TOC, TN
Fox and Martin 2014	3.5, 2.2	Surface reclaimed mining soils, forested areas Streambanks	$\delta^{13}C$, $\delta^{15}N$, TOC, TN
*Smith and Blake 2014**	920	Pastures, cultivated topsoil Streambanks	TOC
Laceby et al. 2015	75, 123, 311	Gullies, cultivated agriculture, grazing pastures, natural grazing land Streambanks	$\delta^{13}C$, $\delta^{15}N$, TOC, TN, C/N
*Stewart et al. 2015**	324	Forested areas, roads, pastures, cropland topsoil Streambanks	$\delta^{13}C$, $\delta^{15}N$, TOC, TN
Laceby et al. 2016	171, 265, 77	Cultivated topsoil, forested areas, subsoils	δ13C, δ15N, TOC, TN
McCarney-Castle et al. 2017	217	Upland surfaces Streambanks	$\delta^{13}C$, $\delta^{15}N$
		Studies considering streambed and other sources	
McConnachie and Petticrew 2006	75	Organic matter sources Leaf litter, detritus Algae, periphyton, decaying salmon	$\delta^{13}C$, $\delta^{15}N$, C/N
Bonn and Rounds 2010	1840	Leaf litter, upland soils, detritus Suspended sediment, macrophytes, phytoplankton, periphyton, wastewater treatment effluent	$\delta^{13}C$, $\delta^{15}N$, C/N
Fox et al. 2010	61.8	Streambanks, bank slumping Streambed	$\delta^{15}N$, TOC, TN, C/N
Schindler Wildhaber et al. 2012	31	Forested areas, Pastures, Arable land Riverbed, Algae	$\delta^{13}C$, $\delta^{15}N$, C/N
*Cooper et al. 2012**	5.4	Organic matter sources Streambed sediments	$\delta^{13}C$
McCorkle et al. 2016	Unspecified	Surface erosion (O horizon) Streambanks Streambed	$\delta^{13}C$, $\delta^{15}N$, C/N
*Rose et al. 2017**	7.25	Agricultural surface soil, forested surface and subsurface soil, pastures, gullies Streambanks, Floodplains Streambed	OC, ON, C/N $\delta^{13}C$, $\delta^{15}N$
*Zhang et al. 2017**	3 (~70 km^2)	Farmyard manures/slurries, damaged road verges, septic tanks Decaying instream vegetation, watercress farms, fish farms	$\delta^{13}C$, $\delta^{15}N$

**Note: These studies also applied inorganic and/or radionuclide tracers. Only organic tracers are tabulated herein.*

***30 m^2 plots within the 25 km^2 catchment*

Table 2.2. Upland erosion model inputs and parameters.

Parameter	Description	Value/Parameter Range	Units
A_1	Contributing area, bin 1	116	m^2
A_3	Contributing area, bin 2	951	m^2
A_3	Contributing area, bin 3	34,079	m^2
$\tau_{cr,\ upland}$	Upland critical shear stress	0.10-10	Pa
S_1	Longitudinal slope, bin 1	0.16	$m\ m^{-1}$
S_2	Longitudinal slope, bin 2	0.13	$m\ m^{-1}$
S_3	Longitudinal slope, bin 3	0.12	$m\ m^{-1}$
w_1	Channel width, bin 1	0.08	m
w_2	Channel width, bin 2	0.12	m
w_3	Channel width, bin 3	0.44	m
ε/D	Upland relative roughness	0.00001-1	Unitless
ρ_d	Bulk density of eroded sediment	1,400	$kg\ m^{-3}$
t_1	Storm length, erosion time bin 1	0.017-0.167	hr
t_2	Storm length, erosion time bin 2	0.183-0.367	hr
t_3	Storm length, erosion time bin 3	0.383-0.667	hr
k_d	Erodibility coefficient	1.0×10^{-10}-1.0×10^{-8}	$cm^3\ N^{-1}\ s^{-1}$
L_1	Channel length, bin 1	Varies daily	m
L_2	Channel length, bin 2	Varies daily	m
L_3	Channel length, bin 3	Varies daily	m
ρ_w	Density of fluid	1,000	$kg\ m^{-3}$

Table 2.3. Instream sediment transport model inputs and parameters.

Parameter	Description	Value/Parameter Range	Units
ρ_w	Density of fluid	1000	kg m^{-3}
ρ_{bank}	Density of bank sediment	1500	kg m^{-3}
ρ_{SFGL}	Density of SFGL sediment	1,000	kg m^{-3}
$C_{\tau(2)}$	Shear stress coefficient for unsteady flow	1-100	Unitless
$C_{tc(low)}$	Transport capacity coefficient for low flows	6.0 x 10^{-7}-1.5 x 10^{-6}	$m^{1/2}$ s^2 $kg^{-1/2}$
$C_{tc(high)}$	Transport capacity coefficient for high flows	6.0 x 10^{-7}-1.5 x 10^{-6}	$m^{1/2}$ s^2 $kg^{-1/2}$
ω_s	Mean settling velocity of suspended material	0.00036-0.00240	m s^{-1}
κ	Von Karmen coefficient	0.4	Unitless
$D_{SFGL,\ max}$	Maximum depth of SFGL	0.001-0.010	m
t_d	Development time of the SFGL layer	300-3000	s
$G_{SFGL,Bio}$	Generation rate of SFGL biofilm	1.81 x 10^{-9}	kg m^{-2} s^{-1}
$\tau_{cr(sfgl)}$	Critical shear of the SFGL source	0.024-1.20	Pa
$\tau_{cr(bed)}$	Critical shear of the bed source	1.0-10.0	Pa
$\tau_{cr(bank)}$	Critical shear of the bank source	10.0-93.0	Pa
$a_{(sfgl)}$	Erodibility of the SFGL source	1.0 x 10^{-4}-1.0 x 10^{-2}	kg Pa^{-1} m^{-2} s^{-1}
$a_{(bed)}$	Erodibility of the bed source	1.0 x 10^{-5}-1.0 x 10^{-3}	kg Pa^{-1} m^{-2} s^{-1}
$a_{(bank)}$	Erodibility of bank source	1.0 x 10^{-6}-2.0 x 10^{-4}	kg Pa^{-1} m^{-2} s^{-1}
k_{ss}	Sediment routing coefficient	0.00-0.50	Unitless
k_s	Flood wave coefficient	0.0	Unitless
N_{reach}	Number of reaches in the stream segment	2	Unitless
Θ	Bank sideslope	16.858	°
B_{upper}	Channel bottom width, upper catchment	6	m
B_{lower}	Channel bottom width, lower catchment	11	m
n_{upper}	Manning's coefficient, upper catchment	0.03	Unitless
n_{lower}	Manning's coefficient, lower catchment	0.03	Unitless
S_{upper}	Channel slope, upper catchment	0.0009	m m^{-1}
S_{lower}	Channel slope, lower catchment	0.00044	m m^{-1}
$L_{reach,\ upper}$	Channel length, upper catchment	18	m
$L_{reach,\ lower}$	Channel length, lower catchment	10	m
$H_{bank,\ upper}$	Bankfull depth, upper catchment	2	m
$H_{bank,\ lower}$	Bankfull depth, lower catchment	2	m
$Q_{boundary,\ upper}$	Boundary flow, upper catchment	1	m^3 s^{-1}
$Q_{boundary,\ lower}$	Boundary flow, upper catchment	2	m^3 s^{-1}
K_p	Settling depth coefficient	0.10-1.0	Unitless
$Exf_{Upper,\ Regime\ 1}$	Upper catchment exchange factor, flow regime 1	0.0-1.0	Unitless
$Exf_{Upper,\ Regime\ 2}$	Upper catchment exchange factor, flow regime 2	0.0-1.0	Unitless
$Exf_{Upper,\ Regime\ 3}$	Upper catchment exchange factor, flow regime 3	0.0-1.0	Unitless
$Exf_{Upper,\ Regime\ 4}$	Upper catchment exchange factor, flow regime 4	0.0-1.0	Unitless
$Exf_{Lower,\ Regime\ 1}$	Lower catchment exchange factor, flow regime 1	0.0-1.0	Unitless
$Exf_{Lower,\ Regime\ 2}$	Lower catchment exchange factor, flow regime 2	0.0-1.0	Unitless
$Exf_{Lower,\ Regime\ 3}$	Lower catchment exchange factor, flow regime 3	0.0-1.0	Unitless
$Exf_{Lower,\ Regime\ 4}$	Lower catchment exchange factor, flow regime 4	0.0-1.0	Unitless

Table 2.4. Optimum parameter values for upland erosion model and instream connectivity model.

Parameter	Optimum Value	Units
$C_{tc(low)}$	8.45×10^{-7}	$m^{1/2}\ s^2\ kg^{-1/2}$
$C_{tc(high)}$	7.12×10^{-7}	$m^{1/2}\ s^2\ kg^{-1/2}$
ω_s	0.00079	$m\ s^{-1}$
$\tau_{cr(sfgl)}$	0.11	Pa
$\tau_{cr(bed)}$	5.68	Pa
$\tau_{cr(bank)}$	12.69	Pa
$a_{(sfgl)}$	7.54×10^{-4}	$kg\ Pa^{-1}\ m^{-2}\ s^{-1}$
$a_{(bed)}$	5.84×10^{-5}	$kg\ Pa^{-1}\ m^{-2}\ s^{-1}$
$a_{(bank)}$	1.64×10^{-4}	$kg\ Pa^{-1}\ m^{-2}\ s^{-1}$
$C_{\tau(2)}$	16.6	Unitless
k_{ss}	0.24	Unitless
t_d	1122	s
$D_{SFGL,\ max}$	0.002	m
K_p	0.98	Unitless
t_1	0.075	hr
t_2	0.235	hr
t_3	0.644	hr
$\tau_{cr,\ upland}$	4.02	Pa
k_d	6.91×10^{-9}	$cm^3\ N^{-1}\ s^{-1}$
ε/D	0.74	Unitless
$Exf_{Upper,\ Regime\ 1}$	0.90	Unitless
$Exf_{Upper,\ Regime\ 2}$	0.10	Unitless
$Exf_{Upper,\ Regime\ 3}$	0.15	Unitless
$Exf_{Upper,\ Regime\ 4}$	0.50	Unitless
$Exf_{Lower,\ Regime\ 1}$	0.90	Unitless
$Exf_{Lower,\ Regime\ 2}$	0.65	Unitless
$Exf_{Lower,\ Regime\ 3}$	0.55	Unitless
$Exf_{Lower,\ Regime\ 4}$	0.50	Unitless

Figure 2.1 Gently rolling watershed configuration and conceptualization. 'Gently rolling' reflects 'undulating' landscape slopes (i.e., not steep) with the potential for steeper sections of complex hillslopes classified as 'rolling' (USDA 2017 pp. 44).

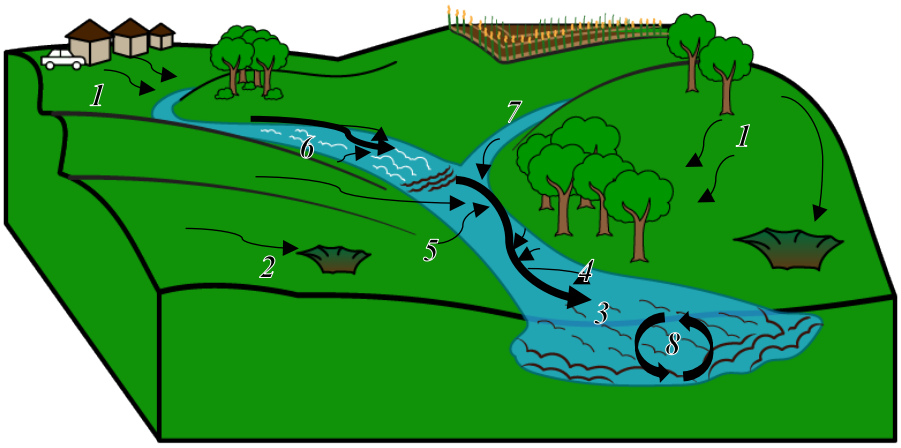

1 – Upland Erosion	*5 –Bank Erosion*
2 – Microtopography Deposition	*6 – SFGL and Bed Erosion*
3 – Instream Sediment Transport	*7 – Gully/Swale Sediment Transport*
4 – Deposition	*8 – Equilibrium Sediment Exchange*

Figure 2.2. Study watershed, land use, instream sample site locations (from Fox et al. 2010), and stream location within the Kentucky River Basin, USA. Land use in the upper catchment is primarily urban (60% urban, 40% agricultural). Land use in the lower catchment is primarily agricultural (72% agricultural, 28% urban). Samples of sediment sources from the stream corridor were collected in eight locations (labeled S1-S8) in the study watershed and defined the isotopic signature of instream sediments, banks sediments, and algae.

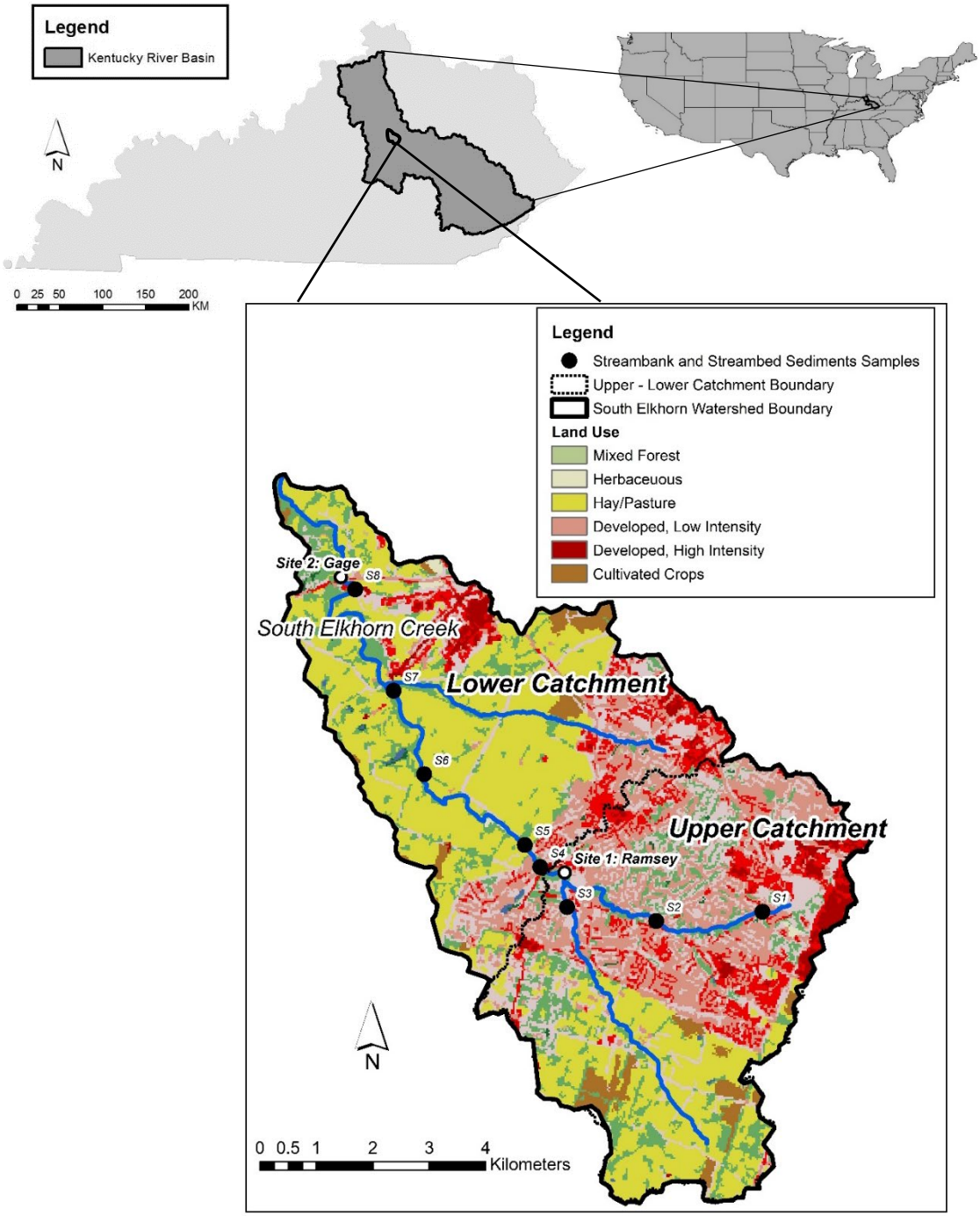

Figure 2.3. Cumulative particle size distribution of fluvial sediments performed using microscopy in the Upper South Elkhorn watershed (see also data reported in Fox et al. 2014). *d* is the diameter of the particle in μm.

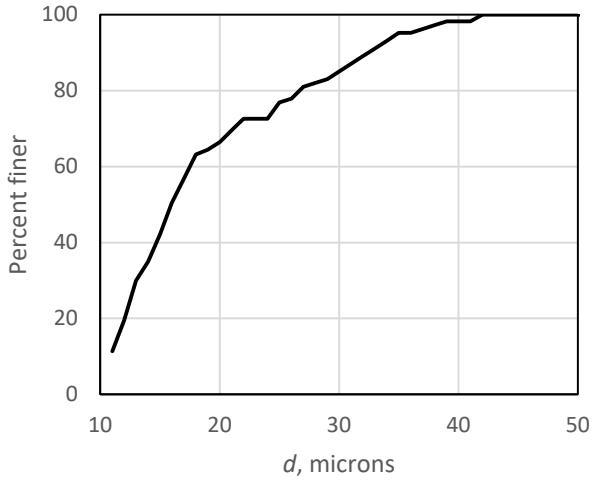

Figure 2.4. Three-stage calibration procedure for: Stage 1 sediment connectivity model calibration; Stage 2 upland erosion model and instream sediment model calibration; and Stage 3 sediment source calibration.

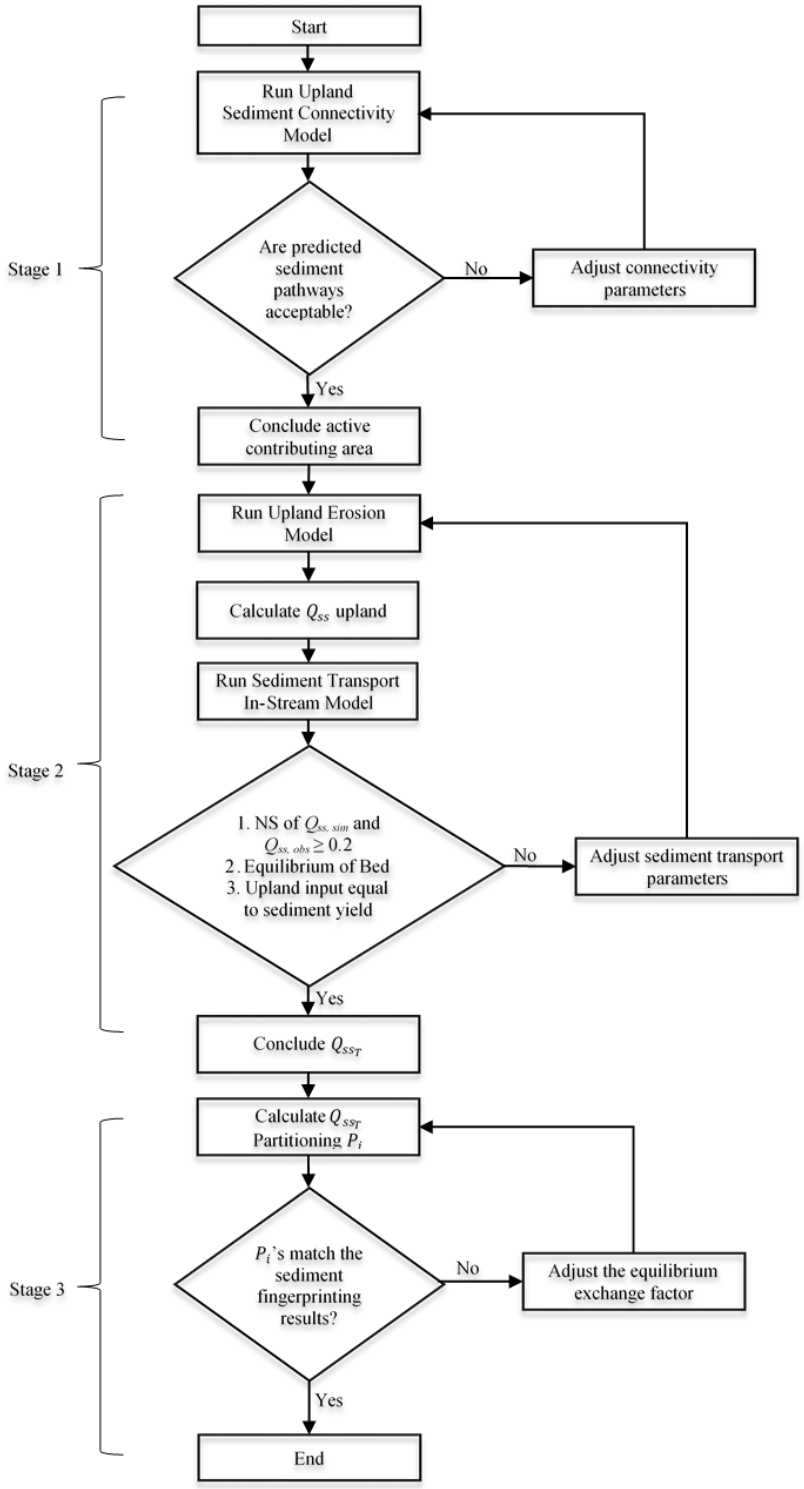

Figure 2.5. Stable carbon isotopes of sediment as a function of water discharge at the watershed outlet for the (a) upper catchment and (b) lower catchment sampling location. Source plots are included for the upland sediment and in-stream sediments. The x-axes plots the hydrograph peak (labeled as Q_p) during which each sediment sample was collected normalized by the mean observed flowrate for all transported sediment data (Q_{pm}). The y-axes plots the stable carbon isotope value of sediments after subtracting the mean. *n* represents the number of samples collected for each flow regime

(a) Upper catchment, site 1

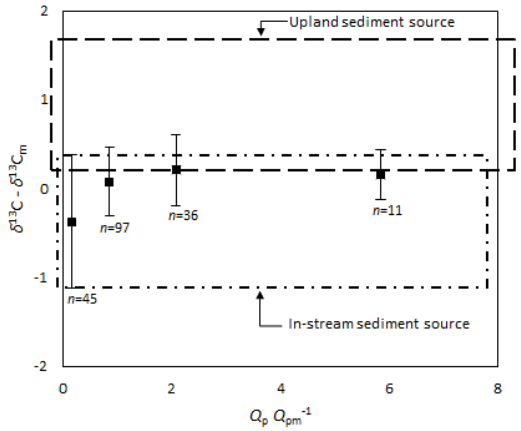

(b) Lower catchment, site 2

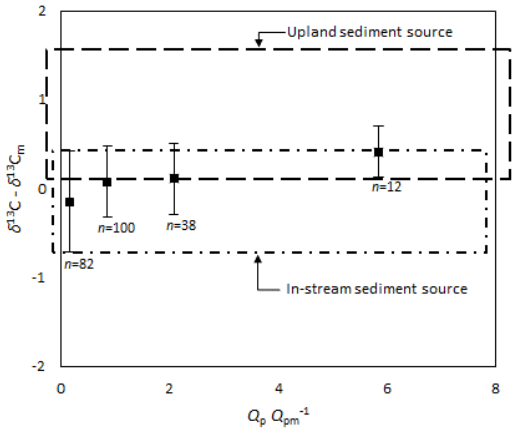

Figure 2.6. Sediment fingerprinting results as a function of water discharge for the (a) upper catchment and (b) lower catchment sampling location. The x-axes plots the hydrograph peak (labeled as Q_p) during which each sediment sample was collected normalized by the mean observed flowrate for all transported sediment data (Q_{pm}). The y-axes plot the percent of upland or streambed contribution, as determined by the sediment fingerprinting results. *n* represents the number of samples collected for each flow regime.

(a) Upper catchment, site 1

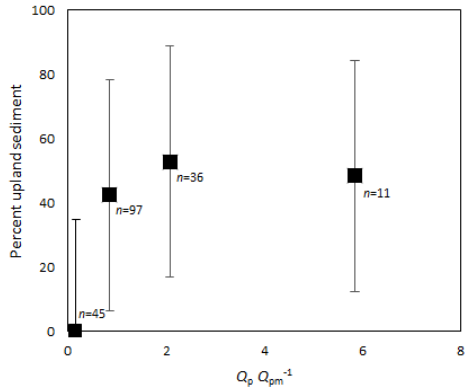

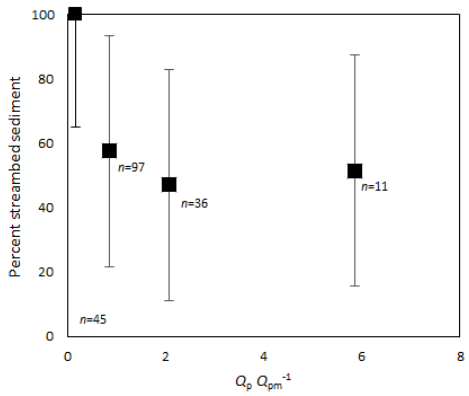

(b) Lower catchment, site 2

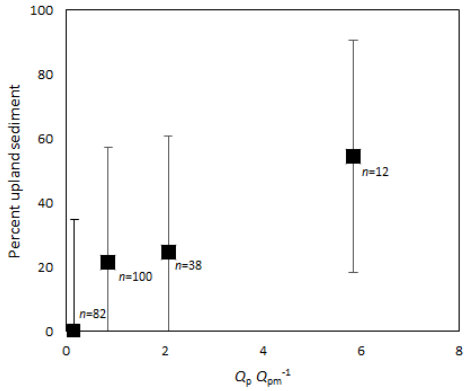

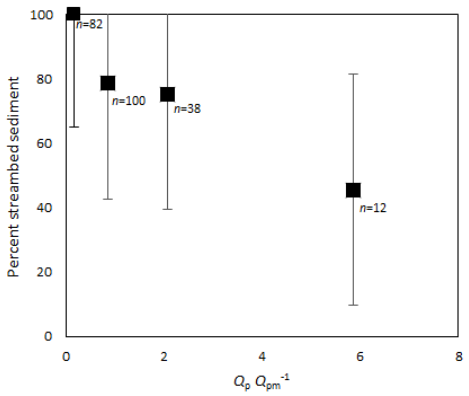

Figure 2.7. Source contributions for each event where transported sediments were collected in the (a) upper catchment and (b) lower catchment sampling locations. Q_p is the hydrograph peak (m^3 s^{-1}) simulated over the four-year study period.

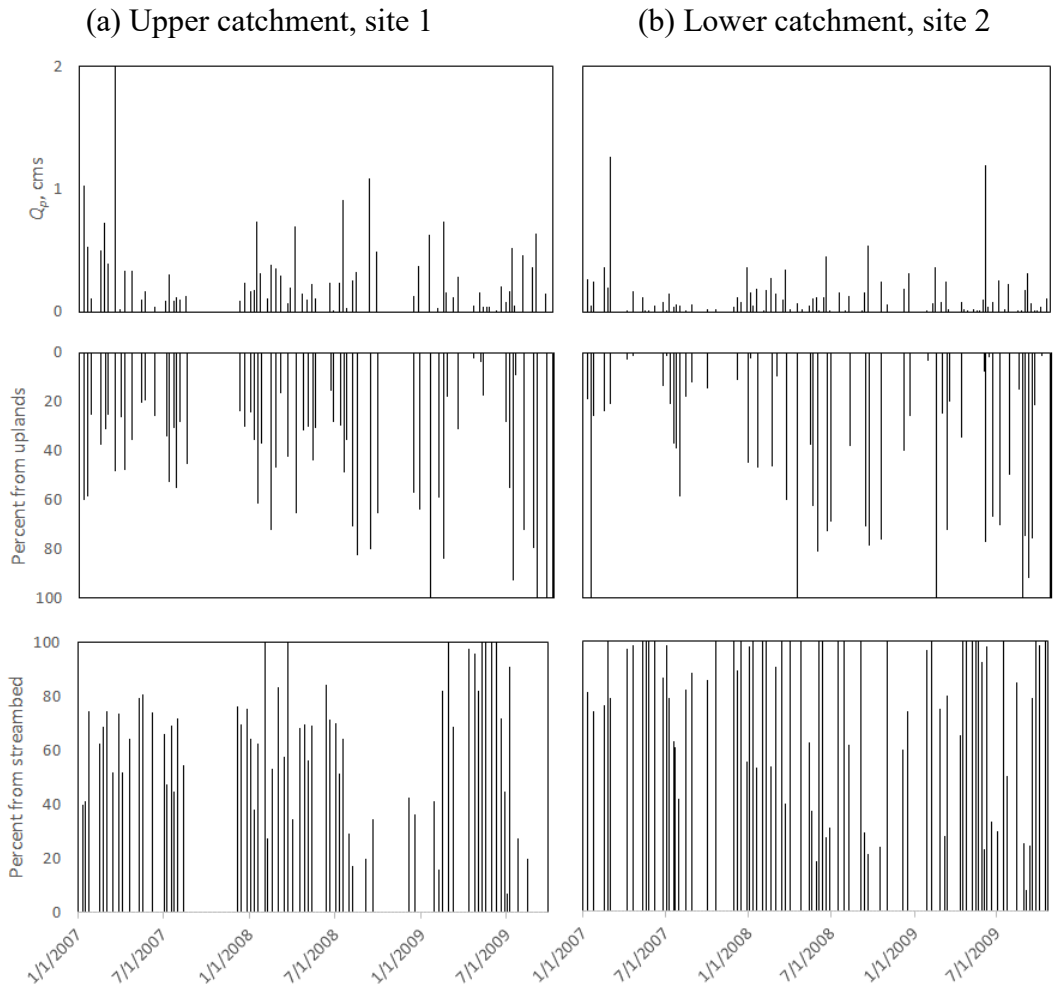

Figure 2.8. Simulated Q_{ss} compared with observed Q_{ss}. Model comparison for Site 1 (a, b, m-o) and Site 2 (c-l, p-r). Data sets (a-f) show events with maximum Q_{ss} of 10 kg s^{-1}. Data sets (g-l) show events with maximum Q_{ss} of 1 kg s^{-1}. Data sets (m-r) show events with maximum Q_{ss} of 0.1 kg s^{-1}. Three data sets from 2010 (k, l, o) are used for model validation.

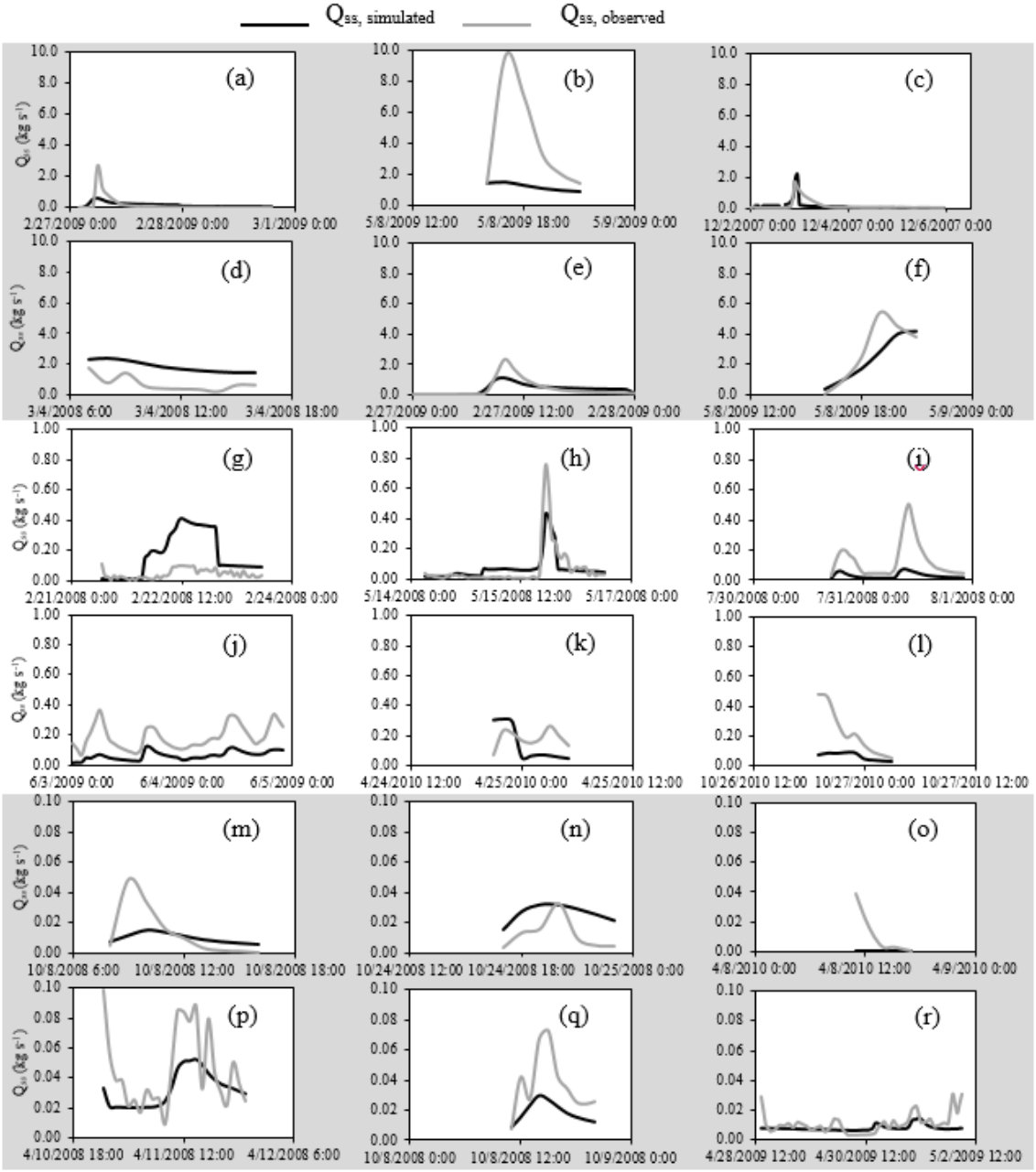

Figure 2.9. Sediment source partitioning during the four flow regimes in the (a) upper and (b) lower catchment. Partitioning results are for scenarios with no simulated equilibrium exchange (i.e., equilibrium exchange equal to zero) and with the calibrated equilibrium exchange. Sediment fingerprinting results aided in calibration of the exchange factor and are included in the plots. Sediment sources include the streambed (shown with solid bars) and uplands (shown with striped bars).

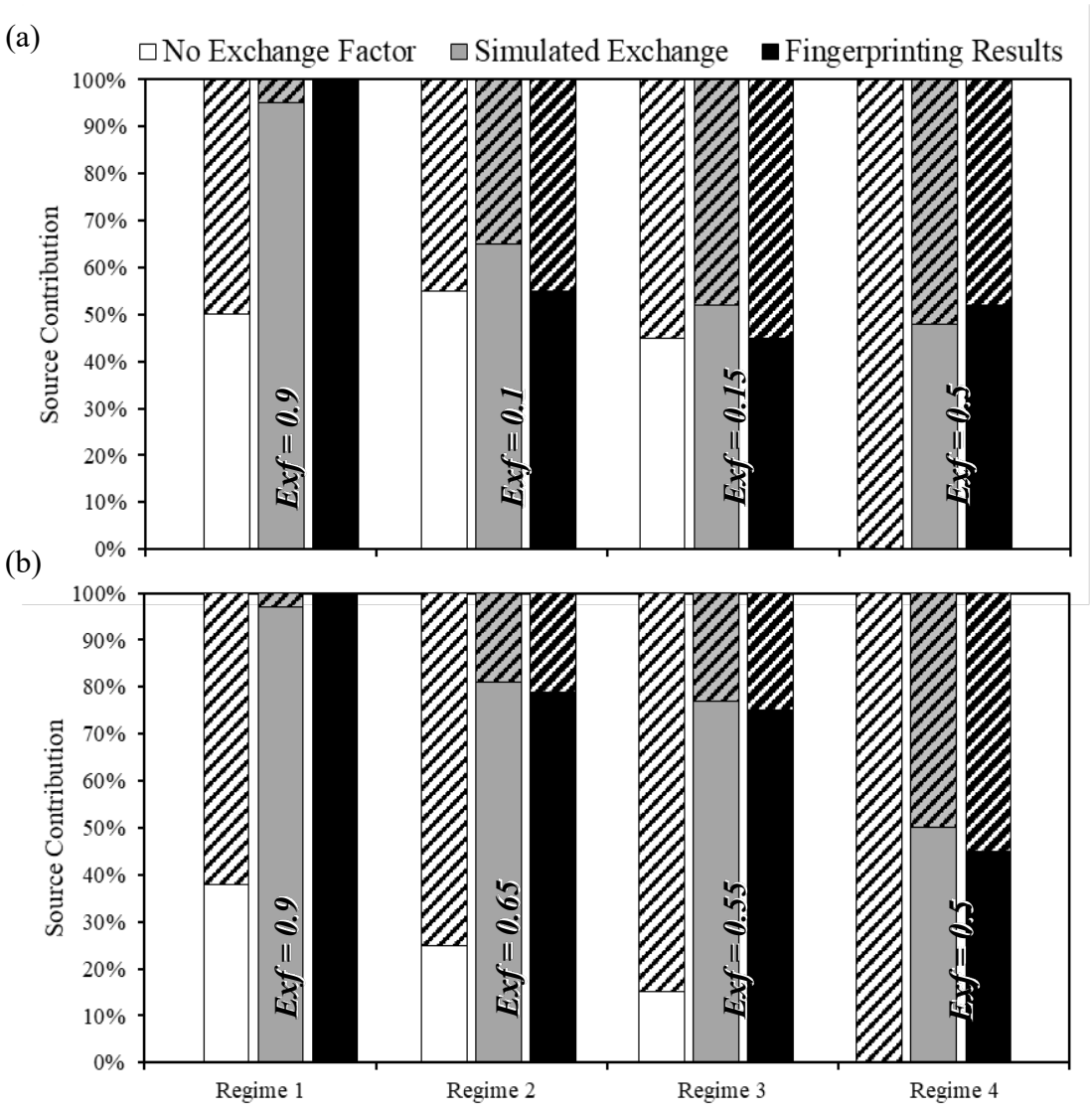

Figure 2.10. Upland erosion and sediment transport outputs from 2007 to 2010 for the (a) upper catchment and (b) lower catchment. Model results include upland erosion rate ($Q_{ss,\ upland}$), sediment flux (Q_{ss} *flux*), instream deposition, instream erosion, and instream equilibrium sediment exchange. For scaling purposes, Q_{ss} plots from 0.0 to 4.0 kg s^{-1} and deposition, erosion, and exchange plots from 0 to 80 tonnes. Peaks greater than the shown range are labeled.

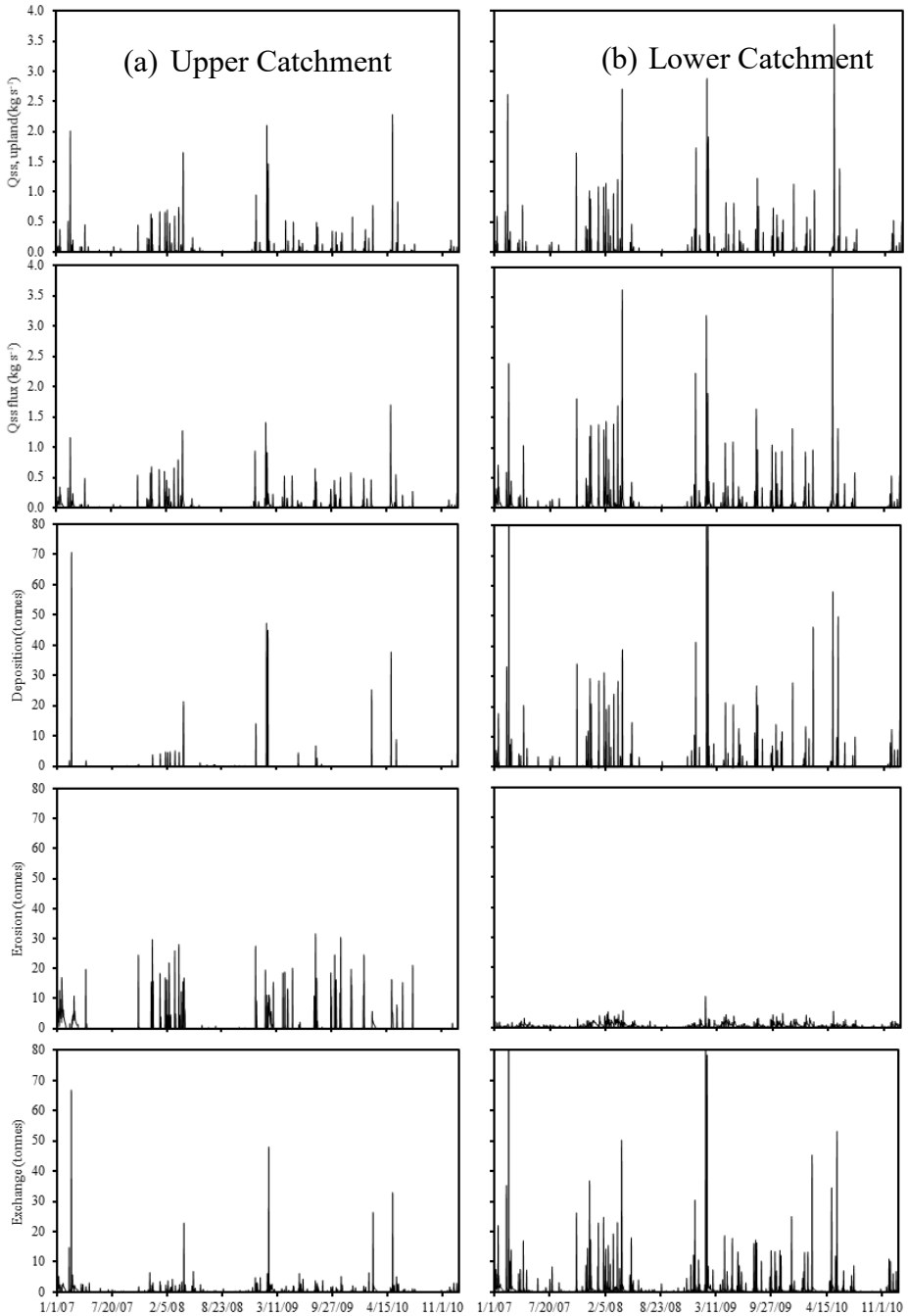

Figure 2.11. Sediment budget including the equilibrium sediment exchange for the (a) upper catchment and (b) lower catchment over the simulation period (2007-2010).

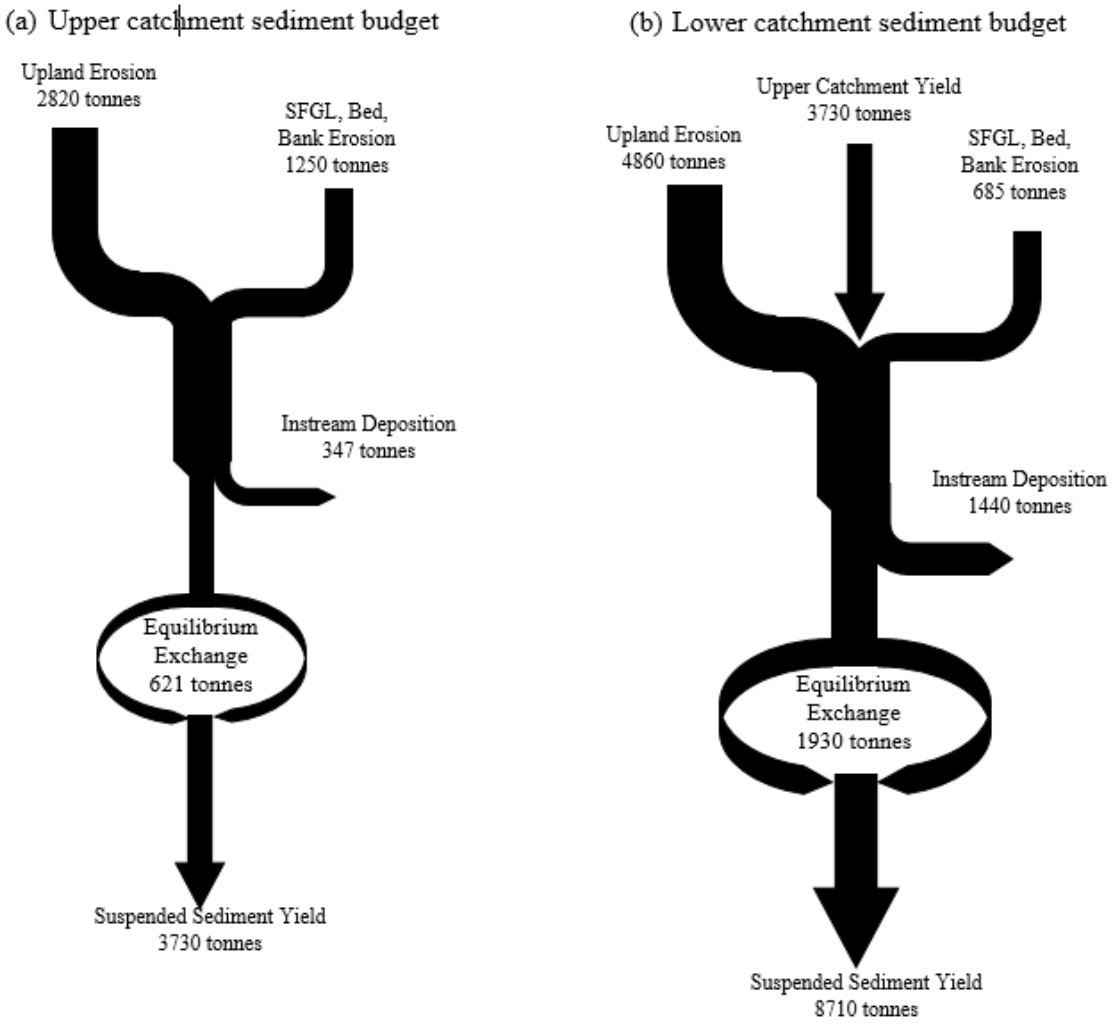

Chapter 3. Integrating Connectivity Theory within Watershed Modelling Part I: Model Formulation and Investigating the Timing of Sediment Connectivity

3.0 ABSTRACT

Integrating connectivity theory within watershed modelling is one solution to overcome spatial and temporal shortcomings of sediment transport prediction, and Part I and II of these companion papers advance this overall goal. In Part I of these companion papers, we present the theoretical development of probability of connectivity formula considering connectivity's magnitude, extent, timing and continuity that can be applied to watershed modeling. Model inputs include a high resolution digital elevation model, hydrologic watershed variability, and field connectivity assessments. We use the model to investigate the dependence of the probability of connected timing and spatial connectivity on sediment transport predictors. Results show the spatial patterns of connectivity depend on both structural and functional characteristics of the catchment, such as hillslope gradient, upstream contributing area, soil texture, and stream network configuration (structural) and soil moisture content and runoff generation (functional). Spatial connectivity changes from catchment-to-catchment as a function of soil type and drainage area; and it varies from event-to-event as a function of runoff depth and soil moisture conditions. The most sensitive connected pathways provide the stencil for the probability of connectivity, and pathways connected from smaller hydrologic events are consistently reconnected and built upon during larger hydrologic events. Surprisingly, we find the probability of connected timing only depends on structural characteristics of catchments, which are considered static over the timescales analyzed herein. The timing of connectivity does not statistically depend on functional characteristics, which relaxes the parameterization across events of different magnitudes. This result occurs because the pathway stencil accumulates sediment from adjacent soils as flow intensity increases, but this does not statistically shift the frequency distribution.

3.1 INTRODUCTION

3.1.1 Overview of part I and part II papers

Fluvial sediment erosion is an important driver of global sediment budgets and has far reaching implications in agriculture, infrastructure, and ecology (e.g., Wood and

Armitage, 1997; Morris and Fan, 1998; Toy et al., 2002). Watershed sediment models serve as an important tool to assess source, transport, and fate of sediment (e.g., Douglas-Mankin et al., 2010). However, a number of shortcomings of watershed sediment models require additional research at this time. Model shortcomings include the following: (1) they rely heavily on conceptualizing and lumping physical processes in their model structure; and (2) they often cannot represent many different active sediment sources and their specific pathways from the erosion sites to the watershed outlet (Wischmeier and Smith, 1978; Laflen et al., 1991; Ricci et al., 2018; Nunes et al., 2017).

Coupling connectivity theory with watershed modeling is one solution to overcome model shortcomings associated with spatial and temporal complexity of watershed properties, processes, and pathways (Mahoney et al., 2018). The proliferation of high-resolution geospatial data, defined as topographic surveys with meter and sub-meter resolution (i.e., greater than one point per m^2; Passalacqua et al., 2015), and water quality data, such as high temporal frequency turbidity measurements, in recent years makes coupling connectivity theory and watershed models feasible (Shoda et al., 2015; Pellerin et al., 2016). However, a unified sediment connectivity framework applicable across spatiotemporal scales remains underdeveloped, especially with respect to time-varying sediment processes (Bracken et al., 2013; Bracken et al., 2015; Wohl et al., 2017; Heckmann et al., 2018; Ali et al., 2018).

Our motivation of these two-part companion papers was to improve the spatial and temporal capabilities of watershed sediment modelling by coupling physically-based connectivity formula with watershed modelling. To do so, we formulate a probability equation that considers sediment connectivity's magnitude, spatial extent, timing, and continuity, which have been highlighted as the components needed for comprehensive connectivity (e.g., Grant et al., 2017; Wohl et al., 2019). We couple the probability of connectivity originally formulated by Mahoney et al. (2018) to represent the spatial patterns of connectivity, with formulations for connectivity's magnitude, timing, and continuity (developed herein) to simulate sediment flux. We investigate the formulation using 1.5 m resolution topographic data with emphasis on timing of connectivity, which is currently underdeveloped (Bracken et al., 2015; Wohl, 2017; Wohl et al., 2017; Ali et al., 2018; Heckmann et al., 2018). Next, we couple connectivity within a watershed model

and use 15-minute turbidity data to evaluate the model's performance. Additional emphasis in model evaluation is placed on using hysteresis analyses (e.g., Williams, 1989; Evans and Davies, 1998) to help calibrate the model because we find this has not been used to our knowledge, yet serves as a potentially fruitful approach when temporally explicit connectivity is considered. These two-part companion papers present: (1) formulation of equations to represent connectivity's magnitude, spatial extent, timing, and continuity and investigation of the dependence of spatial and temporal connectivity patterns on structural and functional watershed characteristics in Part I of these companion papers (this paper); and (2) coupling watershed and connectivity modelling for catchment- and watershed-scales with hysteresis evaluation to understand sensitive connected pathways in Part II of these companion papers (Mahoney et al., 2020).

3.1.2 Brief review of sediment connectivity

Connectivity is defined as the integrated transfer of material, energy, and organisms from source to sink (Pringle et al., 2003; Wohl 2017). In the context of sediment, we define connectivity similarly to Heckmann et al. (2018) as an emergent system property that reflects the strength and continuity of sediment linkages between and within system compartments at a given point in time. The sediment connectivity approach has garnered recent popularity perhaps due to its ability to explain the non-linearity of system response to hydrologic variability (Bracken et al., 2015; Leibowitz et al., 2008), explicitly detail non-point sources, sinks, and transport pathways (Parsons et al., 2015; Ali et al., 2018), and incorporate hydrologic uncertainty *via* coupling with probability theory (Mahoney et al., 2018). Theory and frameworks assessing sediment connectivity at the watershed scale have been well developed over the last two decades (e.g., Hooke, 2003; Fryirs et al., 2007; Ali et al., 2018) with more general attention to catchment linkages reaching back even further (Schumm, 1954; Leopold et al., 1964; Chorley and Kennedy, 1971, Ferguson, 1981; Harvey, 1996).

Many researchers in both engineering and geomorphology fields have significantly advanced methods to quantify connectivity (e.g., Fryirs et al., 2007; Borselli et al., 2008; Bracken et al., 2015; Gran and Czuba, 2017; Mahoney et al., 2018; Ali et al., 2018). Connectivity theory has been applied within models to assess the active contributing area (e.g., Fryirs et al., 2007; Heckmann et al., 2018; Mahoney et al., 2018) representing the

spatial extent (i.e., spatial patterns) of connectivity in watersheds. Within the geomorphologic context, connectivity often serves as a tool to estimate the sensitivity of watersheds to disturbances (Phillips, 2015) and elucidates controlling geomorphologic processes at both fine and course scales (Heckmann et al., 2018; Mahoney et al., 2018). For example, resilience of a system to upstream or downstream feedbacks reflects poor connectivity of the system (Bracken et al., 2015; Cavalli et al., 2019).

3.1.3 New connectivity advancements in Part I companion paper

One area of sediment connectivity that requires new development is formulation of quantitative equations that account for the major tenets now recognized define connectivity in predictive frameworks (Bracken et al., 2015; Ali et al., 2018; Heckmann et al., 2018). Researchers now agree that a holistic definition of connectivity should consider connectivity's magnitude, spatial extent, timing, and continuity (e.g., Bracken et al., 2015; Grant et al., 2017; Ali et al., 2018; Wohl et al., 2019). The magnitude of connectivity represents the strength of initial connections and describes the amount of sediment generation from a source which can be supply limited, shear limited, or transport limited (e.g., Grant et al., 2017). This concept indicates that the higher the magnitude and continuity of connections, the more connected the system is (e.g., Bracken et al., 2015; Grant et al., 2017; Ali et al., 2018; Heckmann et al., 2018; Wohl et al., 2019). Spatial connectivity describes the spatial pattern of fundamental sources and pathways that actively contribute sediment from the watershed uplands to its outlet (Ambroise, 2004; Fryirs et al., 2007; Bracken et al., 2015). The timing of connectivity describes the active period when sources and pathways detach and transport connected sediments (Ambroise, 2004; Ali et al., 2018; Wohl et al., 2019). Continuity is closely linked to connectivity's magnitude and describes the continuous gradient of geomorphic processes along sediment pathways that enhance or impede connections (Grant et al., 2017). In this paper we offer a quantitative approach to assess connectivity's magnitude, spatial extent, timing, and continuity. We do so using the formulation of the probability of connectivity from Mahoney et al. (2018) to represent the spatial extent of connectivity coupled with new probability formulations for connectivity's magnitude, timing, and continuity.

Another area of connectivity requiring development is theory and equations for timing of connectivity. Current connectivity approaches include: (1) index-based

connectivity assessments (see Heckmann et al., 2018 for review); (2) effective catchment area estimation (Fryirs et al., 2007); and (3) network-based connectivity simulations (Heckmann and Schwanghart, 2013; Gran and Czuba, 2017). While these models often adequately represent the structural connections of landscape elements (Fryirs et al., 2007; Borselli et al., 2008), they do not quantify high-temporal variability of connectivity that occurs during hydrologic events (Bracken et al., 2015; Heckmann et al., 2018; Ali et al., 2018). Models that do represent dynamic connectivity processes (referred to as functional connectivity; Wainwright et al., 2011) often neglect upland connected pathways or poorly represent connectivity at temporal scales in which they occur (Parsons et al., 2015; Gran and Czuba, 2017; Nunes et al., 2017; Wohl et al., 2019). We argue connectivity frameworks should consider the locations where connectivity occurs and timing of connectivity because hot-moments of erosion can contribute disproportionately to the sediment load (Ambroise, 2004; Bracken et al., 2015). Therefore, in this paper we develop the *probability of connected timing* equation to estimate when connectivity occurs.

Our objectives of Part I of these companion papers were: (1) theoretical development of a probability of connectivity formula considering connectivity's magnitude, spatial extent, timing and continuity; and (2) investigation of the dependence of the probability of connected timing and spatial connectivity on structural and functional watershed characteristics.

3.2 THEORETICAL DEVELOPMENT

We use a probability approach to predict the tenets of sediment connectivity. A probability approach reflects the stochastic nature of sediment transport and the heterogeneity of water and sediment variables across a watershed scale (Gessler, 1971; Hargrave and Burns, 1979; Wright and Webster, 1991; Borselli et al., 2008; Papanicolaou et al., 2008; Mahoney et al., 2018). Tenets for connectivity's magnitude, spatial extent, timing, and continuity are included by formulating a generation function for magnitude, and probabilities for the spatial extent (i.e., spatial patterns) of connectivity, active time when connectivity occurs, and continuity of connections. We formulate sediment flux, $\dot{m}$, as:

$$\dot{m} = G[P(C) \cap P(\tau) \cap P(\gamma)] \,, \tag{1}$$

where, G is sediment generation rate in a landscape unit, $P(C)$ is the probability of spatial sediment connectivity representing the spatial extent (i.e., spatial patterns), originally formulated by Mahoney et al. (2018), $P(\tau)$ is the probability of connected sediment timing representing active time for eroded sediment to reach a specified stream location, and $P(\gamma)$ is the probability of sediment (dis)continuity representing continuity of connectivity along the transport pathway.

We elaborate the theoretical background for the probabilities specified in Eq. 1. First, $P(C)$ considers structural characteristics of a watershed because each landscape unit (e.g., geospatial cell) may vary in its properties (e.g., slope, critical shear stress of sediment). $P(C)$ also can reflect functional variability because it reflects hydrologic parameters during an event (e.g., soil moisture, rainfall depth) (Borselli et al., 2008; Mahoney et al., 2018; Heckmann et al., 2019). $P(C)$ was originally formulated by Mahoney et al. (2018). Second, we introduce $P(\tau)$ to account for sediment travel time to show the temporal variability of sediment flux during an event (Hoffmann, 2015; Ali et al., 2018). Third, $P(C)$ and $P(\tau)$ estimate where and when sediment is connected, and $P(\gamma)$ is used to represent the fraction of total eroded sediment that is lost along the stream network due to discontinuity (Grant et al., 2017; Wohl et al., 2017). Fourth, Eq. 1 uses intersecting probabilities to estimate sediment connectivity because detachment and transport must occur sequentially and coincidentally with continuity for sediments to be connected to the watershed outlet (Bracken et al., 2015; Grant et al., 2017; Wohl et al., 2019). Fifth, the intersecting probabilities estimate the sufficient conditions for sediment transport but must be multiplied by an erosion generation function, G, to estimate flux (Borselli et al., 2008; Heckmann et al., 2018; Mahoney et al., 2018).

Next, we formulate each probability in Eq. 1. We formulate $P(C)$ considering the probability definition of Borselli et al. (2008) and formulation of Mahoney et al. (2018). $P(C)$ reflects spatial connectivity with co-occurring sediment transport processes of supply, generation, transport, and buffering as:

$$P(C) = P(S) \cap P(G) \cap P(T) \cap \{1 - P(B)\}, \quad (2)$$

where $P(S)$ is the probability that transportable supply of a sediment exists, $P(G)$ is the probability that a sediment can be detached and entrained in flow, $P(T)$ is the probability that transport of sediment can occur from the generating landscape to the stream network,

and $P(B)$ is the probability that a buffer (i.e., an impediment of lateral sediment transport into the stream network; Fryirs, 2013) exists coincidentally (Mahoney et al., 2018). Intersecting probabilities represent connectivity because each process must coincide for sediment transport to occur (Leopold et al., 1964). $P(C)$ can be discretized for each space-time unit when each probability is known or estimated, for example by using detachment and transport equations that incorporate both structural and functional components (Mahoney et al., 2018). Inputs to Eq. 2 representing structural watershed properties (e.g., the spatial configuration of the components of the system; Heckmann et al., 2018) can be realized using either topographic models, field surveying measurements, or landscape evolution modelling (Coulthard, 2001). Inputs representing functional watershed properties (e.g., representing the system's process dynamics; Wainwright et al., 2011; Heckmann et al., 2018) such as soil moisture content and runoff depth can be realized using hydrologic modelling, remote sensing of satellite data, or sensor data (Mahoney et al., 2018).

We formulate $P(\tau)$ as:

$$P(\tau) = \int_{T_1}^{T_2} f(t)\, dt \tag{3}$$

where t is time and $f(t)$ represents the frequency distribution for the amount of time until sediment generated in a connected landscape unit reaches the catchment outlet. $f(t)$ may be specified as parametric or non-parametric and we leave this development and discussion open for the time being. $P(\tau)$ represents the percent of connected landscape units with high probability to contribute a material between times T_1 and T_2, where T_1 and T_2 fall within the temporal domain of the event's extent and $T_2 > T_1$. Also, $T_m \geq T_2 > T_1 \geq T_0$, where T_0 represents the moment when sediment is initially mobilized and T_m represents the longest travel time between a landscape unit generating a sediment and the catchment outlet. When integrated over an entire event, T_1 becomes T_0, T_2 becomes T_m, and $P(\tau)$ is unity because the travel of all connected landscape units has been accounted for. Simulation of $P(\tau)$ is tested further in the methods and considers sediment travel velocity simulation, structural representation of the physical pathways of sediment, and the active contributing area of connected cells.

We represent the continuum of connectivity (e.g., see discussions by Grant et al., 2017; Wohl et al., 2019) using $P(\gamma)$. Continuity is unity when all sediment generated from

a landscape unit reaches the watershed outlet. Continuity is zero when all sediment generated from a landscape unit is removed from transport prior to the outlet. Continuity is non-trivial and is a function of the type of sediment and landscape studied, spatial extent of transport and length along the flow pathway, and hydrologic forcing. For example, continuity has been estimated considering a variety of factors and processes such as catchment area or distance to the catchment outlet (e.g., Borselli et al., 2008; Cavalli et al., 2013; Bracken et al., 2015), upwelling and downwelling motions in streams (e.g., Cellino and Lemmin, 2004), equilibrium exchange along the flow pathway (Mahoney et al., 2019), and energy deficit of the flow (Foster et al., 1995). Considering the potential variability of predicting $P(\gamma)$, we keep our functional relationship general as:

$$P(\gamma) = fn\left\{\left(L, S_f, k_s\right), (\mu, \rho, H, V), (g), (\rho_s, d, SF, w_s), (T_C, G, C_s)\right\}. \quad (4)$$

Each variable in Eq. 4 is not necessarily independent of the others but rather are inclusive of variables used for approximating continuity in different landscape or stream conditions. The first set of variables are mainly landscape-flow variables, where L, S_f and k_s are the length, friction slope, roughness height of the pathway. The second set are fluid variables, where μ, ρ, H and V are fluid viscosity, density, depth and velocity along the pathway. g is gravity. The fourth set are sediment variables, where ρ_s, d, SF and w_s are sediment density, size, shape and fall velocity. The fifth set are secondary variables commonly used in energy models, where T_C, G and C_s are the transport capacity, sediment load and concentration profile. The general functional relationship in Eq. 4 can be made more specific depending on the scale and dominant processes of the basin. For example, if (dis)continuity and sediment deposition are primarily controlled by landscape morphology, a specific relationship using the first set of variables might be developed. We specify our continuity relationship for in-stream transport for the study site in the methods section of Part II of these companion papers (Mahoney et al., 2020).

We discretize Eq. 1 and accompanying formula for a catchment that has spatially varying water and sediment variables, and then perform integration to estimate sediment yield for the entire system. We discretize Eq. 1 considering each spatial and temporal unit (Nunes et al., 2017) and estimate flux for each space-time unit as:

$$\dot{m}_{ij} = G_{ij}\left[P(C)_{ij} \cap P(\tau)_{ij} \cap P(\gamma)_{ij}\right], \quad (5)$$

where j is the spatial unit and i is the time step. The spatial unit specified for individual cells of a high-resolution digital elevation model (i.e. approximately 1 m resolution or less) has been found to capture morphologic features important for estimating spatial extent (i.e., patterns) of connectivity (e.g., Cantreul et al., 2018; Lopez-Vicente and Alvarez, 2018; Mahoney et al., 2018), and is the spatial unit considered in these studies. We estimate sediment yield for the duration of a hydrologic event of variable magnitude by integrating Eq. 5 over the catchment surface and duration of the storm as:

$$Y = \int \int \dot{m}_{ij}\, ds\, dt = \int \int G_{ij}\left[P(C)_{ij} \cap P(\tau)_{ij} \cap P(\gamma)_{ij}\right] ds\, dt\,, \qquad (6)$$

where Y represents the total mass of sediment yielded over the event from the catchment; s is the surface dimensions; and t is time.

3.3 STUDY SITE

We applied the connectivity model to the Upper South Elkhorn watershed (61.7 km^2) in Kentucky, USA (Fig. 1). Land use in the watershed consists of predominantly urban areas (46%) that make up the southwest portion of Lexington, KY and agricultural pastures (35%), which support the thoroughbred equine industry for which the area is known (see Fig. 2; ESR, 2013). The remainder of the watershed consists of sparse forests and cultivated crops (< 20%). Soils within the uplands of the watershed are generally silt-loams and well-drained. In the north-western portion of the watershed, soils consist of greater clay content than the remainder of the uplands and are drained less efficiently (Mahoney, 2017; Mahoney et al., 2018). Morphology of the land is "gently rolling", which is indicative of the generally low-gradient topography and dispersed, mildly-sloping surfaces that dissect the uplands (McGrain, 1983). Elevation of the watershed ranges from 837-1065 m above sea level (see Fig. 2a). Slopes throughout the watershed uplands range from 0.0 to 3.4 m m^{-1}. Hillslopes in upper reaches of the watershed are rolling with locally steep sites and are generally considered well-dissected. Lower in the watershed near the stream, flat floodplains are generally well-developed on either side of the main channel. Features that promote sediment connectivity include roadside ditches and ephemeral gullies with increased concentrated flow and available energy to detach and transport sediment (Mahoney, 2017; Mahoney et al., 2018). The watershed uplands are characterized by undulating microtopography that promotes localized flat gradients disconnecting upland

sediment (Phillips et al., 2017; Mahoney et al., 2018). The region's climate is considered to be humid subtropical with average temperatures ranging between 0.5°C and 24.5°C and average yearly precipitation equal to 1184 mm (Ulack et al., 1977). The stream network is generally low-gradient, with long, flat floodplains present on either side that impede lateral sediment transport (Mahoney et al., 2018). Lithology of the watershed consists primarily of Middle Ordovician limestone known as Lexington Limestone (see Fig. 2d; KGS, 2013). Brannon and Tanglewood members are subdivisions of Lexington Limestone and are located within the watershed. Shale is interbedded sparsely throughout the Brannon member. High karst potential is related to the percentage of limestone making up the lithology in the Upper South Elkhorn. Bedrock outcrops control instream geomorphology by functioning as downstream hydraulic controls that generate long pools with flat gradients that reduce fluid transport capacity and inhibit longitudinal sediment transport (Mahoney et al., 2019).

3.4 MATERIALS AND METHODS

The methods are described for investigating the dependence of the probability of spatial connectivity, $P(C)$, and probability of connected timing, $P(\tau)$, on structural and functional watershed characteristics. The general approach was as follows. First, $P(C)$ and $P(\tau)$ were calculated for the 181 catchments for events during a multi-year simulation period from 2006-2019. Data sources used during the simulation are recorded in Table 1 and Table 2. After testing the sensitivity of the methods, a subset of catchments and storm events with contrasting morphology and net sediment connectivity, respectively, were selected for further analyses to understand structural and functional controls on $P(C)$ and $P(\tau)$ at variable scales and locations throughout the watershed and during events of variable magnitude and duration. We analyzed five catchments of variable contributing area, slope, land use, and soil texture (see Table 3) to understand the control of structural connectivity on $P(C)$ and $P(\tau)$. Catchment contributing areas ranged from relatively small to large (0.05 km^2 to 2.10 km^2). Slopes ranged from flat to steep (0.06 m m^{-1} to 0.13 m m^{-1}). Land use ranged from primarily forest and agricultural pastures (100%) to primarily developed (74.3%). Clay, silt, and soil content varied from catchment to catchment (see Table 3). Events analyzed had variable magnitude and duration and hence captured variable

functional controls of connectivity throughout catchments. Specifically, we analyzed events occurring on days 2, 72, and 97 of the initial study year (2006), which corresponded to low (12 mm rainfall over 2 hours), high (22 mm rainfall over 7 hours), and medium (15 mm rainfall over 3 hours) hydrologic events, respectively (see Table 4). Mahoney et al. (2018) found that these events were representative of the mean connectivity conditions in the watershed (day 2) throughout the initial study year (2006), maximum connectivity (day 72), and an intermediate connectivity condition where important contributions to annual sediment yield are made (day 97; see Mahoney et al., 2018). Visual analyses were carried out to compare $P(C)$ and $P(\tau)$ variability due to structural connectivity (e.g., catchment physical characteristics, Table 3) and functional connectivity (e.g., hydrologic variability, Table 4); and statistical analyses were then performed to fit distributions and test dependence of $P(C)$ and $P(\tau)$ on catchment morphology (structural) and event magnitude (functional). Parameterization of $P(C)$ and $P(\tau)$ are given in the next sub-sections with additional emphasis given to $P(\tau)$ sensitivity.

We used existing materials, including field measurements, geospatial data, modelling, and software, to carry out the probability of connectivity modelling. We used field reconnaissance results and field measurements of upland and instream connectivity processes, hydraulic properties of reaches, channel bathymetry, and locations of bedrock outcrops (Mahoney, 2017; Mahoney et al., 2018, 2019). We used high-resolution geospatial data (see Table 1) to parameterize hydrologic variables of the watershed and create a three-dimensional representation of watershed topography. We utilized geospatial data from National Land Cover Database (NLCD) to identify land cover and land use. We used hydrologic modelling *via* the Soil Water Assessment Tool (SWAT) results to estimate hydrologic variability (Mahoney et al., 2018, 2019). We used our previously developed model for the spatial extent (i.e., spatial patterns) of connectivity, $P(C)$, to simulate the active contributing areas (Mahoney et al., 2018). We used software, including ArcGIS 10.4.1, ArcSWAT 2012.10.21, and Matlab R2017a, to simulate the probability-based connectivity variables, streamflow, and sediment flux. All software was run on a desktop PC (Intel® Core™ i7-6700 CPU at 3.40 GHz; 64-bit operating system, x64-based processor).

3.4.1 Probability of sediment connectivity, $P(C)$

The equations for $P(C)$ simulation are found in Mahoney et al. (2018). In brief, Eq. 2 is expanded as:

$$P(C) = P(S) \cap P(D_H \cup D_{NH}) \cap P(T_H \cup T_{NH}) \cap \{1 - P(B)\}, \quad (7)$$

where D_H is hydrologic-mediated detachment, D_{NH} is non-hydrologic-mediated detachment, and the two terms replace $P(G)$. Likewise, T_H is hydrologic-mediated transport, T_{NH} is non-hydrologic-mediated transport, and the terms replace $P(T)$. Eq. 7 is expanded mathematically as:

$$P(C) = \{P(S)\} \cdot \{P(D_H) + P(D_{NH}) - P(D_H)P(D_{NH})\} \cdot \{P(T_H) + P(T_{NH}) - P(T_H)P(T_{NH})\} \cdot \{1 - P(B)\} \quad (8)$$

Fig. 3 shows the multiplicative structure for $P(C)$ and the inputs we used to parameterize each process-associated probability. Our inputs included a DEM, field results, soils data, land use and land cover data, and meteorological data (see Table 1). A Boolean approach was used to parameterize each 1.5 m geospatial cell across the watershed surface with a probability of zero or one to reflect disconnectivity or connectivity, respectively, for the spatial cell for the day of year simulated.

3.4.2 Probability of connected timing, $P(\tau)$

Fig. 4 shows the simulation method for $P(\tau)$. We first discretized the watershed and stream network into 181 catchments and reaches (see Fig. 1) based on the location of bedrock outcrops that dissect instream morphology (Mahoney, 2017; Mahoney et al., 2018). We estimated the overland velocity for each cell with sediment connectivity using the digital elevation model, length of the flowpath from connected cells to the catchment outlet, slope of the pathway, and an estimate of hydraulic roughness as function of land cover. The time for sediment originating in cell *j* to enter the stream network is estimated using the length of the flow path from cell *j* to the trunk stream and the velocity of fluid in cell *j,* (Grimaldi et al., 2010) as:

$$T_j = \frac{L_j}{V_{ij}} \quad (9)$$

where T_j is the travel time from connected cell *j* to the stream network during an event (hr), L_j is the flowpath length (m) from the connected cell to the stream network, and V_j is the average overland runoff velocity during an event (m s^{-1}). Applying Eq. 9 assumes sediment transport velocity for connected cells is equal to the velocity of runoff, which is reasonable

for the size of fluvial sediment in this basin (d=20μm, Fox et al., 2010). L_j was estimated for each connected cell using ArcMap version 10.4.4 spatial analyst extension by masking the DEM of the entire watershed with each of the 181 catchments and running the flow length tool.

A number of methods are available to approximate V_j in Eq. 9, and we tested the sensitivity of the methods including the Darcy-Weisbach formula, Manning equation, the SCS overland velocity method (Haan et al., 1994), and the overland velocity equation presented in Maidment et al. (1996). The Darcy-Weisbach formula was applied as:

$$V_j = \frac{8gS_j y_j^2}{K\Phi} \tag{10}$$

where g is the gravitational acceleration (m s^{-2}), S_j is the slope (m m^{-1}) in cell j, y_j is the overland flow depth (m) in cell j as determined using analysis from the hydrologic modelling results, K is the Darcy-Weisbach friction factor, and Φ is the kinematic viscosity (m^2 s^{-1}). Darcy-Weisbach is generally applicable to laminar, turbulent or transitional flow regimes (Katz et al., 1995). Manning's equation was applied as:

$$V_j = \frac{1}{n_j} y_j^{\frac{2}{3}} S_j^{\frac{1}{2}} \tag{11}$$

where n_j is Manning's roughness factor in cell j, and other variables are already defined. The Manning formula is appropriate for turbulent flow regimes, and was empirically formulated for relatively flat channels (e.g., Hessel et al., 2003). The SCS method was applied as:

$$V_j = a_j \sqrt{S_j} \tag{12}$$

where a_j is an empirical estimate of the land use and flow type (m s^{-1}) in cell j. According to Grimaldi et al. (2010), this equation is appropriate for overland flow and shallow flow, but overestimates velocity during instances when the slope is greater than 0.04 (m m^{-1}). Slope is thus adjusted to correct for the overestimation with the equation developed in Grimaldi et al. (2010) and references cited therein as:

$$S_j' = 0.05247 + 0.06363 \cdot S_j - 0.182 \cdot e^{-62.38 \cdot S_j} \tag{13}$$

where S_j' is the corrected slope utilized in Eq. 12 for slopes greater than 0.04 (m m^{-1}).

Table 2 shows values of the Darcy-Weisbach K, Manning's n, and SCS a coefficients used to represent land use in the Upper South Elkhorn watershed (Ponce, 1989; Haan et al.,

1994; McCuen, 1998 Grimaldi et al., 2010). The Maidment et al. (1996) equation was used as:

$$V_j = \frac{\bar{V}_J}{\overline{[S_J^b A_J^c]}} \cdot S_j^b A_j^c \quad (14)$$

where $\bar{V}_J$ is the mean velocity for the catchment representing the average kinematic energy of hillslopes and channels, A_j is the upstream drainage area of cell j, $\overline{[S_J^b A_J^c]}$ is the average of the slope in cell j times the upstream drainage area of cell j over the watershed surface, and b, c are calibration coefficients. Maidment et al. (1996) recommends the calibration coefficients to both equal 0.5. We adjusted overland flow velocity using practical considerations. Grimaldi et al. (2010) synthesized literature from Maidment et al. (1996), Chen (1998), and Noto and Loggia (2007) to derive a range of realistic overland flow velocities equal to 0.02 m s^{-1} to 2.0 m s^{-1}, and we have adopted a similar approach to define acceptable overland velocity ranges based on this literature. We present an in-depth review of these papers. Maidment et al. (1996) highlighted the importance of limiting the simulated velocity values of overland flow to an acceptable range to ensure modelled runoff travels at a minimal velocity from flat areas with small drainage areas and to ensure that simulated flow does not move at unrealistically high velocities. Maidment et al. (1996) implemented an upper velocity bound of 220 m min^{-1} (3.67 m s^{-1}) and lower bound of 1.65 m min^{-1} (0.0275 m s^{-1}). Slopes of the watershed analyzed in Maidment et al. (1996) generally range between 0-15° and the morphology is considered to be "rolling hills dissected by steep valleys," which is similar to the Upper South Elkhorn watershed analyzed herein. Noto and Loggia (2007) used minimum overland velocity equal to 0.05 m s^{-1} and maximum velocity of 0.5 m s^{-1} on hillslopes, and found minimum velocity of 0.6 m s^{-1} and maximum velocity of 2.0 m s^{-1} in channels, based on studies conducted by Chow et al. (1988) and Eagleson (1970). Studies mentioned herein set values less than the minimum allowed velocity and greater than the maximum allowed velocity to those respective velocities and were able to successfully recreate hydrographs in their respective studies, thus justifying our use of these criteria herein. In this study, cells with overland velocity estimates less than 0.02 m s^{-1} were set to 0.02 m s^{-1} and cells with overland velocity estimates greater than 2.0 m s^{-1} were set to 2.0 m s^{-1} based on the aforementioned findings of researchers who implemented similar criteria to create synthetic unit hydrographs using

similar distributed approaches (see Eagleson, 1970; Chow et al., 1988; Maidment et al., 1996; Chen, 1998; Noto and Loggia, 2007; Grimaldi et al., 2010).

Sensitivity analyses of V_j was performed for a subset of all data (i.e., the wettest day of the year) used in eventual connectivity simulation. We assume that runoff velocity is time- and discharge-invariant, which is one potential limitation of using this method given the known relationship between velocity and runoff depth (e.g., Jain, 2001). However, Pilgrim (1976) found that medium- and high-flows exhibited flow velocities that were nearly constant, which coincides with days with the most sediment and hydrologic connectivity and the most sediment transport in the Upper South Elkhorn watershed (Mahoney et al., 2018). We simulate overland runoff depth using SWAT simulations from Day 72 of the initial study period (2006) from Mahoney et al. (2018). Day 72 of the initial study period was predicted to have the highest probability of connectivity and 100% runoff contribution from the watershed uplands (Mahoney et al., 2018). The initial study year (2006) from Mahoney et al. (2018) is generally a good representation of hydrology in the Upper South Elkhorn watershed given that the year was not particularly wet or dry for the region. Specifically, the total precipitation during the study year was 1324.4 mm. The average rainfall during the study period (2006-2019) was 1324.2 mm ($\sigma = 228.4$ mm). Minimum rainfall was 1005.1 mm (2010) and maximum precipitation was 1723.9 mm (2018). Therefore we justify the use of this simulation for representing overland flow velocity (NOAA, 2019).

After completing the sensitivity analyses and selecting the most appropriate method, we calculated $P(\tau)$ following Eq. 3. T_j for connected cells in each catchment is produced by masking the distributed overland travel time raster with results from the $P(C)$ model (i.e., $P(C)_j = 1$). The space-time frequency distributions, $f(t)$ of Eq. 3, are then output for application in Eq. 5 and 6 such that separate $f(t)$ are created for each of the 181 catchments and for each hydrologic event where connectivity exists. $P(\tau)$ can then calculated for the entire basin and for any time increment, T_1 to T_2, during a hydrologic event.

We parameterized probability distribution functions for timing frequency distributions to investigate the quantitative dependence of $P(\tau)$ on structural and functional watershed properties. We investigated multiple families of probability distribution functions relative

to the timing frequency distributions to identify the distribution of best fit, including the normal distribution, beta distribution, Weibull distribution, and log-logistic distribution. We used the Kolmogorov-Smirnov test to assess if samples from the frequency distribution could be described with parameters from the probability distribution functions at a significance level of 0.05.

3.5 RESULTS AND DISCUSSION

3.5.1 Structural and functional dependence of the probability of connectivity, $P(C)$

Results from our analyses suggest $P(C)$ is dependent on both structural and functional watershed characteristics for the Upper South Elkhorn study site. Structural dependence is ascertained based on $P(C)$ differences from catchment to catchment; and functional dependence is concluded by comparison of hydrology events with different magnitudes. For example, Fig. 5 shows variability of the probability of connectivity for five different catchments in the basin and for three different hydrologic events. The catchments shown in Fig 5. are constant for each column of images, and the events shown in Fig. 5 are constant for each row of images. As shown, $P(C)$ can vary by as much as 30% from event-to-event for a fixed catchment. $P(C)$ can vary by as much as 40% from catchment-to-catchment for a fixed event. The differences from event to event in Fig. 5 correspond to 2, 7 and 12% connectivity for the entire Upper South Elkhorn watershed, and $P(C)$ for the entire watershed was discussed in Mahoney et al. (2018). These events were chosen herein for comparison in the figure because the mean $P(C)$ for the entire watershed was 2% during days when some connectivity occurred, 12% was the maximum $P(C)$ reached in past analyses, and a value of greater than or equal to 7% watershed connectivity corresponds to nearly 75% of the annual sediment yield being transported (Mahoney et al., 2018). The catchments in Fig. 5 reflect different catchment scales, and distribution of soil and land cover properties (see Table 3).

Comparison of $P(C)$ results between catchments during a single hydrologic event (i.e., across a row in Fig. 5) highlights the dependence on structural catchment properties. For example, on day 2 when the overall watershed probability of connectivity was equal to 2%, the probability of connectivity in individual catchments varied from 0.3% in catchment 87 (Fig. 5e) to 25.3% in catchment 2 (Fig. 5b). Regardless of event, catchments in the

northern portion of the watershed (e.g., catchment 1, 2, and 3; Fig. 5a-5c) generally showed higher $P(C)$ values than catchments in the southern portion of the watershed (e.g., catchment 87; Fig. 5e). Table 3 shows structural properties of the five catchments shown in Fig. 5 and offers potential explanation for the large degree of variability between catchment probability of connectivity values. One reason is the shift in soil type from southern to northern catchments in the Upper South Elkhorn watershed. Soils in southern catchments consist of greater percentages of sand than northern catchments and thus drain more quickly than soils in the northern portion of the watershed, which consist of greater percentages of clay and silt (see Table 3; NRCS, 2009). The texture differences results in greater runoff production in northern catchments during hydrologic events, thus increasing fluid energy available to detach and transport sediment. This is corroborated when visually observing distributed $P(C)$ results for Fig. 5a and Fig. 5e (catchment 1 and catchment 87 are in northern and southern regions, respectively). On day 2, 8.0% (0. 088 km^2) of catchment 1 is predicted to be connected while 0.3% (0.006 km^2) of catchment 87 is predicted to be connected.

Another structural watershed characteristic that $P(C)$ is found to be dependent on is drainage area. Fig. 5 and Table 3 indicate the probability of connectivity generally decreases with increasing drainage area. This is because slopes in small headwater catchments of the Upper South Elkhorn watershed tended to be greater than those in larger catchments. We find that floodplains in larger catchments of the Upper South Elkhorn watershed are typically better-developed than those of smaller catchments and that floodplains impede lateral sediment transport in these areas (Mahoney, 2017; Mahoney et al., 2018). Generally smaller catchments are more dissected and have steeper slopes than larger catchments (see Table 3), and thus are better connected.

Results for $P(C)$ across events for a single catchment (i.e., down a column in Fig. 5) highlight the dependence of $P(C)$ on functional watershed properties (i.e., antecedent conditions and hydrologic event magnitude). For example, the probability of connectivity in catchment 1 increases from 8.0% on day 2 to 38.4% on day 72, which far exceeds the 2% to 12% variation of the entire watershed for these days. The runoff depth estimated via SWAT for day 2 and 72 was 1.1 and 7.6 mm, respectively; and the daily curve number (i.e., a proxy for antecedent moisture content) for day 2 and 72 was 78 and 87, respectively.

Notably, comparison of event-to-event connectivity for a single catchment shows pathways connected from smaller hydrologic events are consistently reconnected during larger hydrologic events. In this way, pathways of the smaller hydrologic events provide the stencil for larger events, which is perhaps best observed in columns b and d of Fig. 5. The result shows the most sensitive connected pathways to hydrologic activity. In this study, these most sensitive connected pathways correspond to ditches surrounding road networks and ephemeral rills and gullies. These ditches and gullies are susceptible to erosion in the South Elkhorn because they have relatively large upstream contributing areas and commensurate increased runoff depth and available energy to detach and transport sediment during events (Russo and Fox, 2012; Mahoney et al., 2018).

The dependence of $P(C)$ on structural and functional watershed characteristics is corroborated by the observed connectivity literature, although few studies allow direct comparison of our catchment-to-catchment results and event-to-event results. For example, in general the dependence of $P(C)$ on structural and functional watershed properties aligns with numerous theoretical statements in recent years (Bracken et al., 2015; Hoffmann, 2015; Nunes et al., 2017; Ali et al., 2018; Wohl et al., 2019; Zingaro et al., 2019). Process-based results from sediment transport studies also corroborate our results. Dependence of $P(C)$ on soil type dominance of catchments in a watershed and functional dependence are not surprising considering soil type, runoff depth and soil moisture content are well known to impact erosion and sediment transport (Jain, 2001; Torri and Poesen, 2014).

The sediment delivery ratio (SDR) is often cited as a simplified proxy of sediment connectivity (see Brierley et al., 2006; Vigiak et al., 2012; Baartman et al., 2013; Hoffmann, 2015; Wohl et al., 2019) and several researchers have correlated morphologic complexity with SDR (and hence connectivity) (e.g., Maner, 1958; Piest et al., 1975; Walling, 1983; Lu et al., 2006). We find similar trends when comparing $P(C)$ results (see Fig. 5) to catchment morphology (see Table 3). Namely, as catchment slope decreases and as drainage area increases, $P(C)$ decreases (see Fig. 5, Table 3). This finding agrees well with those from Baartman et al. (2013), who found that as morphologic complexity increased, connectivity (as measured by SDR) decreased. We found that decreased relief

(and hence increased morphologic complexity in terms of the study of Baartman et al. (2013)) coincided with the catchments with lowest $P(C)$.

Our $P(C)$ result that is least discussed in connectivity literature is the behavior of highly-sensitive sediment pathways to control the probability of connectivity across hydrologic regimes. Our results indicate that the most sensitive connected pathways during small hydrologic events are reconnected across hydrologic events. These most sensitive connected pathways provide the stencil for $P(C)$. Few studies allow direct comparison of our event-to-event results to test the stencil idea for other systems. The reason is that presently, connectivity processes are most often simulated using indices, as identified in the recent review by Heckmann et al. (2018), which are nearly all static in nature thus limiting assessment of inter-event variability of connectivity. We highlight important differences in connectivity indices and connectivity models, as pointed out by Heckmann et al. (2018), where the former represents connectivity from a simplified/conceptual standpoint and the latter refers to spatiotemporal simulations of hydrologic and sediment processes leading to the emergence of connectivity. Perhaps results of our method would be best compared with results of effective catchment area estimation (e.g., Harvey, 2002; Ambroise, 2004; Fryirs et al., 2007; Fryirs, 2013; Nicoll and Brierly, 2017). To this end, Harvey (2002) and Fryirs et al. (2013) discuss the most frequent sediment connectivity occurs in the Howgill Fells region of northwest England due to on-slope gully erosion that occurs approximately 30-35 times per year; and this result shows some corroboration with the stencil idea of our results. The most sensitive connected pathways providing the stencil for $P(C)$ is also corroborated by the general connectivity idea that a connected landscape will be sensitive to event magnitude (e.g., Phillips, 2003; Heckmann et al., 2018).

3.5.2 Structural and functional dependence of the probability of connected timing, $P(\tau)$

We investigated the dependence of $P(\tau)$ on structural and functional characteristics of the watershed, and interestingly find dependence only on structural features. We discuss this result at length given that it is a new concept in the connectivity literature.

Prior to concluding $P(\tau)$ results, we completed the sensitivity analysis and found the overland velocity estimation using the SCS method (Eq. 12) best estimated overland runoff velocity within the permissible range identified by Grimaldi et al. (2010) and references cited therein (i.e., range: 0.02 m s^{-1} to 2.0 m s^{-1}) for the Upper South Elkhorn watershed. We estimated that 94% of cells throughout the watershed had velocity within this range using this method. We found that the Darcy-Weisbach method tended to underestimate overland flow velocity given that velocity in nearly 50% of cells throughout the watershed were estimated to have velocity less than 0.02 m s^{-1}. The Manning equation tended to predict the overland velocity slightly better given that nearly 73% of cells within the watershed fell within the permissible range, however this method also underestimated the overland runoff velocity. The Maidment et al. (1996) method also tended to underestimate the overland flow velocity, where 30% of cells were estimated to have overland flow velocity less than 0.02 m s^{-1}. Given these results, we carried the remainder of connectivity calculations forward using the SCS overland velocity estimation method. Our sensitivity results agree with Grimaldi et al. (2010), who found that the SCS method best estimated overland flow velocity.

Analyses of results suggest the probability of connected timing, $P(\tau)$, depends only on structural characteristics of the watershed. Frequency distributions for sediment travel times for connected cells (see Fig. 6) show variability of the probability of timing for catchments and events described previously in Fig. 5. $P(\tau)$ varies from catchment to catchment, but generally tends to remain relatively unchanged between events, which implies that the probability of timing is highly dependent on structural watershed properties and weakly dependent on functional watershed properties. Visual comparison of frequency distributions from catchment to catchment during a single event highlights variability due to structural watershed properties. Specifically, the time associated with peak sediment contribution (e.g., maximum probability of timing) during the event on day 2 ranges in catchments shown in Fig. 6 between 0.08 hours in catchment 60 (Fig. 6d) to approximately 0.57 hours in catchment 87 (Fig. 6e). Table 3 offers some explanation as to the dependence of the probability of timing on structural watershed properties. For example, given the generally flatter slopes of catchment 87, it is likely that the velocity of transported sediment from the catchment is slower than sediment from, for example, catchment 60.

Additionally, given that drainage area of catchment 87 is fairly large, the lengths of connected flow paths are likely longer than other catchments shown in Fig. 6.

Surprisingly, we find that variability of $P(\tau)$ is relatively minimal in a single catchment between events. Specifically, we find that the peak probability of timing generally aligns between events of a single catchment in Fig. 6. For example, the maximum frequency of connected cells occurs at approximately 0.08 hours in catchment 60, regardless of the event. One explanation for this result is related to sediment pathways that are most sensitive to hydrologic activity. We find that sensitive connected pathways establish a stencil for the probability of timing given that they are reconnected during the majority of hydrologic events. This frequency distribution is slightly altered during larger storm events; however, given that sensitive pathways are reconnected during hydrologic events of increasing magnitude, the frequency stencil from these pathways forms the foundation of frequency distributions of increasing magnitude.

We parameterized probability distribution functions for the frequency distributions shown in Fig. 6 which statistically corroborated the timing dependence on structural and functional watershed properties. The $P(\tau)$ frequency distribution converges to days with higher percentage connectivity regardless of watershed size and configuration in the Upper South Elkhorn watershed, highlighting dependence of the probability of timing on functional watershed characteristics. We found that three-parameter log-logistic functions (scale, shape, and location parameters) generally fit frequency distributions for all catchments and events shown in Fig. 6. We found that scale, shape, and location parameters describing the probability distribution functions varied from catchment to catchment showing statistical support for the dependence of timing on structural watershed properties. However, in general the same scale, shape, and location parameters from the event with greatest connectivity (day 72) could be used to describe the log-logistic function for smaller events within a catchment. We used the Kolmogorov-Smirnov test to assess whether samples from the frequency distribution could be described with the parameters from the log-logistic functions from day 72 at a significance level of 0.05. The null hypothesis was not rejected for most of the catchments, statistically supporting the lack of dependence of the probability of timing on functional variability of the systems. The null hypothesis was only rejected for catchment 87, which was located in the southern portion of the watershed

where less connectivity existed. Table 5 shows values for scale, shape, and location parameters for the log-logistic functions parameterized for probability of timing frequency distributions and whether the null hypothesis was rejected based on the Kolmogorov-Smirnov test. In future research, the log-logistic probability distribution may be a good fit for the probability of timing given its previous use in hydrologic modeling and because it can be solved analytically (Shoukri et al., 1988; Ashkar and Mahdi, 2006).

The probability of connected timing depends predominantly on structural connectivity and little variance is explained by functional connectivity. To our knowledge, this idea has not been discussed in connectivity literature. We find that the travel time of sensitive connected pathways establishes the stencil for the probability of timing given these cells are reconnected during the majority of hydrologic events. Our statistical analysis highlighting common parameterization of log-logistic probability distribution functions between hydrologic events for individual catchments further corroborates this analysis. This result is likely a consequence of the fine temporal scale implemented herein to analyze connectivity, which highlights the sub-event temporal variability of connectivity in the Upper South Elkhorn watershed. The idea of effective timescales of connectivity has been discussed in the connectivity literature for at least the last 20 years (Harvey, 2002; Fryirs, 2013), however, we find that few studies analyze connectivity at the sub-event temporal scale that is presented in this work. We find that as timescales increase, the probability of timing tends towards unity, which is consistent with connectivity literature (Fryirs, 2013; Ali et al., 2018). We emphasize the importance of coupling the probability of connectivity and probability of timing simulations at high spatial and temporal resolutions given that we would not have been able to identify hotspots and hot-moments of sediment connectivity and transport otherwise. Research from Gran and Czuba (2017) generally corroborates this idea on a larger spatial and temporal scale, given that they found network structure must be taken into consideration in order to assess the temporal evolution of sediment pulses in river networks. Network structure was determined to be especially important given its control on instream transport capacity which influenced the bottlenecking of sediment pulses.

Results from the $P(\tau)$ simulations reflect recent sentiment from connectivity literature that indicates sediment flux is an implicit proxy of sediment connectivity (e.g.,

Czuba and Foufoula-Georgiou, 2014; Masselink et al., 2016; Ali et al., 2018; Wohl et al., 2019). Such studies indicate that peak sediment flux, as measured at the outlet of a catchment or watershed, implicitly represents the moment during an event when the greatest sediment connectivity occurs. For example, findings from the Lagrangian connectivity simulations completed by Czuba and Foufoula-Georgiou (2014) and Gran and Czuba (2017) highlight that peak connectivity and flux coincide. In their studies, hotspots of connectivity occur when clusters of parcels are in close proximity, which conceptually represents the peak sediment flux in a reach. In our study, we find that peak $P(\tau)$ is representative of the time when the majority of upland spatial units are connected to the catchment outlet (see Fig. 6). If assuming a unit parcel delivery, similar to the approach of Czuba and Foufoula-Georgiou (2014) and Gran and Czuba (2017), then peak $P(\tau)$ also coincides with peak connectivity and flux in the catchment. In this sense, explicit simulation of $P(\tau)$ and delivery integrates pathways to simulate sediment flux, and corroborates the sentiment of researchers that peak flux and connectivity coincide (e.g., Czuba and Foufoula-Georgiou, 2014; Masselink et al., 2016; Ali et al., 2018; Wohl et al., 2019).

3.5.3 Comparison of the probability of connectivity and index of connectivity

We validate spatial patterns from our probability of connectivity approach by comparing our results with spatial results calculated using the widely implemented Index of Connectivity, or *IC* (Borselli et al., 2008; Cavalli et al., 2013; see Supplementary Material). We calculated the *IC* for the Upper South Elkhorn watershed using the SedInConnect tool developed by Crema and Cavalli (2018). We justify using the *IC* to validate the spatial results of the model because of its wide applicability in the connectivity literature and its ability to represent structural connectivity (see Borselli et al., 2008; Cavalli et al., 2013; Messenzehl et al., 2014; Cavalli et al., 2016; Gay et al., 2015; Lopez-Vicente et al., 2016; Nicoll and Brierly, 2017; Kalantari et al., 2017; Heckmann et al., 2018; Mishra et al., 2019). We compared *IC* results with probability of connectivity results for the events and catchments studied in the Upper South Elkhorn.

We find *IC* results compare especially well with the connected pathways identified from our probability of connectivity approach for high magnitude hydrologic events (see Fig. 5). *IC* results are shown in Fig. 7 for the five catchments previously presented (see Fig. 5), and *IC* results include the full range of *IC* and a subset of the range corresponding to the percentage of cells connected during the hydrologic event with the greatest connectivity, i.e., event 72. For example, column (a) in Fig. 7 shows catchment 1 results for event 72 and includes: (1) $P(C)$ results with 38% connectivity for catchment 1; (2) *IC* results for the range corresponding to the top 38% of *IC* values for catchment 1 during event 72; and (3) the full range of *IC* results for catchment 1. As shown in the figure, spatial patterns of connectivity shown by the $P(C)$ model match well with the *IC* results. For example, in catchment 1 (see Fig. 7a), both $P(C)$ and *IC* identify higher proportions of connectivity in the western part of the catchment near the pour point, due to steep slopes on either side of the road network running laterally through the catchment; and disconnectivity in the eastern portions of the catchment where flat slopes coincide. As another example, $P(C)$ and *IC* results for catchment 3 (see Fig. 7c) both identify the strong presence of connectivity in the western portion of the catchment due to steep hillslopes locally on either side of the stream network; and large amounts of disconnectivity in the eastern portion of the catchment, which was identified during field reconnaissance as a floodplain that buffers sediment from entering the stream network. As a third example, $P(C)$ and *IC* results for catchment 87 (see Fig. 7e) both identify sparse connectivity throughout the watershed. We find that spatial patterns of connectivity identified in both sets of results correspond to roadside ditches and concentrated flow pathways.

Similarity of spatial patterns of connectivity identified during the most connected day by $P(C)$ and *IC* qualitatively validates $P(C)$ results presented herein. The reason suggested for the good comparison on the most connected day of the study year is that as $P(C)$ values increase, control of connectivity shifts from functional connectivity to structural connectivity (Mahoney, 2017; Mahoney et al., 2018; Mahoney et al., 2019; Wohl et al., 2019). *IC* is primarily a function of structural watershed properties (Borselli et al., 2008; Cavalli et al., 2013; Nicoll and Brierley, 2017), and therefore the methods match well when structural connectivity controls $P(C)$.

On the contrary, $P(C)$ results and *IC* results show substantial differences for catchments in the Upper South Elkhorn during events of lesser magnitude, such as associated with low- or moderate-hydrologic events. In general, our comparison showed spatial patterns of connectivity identified with $P(C)$ are distributed in the catchment and occur on steep slopes with high contributing areas (structural connectivity) where fluvial detachment (e.g., $P(D_H)$, functional connectivity) and transport (e.g., $P(T_{H\,up})$, functional connectivity) of sediment are most likely to occur due to high predicted runoff and soil moisture content. Conversely, *IC* values are highest in cells in close proximity to the catchment pour point with steep slopes and large upstream contributing area, which are structural watershed properties. For example, Fig. 8 for catchment 1 during event 2 shows high spatial connectivity predicted by $P(C)$ in the central part of the catchment where flow accumulates in swales promoting hydrologic detachment of sediment and on slopes with high soil moisture content where hydrologic transport is possible. These areas are coincident with areas of highest accumulated runoff and highest soil moisture content during the event, as predicted by hydrologic simulations capturing functional processes. Highest *IC* values occur near the catchment outlet where stream power (e.g., slope and upstream contributing area) is the highest. Variability in $P(C)$ results and *IC* results is attributed to several fundamental differences in the formula for $P(C)$ modelling and *IC*. $P(C)$ is dependent upon both structural connectivity and functional connectivity whereas *IC* is primarily a function of structural connectivity (Borselli et al., 2008; Nicoll and Brierley, 2017; Mahoney et al., 2018). In this regard, *IC* identifies pathways with the highest stream power within proximity to the watershed outlet, but does not consider event to event hydrologic variability. $P(C)$, on the other hand, can be limited by supply, transport, or shear stress, which comprise of both structural and functional variables.

Our comparison provides some validation of *P*(*C*) since *P*(*C*) and *IC* match well during high magnitude events, and also highlights the ability of *P*(*C*) to capture functional connectivity in the basin. Also, results suggest *P*(*C*) may be well suited for identification of sediment source areas and active transport pathways during smaller events when shear stress (functional) and transport capacity (functional) limit overall $P(C)$. In this manner, our probability of connectivity model provides one approach to work towards connectivity tools that capture hydrologic forcings and functional connectivity, which has been

highlighted as a research need recently by a number of scientists (Gay et al., 2015; Chartin et al., 2017; Hooke et al., 2017; Kalantari et al., 2017; Nicoll and Brierley 2017).

The comparison of $P(C)$ and *IC* also adds to an on-going discussion surrounding the evolution of the *IC* approach and its parameterization to capture functional processes. The utility of the *IC* to qualitatively assess catchment-wide connectivity is noteworthy, especially considering we were able to relatively quickly simulate connectivity with the SedInConnect tool (Crema and Cavalli, 2018) for the entire Upper South Elkhorn in a matter of hours to one day. On the other hand, the computational complexity of $P(C)$ (see discussion of computational complexity in Heckman et al., 2018) required many weeks for simulation time. However, simulation of the *IC* may need modification to better represent functional connectivity, in some cases. For example, Nicoll and Brierley (2017) found that static elements of connectivity represented with the effective catchment area simulation (sensu Fryirs et al., 2007) generally agreed with *IC* results, but that localized variability of connectivity due to hydrologic forcings, as identified by field reconnaissance and remote sensing, were uncaptured by the *IC* (Nicoll and Brierley 2017). Nicoll and Brierley (2017) posit that such shortcomings are generally related to the *IC*'s heavy reliance upon geomorphometrics to assess connectivity, which can misrepresent functional processes at localized scales. Nicoll and Brierley (2017) suggest that physical significance of *IC* values might be established by supplementing *IC* with magnitude-frequency analyses of sediment transport processes.

Other researchers have suggested to modify parameterization of the *IC* weighting factor (W), using functional watershed characteristics (e.g., Chartin et al., 2017; Hooke et al., 2017; Kalantari et al., 2017) or the explicit representation of functional connectivity (e.g., Gay et al., 2015), where W is representative of sediment flux impedance (Crema and Cavalli 2017, see Supplementary Material). In this study, we use the probabilities of detachment and transport to simulate functional connectivity, which are functionally dependent on temporally variable runoff and soil moisture content. Perhaps aspects of our approach may assist with defining the weighting factor. Related, sentiment from recent literature suggests *IC* can be used to simulate functional connectivity at the catchment scale when linked with a threshold (see Lopez-Vicente et al., 2015; Neurig et al., 2016; Heckmann et al., 2018). We applied a threshold to the *IC* to compare connectivity across

events, but *IC* and *P*(*C*) were poorly correlated during the lesser magnitude events. While ground-truthing was limited, the *P*(*C*) results were more physically plausible based on our field reconnaissance. Perhaps further parameterization of *W* by our method or the method of others could further modify *IC* results for moderate hydrologic events. It seems that approaches to parameterize *IC* to reflect both structural and functional connectivity remains an open topic. Magnitude-frequency analyses, parameterizing the *IC* weighting factor, and incorporating formula for the probability of connectivity are all future research avenues that might help complete this goal.

3.6 CONCLUSION

The conclusion of Part I of these two-part companion papers is as follows:

1. Theoretical development showed combining connectivity's magnitude, spatial extent (i.e., spatial patterns), timing and continuity provide a holistic representation of sediment connectivity. Simulation for catchments shows spatial and temporal explicit results for sediment connectivity when using the new formulation.
2. Results show the spatial extent (i.e., spatial patterns) of connectivity depends on both structural and functional characteristics of the catchments. Specifically, spatial connectivity changes from catchment-to-catchment as a function of soil type and drainage area; and spatial connectivity varies from event-to-event as a function of runoff depth and soil moisture conditions. Notably, the most sensitive connected pathways provide the stencil for the probability of connectivity. Comparison of connectivity across events show pathways connected from smaller hydrologic events are consistently reconnected and built upon during larger hydrologic events.
3. Surprisingly, we find that the timing of connectivity during an event, as simulated with the probability of timing, only depends on structural characteristics of the watershed, such as the size and watershed morphology. The timing of connectivity does not statistically depend on functional characteristics, which relaxes the parameterization across events of different magnitudes. This result occurs because the sensitive connected pathways identified by probability of connectivity simulations form a stencil representing the timing frequency distribution. The

pathway stencil accumulates sediment from adjacent soils as flow intensity increases, but this does not statistically shift the frequency distribution.

3.7 ACKNOWLEDGMENTS:

We gratefully acknowledge the financial support of this research under National Science Foundation Award 163288. We thank the associate editor Paulo Alexandre da Silva Pereira and two anonymous reviewers for comments and criticisms that have greatly improved the quality of this manuscript.

3.8 SUPPLEMENTARY MATERIAL: EQUATIONS AND SOFTWARE FOR THE INDEX OF CONNECTIVITY (*IC*)

The *IC* is a representation of the effect of topography and land cover on sediment connectivity (Borselli et al., 2008; Heckmann et al., 2018) and accounts for both upstream and downstream sediment connectivity. The *IC* is formulated as:

$$IC = log_{10}\left(\frac{D_{up}}{D_{dn}}\right) \quad \text{(A.1)}$$

$$D_{up} = \overline{W}\,\bar{S}\,\sqrt{A} \quad \text{(A.2)}$$

$$D_{dn} = \sum_i \frac{d_i}{W_i S_i} \quad \text{(A.3)}$$

where IC is the Index of Connectivity with range from $[-\infty, \infty]$, D_{up} and D_{dn} are the upslope and downslope components of connectivity, $\overline{W}$ is the average weighting factor of the upslope contributing area, $\bar{S}$ is the average slope gradient of the upslope contributing area (m m^{-1}), and A is the upslope contributing area (m^2), d is the length of the flowpath along the i^{th} cell in the steepest downstream direction (m), W_i and S_i are the weighting factor and the slope gradient of the i^{th} cell. More negative *IC* values are conceptualized as being "less connected" than more positive *IC* values (Borselli et al., 2008). Inputs to the SedInConnect tool include a high-resolution (1.5 m by 1.5 m) DEM. We parameterize the

weighting factor using methods described in Cavalli et al., (2013). The target of the *IC* simulation was the South Elkhorn stream network. Thus, the *IC* represents the potential connectivity from the uplands to the stream network.

Table 3.1. Geospatial data used to simulate connectivity and sediment flux

Data Type	Resolution	Source
Digital Elevation Model	1.5 m x 1.5 m	KYAPED (2014)
Land Use/Land Cover	10 m x 10 m	2006 National Land Cover Database
Sink Hole Drainage Area	1.5 m x 1.5 m	KGS (2017)
Hydrologic Simulation	1.5 m x 1.5 m	Mahoney et al. (2018)
Soil Type	1:250,000; 1:12,000	STATSGO; SSURGO NRCS (2006)

Table 3.2. Darcy-Weisbach *K*, Manning *n*, and SCS *a* coefficients used to parameterize overland velocity estimates (Ponce, 1989; Haan et al., 1994; McCuen, 1998, Grimaldi et al., 2010).

Land Use Land Cover	Darcy-Weisbach *K*	Manning *n*	SCS *a*
Agro-forestry areas	15000	0.3	2.59
Airports	1000	0.05	2.96
Barren Lands	10000	0.13	2.59
Coniferous Forest	20000	0.6	.073
Construction Sites	1000	0.05	2.96
Cultivated Crops	15000	0.25	2.59
Industrial or commercial Area	1000	0.03	2.96
Mixed Forest	20000	0.6	0.73
Pastures	15000	0.25	2.59
Rock Outcrop	2000	0.1	2.96
Urban-Residential Area	1000	0.05	2.96
Woodland Shrub/Scrub	15000	0.25	2.59

Table 3.3. Structural properties of five catchments in the Upper South Elkhorn Watershed.

Catch-ment	Area (km^2)	Avg. Slope (m/m)	Land Use/Land Cover (NLCD)			Average Soil Content (NRCS, 2006)		
			Developed	Agriculture	Forest	Sand	Silt	Clay
1	1.10	0.09	49.0%	32.8%	18.2%	6.6%	68.3%	25.2%
2	0.05	0.13	1.6%	17.7%	80.6%	6.4%	66.8%	26.8%
3	0.21	0.08	51.2%	40.9%	7.9%	6.0%	66.9%	27.2%
60	0.06	0.11	0.0%	59.7%	40.3%	7.1%	65.9%	27.0%
87	2.10	0.06	74.3%	14.9%	10.8%	9.6%	66.5%	23.9%

Table 3.4. Hydrologic properties of analyzed events.

Event	Date	P(C)	P (mm)	Duration (hr)	I (mm hr^{-1})
2	1/2/2006	2%	12	2	6.0
72	3/13/2006	12%	22	7	3.1
97	4/7/2006	7%	15	3	5.1

Table 3.5. Log-logistic parameter values for probability of timing frequency distributions for catchments located throughout the Upper South Elkhorn watershed for three events. Results of the Kolmogorov-Smirnov test for the parameterization are shown with confidence of 0.05. $\boldsymbol{\alpha}$ is the log-logistic scale parameter, $\boldsymbol{\beta}$ is the shape parameter, and $\boldsymbol{\gamma}$ is the location parameter.

Catchment	Day	α	β	γ	Reject H_0? (α = 0.05)
1	2	2.03	0.30	-0.03	*No*
	72	2.03	0.30	-0.03	*No*
	87	2.03	0.30	-0.03	*No*
2	2	2.29	0.12	-0.02	*No*
	72	2.29	0.12	-0.02	*No*
	87	2.29	0.12	-0.02	*No*
4	2	14.80	0.52	-0.41	*No*
	72	14.80	0.52	-0.41	*No*
	87	14.80	0.52	-0.41	*No*
60	2	1.85	0.06	0.00	*No*
	72	1.85	0.06	0.00	*No*
	87	1.85	0.06	0.00	*No*
87	2	1.80	0.40	0.01	*Yes*
	72	1.80	0.40	0.01	*No*
	87	1.80	0.40	0.01	*Yes*

Figure 3.1. Upper South Elkhorn watershed (61.7 km^2). The watershed's location within the Kentucky River basin in Kentucky, USA is shown. Delineation of catchments within the Upper South Elkhorn was completed based on field reconnaissance of instream (dis)connectivity. USGS Gage 03289000 and the University of Kentucky South Elkhorn sensor station are located at the watershed outlet.

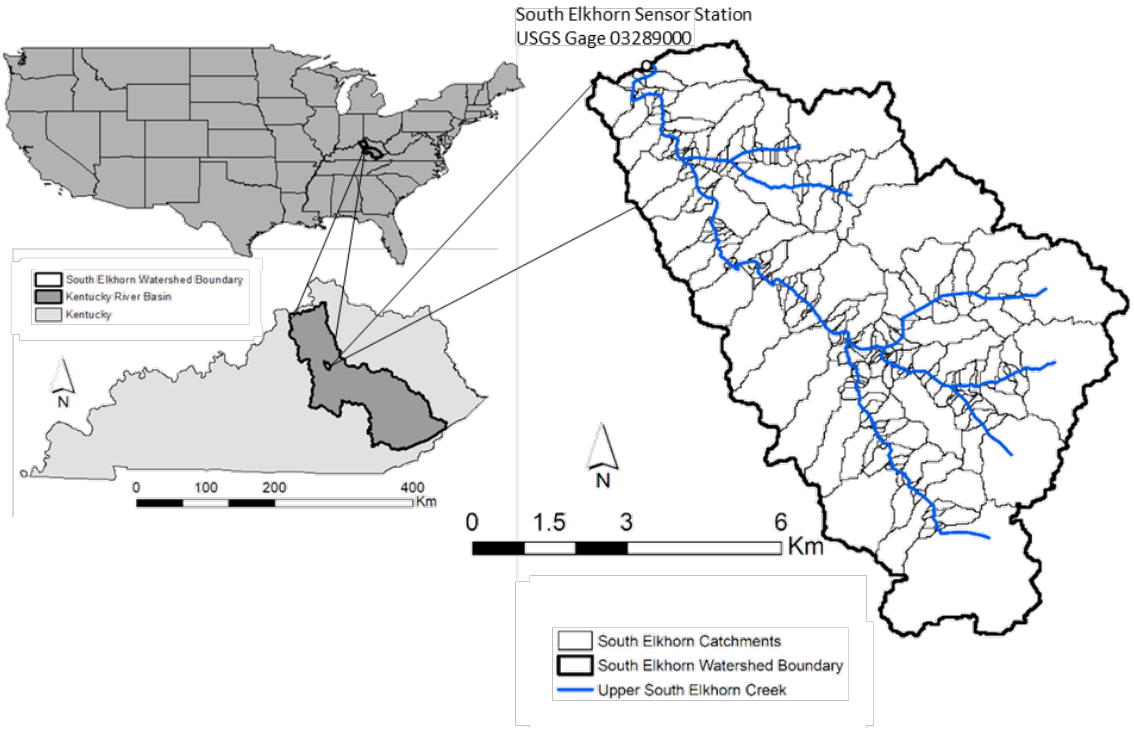

Figure 3.2. (a) Digital elevation model of Upper South Elkhorn watershed; (b) watershed slope (m m^{-1}); (c) land use (55% agricultural and forest; 45% urban land); (d) watershed lithology (primarily fossiliferous limestone with interbedded shale); (e) watershed soil (primarily silt-loams; see symbol key in USDA-NRCS Soil Survey, 2006).

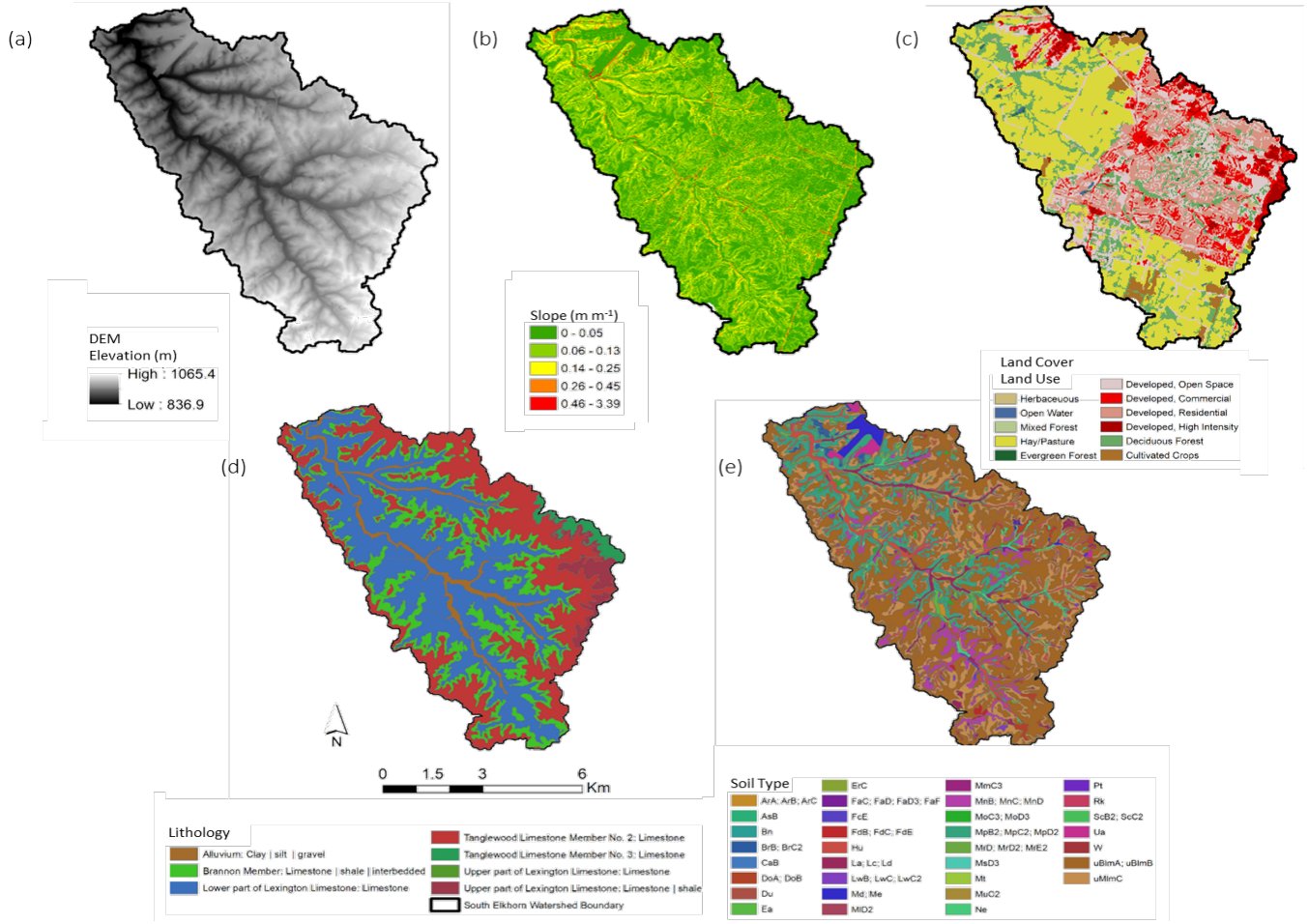

Figure 3.3. Probability-based model of sediment connectivity adapted from Mahoney et al. (2018). $P(C)$ represents the spatial patterns of connectivity.

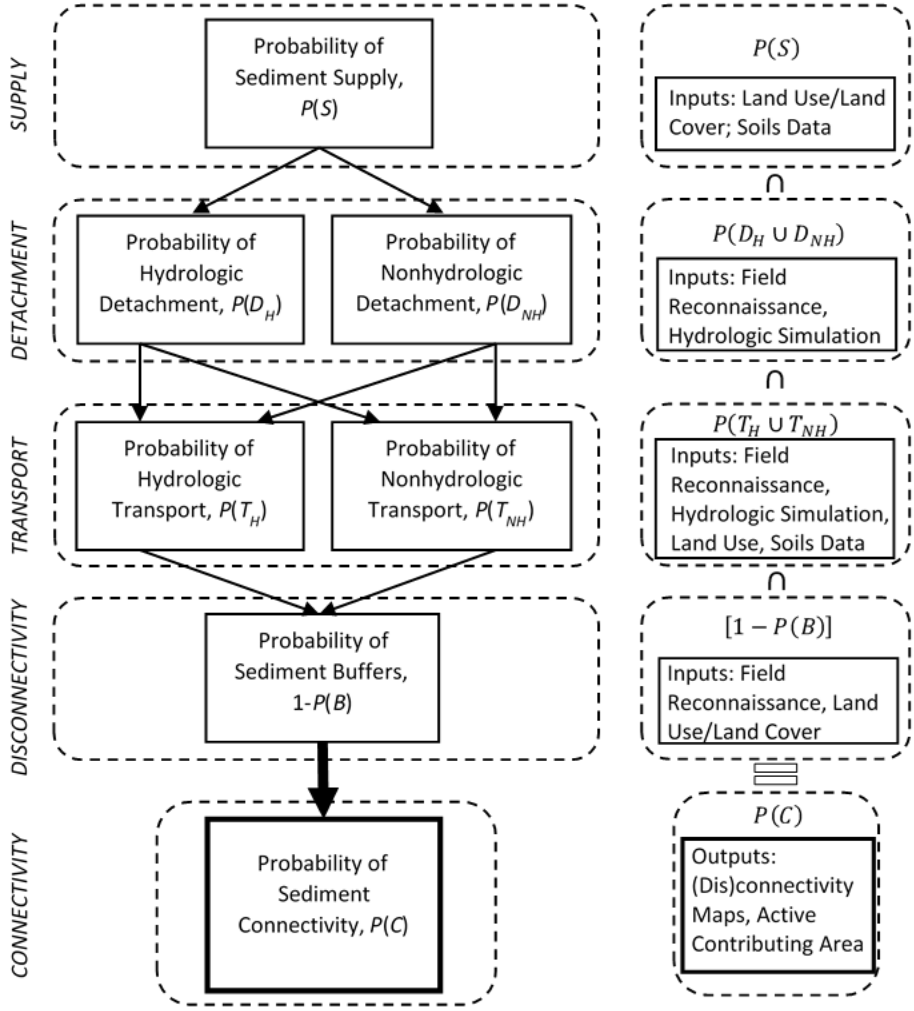

Figure 3.4. $\boldsymbol{P(\tau)}$ simulation framework for sediment timing. Outputs of the $\boldsymbol{P(\tau)}$ framework provide the spatial distribution of travel time for connected pathways and the frequency distribution of travel times.

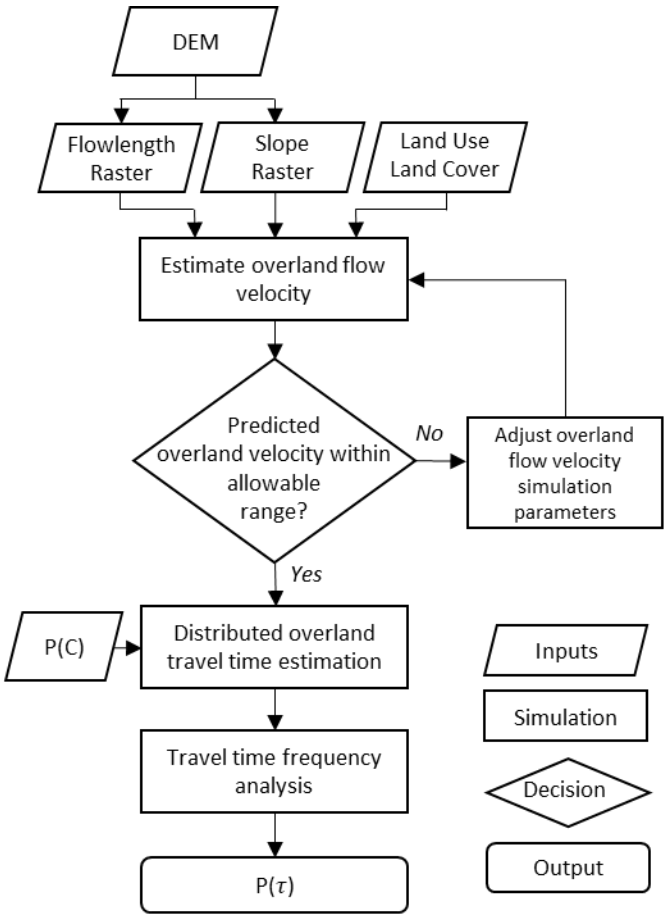

Figure 3.5. Probability of sediment connectivity results for three events in the Upper South Elkhorn watershed. Probability of connectivity is presented for five catchments of varying sizes: (a) catchment 1 (1.095 km^2), (b) catchment 2 (0.050 km^2), (c) catchment 3 (0.213 km^2), (d) catchment 60 (0.061 km^2), and (e) catchment 87 (2.102 km^2). The DEM for each catchment is also shown. We record structural properties of each catchment including, average slope, land use, and average soil content in Table 3. Results indicate that the probability of connectivity varies from catchment to catchment and from event to event, highlighting the probability of connectivity's dependence on structural and functional watershed properties

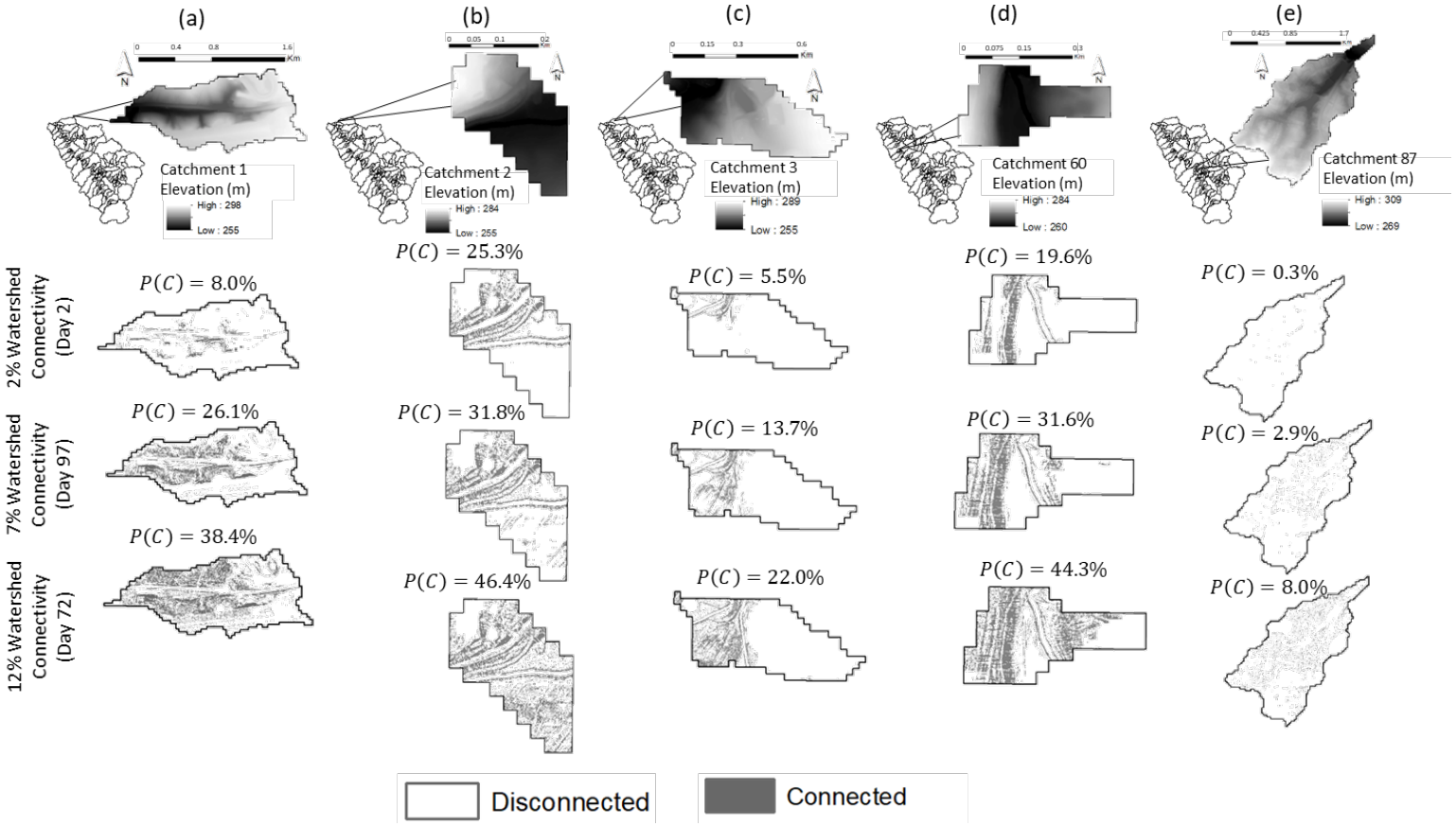

Figure 3.6. Probability of sediment timing results for three events in the Upper South Elkhorn watershed. Probability of timing is presented for five catchments of varying sizes throughout the Upper South Elkhorn watershed: (a) catchment 1 (1.095 km^2), (b) catchment 2 (0.050 km^2), (c) catchment 3 (0.213 km^2), (d) catchment 60 (0.061 km^2), and (e) catchment 87 (2.102 km^2). The probability of timing frequency distribution converges to days with higher percentage connectivity regardless of watershed size and configuration in the Upper South Elkhorn watershed, highlighting dependence of the probability of timing on functional watershed characteristics.

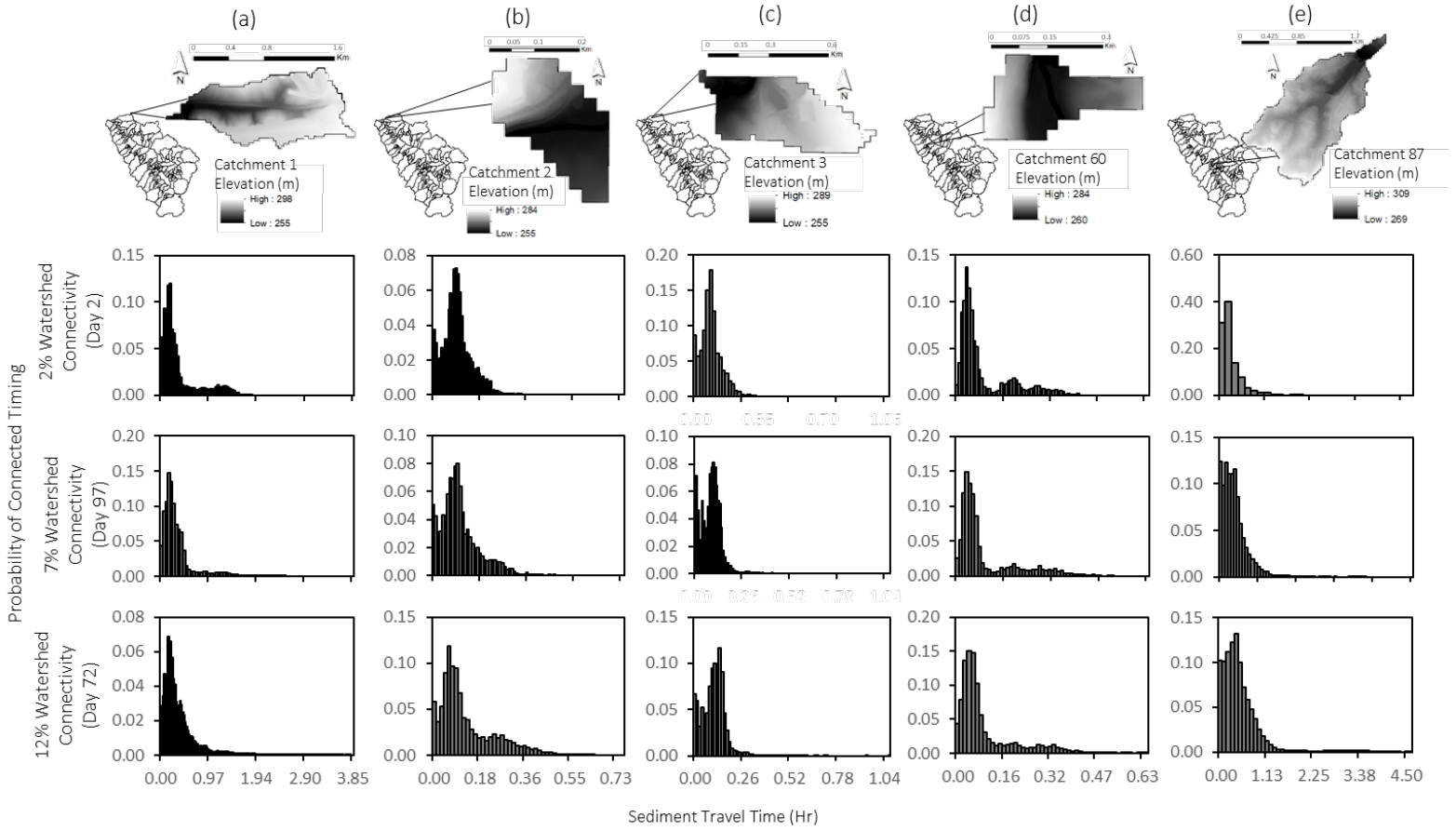

Figure 3.7. $\boldsymbol{P(C)}$ results for the most connected day of the initial study period (Day 72) compared to *IC* simulations (Borselli et al., 2008; Cavalli et al., 2013) using the SedInConnect tool (Crema and Cavalli et al., 2018). We present a subset of *IC* that corresponds to the percentage of land predicted to be connected by the $P(C)$ model to compare *IC* and $P(C)$ results. Generally, we find $P(C)$ and *IC* qualitatively agree during the most connected day of the initial study period. We present results for the five catchments shown in Fig. 5 including: (a) catchment 1; (b) catchment 2; (c) catchment 3; (d) catchment 60; and (e) catchment 87.

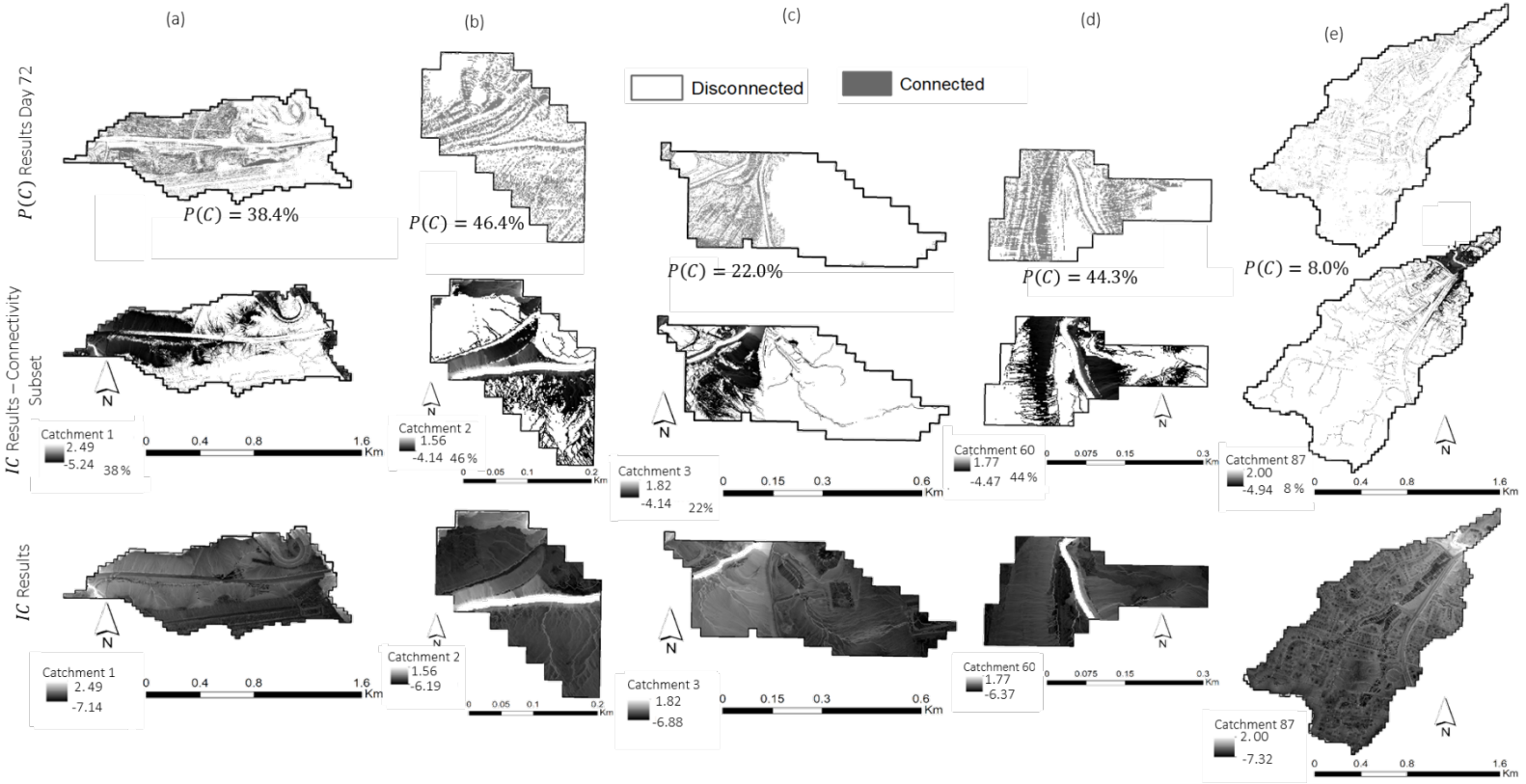

Figure 3.8. (a) $P(C)$ and (b) *IC* results for catchment 1 during event 2. $P(C)$ in catchment 1 is equal to 8.0%. The highest 8% of *IC* values are shown for comparison purposes to $P(C)$ results. We find poor correlation between *IC* and $P(C)$ during small hydrologic events, which perhaps is related to $P(C)$ being representative of both structural and functional connectivity whereas *IC* is a primarily a function of structural connectivity.

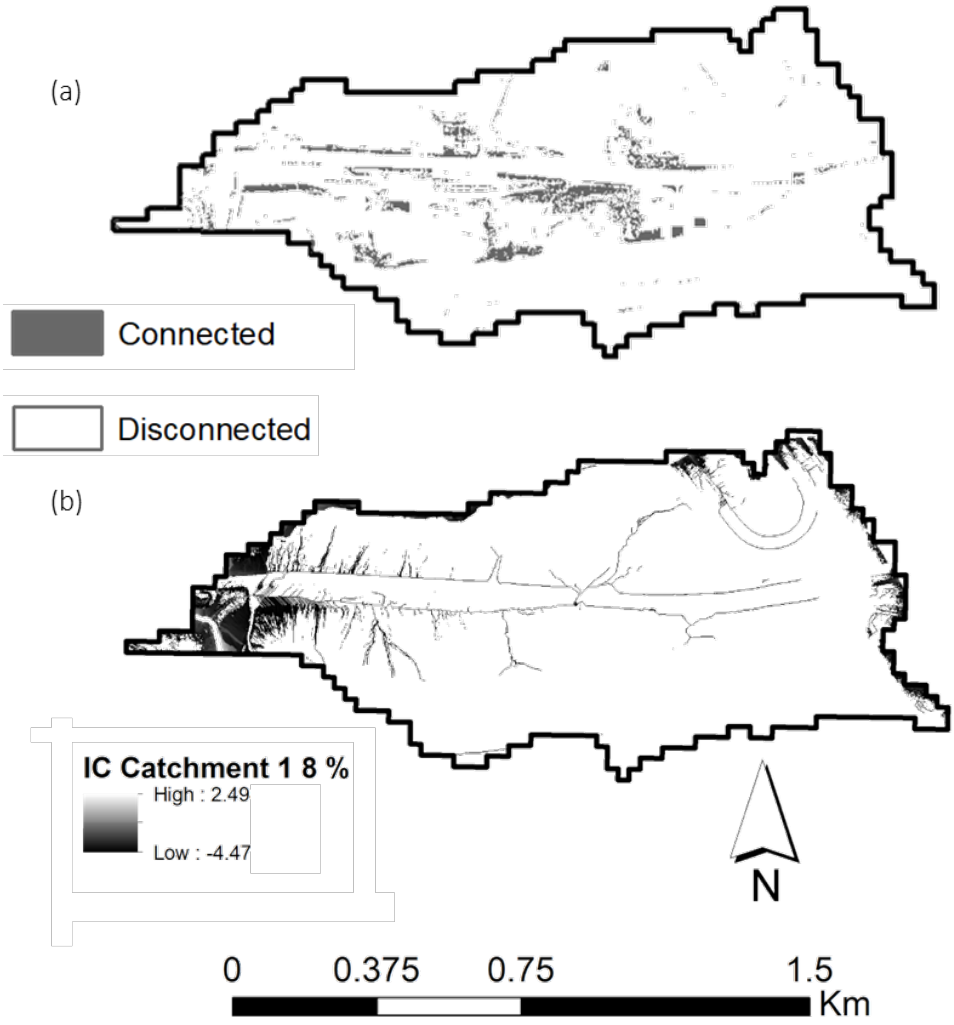

Chapter 4. Integrating Connectivity Theory within Watershed Modelling Part II: Application and Evaluating Structural and Functional Connectivity

4.0 ABSTRACT

Integrating connectivity theory within watershed modelling is one solution to overcome spatial and temporal shortcomings of sediment transport prediction, and Part I and II of these companion papers advance this overall goal. In Part II of these companion papers, we investigate sediment flux via connectivity formula discretized over many catchments and then integrated *via* sediment routing; and we advance model evaluation technology by using hysteresis of sensor data. Model evaluation with hysteresis indices provides nearly a one hundred percent increase in model statistics. Hysteresis loop evaluation shows a shift from near linear behavior at low to moderate events and then clock-wise loops for larger events indicating the importance of proximal sediment sources. Catchment-scale sediment flux varies as function of the probability of timing and extent of connectivity of an individual catchment. Watershed-scale sediment flux shows self-similarity for the main stem of the river channel as the 181 catchments are integrated moving down gradient. Sediment flux varies from event-to-event as a function of the most sensitive connected pathways, including ephemeral gullies and roadside ditches in this basin. These sensitive pathways contribute disproportionately large amounts to overall sediment yield regardless of the total rainfall depth. Prediction requires the connectivity formula, erosion formula and sediment routing formula; and the probability of connectivity alone was a poor predictor for sediment transport. The result highlights the importance of coupling connectivity simulations with sediment transport formula, and our method provides one such approach.

4.1 INTRODUCTION

Integrating connectivity theory within watershed modelling frameworks is one solution to overcome current spatial and temporal shortcomings of watershed sediment modelling (e.g., Ali et al., 2018; Mahoney et al., 2018; Ricci et al., 2018). Part I and II of these companion papers advance this overall goal. In Part I, we showed the theoretical formula for comprehensive connectivity and investigate timing of connectivity (see Part I of these companion papers, Mahoney et al., 2020). In Part II of these companion papers (this paper), we investigate the spatially and temporally explicit behavior of sediment flux

when connectivity formula is differentiated across many catchments and then modelled sediment flux is integrated via sediment routing. Specifically in Part II, we (1) advance modelling of sediment connectivity and sediment routing for the watershed-scaling, (2) advance understanding of the most sensitive connected pathways and their impact on sediment flux, and (3) advance model evaluation technology by using hysteresis of sensor data to assist with quantitative model evaluation.

In Part II of these companion papers, the advancement of modelling for watershed-scale connectivity and results of the net impact of the most sensitive connected pathways on sediment flux build off of theory and methods in Part I of these companion papers (Mahoney et al., 2020). The theoretical development in Part I showed sediment connectivity modelling should consider magnitude, spatial extent, timing and continuity of connectivity because together they can predict the most sensitive connected pathways across the landscape. However, the net impact on sediment results in a river require discretizing the connectivity formula to predict sediment flux for catchments and performing sediment routing to predict sediment flux in the river. Performing watershed modelling allows us to investigate how the sensitive connected pathways contribute to sediment flux at catchment and watershed scales for storm events of different magnitudes.

One contribution unique only to Part II of these companion papers is we advance model evaluation by using hysteresis of sensor data to help calibrate our watershed model. To our knowledge, using hysteresis to evaluation watershed models is rarely, if ever, been reported in the literature. The reason for lack of hysteresis evaluation is data-driven sensing technology has outpaced the existing structure and simulation capabilities of watershed models (Nunes et al., 2017). However, coupling sediment connectivity within watershed modelling simulates explicit pathways of sediment transport and timing of sediment transport using highly resolved topographic data (e.g., 1.5 meter DEMs) resulting in minute temporal resolution results. These model results are ripe for evaluating the structural and functional behavior of the model using methods such as hysteresis. Hysteresis loops (e.g., Williams, 1989; Evans and Davies, 1998) plot normalized sediment concentration versus normalized flowrate and have traditionally been used to assess timing of sediment sources. For example, hysteresis loop direction (e.g., clock-wise or anti-clockwise) is indicative of the connected timing of proximal or distal sediment sources, respectively (Evans and

Davies, 1998; Sherriff et al., 2016; Clare, 2019). Hysteresis analyses explain implicitly the spatiotemporal nature of sediment connectivity from an Eulerian perspective. We argue incorporating hysteresis, both qualitatively and quantitatively, with traditional watershed model evaluation metrics (e.g., Nash-Sutcliffe efficiency and percent bias; Moriasi et al., 2007) serves as an improved evaluation approach; and this approach is tested herein. The hysteresis evaluation is made possible using high resolution, continuous sensor measurements, which have become more and more common in river and watershed studies (Shoda et al., 2015; Pellerin et al., 2016).

Our objectives in this paper were to (1) carry out coupled modelling of sediment connectivity, sediment routing, sediment flux and yield catchment and watershed scales, (2) use hysteresis of sensor data to assist with quantitative model evaluation, and (3) analyze the sensitivity and connectivity of pathways and their impact on sediment flux and yield in the gently rolling watershed setting.

4.2 STUDY SITE

We applied the connectivity model to the gently-rolling Upper South Elkhorn watershed (61.7 km^2) in Kentucky, USA, and the watershed is fully described in Part I of these companion papers (Mahoney et al., 2020). Some brief additional comments are described here. We emphasize the gently-rolling nature of the Upper South Elkhorn watershed given that this type of morphology prompts well-dissected, mildly sloping surfaces that cause sediment connectivity in ephemeral gullies and analogous accumulated flow pathways throughout the uplands (McGrain, 1983; Mahoney et al., 2018). Sediment transport in the region is predominantly fluvial-mediated, and non-hydrology detachment and transport of sediment (e.g., mass wasting; Aeolian transport) is minimal (Russo and Fox, 2012, Mahoney et al., 2018). The watershed has historically been well-monitored by the University of Kentucky, the United States Geological Survey (USGS), and the National Oceanic and Atmospheric Administration (NOAA). For detailed description of the study site, we refer the reader to Part I of these companion papers (Mahoney et al., 2020).

4.3 METHODS

4.3.1 Watershed model formulation using sediment connectivity

The watershed model formulation couples catchment modelling using connectivity and sediment routing through the stream network. Catchment sediment flux is modelled as:

$$\dot{m}_{ij} = G_{ij}\left[P(C)_{ij} \cap P(\tau)_{ij} \cap P(\gamma)_{ij}\right], \quad (1)$$

where $\dot{m}$ is the flux of material with dimensions of mass per time, G is the mass per time sediment generation rate in a landscape unit, $P(C)$ is the probability of sediment connectivity representing connectivity's spatial extent, $P(\tau)$ is the probability of sediment timing representing the amount of time it likely takes for the sediment to reach the stream network, and $P(\gamma)$ is the probability of sediment (dis)continuity representing continuity of connectivity along the transport pathway, j is the fundamental spatial unit where connectivity and flux occur and i is the fundamental temporal unit when connectivity and flux occur. The fundamental spatial unit of this study is a 1.5 m by 1.5 m DEM cell. This resolution has been identified to capture important morphologic features influencing connectivity and sediment transport (Cantreul et al., 2017; Lopez-Vicente and Alvarez, 2018; Mahoney et al., 2018).

Sediment flux at the catchment outlet during timestep *i* is calculated by integrating Eq. 1 across catchment surfaces as:

$$\dot{m}_{ik} = \int G_{ij}\left[P(C)_{ij} \cap P(\tau)_{ij} \cap P(\gamma)_{ij}\right] ds_k \ , \quad (2)$$

where $\dot{m}_{ik}$ is sediment flux (kg s^{-1}) at the outlet of catchment *k* during time step *i* and s_k is the surface of catchment *k*. Mathematically Eq. 2 can be expressed by writing the probabilistic intersections algebraically and with spatial or time averaging some terms as:

$$\dot{m}_{ik} = \int \bar{\bar{G}} \cdot \overline{\overline{P(C)}} \cdot P(\tau)_{ij} \cdot \overline{\overline{P(\gamma)}}_k ds_k \ . \quad (3)$$

where $\bar{\bar{G}}$ is the spatially and temporally averaged erosion rate over the watershed during an event (kg s^{-1} m^{-2}), $\overline{\overline{P(C)}}$ is the spatially and temporally averaged probability of connectivity during an event (dimensionless), $P(\tau)_{ij}$ is the probability of sediment timing which is explicit in space and time (dimensionless), and $\overline{\overline{P(\gamma)}}$ is the probability of sediment (dis)continuity, which is averaged temporally for an event but varies from catchment to catchment. By expanding $P(\tau)_{ij}$ using the $\int_{t_i}^{t_{i+1}} f(t)\, dt$ (see Part I of these companion papers, Mahoney et al., 2020) and numerically approximating the integral, Eq. 3 can

calculate the spatial and continuous nature of sediment flux generated from each catchment in the watershed as:

$$\dot{m_{ik}}(t) = \bar{\bar{G}} \cdot \overline{\overline{P(C)}} \cdot \overline{\overline{P(\gamma)_k}} \cdot \sum_i^{i+1} f(t) \cdot s_k. \quad (4)$$

Additional terms in Eq. 4 are formulated considering process-based connectivity formula and empirical coefficients and fitting, as needed. Equations for $P(C)$ were presented previously as were the potential variables impacting $P(\gamma)$ (Mahoney et al., 2018; Part I of these companion papers, Mahoney et al., 2020). $P(\gamma)$ is the longitudinal (dis)continuity from the catchment outlet to the watershed outlet and is formulated recognizing continuity decreases as distance to the catchment outlet increases (e.g., Borselli et al., 2008; Cavalli et al., 2013; Bracken et al., 2015). We formulate $P(\gamma)$ as a first-order decay function as:

$$P(\gamma) = \alpha e^{-\lambda \cdot L} \quad (5)$$

where $P(\gamma)$ varies between zero and one to indicate full discontinuity or full continuity, respectively, α is the initial connectivity at the catchment outlet, λ the discontinuity loss rate (m^{-1}), and L is the length of the flow path (m). We represent the length of the flowpath using the stream distance from the catchment outlet to the watershed outlet in Eq. 5 because $P(\gamma)$ is parameterized here to represent longitudinal discontinuity due to instream processes (e.g., Fryirs, 2013). λ is a calibration parameter during model evaluation to account for variables not included in the current parameterization of $P(\gamma)$ (see discussion of Eq. 4 in Part I of these companion papers, Mahoney et al., 2020). G is formulated by investigating the functional relationship as:

$$G = f\{Q_R, H_{bd}, I, CN_{daily}, P(C)\}, \quad (6)$$

where Q_R is the overland runoff depth (m), H_{bd} is the peak baseflow contribution to streamflow, I is rainfall intensity (mm hr^{-1}), and CN_{daily} is the daily curve number and varies based on daily soil moisture (dimensionless). We suggest parameterizing G with variables included in Eq. 6 to predict erosion rate because: Q_R and H_{bd} capture fluvial shear to detach sediment (e.g., Jain, 2001); I captures detachment from rain drop impact (e.g., Toy et al., 2002); CN_{daily} captures antecedent moisture conditions and estimates the critical slope at which rill and ephemeral gully erosion begin (Torri and Poesen, 2014); and

$P(C)$ accounts for the spatial variation of soil properties and integrates erosive intensity of the fluid.

The watershed model routes sediment transport from the outlet of catchments through the stream network to the watershed outlet following a continuity approach. We formulated sediment continuity following the methods for low gradient streams with cohesive banks applied previously in this region (Russo and Fox, 2012; Mahoney et al., 2019). The sediment flux, Q_{ss}, is calculated as:

$$SS^{j}_{i+\frac{1}{2}} = \left[SS^{j}_{i-\frac{1}{2}} + Q^{j}_{SS,in\,i}\,\Delta t \; + Q^{j}_{SS,up\,i}\,\Delta t - kss \left(\frac{SS^{j}_{i-\frac{1}{2}}}{V^{j}_{i-\frac{1}{2}}} \right) Q^{j}_{out\,i-\frac{1}{2}} \Delta t \right] \left[1 + (1 - kss) \left(\frac{Q^{j}_{out\,i+\frac{1}{2}}}{V^{j}_{i+\frac{1}{2}}} \right) \Delta t \right]^{-1}, \quad (7)$$

$$Q^{j}_{SS,up\,i} = G \cdot \overline{\overline{P(C)}} s^{j} e^{-\lambda \cdot L^{j}} \sum_{i-\frac{1}{2}}^{i+\frac{1}{2}} A_{sed} f(t)_{sed}\,, \quad (8)$$

$$Q^{j}_{SS,in\,i} = k_{ss} \left(\frac{SS^{j-1}_{(i-1)-\frac{1}{2}}}{V^{j-1}_{(i-1)-\frac{1}{2}}} \right) Q^{j-1}_{out\,(i-1)-\frac{1}{2}} + (1 - k_{ss}) \left(\frac{SS^{j-1}_{(i-1)+\frac{1}{2}}}{V^{j-1}_{(i-1)+\frac{1}{2}}} \right) Q^{j-1}_{out\,(i-1)+\frac{1}{2}}\text{, and} \quad (9)$$

$$Q^{j}_{SS,out\,i} = k_{ss} \left(\frac{SS^{j}_{i-\frac{1}{2}}}{V^{j}_{i-\frac{1}{2}}} \right) Q^{j}_{out\,i-\frac{1}{2}} + (1 - k_{ss}) \left(\frac{SS^{j}_{i+\frac{1}{2}}}{V^{j}_{i+\frac{1}{2}}} \right) Q^{j}_{out\,(i-1)+\frac{1}{2}}\,, \quad (10)$$

where SS is the mass of suspended sediment (kg); Q and Q_{ss} denote water and sediment discharge ($m^3\ s^{-1}$ and $kg\ s^{-1}$); *in* and *out* denote flux into or out of a model stream reach; k_{ss} is the sediment routing coefficient (dimensionless); V is the volume of water (m^3); A_{sed} is a sediment attenuation factor (dimensionless).

4.3.2 Model Application

We applied the watershed model using sediment connectivity to the South Elkhorn watershed. Several materials were used to carry out analyses in Part II of these companion papers. First, catchment sediment connectivity, as predicted in Part I of these companion papers, were input to the model. Second, we used ArcGIS 10.4.1 to simulate $P(\tau)$ and $P(C)$ in each of the 181 catchments. We used ArcSWAT 2012.10.21 to simulate hydrologic variables such as runoff and Daily Curve Number (a proxy of soil moisture

content). We used MATLAB R2016b to route runoff and upland sediment flux using compiled results from $P(\tau)$ and $P(C)$ simulations. We completed model evaluation using MATLAB R2016b. All software was run on a desktop PC (Intel® Core™ i7-6700 CPU at 3.40 GHz; 64-bit operating system, x64-based processor). Third, we used 15-minute streamflow data from USGS station 03289000, NOAA weather data from the Bluegrass Airport at the watershed's geographic center, a high-resolution turbidity sensor (YSI 600 OMS with optical turbidity probe 6136) at the University of Kentucky South Elkhorn Sensor Station, and total suspended solids (TSS) samples to monitor discharge and sediment flux at the watershed outlet. We programmed turbidity sensors to collect data every 15-minutes concurrent with USGS measurements. TSS samples were collected using a Teledyne ISCO automated sampler over a 14-month period at 7-hour resolution and compared to turbidity data to empirically relate TSS and turbidity. Sampled TSS values ranged between 0.5 and 213.8 mg l^{-1}. Corresponding turbidity measurements ranged between 0.6 and 245.2 NTU. The coefficient of determination for TSS samples and turbidity measurements was 0.86. A summary of data requirements for the model is recorded in Table 1. We completed quality assurance/quality control of turbidity data by: (1) running the time series through an automated program to flag questionable, suspect, missing, and invalid data points; (2) visually assessing time series to correct instances of observable drift; and (3) comparing other water quality constituents collected at the University of Kentucky South Elkhorn Sensor Station with water quality constituents measured by the USGS at the watershed outlet to ensure the time series coincided.

The watershed was divided into 181 catchments, and sediment transport was predicted with 15-minute time steps. The space-time discretization satisfied the CFL condition (Courant et al., 1967), and water and sediment sensor data was collected at 15-minute resolution for evaluation. We applied the sediment model to 19 events between September 2017 and February 2019 when sediment transport occurs. We used the 19 events to calibrate and validate the model. The events chosen for model simulation fulfilled the following criteria: (1) quasi-continuous discharge and sediment time series collected every 15-minutes existed for the duration of the event; (2) anomalous hydrologic activity was not present; and (3) hydrologic properties of the watershed could be predicted for the time period *via* field or physically-based estimates. Also, we chose hydrologic events that

represented a variety of flow regimes. 2018 was an uncharacteristically wet year, and 2017 and 2019 were more normal years.

We specified model inputs and parameters using field measurements, estimates with geospatial modelling and hydrologic modelling, and using literature ranges (see Table 2). We input bed roughness, longitudinal slope, channel bathymetry, and contributing area of reaches with geospatial analyses in ArcMap version 10.4 and field reconnaissance in 2016 and 2017. We input the initial sediment concentration obtained from turbidity data prior to the start of the event. We specified initiation and termination of storm events by observing increases and decreases in discharge and turbidity data collected at the watershed outlet following the approach of Sherriff et al. (2016). Additional inputs for $P(C)$ and $P(\tau)$ are described in Part I of these companion papers (Mahoney et al., 2020). Parameterization of G in Eq. 6 was carried out by performing logarithmic transformation of all variables to produce non-zero sediment transport predictions and carrying out multiple linear regression (see coefficients in Table 2). Q_R and H_{bd} were parameterized semi-empirically by optimizing flowrate simulations and flowrate data collected from the USGS gage at the watershed outlet. I was input using NOAA rainfall gage data, and CN_{daily} was parameterized using hydrologic modelling from SWAT, as presented in Al-Aamery et al. (2016) and Mahoney et al. (2018). During parameterization and later during calibration, we grouped events to two hydrologic regimes including: events with watershed-averaged overland runoff less than 0.5 mm were grouped to the lower regime; and events with overland runoff greater than 0.5 mm were grouped to the upper regime. A_{sed}, λ and k_{ss} ranges were parameterized separately for the sets of events, and these variables were fit during model calibration. We parameterized a k_{ss} range using information regarding the travel time between reaches and flood routing theory (e.g., Gupta, 2016; Mahoney et al., 2019). We parameterized a A_{sed} range based on knowledge of overland flow velocity in the watershed (e.g., Russo and Fox, 2012; Mahoney et al., 2018) and was chosen such that overland velocity of sediment is generally between 0.02 and 2 m s^{-1} (Grimaldi et al., 2010). We parameterized a λ range to represent varying ranges of depositional patterns in the watershed (Grant et al., 2017). We input Q for the 181 reaches by estimating runoff and groundwater produced in catchments. We routed water through the stream network using

the Muskingum-Cunge method and iteratively estimated runoff and groundwater production such that simulated results matched well with observed discharge.

4.3.3 Model evaluation

We carried out model evaluation using three-stages of calibration and validation (see Fig. 1). In the first stage, we evaluate performance of the connectivity model as simulated using equations found in Mahoney et al. (2018) and in Part I of these companion papers (Mahoney et al., 2020). Upon running the connectivity model, we qualitatively compared simulated connected pathways to known connected pathways as identified by remote sensing and field reconnaissance. We adjusted parameters of the $P(C)$ model until the calibration was acceptable such that simulated connected pathways visually matched with known connected pathways (Mahoney et al., 2018; Mahoney et al., 2019). Additionally, we compared the simulated overland velocity of connected sediments to literature values of estimated overland velocity. We adjusted $P(\tau)$ parameters until simulated overland velocity was generally between 0.02 and 2.0 m s^{-1} (Grimaldi et al., 2010; see Part I of these companion papers, Mahoney et al., 2020).

In stage two, we calibrated and validated the instream sediment routing model using 19 events from September 2017 to February 2019. We used the first 13 events for calibration and the last 6 events for validation. Both sets of events contained a range of hydrologic regimes in terms of water discharge and sediment concentration magnitude and duration, and therefore were deemed representative of variable connectivity conditions. Dates and hydrologic properties (Q_R, H_{bd}, intensity, Daily CN) of events are recorded in the Supplementary Material Table S1. The Nash-Sutcliffe Efficiency (NSE) of the simulated sediment flux and observed sediment flux at the watershed outlet was used as an objective function to assess model performance (Moriasi et al., 2007) as:

$$NSE = 1 - \frac{\sum_{i=1}^{n}(o_i - s_i)^2}{\sum_{i=1}^{n}(o_i - o_{avg})^2} \quad (11)$$

where n is the number of temporal steps in the model, o_i is the observed sediment flux during a time step, s_i is the simulated sediment flux during a time step, and o_{avg} is the average observed sediment flux. We manually adjusted the sediment attenuation parameter, sediment discontinuity parameter, and sediment routing coefficient for

hydrologic regimes until average NSE for all events was acceptable (e.g., greater than 0.2). We additionally used the coefficient of determination to compare simulated and observed event sediment yield.

In stage three, we repeat the evaluation process from stage two but include additional objective functions for hysteresis as well as qualitative information. Hysteresis was calculated by normalizing discharge and sediment concentration for each event and plotting normalized discharge on the *x*-axis and normalized sediment concentration on the y-axis. In calibration, we minimized the difference between observed and simulated hysteresis indices (HI). HI serves as one method to quantify hysteresis loop characteristics such as direction, magnitude, and shape (e.g., Lloyd et al., 2016); and the HI varies between -1 and 1 for normalized event data, with positive values indicating clockwise loop direction and negative values indicating anti-clockwise loop direction (Sherriff et al., 2016; Lloyd et al., 2016). The HI was calculated as:

$$HI_{Q_i} = C_{RL_{Q_i}} - C_{FL_{Q_i}} \quad (12)$$

where Q_i is the discharge at the i^{th} percentile of total normalized discharge for the event, $C_{RL_{Q_i}}$ is the concentration corresponding to the designated discharge percentile on the rising limb of the hydrograph, and $C_{FL_{Q_i}}$ is the concentration corresponding to the designated discharge on the falling limb of the hydrograph. Event HI for each simulated event was calculated as the average value of the Hysteresis Index calculated at each quartile of normalized discharge over the course of the event (i.e. the HI calculated at 25%, 50%, and 75% of maximum normalized discharge). We calculated event HI from quartiles of normalized discharge because this approach is commonly implemented in the hysteresis literature (e.g., Fovet et al., 2018; Aguilera et al., 2018). We also qualitatively evaluated the model performance by comparing the shape of the simulated hysteresis loop to the observed hysteresis loop. Throughout the hysteresis evaluation, we iteratively adjusted the sediment attenuation parameter, sediment discontinuity parameter, and sediment routing coefficient for hydrologic regimes until average NSE was acceptable (e.g., greater than 0.2), observed and simulated hysteresis qualitatively matched, and the difference in observed and simulated HI was minimized. We compared the NSE from stage two of the

modelling with stage three to determine whether incorporation of hysteresis improved model results.

We investigated the relationship between $P(C)$ and peak sediment flux by grouping events by increasing sediment flux into low, medium, and high regimes. We carried out one-way ANOVA tests to assess statistical differences in $P(C)$ between groups of events. We used the coefficient of determination to further investigate the relationship between event $P(C)$ and event sediment yield. We also used the coefficient of determination to investigate the relationship between $P(C)$ and event average erosion rate per cell.

A summary of qualitative and quantitative methods used to validate the model structure have been recorded in the Supplementary Material Table S2. These include field reconnaissance of sediment pathways to qualitatively validate predicted results; comparison of $P(C)$ with the Index of Connectivity (IC) (e.g,. Borselli et al., 2008; Cavalli et al., 2013; Heckmann et al., 2018); optimization of the Nash Sutcliffe Efficiency (NSE) for observed and simulated sediment flux; comparison of the NSE of observed and simulated flux when hysteresis was considered with the NSE when hysteresis was not considered; minimization of the difference in observed and simulated hysteresis index (HI); qualitative visual comparison of observed and simulated hysteresis loop, shape, and direction; and qualitative comparison of observed and simulated sediment flux.

4.4 RESULTS AND DISCUSSION

4.4.1 Model evaluation using sediment hysteresis

We found that model evaluation statistics improved by nearly a factor of two when hysteresis was considered during model calibration versus when hysteresis was not considered (see Table 3). We found that the average NSE for the calibration and validation periods were 0.46 and 0.59, respectively, when hysteresis and event NSE were considered as objective functions. When only event NSE was considered as an objective function, average NSE was 0.24 during the calibration period and 0.34 during the validation period. Optimal parameter values for events as inputs for the model are recorded in the Supplementary Material Table S1, and hysteresis assisted with adjusting sediment attenuation and discontinuity parameters. These coefficients were difficult to estimate using physical grounds because the former reflects the lag between sediment and water

during transport and the latter scales deposition longitudinally in the main channel; and the hysteresis calibration showed usefulness to help with quantitative model evaluation for these coefficients. The final values for model statistics (Table 3) show very good model performance based on existing criteria, especially considering the time step in this study and that results are for sediment (Moriasi et al., 2007).

Evaluation of hysteresis results were also shown to be adequate for individual storm events as well as quantitatively for the hysteresis index and for sediment yield overall in the basin. During the modelling evaluation, we calibrated the model by minimizing the difference between simulated and observed hysteresis indices for the events (Table 4) and visually comparing hysteresis loops (e.g., Fig. 2). Visually, the good relation between observed and simulated hysteresis and sediment flux shown in Fig. 2, Fig. 3 and Fig. 4. Visual results show qualitative validation of hysteresis. In addition, comparison of simulated and observed hysteresis indices for individual storm events shows also quantitative validation of the modelling (see Table 4). The model generally performs well with respect to hysteresis indices for individual events. 80% of simulated hysteresis loops correctly capture the loop direction calculated from the turbidity and discharge data. The model correctly predicted 3 of the 6 events with negative hysteresis; and these events with observed negative hysteresis had hysteresis indices very close to zero for both modelled and observed values. These 6 storm events with negative hysteresis were the smallest sediment transport events and had sediment yield that was one to two orders lower by metric tonnes as compared to the other 13 storm events. The model correctly predicted 12 of the 13 events with positive hysteresis. The HI was predicted correctly for 95% of simulated sediment yield over the course of the 19 events.

One reason why inclusion of hysteresis improved sediment flux modelling is because hysteresis accounts for structural and functional connectivity of distal and proximal sediment sources, which was observed by investigating our connectivity model results (Fig. 5). Generally, the loop direction is an important indication of overall event connectivity and timing of connected sources given that distal versus proximal sources of sediment will cause anti-clockwise versus clockwise loop direction, respectively (e.g., Lloyd et al., 2016; Sherriff et al., 2016). In the South Elkhorn watershed, hysteresis modelling and observations show hysteresis loops for events with smaller sediment flux

(Fig. 2a – Fig. 2l; Fig. 4c,) tend to be relatively linear (hysteresis index near zero) or slightly negative, indicating that peak sediment concentration and peak discharge occur approximately coincidently. As hydrologic regime increases (e.g., Fig. 2m – Fig. 2r) shape of the hysteresis shifts from linear to generally clock-wise loops where sediment concentration peaks prior to peak of discharge, implicitly indicating strong connectivity of proximal sources during large events (e.g., Lloyd et al., 2016; Sherriff et al., 2016). The weak hysteresis trends shown in Fig. 2a – Fig. 2l indicate that equal contribution of proximal and distal sediment sources occur during this time. As hydrologic regime increases, proximal sediment sources dominate sediment flux.

Results of the event hysteresis loops adds to our understanding of sediment connectivity in the watershed. We find that the majority of connected sediment in the Upper South Elkhorn watershed is located proximally to the watershed outlet. Generally, (dis)continuity of distal sediment in the eastern portion of the watershed limits connectivity of distal sediment to the watershed outlet due to instream bedrock outcrops that cause discontinuity and deposition of sediment. Additionally, we find that limited connectivity occurs in the eastern and southern portions of the Upper South Elkhorn watershed due to soils being better-drained than soils near the catchment outlet in the northwestern portion of the watershed. Poorly drained soils in the northwestern portion of the catchment are a structural property of the northwestern portion of the watershed that promotes runoff generation (and thus sediment connectivity) proximal to the watershed outlet. This is corroborated by work from Sherriff et al. (2016) who found that regardless of land use type, drainage efficiency of catchment soils limited (or promoted) runoff generation and controlled overall sediment connectivity.

4.4.2 Sediment Flux at catchment and watershed scales

Analyses of results suggests catchment-scale sediment flux is linked to morphology and structural characteristics of the catchments (see Fig. 5); and varies from catchment-to-catchment as function of the probability of timing and extent of connectivity of an individual catchment. This result was found by examining timing, spatial extent connectivity and flux for the catchments. For example, Fig. 5 shows differences in sediment connectivity and transport for two catchments in the South Elkhorn watershed;

and comparison of the two catchments shows differences for sediment travel time (Fig. 5a) and sediment flux and yield (Fig. 5b, 5c) for the 27 January 2018 even when watershed $P(C)$ was equal to approximately 10.4%. The majority of connected cells in catchment 1 contribute sediment to the watershed outlet between 0 and 3.8 hours (e.g., black and magenta cells/bars in Fig. 5a and 5b), and the majority of connected cells in catchment 87 contribute sediment to the watershed outlet between 0.3 and 5 hours (e.g., magenta, blue, and cyan cells/bars in Fig. 5a and 5c). The spatially connected area of catchment 1 was predicted to be 0.42 km^2 while the connected area of catchment 87 was 0.17 km^2. Catchment 1 produced 1.3 t sediment during the event, and catchment 87 produced 0.4 t sediment. The prolonged contribution of sediment flux from catchment 87 occurs from the lower gradient landscape and larger contributing area of the catchment, which slows velocity of transported sediment.

It is noteworthy that Euclidian distance does not necessarily indicate connectivity and relate with sediment flux. Distributed $P(\tau)$ results (Fig. 5a) show cells with travel time between 0 to 1.3 hours are located throughout the western half of catchment 1, far from the watershed outlet, and cells with travel time between 1.3 to 2.5 hours are located close to the watershed outlet. This might seem counter-intuitive, however the morphology of catchment 1 promotes pockets of overland runoff with high velocity, especially in roadside ditches and ephemeral gullies where increased velocity of runoff is possible. In this regard, while Euclidian distance to the watershed outlet does influence $P(\tau)$, the travel time is also dependent upon proximity of the connected cell to a transport pathway or morphologic feature that efficiently moves sediment such as a roadside ditch or gully. Delineation of isochrons to define sediment travel times should not solely follow contours, but should also include morphologic features.

The result that Euclidian distance is not necessarily a good predictor of sediment connectivity and flux in our study corroborates well with results of Fryirs et al. (2007) and the on-going discussion of the impact of buffers, barriers, and blankets on sediment connectivity (see Fryirs et al., 2007; Fryirs, 2013). Buffers, barriers and blankets are defined by Fryirs et al. (2007) as structural morphologic features that impede sediment transport in lateral, longitudinal, and vertical dimensions, respectively. Fryirs (2013) uses the term “buffers” to represent features that promote specifically disconnectivity of

sediment from the uplands a catchment to the catchment outlet. In this study, we explicitly incorporate buffers, here in the form of floodplains and farm dams, into the formulation of the $P(C)$ model to represent disconnectivity. Our results extend an understanding of buffer's impact on connectivity because our inclusion of $P(\tau)$ to our connectivity model shows how buffers can impact sediment timing results. We see the implicit impact of buffers because they impede the timing of sediment transport and connectivity. In this sense we use the term "buffers" to mean both the lateral impedance of sediment travel time and disconnected spatial regions from the source to the stream network. One impact of buffers is the Euclidean distance is not always a good timing predictor. For example, we find that microtopography, defined as localized areas with flat gradients or "rough" slopes (Lopez-Vicente and Alvarez, 2018), impedes the travel time of sediment from the uplands of catchment 1 to the catchment outlet (see circled area in Fig 5a), although the proximity of these features to the watershed outlet is relatively close. Microtopography typically consists of slopes with characteristically low gradient, but can have high upstream contributing area. Sediment connectivity is possible on microtopography, but travel time from the uplands of the catchment to the catchment outlet is prolonged due to decreased fluid velocity on the low gradient slopes (e.g., Jain, 2001), as shown here. Consequently, the morphologic feature is impeding sediment transport, and implicitly is a buffer (Fryirs, 2013).

The importance of buffers on timing extends the discussion of buffer impact on spatial connectivity, which is shown in our results, the work of Fryirs et al. (2007) and a number of recent connectivity studies. For example, this concept is consistent with recent connectivity literature from Cavalli et al. (2013) and Lopez-Vicente and Alvarez (2018) in the sense of spatial connectivity, who found that pathway roughness and discontinuity elements such as microtopography along the flowpath were important controls of sediment connectivity. Specifically, Cavalli et al. (2013) found that an index used to represent roughness of flow paths significantly impacted results of the *IC* (see Borselli et al., 2008; Part I of these companion papers, Mahoney et al., 2020) and that roughness and *IC* were inversely proportional. Cavalli et al. (2013) verified simulated (dis)connectivity using field reconnaissance, indicating that the degree of sediment linkage is a function of pathway roughness. Similarly, Lopez-Vicente and Alvarez (2018) found that simulated *IC* values

decreased as DEM resolution (and hence the ability to capture microtopography features) increased. In summary, we add to this on-going discussion because we find that not only do buffers tend to control (dis)connectivity spatially (e.g., Cavalli et al., 2013; Lopez-Vicente and Alvarez, 2018), but buffers, or lack thereof, also control the timing of sediment connectivity from the uplands to the stream network.

As sediment flux and connectivity are integrated to the watershed scale, the shape of sedigraphs tends to become self-similar (see Fig. 6). This result occurs from the routing of sedigraphs from the 181 individual catchments. With respect to temporal integration of sediment flux over events, we find that generally sediment yield simulations matched well with the observed sediment yield for events (NSE = 0.84; R^2 = 0.94). These results for the watershed scale show how leveraging structural and functional connectivity at the fundamental unit can be upscaled, which has been promoted in a number of recent papers (e.g., Vigiak et al., 2012; Nunes et al., 2017; Ali et al., 2018).

4.4.3 Sediment flux depends on the most sensitive connected pathways

Based on analyses of model results, sediment flux varied from event-to-event and was found to be dependent on the most sensitive connected pathways existing across the watershed. The most sensitive connected pathways were ephemeral gullies, rills and roadside ditches (see Part I of these companion papers, Mahoney et al., 2020). We find that as the density of sensitive pathways (i.e., the area of cover of these pathways per catchment area) increases between catchments, so too does the sediment flux. For example, we find that Catchment 1 contains a greater density of sensitive connected pathways compared to Catchment 87 (see Fig. 5a) and that peak flux of catchment 1 (Fig. 5b) is approximately five times as much as catchment 87 (Fig. 5c) during the event on 1/27/2018. The sensitive pathways were associated with relatively steep slopes and larger upstream contributing areas where water in the ephemeral gullies, rills and roadside ditches were more erosive. The sensitive pathways in our study are corroborated by active contributing areas identified previously in connectivity literature (e.g., Trimble, 1997; Fryirs, 2013; Latocha, 2014). The urban and suburban ephemeral networks were at least as important as the agricultural sensitive pathways in terms of sediment production, likely due to increased runoff

production from impervious surface and increased accumulated flow from well-defined urban drainage systems (Fig. 5a).

Analyses of results showed the sensitive connected pathways contribute disproportionately large amounts to overall sediment yield regardless of the total rainfall depth. Event-to-event results for $P(C)$, gross erosion generated per cell, and simulated sediment yield (see Table 5) show storm events with lower $P(C)$ can have a one order of magnitude higher sediment production per connected cell than events with higher $P(C)$. Averaging data in Table 5 shows erosion generation per cell for events with less than 5% $P(C)$ is estimated to be 0.9 kg cell^{-1} while average erosion generation per cell for events with greater than 5% $P(C)$ is estimated to be 0.06 kg cell^{-1}. The high erosion rates for less connected days occur because the most sensitive connected pathways almost always produce sediment, at least for the 19 storm events studied. The gently-rolling watershed has artificially-created concentrated flow pathways from gullies and road networks leading to connectivity and erosion for the events studied. As the system becomes more connected, the landscape neighboring the sensitive pathways contribute sediment but at a much smaller rate. The connectivity modelling highlights the importance of the most sensitive sediment pathways, regardless of event magnitude, which might not be expected otherwise.

4.4.4 Sediment transport prediction needs both connectivity and erosion formula

While the contribution of sensitive connected pathways is indicated using $P(C)$, we find $P(C)$ alone is a poor predictor for sediment yield during events (R^2 = 0.007) and sediment flux. Fig. 3 shows sediment flux is poorly related with event $P(C)$ results. Events in Fig. 3 are grouped by increasing sediment flux. Fig. 3a-3f show events with maximum Q_{ss} equal to 0.7 kg s^{-1}. Fig. 3g -3l show events with maximum Q_{ss} equal to 2.5 kg s^{-1}. Fig. 3m-3r show events with maximum Q_{ss} equal to 15.0 kg s^{-1}. There is no statistically significant difference between $P(C)$ results between groups of events shown in Fig. 3 (one-way ANOVA, α = 0.05). Additionally, the simulated erosion rate per cell alone is a poor predictor for sediment yield (R^2 = 0.05). The poor relation between individual components of Eq. 1 reflects the fact that sediment transport and connectivity encompass both structural and functional connectivity and consideration of both facets is necessary in order to

simulate sediment flux at the watershed scale (Fryirs, 2013; Bracken et al., 2015; Grant et al., 2017; Ali et al., 2018; Wohl et al., 2019).

The result is noteworthy and shows the importance of coupling connectivity simulations with erosion formula and routing to quantify sediment yield. Recent literature review indicates that few connectivity-based models couple with erosion formulae to predict sediment flux (e.g., Ali et al., 2018; Heckmann et al., 2018; Wohl et al., 2019). Our results are corroborated by Lopez-Vicente et al. (2015), who coupled the *IC* (e.g., Borselli et al., 2008; Cavalli et al., 2013) with soil erosion estimation to assess potential soil redistribution at the plot scale for differing runoff scenarios. Lopez-Vicente et al. (2015) found that while the *IC* map reflected the spatial pattern of soil erosion, there was poor correlation between soil erosion rate and the *IC*. In this regard, we emphasize the importance of future iterations of sediment connectivity models to consider erosion and sediment transport formulae to assess sediment flux and yield.

The notion that $P(C)$ is a poor predictor of sediment yield slightly contrasts findings from Vigiak et al. (2012) who found that calibrated hillslope sediment delivery ratio (HSDR), a function of the *IC* (Borselli et al., 2008), was well correlated with specific sediment yield, which ultimately adds to an ongoing discussion regarding timescales of connectivity in recent literature (e.g., Ali et al., 2018). In their study, Vigiak et al. (2012) linked HSDR and *IC* using a Boltzmann-type sigmoid function and HSDR was coupled within the deposition component of the erosion model in order to predict net sediment yield at a yearly timescale. Generally, Vigiak et al. (2012) found that HSDR predicted specific sediment yield well, which contrasts our findings that connectivity and sediment yield are poorly correlated.

There are several potential reasons for these discrepancies regarding $P(C)$ as a predictor of sediment yield in our study compared to the study by Vigiak et al. (2012), and we primarly relate these differences to the timescales of observation in each study. For example, timescales monitored in the study of Vigiak et al. (2012) (monthly – yearly) were much longer than those analyzed herein (subhourly – event). Recent study has shown that while both structural and functional processes are important considerations for connectivity simulations at the event time scale (e.g., Mahoney et al., 2018), long-term connectivity patterns are controlled by structural watershed properties (e.g., Fryirs, 2013). In this regard,

since *IC* is primarily a function of structural properties, (see discussion in Part I of these companion papers, Mahoney et al., 2020), the finding that sediment yield, as simulated on a yearly basis in Vigiak et al. (2012), and *IC* are well correlated is reasonable considering structural properties tend to control both connectivity and flux at such timescales (Fryirs, 2013; see discussion in Part I of these companion papers, Mahoney et al., 2020). Further, Vigiak et al. (2012) and Jamshidi et al. (2014) acknowledge that *IC* is a good candidate for linkage with HSDR when climatic homogeneity is prevalent in the catchment, which again is a reflection of the structural nature of the *IC*. During low and moderate-hydrologic events, we find that $P(C)$ is controlled by highly variable functional processes, and that during these instance $P(C)$ and *IC* were poorly correlated because $P(C)$ formulation considers both structural and functional connectivity while *IC* primarily considers structural connectivity (see Section 5.3 of Part I of these companion papers, Mahoney et al., 2020). Better correlation between $P(C)$ and sediment yield might be expected during high-magnitude hydrologic events, however, when control of $P(C)$ shifts from functional processes to structural watershed properties (Mahoney et al., 2018; see Part I of these companion papers, Mahoney et al., 2020). Ultimately this distinction points towards recent sentiment from researchers (e.g., Fryirs, 2013; Ali et al., 2018; Wohl et al., 2019), who indicate that connectivity, and structural versus functional control of connectivity, is variable over variable timescales.

4.4.5 Future directions and limitations

Several other methods currently present promising potential for quantifying watershed sediment flux using connectivity theory similarly to the study presented herein. One example, includes the previously mentioned hillslope sediment delivery ratio (HSDR) parameter, as described in Vigiak et al. (2012) and derivatives thereof (e.g., Jamshidi et al., 2014; Hamel et al., 2015). HSDR can be used to predict sediment yield when coupled with empirical erosion equations, such as the universal soil loss equation (Jamshidi et al., 2014; Hamel et al., 2015). The HSDR framework shows promise for future simulations of watershed connectivity and sediment yield, however important limitations currently persist with the model related specifically to the lack of functional connectivity considerations in the *IC*, thus limiting the simulation timescale to, at shortest, monthly or seasonal simulations. Incorporation of functional connectivity processes into the *IC* and HSDR

structures through alterations of the *IC* weighting factor (e.g., Chartin et al., 2017; Hooke et al., 2017; Kalantari et al., 2017; Gay et al., 2015; see Section 5.3 in Part I of these companion papers, Mahoney et al., 2020), or as shown herein with the probability of connectivity formulations, warrants further investigation as another avenue to couple connectivity theory and sediment flux modelling at high temporal resolutions.

One limitation of the modelling presented herein is the lack of evaluation of the erosion rate rates at field plot-scales predicted using the erosion generation function. Our limitation stems from the lack of spatially explicit and continuous soil erosion measurements across the landscape needed to fully validate erosion rates. Our limitation is consistent with other studies. The lack of sediment erosion data to validate upland erosion rates has been a common discussion point in the connectivity literature for some time now, dating back to at least the study of Vigiak et al. (2012), with implicit recognition dating back as early as Walling's "sediment delivery problem" (Walling, 1983). The problem currently persists as identified in the recent review by Heckmann et al. (2018). Currently, sediment connectivity modelling is made possible by the proliferation of sub-meter resolution topographic surveys and high-temporal resolution sediment data. An important dataset currently underdeveloped, however, is continuous, spatially explicit erosion data collected at the field-plot scale for both event and seasonal timescales (Heckmann et al., 2018). While such a dataset is conceptually ideal, practical limitations will likely persist for the foreseeable future limiting the development of such data (Heckmann et al., 2018; Wohl et al., 2019).

Potential solutions to the lack of sediment data and to better-quantify sediment connectivity are both scale and process dependent (Heckmann et al., 2018; Wohl et al., 2019), and might include the following: (1) sediment fingerprinting studies at the catchment and watershed scales that help estimate erosion rates from specific sources at the field-plot scale, as recommended by a number of researchers (Vigiak et al., 2012; D'Haen et al., 2013; Koiter et al., 2013; Evrard et al., 2011; Fox and Martin, 2015; Heckmann et al., 2018; Mahoney et al., 2019; Wohl et al., 2019); (2) plot-scale estimates of erosion rates in controlled settings (Renard et al., 1996; Heckmann et al., 2018); (3) upscaling of plot-scale erosion rates to hillslope and subcatchment scales (Heckmann et al., 2018); (4) wireless sensor networks at the catchment scale (Wohl et al., 2019); and (5)

improved technologies for tracing and tracking sediments at the watershed scale (e.g., Entekhabi et al., 2010; Jaeger and Olden, 2012; Smith and Vericat, 2015; Wohl et al., 2019). All of these methods show potential for helping to validate erosion rates used in connectivity modelling, however we also point out that these measurements are rather expensive and time-consuming, especially when attempting over sites across multiple land uses of a watershed. We highlight that the advancement of spatially explicit sediment data may improve connectivity and flux simulation validation in the next generation of watershed models, and warrants further development given the advancement of remote sensing sciences.

Generally speaking, we recognize that both succession of hydrologic events prior to those studied herein (including frequency and magnitude), antecedent soil moisture reflective of the previous event and its timing, and the configuration of the stream network likely impact sediment flux at the watershed outlet in the sense of threshold breaches, sediment supply availability, and transport capacity of the fluid. The present study carries out modelling for events although antecedent conditions, for example, are parameterized within the sediment connectivity modelling. Continuous simulation in future work may add further insight to sediment transport in this basin, although there are several features of sediment transport processes that are likely to show similar results for both event based and continuous simulation. For example, we note that the Upper South Elkhorn system neither aggrades nor degrades at longer time scales (monthly, yearly), indicating that upland sediment continuously replenishes bed sediments eroded during storm events, which is consistent with our past findings (Russo and Fox, 2012; Mahoney et al., 2018; Mahoney et al., 2019). Past study has also found that bank erosion contributes very little to overall sediment yield (Russo and Fox, 2012). Previous investigations in the stream found almost no instances when supply limited erosion and sediment transport of bed sediments (Russo and Fox, 2012; Mahoney et al., 2019). Thus, we expect some similarities between continuous simulation and event based results. That said, we are limited to event simulations in this study and continuous simulation might add further insight that builds upon these results herein.

4.6 CONCLUSION

These two-part companion papers show the usefulness for integrating connectivity theory with watershed modelling. The conclusion of Part II of these companion papers is as follows:

1. Our model evaluation shows inclusion of hysteresis indices improves both quantitative calibration/validation metrics and provides a deeper understanding of the physical processes occurring in the watershed. Including hysteresis indices provides nearly a 100% increase in model statistics, and in turn improves our prediction of sediment flux. Hysteresis loop evaluation shows a shift from near linear behavior at low to moderate events and then clock-wise loops for larger events indicating the importance of proximal sediment sources in the system studied.
2. Catchment-scale sediment flux is linked to morphology and structural characteristics of the catchments. Sediment flux leaving catchments varies from catchment-to-catchment as function of the probability of timing and extent of connectivity of an individual catchment. Watershed-scale sediment flux shows self-similarity for the main stem of the river channel as sediment from the 181 catchments is integrated moving down gradient.
3. Sediment flux varies from event-to-event and is found to be dependent on the most sensitive connected pathways existing across the watershed. The sensitive connected pathways in our gently-rolling watershed were ephemeral gullies and roadside ditches. As the density of these networks increases so too does sediment flux for both small and large magnitude hydrologic events. These sensitive connected pathways contribute disproportionately large amounts to overall sediment yield regardless of the total rainfall depth.
4. Sediment transport prediction to the watershed outlet requires both the connectivity formula, erosion formula and sediment routing formula. $P(C)$ alone was a poor predictor for sediment flux and sediment yield. The result highlights the importance of coupling connectivity simulations with erosion formula, and our method provides one such approach.

4.7 ACKNOWLEDGMENTS

We gratefully acknowledge the financial support of this research under National Science Foundation Award 163288. We thank the associate editor Paulo Alexandre da Silva Pereira and two anonymous reviewers for comments and criticisms that have greatly improved the quality of this manuscript.

4.8 SUPPLEMENTARY MATERIAL

Table S1. Instream sediment routing model inputs and optimal parameters for events. A_{sed} is the sediment attenuation coefficient, λ is the sediment discontinuity coefficient, k_{ss} is the sediment routing coefficient, SS_1 is the initial sediment flux prior to the start of the event, Q_R is the event runoff depth, H_{bd} is the peak baseflow depth, Daily CN is the daily curve number (a proxy of soil moisture content), and $P(C)$ is the probability of connectivity.

Event	A_{sed}	λ	k_{ss}	SS_1 (kg s^{-1})	Q_R (mm)	H_{bd} (mm)	Intensity (mm hr^{-1})	Daily CN	P(C)	Avg. Erosion Generation per Cell (kg cell^{-1})	
9/19/2017	2.5	3.5E-04	0.5	0.01	0.35	2.20	3.81	77.3	1.4%	0.14	
11/18/2017	2.5	3.5E-04	0.5	0.02	0.37	1.80	4.06	84.9	3.6%	0.03	
12/5/2017	2.5	3.5E-04	0.5	0.02	0.42	1.30	3.89	80.9	3.1%	0.08	
1/27/2018	5.2	2.0E-04	0.5	0.10	0.90	16.00	2.60	86.1	10.4%	0.03	
3/10/2018	2.5	3.5E-04	0.5	0.02	0.14	0.90	1.65	83.8	3.1%	0.01	
5/5/2018	5.2	2.0E-04	0.5	0.05	20.50	14.00	4.00	80.2	3.0%	1.39	Calibrate
5/31/2018	5.2	2.0E-04	0.5	0.30	2.70	7.60	8.72	77.0	1.5%	1.36	
6/21/2018	2.5	3.5E-04	0.5	0.02	0.58	2.10	1.87	63.8	0.1%	3.81	
10/15/2018	5.2	2.0E-04	0.5	0.02	0.50	2.20	1.09	82.9	2.5%	0.02	
11/15/2018	5.2	2.0E-04	0.5	0.03	0.90	10.50	1.82	86.9	12.2%	0.02	
12/1/2018	5.2	2.0E-04	0.5	0.20	5.80	7.80	1.64	87.2	13.3%	0.06	
12/15/2018	5.2	2.0E-04	0.5	0.03	1.60	9.98	1.99	85.7	9.8%	0.04	
12/20/2018	5.2	2.0E-04	0.5	0.03	0.90	9.80	1.31	85.4	8.8%	0.02	
12/23/2018	5.2	2.0E-04	0.5	0.05	0.50	5.30	2.07	87.0	5.9%	0.01	
1/4/2019	5.2	2.0E-04	0.5	0.07	5.00	4.00	2.34	86.4	11.5%	0.09	
1/19/2019	5.2	2.0E-04	0.5	0.07	2.70	6.00	1.54	86.8	12.4%	0.03	Validate
1/23/2019	5.2	2.0E-04	0.5	0.06	0.70	5.20	1.76	87.4	13.7%	0.01	
2/20/2019	5.2	2.0E-04	0.5	0.15	7.20	2.00	2.60	86.0	10.7%	0.14	
2/23/2019	5.2	2.0E-04	0.5	0.11	9.00	5.00	3.81	86.1	10.9%	0.22	

Table S2: Qualitative and quantitative metrics used to validate the coupled connectivity and watershed modelling results.

Method	Source	Validation Type
Sediment pathway verification using field reconnaissance and remote sensing	Fryirs et al., 2007; Borselli et al., 2008; Nicoll and Brierley, 2017	Qualitative
Visual comparison of P(C) results with the Index of Connectivity for variable events of hydrologic magnitude	Borselli et al., 2008; Crema and Cavalli et al., 2017	Qualitative
Nash Sutcliffe Efficiency (NSE) of simulated and observed sediment flux for calibration and validation periods	Arnold et al., 1998; Moriasi et al., 2007	Quantitative
Visual comparison of simulated and observed sedigraphs for calibration and validation periods	Wohl et al., 2019	Qualitative
Comparison of calibration and validation NSE when hysteresis was considered and when hysteresis was not considered	Developed herein	Quantitative
Comparison of the hysteresis index for simulated and observed hysteresis loops	Evans and Davies, 1998; Sheriff et al., 2016; Clare, 2019	Quantitative
Visual comparison of simulated and observed hysteresis loop shapes, areas, and direction	Evans and Davies, 1998; Sheriff et al., 2016; Clare, 2019	Qualitative
Comparison of simulated and observed event sediment yield statistics (NSE, coefficient of determination)	Moriasi et al., 2007	Quantitative

Table 4.1. High-resolution data used to simulate connectivity and sediment flux.

Data Type	Resolution	Collection Method
Digital Elevation Model	1.5 m by 1.5 m	LiDAR (KYAPED, 2014)
Total Suspended Solids Samples	7 hours	Teledyne ISCO Sampler
Turbidity	15 minutes	YSI 6-Series Optical Sensor; YSI EXO Series Optical Sensor
Upland Flux Simulation	15 minutes	Connectivity model (see Part I of these companion papers, Mahoney et al., 2020)
Discharge	15 minutes	USGS Gage 03289000
Precipitation	Hourly	NOAA Lexington Bluegrass Airport Station

Table 4.2. Parameter ranges and structural channel properties used to simulate sediment flux.

Parameter	Description	Value/parameter range	Units
k_{ss}	Sediment Routing Coefficient	0.00-0.50	Unitless
λ	Sediment Discontinuity Coefficient	0.00001-0.001	m^{-1}
A_{sed}	Sediment Attenuation Coefficient	0.1-10.0	Unitless
n	Manning's n	0.03	Unitless
S	Longitudinal Slope	Varies	$m\ m^{-1}$
m	Side Slope	Varies	Unitless
L	Reach Length	Varies	m
w	Channel Width	Varies	m
N_{reach}	Number of Reaches	181	Unitless
α	Intercept Parameter for G Estimation	82.590	Unitless
β_1	Q_R Parameter for G Estimation	0.740	Unitless
β_2	H_{bd} Parameter for G Estimation	0.054	Unitless
β_3	I Parameter for G Estimation	0.889	Unitless
β_4	CN_{daily} Parameter for G Estimation	19.452	Unitless
β_5	$P(C)$ Parameter for G Estimation	0.081	Unitless

Table 4.3. Nash-Sutcliffe Efficiency values where hysteresis is not considered and hysteresis is considered for the 19 events analyzed.

Event	NSE No Hysteresis	NSE Hysteresis	
9/19/2017	0.85	0.74	Calibrate
11/18/2017	0.74	0.58	
12/5/2017	0.49	-1.57	
1/27/2018	0.53	0.71	
3/10/2018	-3.66	0.69	
5/5/2018	0.81	0.76	
5/31/2018	0.81	0.76	
6/21/2018	0.93	0.80	
10/15/2018	0.51	0.61	
11/15/2018	0.31	0.04	
12/1/2018	0.04	0.57	
12/15/2018	0.71	0.85	
12/20/2018	0.06	0.43	
12/23/2018	0.30	0.75	Validate
1/4/2019	0.36	0.70	
1/19/2019	0.29	0.35	
1/23/2019	0.20	0.42	
2/20/2019	0.50	0.76	
2/23/2019	0.40	0.57	

Table 4.4. Observed and simulated hysteresis indices (HI) for simulated events. Positive HI indicates clockwise hysteresis and negative HI indicates anti-clockwise hysteresis.

Event	Hysteresis Index Observed	Hysteresis Index Simulated	Sediment Yield Sim (tonnes)	
9/19/2017	-0.07	-0.05	6.0	
11/18/2017	-0.17	0.16	4.1	
12/5/2017	-0.04	-0.03	7.1	
1/27/2018	0.09	-0.02	27.7	
3/10/2018	-0.15	-0.10	2.3	
5/5/2018	0.47	0.52	254.2	Calibrate
5/31/2018	0.21	0.67	135.4	
6/21/2018	0.14	0.42	15.1	
10/15/2018	-0.27	0.40	4.4	
11/15/2018	0.27	0.89	20.1	
12/1/2018	0.33	0.53	80.9	
12/15/2018	0.30	0.37	26.3	
12/20/2018	0.21	0.85	16.0	
12/23/2018	-0.12	0.68	9.9	
1/4/2019	0.17	0.74	79.9	
1/19/2019	0.20	0.59	48.1	Validate
1/23/2019	0.32	0.66	31.1	
2/20/2019	0.44	0.68	125.2	
2/23/2019	0.46	0.59	166.4	

Table 4.5. Results for simulated probability of connectivity, erosion, and sediment yield considering hysteresis during calibration. Nash-Sutcliffe Efficiency of simulated sediment yield was determined to be 0.84 and R^2 was determined to be 0.94.

Event	P(C)	Avg. Erosion Generation per Cell (kg cell^{-1})	Simulated Sediment Yield (tonnes)	Observed Sediment Yield (tonnes)
9/19/2017	1.40%	0.14	6.0	10.8
11/18/2017	3.57%	0.03	4.1	8.8
12/5/2017	3.08%	0.08	7.1	4.4
1/27/2018	10.42%	0.03	27.7	48.9
3/10/2018	3.14%	0.01	2.3	3.0
5/5/2018	3.00%	1.39	254.2	305.1
5/31/2018	1.50%	1.36	135.4	149.4
6/21/2018	0.13%	3.81	15.1	28.8
10/15/2018	2.54%	0.02	4.4	5.3
11/15/2018	12.16%	0.02	20.1	26.2
12/1/2018	13.34%	0.06	80.9	162.6
12/15/2018	9.79%	0.04	26.3	44.4
12/20/2018	8.82%	0.02	16.0	29.4
12/23/2018	5.91%	0.01	9.9	12.6
1/4/2019	11.49%	0.09	79.9	94.0
1/19/2019	12.36%	0.03	48.1	58.6
1/23/2019	13.74%	0.01	31.1	47.2
2/20/2019	10.68%	0.14	125.2	223.72
2/23/2019	10.90%	0.22	166.4	198.7

Figure 4.1. Sediment model evaluation flowchart. Flowcharts assessing probability of connectivity and probability of timing are shown in Part I.

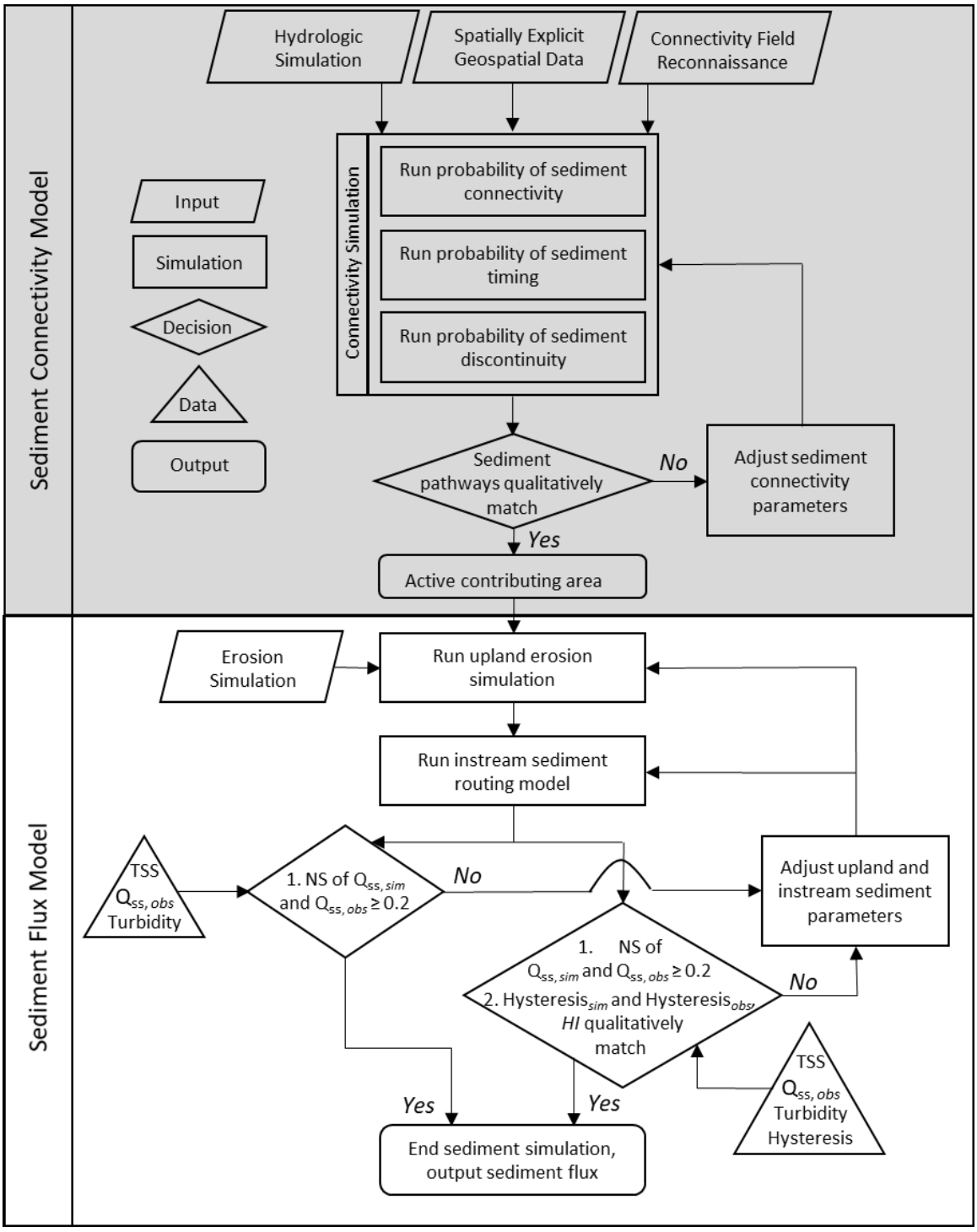

Figure 4.2. Comparison of simulated sediment hysteresis at the watershed outlet to sediment hysteresis measured with turbidity sensors, total suspended solids samples, and USGS Gage 03289000. Events are organized by increasing observed sediment flux. We qualitatively compared observed and simulated hysteresis during model calibration, which improved model evaluation statistics.

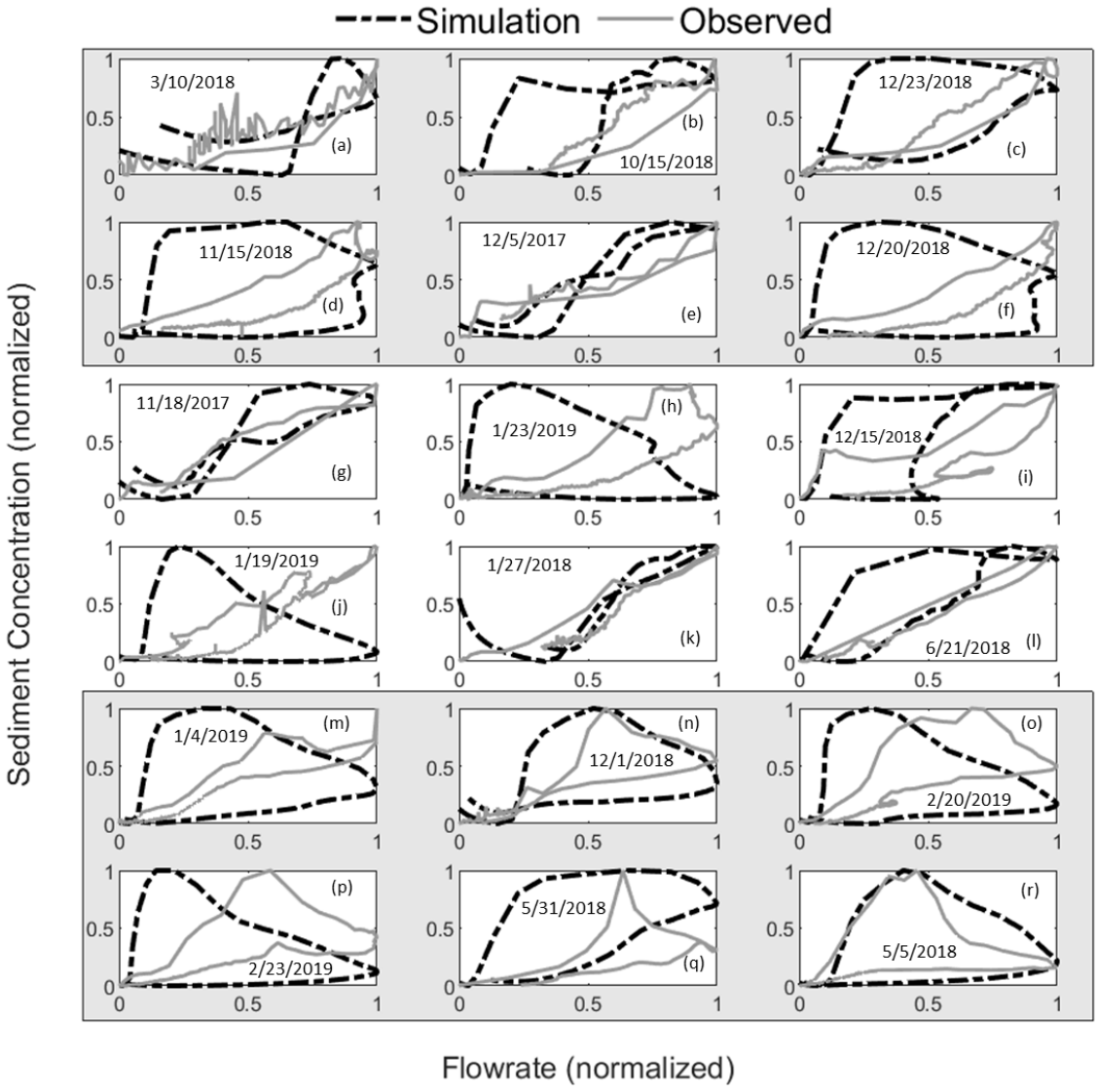

Figure 4.3. Comparison of predicted sediment flux at the watershed outlet to sediment flux measured with turbidity sensors and total suspended solids samples. Events are organized by increasing observed sediment flux. (a)-(f) show events with maximum Q_{ss} equal to 0.7 kg s^{-1}. (g)-(l) show events with maximum Q_{ss} equal to 2.5 kg s^{-1}. (m)-(r) show events with maximum Q_{ss} equal to 15 kg s^{-1}. Events (c), (h), (j), (m), (o), and (p) were used for model validation.

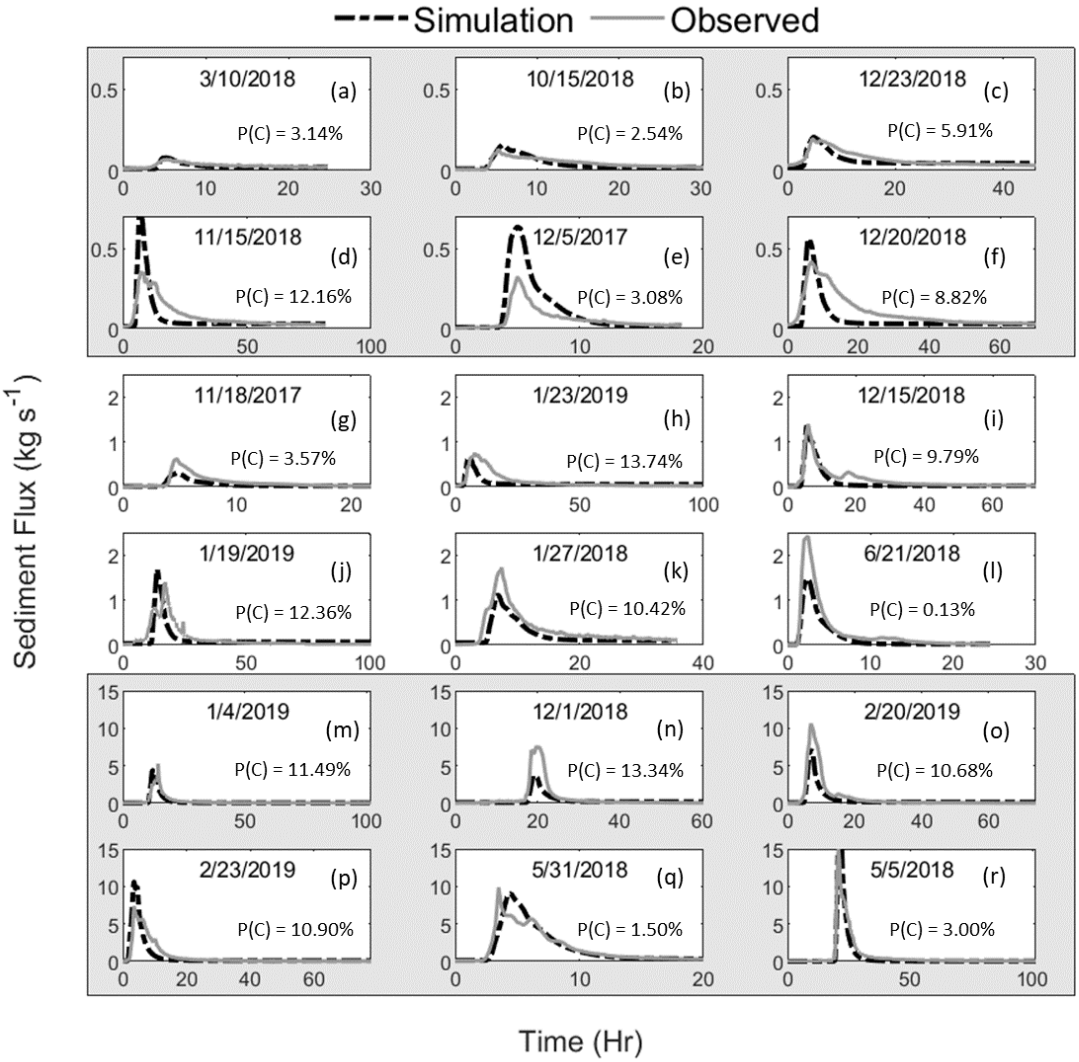

Figure 4.4. Model results for 9/19/2017. (a) Shows predicted and observed sediment flux at the watershed outlet. Observed sediment flux was measured by creating an empirical TSS-Turbidity relationship using a YSI 6-series optical turbidity probe and TSS samples collected from an ISCO automated sampler. (b) Shows simulated and observed sediment concentration throughout the event. (c) Shows the simulated and observed sediment hysteresis loops.

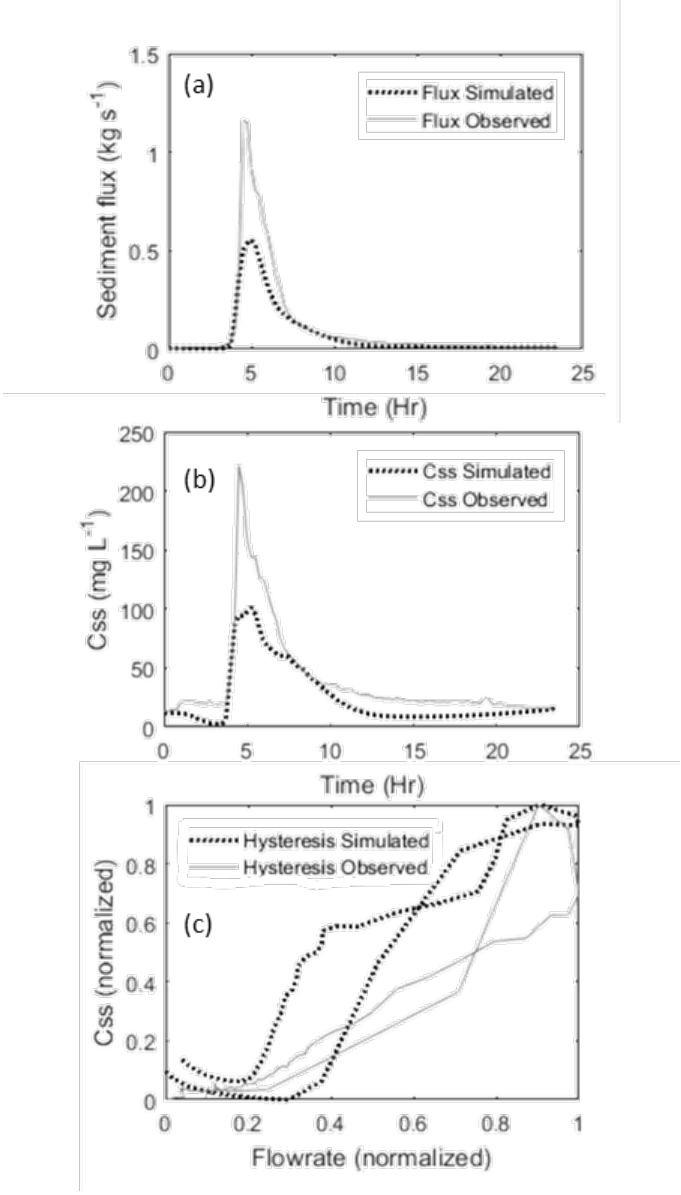

Figure 4.5. Integrated connectivity modelling results for two catchments in the Upper South Elkhorn watershed when watershed probability of connectivity was equal to 10% on 1/27/2018. (a) Shows distributed geospatial results of coupling the probability of connectivity and the probability of timing for catchment 1 and catchment 87. (b) Shows integrated sediment flux estimation for catchment 1. (c) Shows integrated sediment flux estimation for catchment 87. Colored bars in (b) and (c) relate to cells shown in (a). Circled area in (a) shows location where microtopography inhibits sediment travel time.

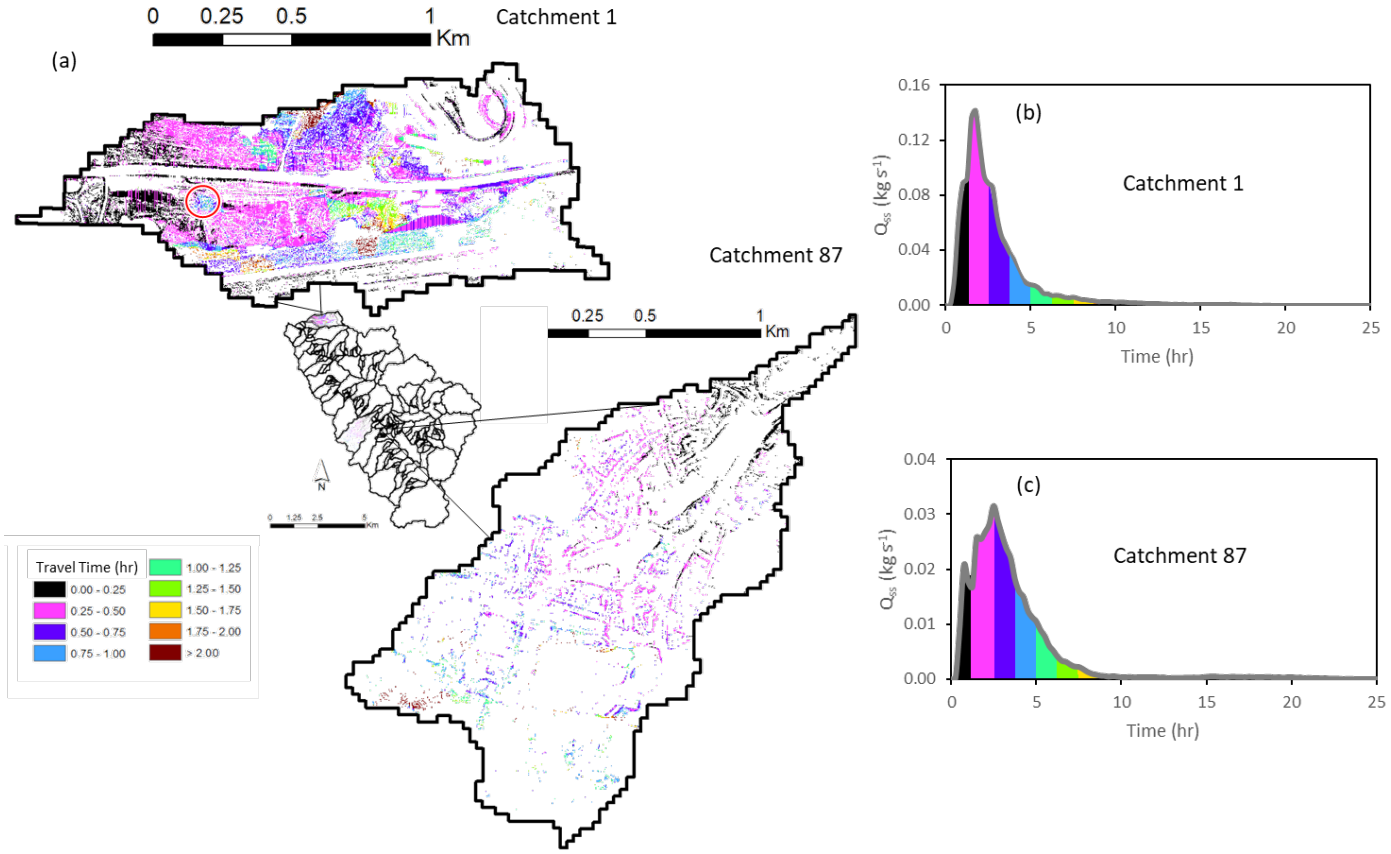

Figure 4.6. Multiplication of erosion generation per cell, $P(C)$, $P(\tau)$, and $P(\gamma)$ to estimate sediment flux during the 1/27/2018 hydrologic event at varying spatial scales. (a) Shows spatially explicit *E,* $P(C)$, $P(\tau)$, and $P(\gamma)$ results at the catchment scale for catchment 161 (2.25 km^2). (b) Shows spatially explicit results of integrating and routing connectivity, runoff, and erosion across upper catchment surfaces (32.82 km^2) and through the upper catchment stream network. (c) Shows simulated discharge and sediment flux at the catchment outlet (61.7 km^2) after integrating and routing *E,* $P(C)$, $P(\tau)$, and $P(\gamma)$ over the watershed surface and through the stream network.

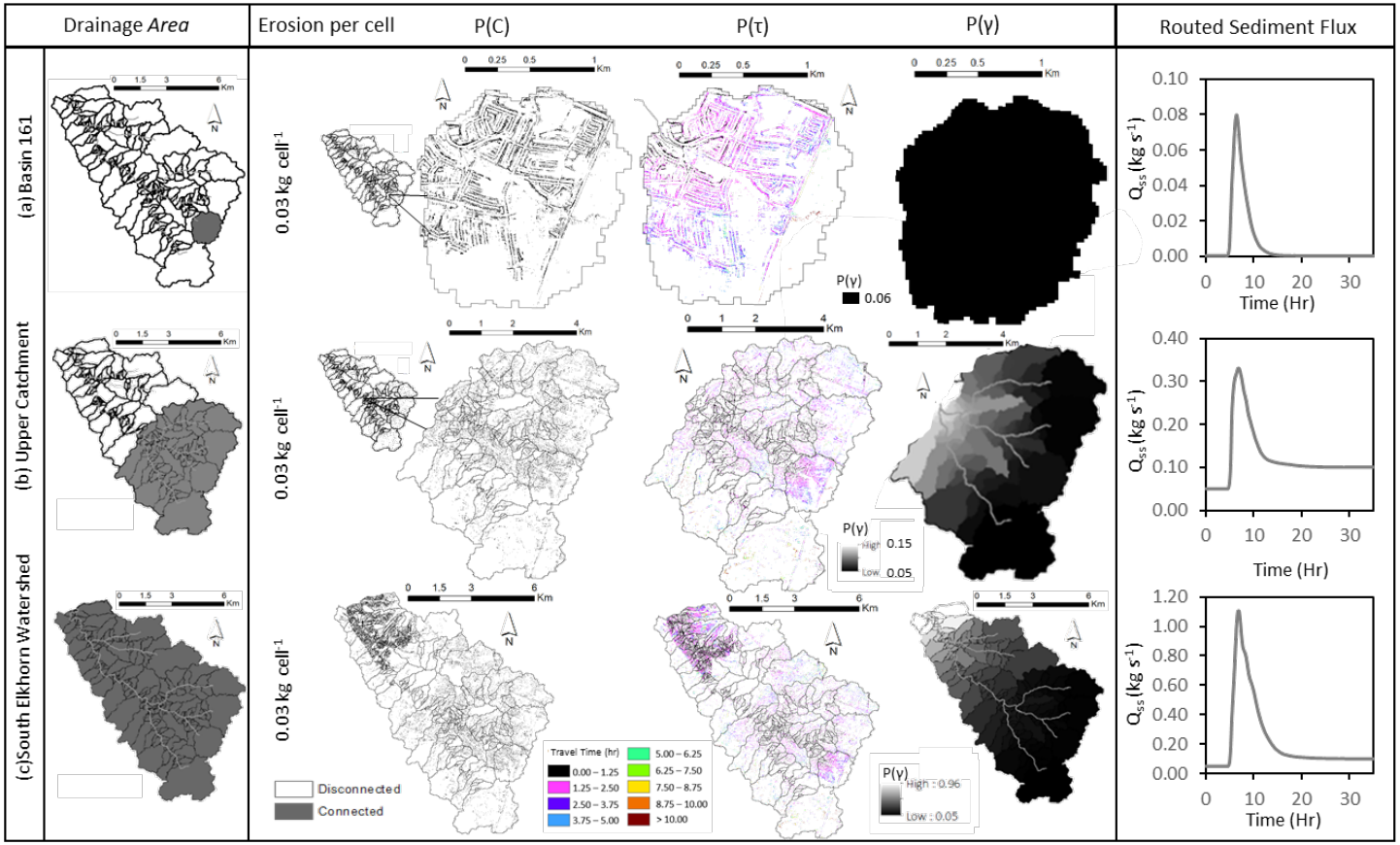

Chapter 5. Coupling the probability of connectivity and RUSLE reveals pathways of sediment transport and soil loss rates for forest and reclaimed mine landscapes

5.0 ABSTRACT

This work couples the connectivity modelling with soil erosion modelling to simulate pathways that actively erode and transport sediment in a steep, forested catchment with reclaimed mine lands. The probability of connectivity approach is formulated by substituting soil loss generated from the revised universal soil loss equation (RUSLE). Methods are carried out for a catchment in Eastern Kentucky USA and supported by one meter resolution digital elevation model and a suite of previously published sediment transport data for the basin.

We find that the coupled modelling simulates sediment transport well, which agrees with recent sentiment and suggestions by others. However, evaluation results show unforeseen dependency between connectivity formula and RUSLE that needs to be accounted for when coupling the models. Future modelling of connectivity and RUSLE together should consider incorporating feedback calibration schemes to resolve lack of model independence.

Results estimate 12% and 47% of the drainage area of Appalachian forests and reclaimed minelands, respectively, was connected for the hydrologic events studied; and sediment is transported from concentrated flow paths on steep surfaces. The soil loss rates of the reclaimed mine are approximately 30 times greater than the forest land despite the fact that the reclamation is classified as phase 3. Disconnectivity occurs due to legacy terracing in the forest, the high sand content of the forest soils that increase water infiltration, and constructed berms between compacted spoil lifts on the reclaimed mine.

Two results of this study point to a need for future work: (i) Our results generally point to structural control as dominating net connectivity in this study, which is contrary to the notion that functional (dynamic) processes control sediment connectivity in all landscapes. (ii) Relationships between soil loss and connectivity in the forest and reclaimed mine show trends of self-similarity, which remains a topic that is open one recent

study agrees with our findings but others suggest the probability of connectivity can be poorly correlated with soil loss and sediment yield in some basins.

5.1 INTRODUCTION

Structural and functional watershed properties are now well known to control sediment yield and connectivity (Bracken et al., 2015; Wohl et al., 2018; Zingaro et al., 2019). Over the past six decades, watershed models have been widely implemented to simulate soil loss and understand controlling sediment processes at the watershed scale (USEPA, 2004), and now play an important role in measuring impacts of sediment on ecology, water supply, and water quality (Morris and Fan, 2009). We find, however, that watershed models currently are hindered for a number of reasons. Namely, seldom do watershed models represent structural and functional watershed variability at the fundamental spatial and temporal units at which sediment processes occur (Bracken et al., 2015; Nunes et al., 2017; Wohl et al., 2018; Batista et al., 2019). This results from spatial and temporal lumping of sediment processes across landscapes and hydrologic events, disassociating models from physical process and introducing empiricism. In years past, such lumping resulted from limited computing power and availability of spatially explicit data (Walling et al., 1983; Fryirs, 2013).

Coupling sediment models with connectivity theory (see Fryirs, 2013; Bracken et al., 2015; Wohl et al., 2017) and now widely available geospatial data (e.g., KYAPED, 2014) serves as one promising approach to better represent structural and functional variability of watershed properties. The ubiquity of high resolution geospatial data serves as one means to overcome data limitations that currently hinder sediment models, even in environments that have previously been considered “data sparse” (e.g., Fox, 2009).

Our motivation was to better understand structural and functional processes that control sediment yield and sediment connectivity by coupling watershed soil loss modeling with spatially explicit sediment connectivity simulations. We applied the coupled model to a steep, forested watershed with reclaimed mine land in the Appalachian Region of Eastern Kentucky, USA. In this regard, this paper serves the motivations of: (1) advancing methods for coupling connectivity modelling with erosion rate modelling; (2) understanding

spatially explicit soil loss in forested and reclaimed mine land uses; and (2) understanding and discussing controlling structural and functional watershed properties that limit sediment yield and sediment connectivity on forested and reclaimed mine hillslopes. Our intent was to improve process-based knowledge of active sediment pathways and assist with management of soil loss in watersheds.

We couple the widely popular Revised Universal Soil Loss Equation (e.g., RUSLE, Renard et al., 1997) with connectivity theory (Bracken et al., 2015; Wohl et al., 2018) to better represent spatially explicit pathways that actively contribute sediment to the stream network. We chose to couple connectivity theory with RUSLE for a number of reasons. First, RUSLE has been widely applied across the United States and Europe (Batista et al., 2019), partially due to its success of implementation and relatively few input requirements (Fox and Martin, 2015). Second, the RUSLE formulation serves as the conceptual foundation for many popular non-point source sediment models, including (Ann)AGNPS (Bingner and Theurer, 2001) and the Soil and Water Assessment Tool (SWAT; Arnold et al., 1998). Third, the availability of high-resolution geospatial data, such as 1 m digital elevation models (DEMs), serves as a basis to improve the spatial resolution of hillslope erosion simulations.

While RUSLE has been widely applied, one underlying assumption of the model is that all soil generated on a hillslope or within a HRU reaches the stream network (Lenhart et al., 2005) and that deposition along hillslope pathways is negligible (de Vente et al., 2013). Such assumptions limit the applicability of the model to predict sediment yield only on surfaces with known active erosion pathways (Renard et al., 1997).

To overcome limitations of current watershed models and simulate actively eroding pathways, we suggest coupling RUSLE simulations with connectivity theory. We define connectivity similarly to Heckmann et al., (2018) as an emergent system property that reflects the strength and continuity of sediment linkages between and within system compartments at a given point in time. Connectivity is an emerging field that aims to understand spatially and temporally explicit pathways that facilitate sediment transport (Fryirs, 2013; Bracken et al., 2015; Wohl et al., 2019). Theory and frameworks to understand sediment connectivity have been well developed within the geomorphology and engineering communities (e.g., Hooke, 2003; Borselli et al., 2008; Fryirs 2013; Bracken et

al., 2015; Gran and Czuba, 2017; Mahoney et al., 2018, 2020a,b; Ali et al., 2018). We find that seldom in the literature have connectivity simulations been coupled with soil loss prediction, yet that connectivity processes control sediment transport and yield (Bracken et al., 2015; Wohl et al., 2018; Mahoney et al., 2018; Mahoney et al., 2019; Ali et al., 2018).

In this study, we couple RUSLE with connectivity while seeking to advance methods to quantify the tenets of structural and functional connectivity that considers the magnitude of connections. It is now recognized that connectivity simulations should consider connectivity's magnitude, extent, timing, and continuity (Bracken et al., 2015; Grant et al., 2017; Ali et al., 2018; Wohl et al., 2019). The model recently updated by Mahoney et al. (2020a,b) serves this goal. We consider event variability of structural and functional watershed properties using the Probability of Connectivity $P(C)$ model from Mahoney et al., (2018, 2020a,b) and suggest that representing the magnitude of connectivity by coupling $P(C)$ with RUSLE serves as one approach to quantify connectivity's magnitude that is comparable across catchments.

Another motivation of this work is to better understand structural and functional processes that control sediment connectivity and transport in steep, forested catchments and on reclaimed mines, such as those found throughout the Appalachian Coal Belt region, USA (Taylor et al., 2008). Steep, forested catchments in the Appalachian region are well-known for soils with very high infiltration rates and limited runoff production (Hewlett and Hibbert, 1965; Khan and Ormsbee, 1989; Taylor et al., 2009; Fox and Martin, 2015), which is generally attributed to soil texture and macropore formations. Soil macropores efficiently transport subsurface interflow to stream networks (Gupta et al., 2016) and are formed from freeze-thaw processes, dissolution of limestone, and activity and decomposition of flora and fauna (Sloan et al., 1983; Guebert and Gardner, 2001; Warner et al., 2010). The Appalachian Coal Belt's namesake originates from the presence of coal seams located frequently throughout the mountainous region. Surface coal mining is one method commonly used to extract coal in the region and involves removing vegetation, timber, and topsoil from surfaces (Bonta, 2000) to access underlying coal seams which are subsequently excavated (Shrestha and Lal, 2006). During reclamation, land surfaces are regraded with mine spoils, crushed rock, and coal fragments (Wickham et al., 2007) and heavily compacted and reseeded to prevent mass wasting and landslides (Taylor et al.,

2009; Warner et al., 2010). Generally, regraded hillslopes remain relatively steep post-reclamation, but are slightly flatter than the surrounding forest hillslopes (Fox and Martin, 2015). Marked difference in hydrology have been observed in reclaimed mine hillslopes compared to forested hillslopes in the region. Namely, compacted surfaces have much lower infiltration rates compared to forested hillslopes resulting in greater runoff production (Warner et al., 2010). We find that structural and functional controls on sediment connectivity in steep, forested hillslopes and reclaimed mine lands in the Appalachian Coal Belt region are understudied. The use of coupled models, such as the probability of connectivity and RUSLE, serves as one approach to better understand controls of sediment processes in these remote regions.

The objectives of this paper were to: (1) couple and evaluate the probability of connectivity model and RUSLE to advance spatially explicit watershed sediment modeling and (2) advance understanding structural and functional variables that control connectivity and sediment yield in steep, forested watersheds and reclaimed mine land. We apply the model to a steep, forested watershed in Eastern Kentucky, USA with reclaimed mine land to fulfill these objectives.

5.2 STUDY SITE AND MATERIALS

The study site is the Whitaker Branch watershed (2.63 km^2) located in Letcher County, Kentucky (see Fig. 1). Land use in the watershed is primarily second growth deciduous forest (2.47 km^2) and pastureland (0.16 km^2) which coincides with reclaimed surface mining. Average slope of the reclaimed mine is 0.44 m m^{-1} and average slope of the forest land is 0.51 m m^{-1}. The deciduous forest consists primarily of maple beech, yellow polar, oak, hickory, buckeye, and basswood. Soils in the watershed are primarily silt-loams with high infiltration capacity (Fox, 2009). In the late 19th century timber within the watershed was harvested and subsequently farmed, where contours were implemented for resource conservation purposes. The watershed was subsequently reforested and remained relatively undisturbed for approximately one hundred years, although some farming and residence existed in the lower part of the basin. Whitaker Branch watershed is located in the Appalachian Coal Belt and was subjected to surface mining between 1982

to 1988 and between 1998 to 2004 (Fox, 2009; Fox and Martin, 2015). Reclamation of the surface mining site began in 2004 and was completed according to regulations specified from the Surface Mine Reclamation Act (SMCRA). Notably, surfaces were regraded with mine spoils, crushed rock, and residual coal and were heavily compacted to prevent mass wasting (Fox, 2009). Limited regrowth from native trees has been observed as consequence from compaction procedures and due to reseeding with grasses (Fox, 2009; Fox and Martin, 2015).

Watershed morphology is considered to be steep and very steep, with long, narrow ridgetops, and narrow valleys, with some variability due to the reclaimed mine. Average slope in the forested land is 0.51 m m^{-1} and average slope on the reclaimed mine is 0. 44 m m^{-1}. Features that promote sediment connectivity include concentrated flow pathways, roads, and surfaces throughout the reclaimed mine (Bonta, 2000; Fox and Martin, 2015). Disconnecting morphology includes soil macropores that limit overland runoff production, and historic terracing, which dissects hillslopes (Fox and Martin, 2015).

Climate in Letcher County, Kentucky is temperate-humid with on average 102 cm of rainfall per year and average temperature of 1.7°C during winter and 22.8°C in summer. During the study period (2007), 12 storm events with rainfall that contributed to soil loss were identified. High infiltration rates on the order of 120 mm hr^{-1} are common in steep, forested catchments throughout the Appalachian Coal Belt (Harden and Scruggs, 2003). High infiltration rates are due to soil texture and the formation of macropores from flora and fauna, freeze-thaw cycling, and dissolution of limestone in the area (Sloan et al., 1983; Taylor et al., 2009; 1971; Guebert and Gardner et al., 2001; Warner et al., 2010; Fox and Martin, 2015), which form preferential flow paths that increase interflow during events. Observations throughout watersheds in the Appalachian Coal Belt region indicate that little overland flow is typically generated during storm events due to interception from the forest canopy and high infiltration rates due to the soil texture and macropore pathways (Taylor et al., 2009; Hewlett and Hibbert, 1965; Khan and Ormsbee, 1989; Sloan et al., 1983).

Hydrology in reclaimed surface mines varies from hydrology of the steep forested land uses. Reclamation of surface mines impacts infiltration rates of rainfall due to earthwork and compaction, and results in notable runoff production (Shulka et al., 2004; Guebert and Gardner et al., 2001; Warner et al,. 2010). Researchers have observed

decreases in infiltration from 120 mm hr^{-1} to 10-20 mm hr^{-1} from pre-mining conditions to post-reclamation (Warner et al., 2010; Taylor et al., 2008). Interception of rainfall is also impacted because compacted reclaimed soils limit water and carbon transport important for tree growth (Angel et al., 2005), thus the reclaimed mine land is typically populated by short-rooted grasses (Acton et al., 2011). A conceptual model highlighting differences in hydrology on steep, forested hillslopes and reclaimed mine hillslopes is shown by Fig. 2.

We used a number of materials to conduct probability of connectivity and RUSLE modeling including geospatial data, sediment field measurements, sediment fingerprinting results, previous sediment and hydrologic modeling, and field reconnaissance (see Table 1). Highly-resolved geospatial data used include 1.5 x 1.5 m digital elevation models, land use and land cover data, and soil data. All geospatial data are freely available across the Commonwealth of Kentucky. Precipitation data collected at the nearby USGS gage in Whitesburg, KY were used as an input to both the hydrologic model and the RUSLE model. Delineation of the reclaimed mine was completed using remote sensing, field reconnaissance, and spatial mapping of statewide mined out areas. We carried out hydrologic modeling using the Soil and Water Assessment Tool (SWAT) *via* ArcSWAT 2012.10.21 to predict event runoff generation and daily soil moisture content. Since the basin is ungauged, we verified hydrologic modeling by comparing annual water budget results generated from the modeling with results from similar catchments in the Appalachian Coal Belt, which improves our confidence in yearly sediment yield results. We applied the probability of connectivity, $P(C)$, model developed by Mahoney et al., (2018, 2020a,b) to the Whitaker Branch watershed to determine the spatial extent of sediment connectivity during events. Connectivity modeling was carried out using ArcGIS 10.4.1 on a desktop PC (Intel® Core™ i7-6700 CPU at 3.40 GHz; 64-bit operating system, x64-based processor). RUSLE modeling and subsequent uncertainty analyses were performed in ArcGIS 10.4.1 and in Microsoft Excel on a desktop PC (Windows 10, Dell OptiPlex 9010, Intel i7-3770 3.40 GHz, 4 Cores). We utilize total suspended solids (TSS) samples and sediment fingerprinting results presented in Fox and Martin (2015) to determine soil loss rates on forest and reclaimed mine land uses in the watershed, which we use to evaluate the model. Sediment fingerprinting was conducted using stable carbon

and nitrogen isotope tracers to identify contribution of sediment sources (Fox and Martin, 2015).

5.3 METHODS

5.3.1 Connectivity Model Application

Simulation of sediment flux required multiplication of connectivity formulae and erosion generation functions simulated using RUSLE. Connectivity is formulated using probability theory to reflect the stochastic nature of sediment transport and heterogeneity of hydrologic variables at the watershed scale (Wright and Webster, 1991; Papanicolaou et al., 2003; Borselli et al., 2008; Mahoney et al., 2018). Formulation of connectivity equations is presented in Mahoney et al., (2020a,b) to reflect tenets of connectivity theory including connectivity's magnitude, extent, and timing (Bracken et al., 2015; Grant et al., 2017; Ali et al., 2018; Wohl et al., 2019) as

$$\dot{m} = E[P(C) \cap P(\tau) \cap P(\gamma)] \quad (1)$$

where E is the event erosion rate, $P(C)$ is the probability of sediment connectivity representing the spatial extent of connectivity, $P(\tau)$ is the probability of sediment timing representing the variability of connectivity and active erosion periods during an event, and $P(\gamma)$ is the probability of sediment (dis)continuity representing the continuity of sediment connectivity along the pathway.

During this analysis, we focus on estimating connectivity over the entire duration of storm events rather than inter-event variability, thus $P(\tau)$ becomes unity (see Mahoney et al., 2020a,b). Additionally, we find that very little instream deposition of fine fluvial sediment occurs due to the steep stream gradient (Fox, 2009; Fox and Martin, 2015), thus $P(\gamma)$ becomes unity. Thus, Eq. (1) is representative of sediment transport over an entire event and is simplified as:

$$Y = E[P(C)] \quad (2)$$

where Y is sediment yield. Eq. (2) is discretized across the watershed to represent spatially distributed connectivity and flux in fundamental spatial units (e.g., geospatial cells) where erosion and transport processes occur during an event as:

$$\dot{m}_{ij} = E_{ij}[P(C)]_{ij} \quad (3)$$

where *j* is the spatial unit and *i* is the event. We utilize 1.5 x 1.5 m DEM cells to represent fundamental spatial units because such resolution has been found to adequately capture morphologic features that sediment flux (Lopez-Vincent and Alvarez, 2018; Cantreul et al., 2017; Mahoney et al., 2018). Eq. (3) is integrated across the watershed surface to determine sediment yield for the event.

5.3.2 Applying probability of sediment connectivity, P(C) to Forest Land and Reclaimed Mine

The probability of sediment connectivity $P(C)$ is defined as the probability that a landscape unit can detach and transport sediment laterally to the fluvial network (Borselli et al., 2008; Mahoney et al., 2018). $P(C)$ reflects the co-occurrence, or intersection, of several structural and functional (Wohl et al., 2019) sub-processes requisite of transport including sediment supply, sediment detachment, and sediment transport, as formulated by Mahoney et al., (2018). $P(C)$ is formulated as

$$P(C) = P(S) \cap P(G) \cap P(T) \cap \{1 - P(B)\} \quad (4)$$

where $P(S)$ is the probability of sediment supply, $P(G)$ is the probability of sediment generation, $P(T)$ is the probability sediment transport, and $P(B)$ is the probability of a buffer that impedes lateral sediment transport (e.g., Fryirs, 2013). Eq. (4) considers intersecting probabilities because each sub-process must occur coincidentally or sequentially for sediment originating in a spatial unit to reach the stream network (Leopold et al., 1964).

When considering that sediment generation and transport can occur *via* both hydrologic and non-hydrologic (e.g., mass wasting) processes, Eq. (4) is expanded as

$$P(C) = P(S) \cap P(D_H \cup D_{NH}) \cap P(T_H \cup T_{NH}) \cap \{1 - P(B)\} \quad (5)$$

where D_H and D_{NH} represent hydrologic and non-hydrologic detachment, respectively, and T_H and T_{NH} represent hydrologic, and non-hydrologic transport, respectively. Eq. (5) is expanded mathematically as

$$P(C) = P(S) \cdot \{P(D_H) + P(D_{NH}) - P(D_H)P(D_{NH})\} \cdot \{P(T_H) + P(T_{NH}) - P(T_H)P(T_{NH})\} \cdot \{1 - P(B)\} \quad (6)$$

We discretize Eq. (6) for all spatial units across the watershed surface during an event and integrate results to determine the percentage of the watershed that actively contributes sediment.

Fig. 3 shows the probability of connectivity simulation structure adapted from Mahoney et al., (2018) and inputs used to parameterize sub-processes. We implement a Boolean approach in conjunction with Mahoney et al. (2018) to parameterize each geospatial cell across the Whitaker Branch watershed, where a value of 1 represents that a geospatial cell is connected with respect to the sub-process, and a value of 0 represents that a geospatial cell is disconnected with respect to the sub-process. Hydrologic variables used to predict $P(D_H)$ and $P(T_H)$ for the 12 events analyzed during the study period were estimated using ArcSWAT 2012.10.21 (see Table 2). Herein we do not explicitly consider non-hydrologic detachment or transport processes based on previous studies in the watershed (Fox, 2009; Fox and Martin, 2015). Additionally, we do not explicitly parameterize buffers $P(B)$ in the watershed because we did not observe the presence of morphologic features known to prohibit sediment transport and connectivity during field reconnaissance and geospatial analysis (Fox, 2009; Fox and Martin, 2015). Equations used to parameterize sub-processes shown in Eq. (6) are found in Mahoney et al., (2018) and in Appendix A. Connectivity parameter ranges are recorded in Table 3. Structural connectivity, which represents physical properties of watersheds with little variability from event to event (slope, soil texture) are represented with the probability of sediment supply $P(S)$ and probability of downstream hydrologic transport $P(T_{H-Dwn})$ (Mahoney et al., 2018; Wohl et al., 2018). We represent functional connectivity, representative of variable connectivity processes due to, for example, runoff generation and soil moisture content using the probability of detachment $P(D_H)$ and the probability of upstream hydrologic transport $P(T_{H-Up})$ respectively (see Mahoney et al., 2018; Wohl et al., 2018).

5.3.2 RUSLE application to forested land and reclaimed mine

We apply the RUSLE model to represent erosion rates in geospatial cells to simulate sediment flux in Eq. (3). We assume that surface erosion occurs primarily *via* rill and sheet erosion in both the steep, forested hillslopes and the reclaimed mine sites,

justifying our use of RUSLE to simulate erosion rates (Renard et al., 1997; Fox and Martin, 2015). The RUSLE model simulates soil loss on hillslopes at an event-bases (Renard et al., 1997) as

$$A = EI \cdot K \cdot LS \cdot C \cdot P, \quad (7)$$

where A represents hillslope soil-loss (tonne ha^{-1}), EI is the storm erosivity factor (MJ · mm [ha · hr]$^{-1}$), K is the soil erodibility coefficient (tonne · ha · hr [ha · MJ · mm]$^{-1}$), LS is the slope length and steepness factor (m m^{-1}), C is the cover-management factor (unitless), and P is the supporting practice factor (unitless). We discretize Eq. (7) for geospatial cells to estimate annual soil loss throughout the Whitaker Branch watershed from both steep, forested hillslopes as well as slopes on the reclaimed mine. We modify Eq. (7) to account for connectivity by multiplying cells by $P(C)$ results, which represents the complete parameterization of Eq. (1). Additionally, we make the following assumptions: (1) the EI factor is uniform spatially across the watershed during an event; (2) the K, LS, C, and P factors remain constant temporally throughout the study period; (3) C factors vary between forest and reclaimed mine land uses; and (4) disconnected cells (i.e., $P(C) = 0$) do not yield sediment ($A = 0$). Eq. (7) is thus rewritten as

$$A_{ij} = EI_i \cdot K_j \cdot LS_j \cdot C_j \cdot P_j \cdot P(C)_{ij}. \quad (8)$$

Average annual soil loss (tonne ha^{-1}) for steep, forested and reclaimed mine land uses is thus determined as

$$A_{forest} = \sum_{i=1}^{m} \frac{\sum_{j=1}^{n} A_{ij}}{n},\ j \in [\text{steep, forest land}] \quad (9)$$

$$A_{mine} = \sum_{i=1}^{m} \frac{\sum_{j=1}^{k} A_{ij}}{k},\ j \in [\text{reclaimed mine}] \quad (10)$$

where A_{forest} is the average annual soil loss (tonne ha^{-1}) across the entire steep, forested land use, i is an index representing the storm event, m is the total number of storm events during the study year, j is an index representing the geospatial cell, n is the total number of geospatial cells belonging to the forested land use, A_{mine} is the average annual soil loss (tonne ha^{-1}) across the entire reclaimed mine land use, and k is the total number of geospatial cells belonging to the reclaimed mine land use.

Since Eqs. (9) and (10) are divided by n and k, the total number of geospatial cells that belong to the land use, A_{forest} and A_{mine} represent soil loss rates from the entirety of

each land use. Since sediment connectivity occurs on only a fraction of cells belonging to the varying land uses, we modify Eqs. (9) and (10) to represent normalized soil loss for only connected areas as

$$AC_{forest} = \sum_{i=1}^{m} \frac{\sum_{j=1}^{n} A_{ij}}{\alpha_i},\ j \in [\text{steep, forest land}] \quad (11)$$

$$AC_{mine} = \sum_{i=1}^{m} \frac{\sum_{j=1}^{k} A_{ij}}{\beta_i},\ j \in [\text{reclaimed mine}] \quad (12)$$

where AC_{forest} represents annual soil loss (tonne ha^{-1}) for connected forested land use, α_i is the total number of steep, forested geospatial cells connected during an event, AC_{mine} is the annual soil loss (tonne ha^{-1}) for the reclaimed mine land use, and β_i is the total number of reclaimed mine geospatial cells connected during an event. We emphasize that $\alpha_i \leq n$ and $\beta_i \leq k$.

We parameterize RUSLE as follows: To parameterize the storm erositvity (*EI*) parameter, we focus only on rainfall events that produce more than 1.3 cm of rainfall and storms that produce at least 0.6 cm of rain in 15-minutes in accordance with Renard et al. (1997; p. 23). We utilize hourly rainfall data measured at the USGS gage in Whitesburg, Kentucky for 2007 to determine storms appropriate for analysis. 12 events during the study year were identified to produce sediment based on these requisites during 2007 (Renard et al., 1997). We determine *EI* (MJ · mm [ha · hr]$^{-1}$) values in accordance with Renard et al., (1997) as

$$EI = \sum_{r=1}^{p} 1099 \cdot \left[1 - 0.72 \cdot \exp\left(-1.27 \cdot \frac{\Delta V_r}{\Delta t_r}\right)\right] \cdot I_{30} \cdot 0.1702 \quad (13)$$

where r is a temporal index representing increments of a storm event, p is the total increments in the storm event, ΔV is the depth of rainfall during the increment r (in), Δt is the duration of the increment (hr), and I_{30} is the 30-min rainfall intensity. We record *EI* values in Table 2.

We parameterize the soil erosivity (*K*) factor using USDA soils maps for the Whitaker Branch watershed and reported *K* values for each soil type (see Fig. 1 and Table 3). We parameterize the slope length and steepness (*LS*) factor by: (1) delineating slope lengths from the watershed boundary to the nearest downstream concentrated flow pathway, (2) defining slope along the slope length using the *Slope* tool in ArcGis 10.4.1, and (3) interpolating *LS* values reported in Table 4-1 from Renard et al., (1997). We

parameterize the support practice (P) factor as being equal to 1.0. We justify this given that slopes are relatively steep in both forested hillslopes and reclaimed mine hillslopes (Renard et al., 1997). Additionally, we argue that this avoids overparameterization of the model given that disconnectivity due to terracing is already accounted for in $P(C)$ results (see Section 4.1). We treat the cover-management (C) factor as a calibration parameter in order to more accurately understand impacts of the reclaimed mine on soil loss, as discussed in Section 3.4. We justify using temporally-constant values for *K, LS, C*, and *P* given previous study in the watershed (Fox, 2009; Fox and Martin, 2015). RUSLE factor ranges are reported in Table 3.

5.3.4 Model Calibration and Evaluation

Data used to calibrate the coupled probability of connectivity and RUSLE models includes geospatial analysis and field reconnaissance of sediment transport pathways, sediment fingerprinting analyses, and sediment concentration samples. Field reconnaissance of sediment transport pathways was conducted by Fox (2009) and geospatial analyses were conducted using DEMs (KYAPED, 2014) and orthophotographs. Samples to conduct sediment fingerprinting were collected from forest and reclaimed mine sources as described in Campbell et al. (2009), and instream samples were collected five times during 2007 as described in Fox (2009). TSS samples collected were collected using a Teledyne ISCO automated pump sampler as reported in Fox (2009) and Fox and Martin (2015). Observed soil loss estimates from forest and reclaimed mine land uses in 2007 were derived from TSS samples and fingerprinting results.

We completed evaluation of the model in two stages (see Fig. 4). In stage one, we calibrated results from the probability of connectivity model by qualitatively comparing spatially distributed connectivity results with sediment pathways identified *via* field reconnaissance and remote sensing. If simulated sediment transport pathways were considered unacceptable, we adjusted connectivity parameters until the realization qualitatively matched known transport pathways. Connectivity parameters calibrated in this stage included: (1) b, the connectivity runoff turbulence exponent, (2) c the rill/gully threshold coefficient, and (3) τ_{cr} the critical shear stress of erodible surfaces. We used literature values to define ranges of parameter values (Torri and Poesen, 2014; McCool et

al., 1993; Hanson and Simon, 2001). Since calibration is completed qualitatively, we defined wide parameter ranges to account for potential uncertainty (see Table 3). We justify the use of large parameter ranges given the difficulty of calibrating and validating spatially explicit sediment transport processes.

In stage two, we calibrated results from the combined connectivity and RULSE modeling by comparing simulated sediment yield to observed sediment yield for the forested land use and reclaimed mine (Fox, 2009; Fox and Martin, 2015). If simulated sediment yield was not within ± 35% of observed sediment yield, we adjusted *C* factor for the forested and/or reclaimed mine land use until sediment yield results were acceptable. 35% uncertainty bounds surrounding modeling results considers error due to sediment fingerprinting (approx. 15%, Fox and Martin, 2015) and error due to sediment concentration measurements. Based on previous work, we estimate 20% error from sediment concentration measurements after empirical observations of the variability of ISCO sediment concentration samples.

We quantified model uncertainty by permuting realizations of parameter ranges and running the probability of connectivity and RUSLE model. We created over 300 permutations of the connectivity and RUSLE model to simulate sediment yield. We justify using a low number of model realizations due to logistical reasons related to model computing requirements and file size. We iteratively chose parameter ranges to reduce limitations related to the number of realizations (see Table 3). Realizations with simulated sediment yield within ± 35% of the observed sediment yield were included in the solution space. We qualitatively validated RUSLE modeling by comparing spatially-explicit *R*, *LS*, *K*, and calibrated *C* parameters with separate RUSLE modeling that considered lumped *R*, *LS*, *K*, and calibrated *C* parameters. All lumped parameters were on the same order of magnitude as the zonal average of the spatially explicit analysis.

5.4 RESULTS AND DISCUSSION

5.4.1 Evaluation of coupled connectivity and RUSLE modelling: a need for iterative validation

We found that coupling the probability of connectivity model with RUSLE simulated both observed sediment yield and sediment fingerprinting results well. Optimal parameter values determined during model calibration are recorded in Table 4, and simulated and observed sediment yield results are recorded in Table 5. Uncertainty results suggest that variable ranges of connectivity parameters adequately simulate sediment transport whereas the range for acceptable *C* factor values is much smaller. This perhaps points to the need of future quantification of equifinality in connectivity simulations and exploration of methods to reduce equifinality in spatially-explicit sediment connectivity simulations. We generally find that optimal parameters make physical sense, however some parameter values warrant further discussion, which is the focus below.

Calibrated cropping and management (*C*) factor values are on the low end of proposed range, but still within the range suggested in research literature (see Table 3), for both the forest and reclaimed mine land surfaces. Low *C* factors have physical significance in the forested and reclaimed mine land use and likely reflect the presence of morphologic features that buffer sediment transport. In the forested land, subsurface macropore pathways increase rainfall infiltration rates and reduce the depth of runoff produced during storm events (Sloan et al., 1983), which is then manifested as the low *C* factors. Additionally, microtopography resulting from dense forest root mats and shielding from leaf detritus further reduce sediment transport and hence forest *C* factor values. Calibrated *C* factor values were an order of magnitude greater for the reclaimed mine site as compared to the forest, which is to be expected considering the increase in event runoff generation due to the high bulk density and low infiltration capacity of the soils on the reclaimed mine relative to the neighboring forests (Acton et al., 2011). The fact that the *C* factor was on the low end of suggested ranges for grassland reclaimed coal mine lands is reasonable because the land surface was classified as 'phase 3' of reclamation where final reclamation has been achieved (Fox, 2009). Erosion results in this region have shown erosion rates to reduce drastically once the land surface has entered phase 3 reclamation (Curtis, 1978; Bonta, 2000).

We parameterized the optimal RUSLE practice (*P*) factor as being equal to one, which indicates that no anthropogenic practices, such as associated with terracing, exist in the watershed to reduce soil loss (Renard et al., 1997). As will be shown in our connectivity

results, we found that legacy-associated terracing occurred across the forest landscape of this system. Anthropogenic terracing existed from farming the mountains in the 19th century and early 20th century. This farming and terracing was common in this Appalachian forest region despite the steep slopes, and corn was grown for animal feeding, human consumption and illegally producing alcohol regionally known as 'moonshine' (Kalisz, 1986; Stewart, 2003). The legacy terracing typically would warrant parameterization of a P factor less than one. However, our probability of connectivity model results causes these terraced areas to become disconnected. Therefore, the land surface area of the disconnected regions are not included in the calculation of mass flux because mass flux is the product of generation via RUSLE soil loss estimates and the probability of connectivity (see Equation 1). A P factor of less than one would over-account for terracing and erroneously reduce the estimated sediment mass flux estimate. For this reason, iterative calibration between RUSLE and connectivity modelling was important to account for unforeseen dependency between variables in Equation (1). We set the P factor as equal to unity to avoid the dependency in this instance.

Our results suggest coupled connectivity-erosion rate modelling incorporate iterative, dual-calibration strategies where calibration of one model should feed-back or loop into calibration of the second model. Our results present evidence of the utility of such approach in two instances. First, as previously mentioned, we found that calibration of the P factor in RUSLE was unnecessary upon multiplication of the RUSLE results with $P(C)$. In this regard, care should be taken by the researcher because parameterization of the $P(C)$ model may sometimes alter RUSLE parameterization and calibration to avoid unforeseen dependency between the formula. Second, we noticed that upon completing RUSLE modeling that some landscape units in the forest were predicted to produce little to no sediment although they were predicted to be connected according to $P(C)$. The lack of generation as predicted with RUSLE indicates the magnitude of connectivity is in fact weak on some landscape units such that sediment contribution from these areas is negligible and can be classified as disconnected following the criteria/definition of Heckmann et al., (2018); Wohl et al. (2018) and Ali et al. (2018). We present results from determining event $P(C)$ with and without considering feedbacks between the models,

referred to as initial calibration and final calibration in Table 6. Notably, considering the feedback between the models and iterative calibration caused a reduction in overall connectivity for all events. The result ranges from 0.1% to 13.8% reduction in connectivity, which is relatively high considering final connectivity ranges from 2.9% to 22.4%. This result and need for feedbacks between sediment generation and connectivity estimates is corroborated by recent sentiment in the literature and highlights the importance of considering not only the Boolean connectivity processes (e.g., Fryirs, 2013), but also the magnitude or continuity of connectivity (Grant et al., 2018; Wohl et al., 2018).

The iterative, dual-calibration carried out for the probability of connectivity and RUSLE in our study highlights both advantages of coupling connectivity with erosion modelling and also points out unforeseen problems that could arise unless the researcher uses caution. The advantages in calibration are by iterating models and inspecting results qualitatively as well as assessing quantitative metrics, the researchers is able to arrive at a better understanding of landscape processes and gain confidence in prediction. This sentiment corroborates well with the recent connectivity literature where a number of reviews discuss the importance of coupling connectivity simulations with erosion formula yet at the same time highlight that few such studies are available and this topic is still emerging (e.g., Ali et al., 2018; Heckmann et al., 2018; Wohl et al., 2019). Recent studies by our group have shown the validity and advantages of coupling the probability of connectivity within watershed modelling (Mahoney et al., 2018; 2019; 2020a,b); Lopez-Vicente et al. (2015) coupled the Index of Connectivity erosion estimates to assess soil redistribution at the plot scale; and other existing methods such as the hillslope sediment delivery ratio show promise for quantifying watershed sediment flux using connectivity theory with erosion estimates (Vigiak et al., 2012; Jamshidi et al., 2014; Hamel et al., 2015).

However, the model evaluation results of this study point out the researcher should use caution when coupling connectivity and erosion formula because parameters of the two model types are not necessarily independent. In the present study, the process of terracing impacts both erosion formula in the empirical RUSLE model and net connectivity estimates for predicting the erodible surface area of the basin. We may have under-predicted watershed erosion, however, careful, iterative calibration allowed us to account

for dependence of the models on one another. As permeations of coupling connectivity models with erosion models take hold in future years, researchers should at the same time develop new evaluation procedures with qualitative and quantitative checks-and-balances to correct for unforeseen problems from model dependency.

5.4.2 Event P(C) results: connectivity and disconnectivity in Appalachian forests and minelands

Results highlight behavior of event-based connectivity in the Whitaker Branch watershed. $P(C)$ results vary between 3.0% connected (event 8) and 36.2% connected (event 5) at the watershed scale (see Table 5). This implies that 3.0% of the catchment and 36.2% of the catchment actively contribute sediment to the stream network during respective events (Ambroise, 2004; Mahoney et al., 2018). $P(C)$ varied greatly between land uses throughout the 12 events. Namely, $P(C)$ ranged from 34.4% to 57.1% in the reclaimed mine (μ = 46.8%, σ = 8.1%) and 1.0% to 34.9% in the forested land (μ = 12.1%, σ = 9.8%). We attribute the high percentages of connectivity in the reclaimed mine to increased runoff production and hence energy available to transport sediment caused by compaction of soils during reclamation processes.

Predicting the most connected pathways across the landscape was a notable result of this study, and our spatially explicit $P(C)$ results highlight morphologic pathways most sensitive to hydrologic activity in the Whitaker Branch watershed (Figs 5 and 6). Specifically, our results indicate that landscape units within the reclaimed mine are connected during hydrologic events of low magnitude, and remain connected during events of increased hydrologic magnitude (see Fig. 5a – 5d). Events shown in Fig. 5, Fig. 6, and Fig. 7 are approximately representative of minimum (event 8), 25% quartile (event 12), 75% quartile (event 1), and maximum (event 5) $P(C)$ results. Within the forest, we find that only areas with large upstream contributing area within close proximity to the stream network are connected during events with low hydrologic magnitude (see Fig. 5a and Table 2); and forest hillslopes only become connected during high magnitude events (Fig 5d). Low connectivity on forested hillslopes in low and moderate events is attributed to the high infiltration rates in forest soils due to soil texture and macropores (Khan and Ormsbee,

1987). In contrast, connectivity occurs on both flat and steep reclaimed mine surfaces with variable upstream contributing areas during events with low hydrologic activity (see Fig. 5a). The connectivity of reclaimed mines is attributed to runoff generation during low and moderate events because of the high bulk density measured for the compacted reclaimed mine sites (Acton et al., 2011). We classify the landscape units within the reclaimed mine as highly sensitive, active pathways for this watershed since they are connected in much greater proportions and more frequently than forested hillslopes. Morphologic features promoting connectivity can be seen visually for both land cover types using orthophotos, gradient models and our connectivity results (Fig 6). As shown, morphology causing connectivity in both the forest and reclaimed mine land include: (1) concentrated flow paths on steep surfaces in the forestland (Fig. 6a); (2) steep hillslopes between historic terracing (Fig. 6b); and (3) surfaces throughout the reclaimed mine (Fig. 6c).

Disconnectivity of the landscape was another important result of this study, and spatially explicit results also highlight morphologic buffers that disconnect sediments and impede sediment transport throughout the watershed (see Fig. 6a – 6c; Fryirs, 2013). We examine disconnectivity in Fig. 6 during the event with highest hydrologic activity (event 5), which highlights impedances due to structural watershed properties as opposed to impedances from functional hydrologic variability (e.g., runoff depth or soil moisture content). Fig. 6a indicates that even on the steepest surfaces, sediment connectivity seldom occurs in forested hillslopes. The prevalence of disconnectivity on these hillslopes is attributed to relatively high sand content of the soil texture and infiltration capacity of the soil. These soil drainage characteristics limit runoff generation and fluid energy to detach and transport sediment despite the steep hillslope gradient (i.e., average gradient = 0.51 m m^{-1}). Other morphologic features influencing disconnectivity on forested hillslopes include microtopography created from exposed tree roots and tree fall which promotes localized pockets of very flat slopes (e.g., 0-10 degrees), decreasing fluid transport capacity. Also, Fig. 6b highlights disconnectivity due to historic terracing found throughout the watershed. Locally flat swaths (see Fig 6b – slope) occur in contours throughout forested hillslopes and decrease overland fluid energy available to detach and transport sediment. We find that terraces particularly impacted the probability of downstream sediment transport ($P(T_{H-Down})$) and cause localized regions where

deposition is likely. Disconnected landscape across the reclaimed mine was found to occur near ridgelines and locally flat areas created during reclamation (seFig. 6c). Disconnectivity near ridgelines occurs because with very little upstream contributing area is available to accumulate water and produce shearing able to eroded sediment. Disconnectivity of flat contours occurs because spoil is placed in lifts during surface mine reclamation (e.g., Skousen and Zipper, 2014). Each lift is constructed with near constant gradient with a slope length on the order of 50 meters in this study, and the lifts are compacted in place. In between lifts, a near zero gradient berm of spoil is compacted across the contour and is between 5 to 10 meter wide. These berms cause disconnectivity across the mining landscape.

5.4.3 Functional and structural controls on $\mathbf{P(C)}$

Event variability of $P(C)$ sub-processes highlights structural and functional behavior that controls connectivity throughout the Whitaker Branch watershed. Sub-process connectivity probabilities for the Whitaker Branch watershed are shown in Fig. 7a.

We find that generally functional control associated with the probability of hydrologic detachment $P(D_H)$ controls overall probability of connectivity results in the forest and the Whitaker Branch watershed as a whole (see Fig. 7a). $P(D_H)$ limits $P(C)$ during all events at and below the 75% quartile (event 1, 8, 12), which indicates that detachment processes control sediment transport and connectivity across most surfaces in the Whitaker Branch watershed. Physically, this result is related to the very high infiltration rates in most soils in the Whitaker Branch watershed, which limits runoff production and hence sediment detachment. Only during the event with most extreme hydrologic activity (event 5) did $P(D_H)$ not limit overall connectivity, which is not representative of average connectivity conditions in the watershed. We notice similar trends in forest sub-process probabilities (see Fig. 7b), which is to be expected considering forest land covers 94% of the watershed.

Our results indicate notably different processes control the behavior of sediment connectivity in the reclaimed mine, and the structural control and to a lesser degree the functional control associated with the probability of hydrologic transport and detachment,

respectively, play a role in the minelands (Fig. 7c). In nearly all events, the structurally dependent probability of downstream hydrologic transport $P(T_{H-Dwn})$ is the limiting connectivity sub-process, indicating that structural watershed variables (e.g., slope, stream density) limit connectivity in the reclaimed mine as opposed to functional variability (e.g., soil moisture content, runoff generation). One reason that this occurs is because soil texture disturbance reduces infiltration rates such that storms frequently produce relatively large runoff volumes compared to the surrounding forest. This results in elevated energy to detach and transport sediment manifested within the model by increased probability of functional sub-processes ($P(D_H)$ and $P(T_{H-Up})$), thus reducing functional control over $P(C)$ results.

Our findings add to an existing discussion of structural and functional control of connectivity in other watersheds, and specifically our results relax the notion that functional (dynamic) processes control sediment connectivity in all landscapes (Bracken et al., 2015; Mahoney et al., 2018). Rather, based on our review and experiences, structural connectivity shows the dominant control on connectivity for steep basins and/or during high magnitude hydrologic events. Functional connectivity becomes more-and-more controlling on net connectivity during for lower gradient basins, well-drained landscapes and/or low and moderate hydrologic events. For example, application of both the probability of connectivity and index of connectivity methods showed the importance of the dominant structural control for high magnitude events in the comparison by Mahoney et al. (2020a). Results of this basin show the importance of structural control for the steep Whitaker Branch catchment and structural control showing differences between land cover types (see Fig. 8). Functional control associated with $P(T_{H-Up})$ seldom limits $P(C)$ in the Whitaker Branch watershed likely because: (i) soil moisture is relatively high in the catchment promoting low critical slope thresholds to initiate rill and gully erosion; and (ii) the steep slopes throughout the watershed easily overcome critical slope thresholds necessary to initiate rill or gully development. On the other hand, recent study has shown the importance of functional controls for lower gradient basins and lower magnitude events. Mahoney et al., (2018) found in the Upper South Elkhorn watershed (65.1 km^2), a gently rolling catchment (average slope 0.07 m m^{-1}) in central Kentucky, that sediment

connectivity is generally controlled by the functional probability of upstream transport, $P(T_{H-Up})$, which is a function of soil moisture content, slope, and upstream contributing area. Soils within the Upper South Elkhorn are primarily silt loams and produce large runoff volumes during events, thus promoting detachment of sediment. The relatively flat slopes of the Upper South Elkhorn lack energy required to overcome critical slopes requisite of rill and gully development, explaining the control of $P\left(T_{H-Up}\right)$ on connectivity in the Upper South Elkhorn.

5.4.4 Coupled P(C) and RUSLE model reveals connectivity and sediment loss rates

Our coupled $P(C)$ and RUSLE model indicates that sediment yield from the reclaimed mine is nearly two times the amount of sediment yield from the forest during the simulation period (see Table 5). This result is significant because the reclaimed mine makes up only 6.0% of the Whitaker Branch watershed. We find that soil loss rates (A) throughout the reclaimed mine are approximately 30 times greater than the forest land. We emphasize that this rate is normalized across the entire surface of the Whitaker Branch watershed (see Eq. (9) and (10)) as opposed to surfaces where erosion actually occurs (see Eq. (11) and (12)). When only considering soil loss on connected surfaces (AC), soil loss rates increase by nearly an order of magnitude in the forest land use and by a factor of two in the reclaimed mine (see Table 5). Increased simulated soil loss rates result from connected surfaces occurring, on average, on 12.1% of the forest land use and 46.8% of the reclaimed mine. We emphasize this result because AC soil loss rates are likely more realistic of soil loss occurring in the Whitaker Branch watershed. From a management standpoint, this result highlights pathways that should be targeted for remediation within the watershed. Mahoney et al., (2018) found that approximately 90% of sediment is transported in during events with greater than 3% connectivity, which gives us confidence that this analysis captures the majority of important sediment transport events during 2007.

Spatially explicit $P(C)$ and RUSLE modeling extends our view of sediment transport in the Whitaker Branch watershed and highlights connected pathways that produce the most sediment in the watershed (see. Fig. 9). In the four events presented in Fig. 9, soil loss rates within the reclaimed mine are greater than rates in the forest. This

result highlights that the pathways most sensitive to connectivity are also pathways that contribute the greatest soil loss rates. Spatially explicit results of the coupled $P(C)$ and RUSLE model also highlight areas that are predicted to be connected but ultimately produce little sediment (see for example Fig.5d and Fig. 9d). In particular, we find that forested regions of the watershed north of Whitaker Branch are predicted to be connected (Fig. 5d), yet produce zero or near zero soil loss, implying disconnectivity (Fig. 9d). We attribute this result to particularly rocky soils located throughout the forested hillslopes that increases effective critical shear stress of the soil and reduces potential for soil loss. This result highlights the importance of considering connectivity's magnitude in addition to the extent of connectivity during connectivity simulations (Fryirs, 2013; Bracken et al., 2015; Wohl et al., 2017).

Recent reclamation literature suggests that in addition to detrimentally impacting rainfall and runoff infiltration processes, excessive compaction of reclaimed soils reduces rates of native tree growth and promotes growth of short-rooted grasses (Acton et al., 2011). Our spatially explicit results highlight that connectivity occurs frequently and soil loss rates are greatest within the reclaimed mine. These results reflect findings from Fox (2009) and Fox and Martin (2015). Angel et al. (2005) has suggested that one strategy to improve soil stabilization and regrowth of native trees on reclaimed mines is to compact soils and leave approximately 1 meter of loose spoil on top of compacted surface. This method limits mass wasting and recreates soil conditions akin to forested land uses. Related to the results herein, we suggest that this method likely decreases sediment connectivity and soil loss in the reclaimed mine because reestablishment of native trees and recreation of surface microtopography increases interception and infiltration of precipitation and runoff.

We plotted event soil loss against probability of connectivity results (see Fig. 10) and noticed a positive linear trend for both the forest (R^2 = 0.95) and reclaimed mine (R^2 = 0.55), implying a strong relationship exists between connectivity and soil loss. Relationships between soil loss and connectivity in the forest and reclaimed mine show trends of self-similarity, which implies that in steep watersheds, probability of connectivity might be a predictor of normalized soil loss based on land use.

Our results that P(C) is a good predictor of sediment yield agrees with findings from Vigiak et al., (2012) who found that calibrated hillslope sediment delivery ratio (HSDR), a function of the Index of Connectivity (Borselli et al., 2008), was well correlated with specific sediment yield. Vigiak et al., (2012) linked HSDR and IC and found HSDR predicted specific sediment yield well.

However, it is noteworthy that this result contrasts findings from Mahoney et al., (2018) and Mahoney et al., (2020a,b) where probability of connectivity was poorly correlated with soil loss and sediment yield (R^2 = 0.26 and R^2 = 0.007, respectively). This is because connectivity simulations presented in Mahoney et al., (2018; 2020a,b) were conducted in the much flatter Upper South Elkhorn watershed. We find that sub-processes controlling connectivity vary in the Whitaker Branch and Upper South Elkhorn watershed. Specifically, in the Whitaker Branch watershed, the probability of hydrologic detachment, $P(D_H)$, a function of runoff depth and slope, controls $P(C)$ results. Variability of soil loss (A), as determined by RUSLE, is also largerly a function of event rainfall and runoff, which may explain the good relationship. The contrasts the Upper South Elkhorn where $P(C)$ is largely controlled by $P(T_{H-Up})$. This implies that such self-similarity is only realized in certain systems with very steep slopes where rill and gully development does not control sediment transport.

5.5 CONCLUSION

The conclusions of this study are as follows:

(1) We find that the coupled probability of connectivity and RUSLE model is able to simulate sediment transport from forested and reclaimed mine hillslopes well, so long as overlap between the models is accounted for. An ensemble of sediment concentration data, sediment fingerprinting results, and field reconnaissance from previous studies gives confidence to our calibration. Our model evaluation results are consistent with recent sentiment in the literature supporting the coupling of connectivity and erosion formula. However, our evaluation also point out unforeseen dependencies between connectivity formula and RUSLE that need to be accounted for when the models are coupled together. We suggest future modelling of connectivity and RUSLE together should consider

incorporating feedback calibration schemes, as was carried out in this study, to resolve potential overlap and discrepancies between connectivity modelling and RUSLE modelling.

(2) Results show, on average, 12% of the drainage area of Appalachian forests was connected and 47% of the drainage area of reclaimed minelands was connected for the hydrologic events studied. Sensitive connected pathways occur at concentrated flow paths on steep surfaces in the forest and more generally across the steep surfaces of the minelands. Disconnectivity occurs due to legacy terracing observed in the forest, the high sand content of the forest soils that increase water infiltration, and constructed berms between compacted spoil lifts on the reclaimed mine.

(3) Our results generally point to structural control as dominating net connectivity in this study, which is contrary to the notion that functional (dynamic) processes control sediment connectivity in all landscapes. Structural connectivity shows the dominant control on connectivity for steep basins and/or during high magnitude hydrologic events. Functional connectivity becomes more-and-more controlling on net connectivity during for lower gradient basins, well-drained landscapes and/or low and moderate hydrologic events.

(4) The soil loss rates of the reclaimed mine are approximately 30 times greater than the forest land despite the fact that the reclamation is classified as phase 3. Soil loss rates that consider spatially explicit connectivity are, on average, an order of magnitude higher in the forested land use and double in the reclaimed mine compared to analyses that assume lumped contributions from land uses. From a management perspective, spatially explicit results highlights pathways that should be targeted for remediation. Reforestation has been promoted in the region, and this study supports the idea that reforestation will likely decrease sediment connectivity and soil loss in the reclaimed mine because reestablishment of native trees and recreation of surface microtopography increases interception and infiltration of precipitation and runoff.

(5) Relationships between soil loss and connectivity in the forest and reclaimed mine show trends of self-similarity, which implies that in steep watersheds, probability of connectivity might be a predictor of normalized soil loss based on land use. This topic remains somewhat open because one recent study agrees with our findings but others

suggest the probability of connectivity can be poorly correlated with soil loss and sediment yield in some basins.

5.6 ACKNOWLEDGMENTS

We gratefully acknowledge the financial support of this research under National Science Foundation Award 163288. We thank LIF Creative (www.lif-creative.com) for illustration and graphic design assistance. We thank Chris Barton for sharing information regarding legacy farming and soil properties in the Appalachian region.

5.7 APPENDIX A: PROBABILITY OF CONNECTIVITY MODEL EQUATIONS

$$P(S)_{ij} = \begin{cases} 1, & \text{if sediment is present within the cell} \\ 0, & \text{if sediment is absent within the cell} \end{cases} \quad \text{(A.1)}$$

$$Q_{surface} = \frac{(R_i - I_a)^2}{R_i - I_a + S} \quad \text{(A.2)}$$

$$SW_t = SW_0 + \sum_{i=1}^{t}\left(R_i - Q_{surface} - E_a - w_{seep} - Q_{gw}\right) \quad \text{(A.3}$$

$$P(D_H)_{ij} = \begin{cases} 1, & \text{if } \tau_{f\,ij} - \tau_{cr\,j} > 0 \\ 0, & \text{if } \tau_{f\,ij} - \tau_{cr\,j} \le 0 \end{cases} \quad \text{(A.4)}$$

$$\tau_{f\,ij} = \gamma H_{ij} S_j \quad \text{(A.5)}$$

$$P(T_H)_{ij} = P\left(T_{H-up}\right)_{ij} P(T_{H-dwn})_{ij} \quad \text{(A.6)}$$

$$P\left(T_{H-up}\right)_{ij} = \begin{cases} 1, & \text{if } S_j - S_{cr\,ij} > 0 \\ 0, & \text{if } S_j - S_{cr\,ij} \le 0 \end{cases} \quad \text{(A.7)}$$

$$S_{cr\,ij} = a_j A_j^{-b} \quad \text{(A.8)}$$

$$S_{cr\,ij} = 0.73 c_i e^{1.3 RFC_i}\left(0.00124 S_{0.05\,ij} - 0.37\right) A_j^{-0.38} \quad \text{(A.9)}$$

$$S_{0.05} = 0.819\left(25.4\left[\frac{1000}{CN_{ij}} - 10\right]^{1.15}\right) \quad \text{(A.10)}$$

$$P(T_{H-dwn})_j = \begin{cases} 1, & \text{if } S_j - \frac{\sum S_{up}}{N} > 0 \\ 0, & \text{if } S_j - \frac{\sum S_{up}}{N} \le 0 \end{cases} \quad \text{(A.11)}$$

$$P(B)_j = \begin{cases} 1, & \text{if disconnectivity exists} \\ 0, & \text{if disconnectivity does not exist} \end{cases} \quad \text{(A.12)}$$

5.8 APPENDIX B: LIST OF SYMBOLS

$P(C)$	=	probability of sediment connectivity
$P(S)$	=	probability of sediment supply
$P(D_H)$	=	probability of hydrologic detachment
$P(D_{NH})$	=	probability of nonhydrologic detachment
$P(T_H)$	=	probability of hydrologic transport
$P(T_{NH})$	=	probability of nonhydrologic transport
$P(B)$	=	probability of buffers
SW_t	=	final soil water content
SW_0	=	initial soil water content
R_i	=	amount of precipitation
$Q_{surface}$	=	amount of surface runoff
E_a	=	amount of evapotranspiration
w_{seep}	=	amount of lateral flow
Q_{gw}	=	amount of return flow
S	=	retention parameter
I_a	=	initial abstraction
CN	=	curve number
τ_f	=	fluid shear stress
τ_{cr}	=	critical shear stress of the eroding surface
S	=	slope of geospatial cell
S_{cr}	=	critical slope required to initiate ephemeral gully incision of cell
a	=	local climate and land use and soil characteristics of geospatial cell
A	=	upstream drainage area of geospatial cell
b	=	connectivity runoff turbulence exponent
$S_{0.05}$	=	maximum potential loss to runoff
RFC	=	rock fragment cover of the soil
c	=	connectivity rill/gully threshold coefficient
N	=	number of upstream cells flowing in cell
$\sum S_{up}$	=	sum of the slopes of each cell upstream of cell
$P(T_{H-dwn})_j$	=	probability of downstream hydrologic transport
$P\left(T_{H-up}\right)_{ij}$	=	probability of hydrologic transport from upstream

Table 5.1. Data inputs and model requirements

Data Type	Source
1.5 m x 1.5 m DEM	KYAPED (2014)
Land Use/Land Cover Data	NLCD (2006)
Precipitation	NOAA (2007)
Soil Type	USDA (2016)
Runoff	Hydrologic Simulation (SWAT)
Daily Curve Number	Hydrologic Simulation (SWAT)
Event *EI*	NOAA (2020)
Soil *K*	USDA (2016)
Landscape *LS*	KYAPED (2014)
Total Suspended Solids Samples	Fox and Martin (2015)
δ^{13}C δ^{15}N Sediment Samples	Fox and Martin (2015)
Sediment Fingerprinting	Fox (2009); Fox and Martin (2015)
Soil Loss	Fox and Martin (2015)
Watershed Slope	Fox (2009)

Table 5.2. Event hydrologic parameters including precipitation, average simulated runoff and curve number across Whitaker Branch watershed, and *EI*, as calculated using Appendix B of Renard et al., (1997).

Event	Date Begin	Date End	Total Precip. (mm)	Avg. SWAT Runoff (mm)	Avg. SWAT Daily CN	EI (MJ·mm·[ha·h]$^{-1}$)
1	3/1/2007	3/1/2007	21.8	1.1	73.1	176.7
2	3/16/2007	3/16/2007	18.0	0.6	73.3	100.4
3	4/3/2007	4/4/2007	16.3	0.4	73.4	100.3
4	4/11/2007	4/11/2007	18.3	0.6	73.4	93.7
5	4/14/2007	4/15/2007	52.8	11.3	73.5	412.4
6	4/27/2007	4/27/2008	22.1	1.2	73.7	185.2
7	7/11/2007	7/11/2007	20.1	0.7	70.0	112.3
8	7/19/2007	7/19/2007	13.5	0.2	69.3	49.1
9	7/24/2007	7/24/2007	14.7	0.3	70.7	67.8
10	8/2/2007	8/2/2007	30.2	2.5	71.5	233.3
11	8/5/2007	8/5/2007	14.0	0.2	71.6	64.8
12	10/24/2007	10/24/2007	19.8	0.6	63.8	91.4

Table 5.3. Connectivity and RUSLE parameter ranges. b, c, τ_{cr}, C_{Mine}, and C_{Forest} are calibrated parameters. EI, LS, K, and P are inputs.

Parameter	Description	Range	Units	Source
b	Connectivity runoff turbulence exponent	0.1-0.5	Unitless	Torri and Poesen (2014)
c	Connectivity rill/gully threshold coefficient	0.1-1.0	Unitless	Torri and Poesen (2014)
τ_{cr}	Critical shear stress	0.5-20.0	Pascal	Renard et al., (1993); Hanson and Simon (2001)
EI	RUSLE storm erosivity parameter	Varies	$MJ \cdot mm \cdot [ha \cdot h]^{-1}$	Renard et al., (1997)
C_{Mine}	RUSLE cropping and management factor for reclaimed mines	0.001-0.1	Unitless	Wischmeier and Smith (1978); Dissmeyer and Foster (1980)
C_{Forest}	RUSLE cropping and management factor for forest land	0.0001-0.01	Unitless	Wischmeier and Smith (1978); Dissmeyer and Foster (1980)
LS	RUSLE slope length and steepness parameter	Varies	$m \cdot m^{-1}$	Renard et al., (1997)
K	RUSLE soil erosivity parameter	0.0-0.37	$tonne \cdot ha \cdot hr \cdot [ha \cdot MJ \cdot mm]^{-1}$	Renard et al., (1997)
P	RUSLE practice parameter	0.0-1.0	Unitless	Renard et al., (1997)

Table 5.4. Optimal parameter values for connectivity and RUSLE models

Parameter	Description	Value	Units
b	Connectivity runoff turbulence exponent	0.38	Unitless
c	Connectivity rill/gully threshold coefficient	0.5	Unitless
τ_{cr}	Critical shear stress (Average)	3.75	Pascal
C_{Mine}	RUSLE cropping and management factor for reclaimed mines	0.006	Unitless
C_{Forest}	RUSLE cropping and management factor for forest land	0.0006	Unitless

Table 5.5. Results of probability of connectivity, soil loss from connected surfaces (*AC*), soil loss rate (*A*) and sediment yield (*SY*) Observed sediment loss from forest and reclaimed mine land uses for 2007 are included.

Event		*P*(C)		*AC* (tonne ha^{-1})		*A* (tonne ha^{-1})		*SY* (tonne)	
		Forest	Mine	Forest	Mine	Forest	Mine	Forest	Mine
1		16.7%	52.60%	0.054	0.508	0.009	0.267	2.212	4.27
2		12.60%	49.60%	0.037	0.308	0.005	0.153	1.167	2.445
3		5.40%	37.90%	0.027	0.318	0.001	0.121	0.36	1.931
4		12.90%	50.30%	0.037	0.307	0.005	0.155	1.191	2.471
5		34.90%	57.10%	0.071	1.171	0.025	0.669	6.143	10.694
6		19.90%	52.70%	0.051	0.559	0.01	0.294	2.488	4.701
7		10.30%	50.50%	0.041	0.36	0.004	0.182	1.028	2.905
8		1.00%	34.40%	0.017	0.16	0	0.055	0.042	0.879
9		1.20%	35.40%	0.023	0.212	0	0.075	0.068	1.202
10		22.40%	54.80%	0.056	0.697	0.012	0.382	3.081	6.106
11		1.30%	35.10%	0.023	0.212	0	0.074	0.076	1.19
12		6.60%	50.50%	0.026	0.255	0.002	0.129	0.42	2.062
Sum	Avg.	12.10%	46.80%	0.462	5.068	0.074	2.557	18.28	40.86
Obs.						0.08	2.5		

Table 5.6. Probability of connectivity results using initial calibration and final calibration after considering the iterative feedback loop using RUSLE for the entire Whitaker Branch Watershed.

Event	P(C) – Initial calibration	P(C) – Final calibration
1	18.8%	13.7%
2	14.9%	12.3%
3	7.3%	5.5%
4	15.2%	12.5%
5	36.2%	22.4%
6	21.9%	14.0%
7	12.7%	10.2%
8	3.0%	2.9%
9	3.3%	3.2%
10	24.4%	13.9%
11	3.4%	3.3%
12	9.3%	7.5%

Figure 5.1. Whitaker Branch watershed (2.63 km^2) maps in Letcher County, Kentucky including: (a) slope; (b) soil type; (c) elevation; (d) land use and land cover including stream network, forest land (2.47 km^2) and reclaimed mine (0.16 km^2); and (e) location of Whitaker Branch in Kentucky, USA.

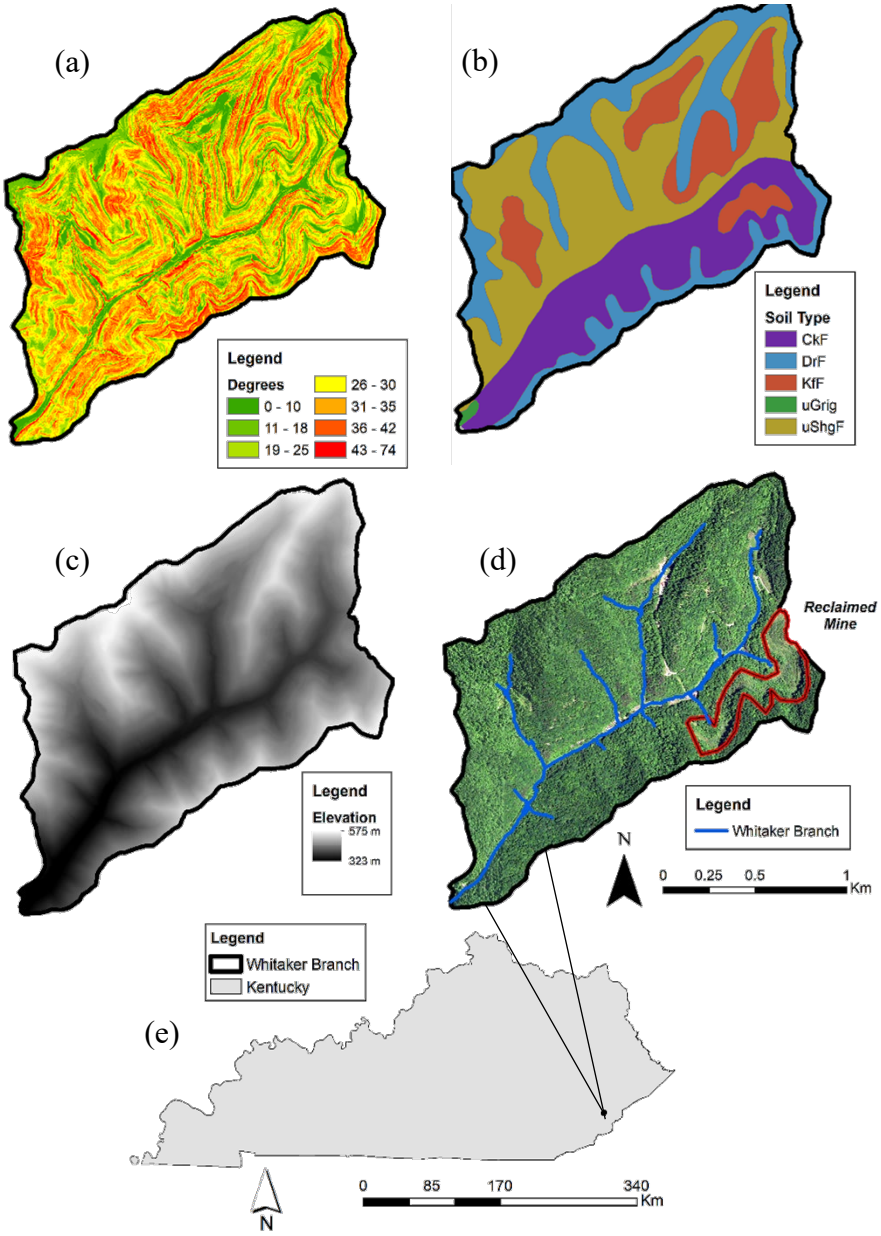

Figure 5.2. Conceptual models of sediment connectivity on (a) steep, forested hillslopes and (b) on reclaimed mine land that has been converted to grassland. The following processes are highlighted for steep, forested hillslopes: (1) dense tree canopy increases rainfall interception; (2) frequent presence of subsurface macropores increases infiltration rates and creates preferential flow pathways; (3) sparse concentrated flowpaths transport water and sediment rapidly to stream networks; and (4) attenuated slowflow pathways contribute to baseflow following events. The following processes are highlighted for reclaimed mine lands: (5) conversion to grassland decreases interception rates; (6) compaction of earth during reclamation reduces macropore flow and decreases infiltration rates; and (7) prevalent overland flow pathways efficiently transport water and sediment.

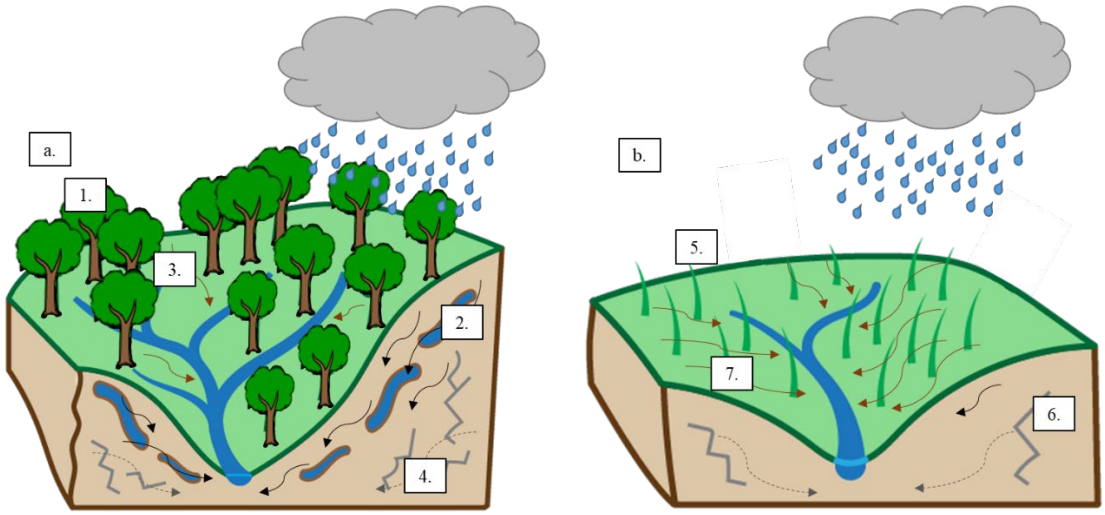

Figure 5.3. Probability of connectivity parameterization, adapted from Mahoney et al., (2018).

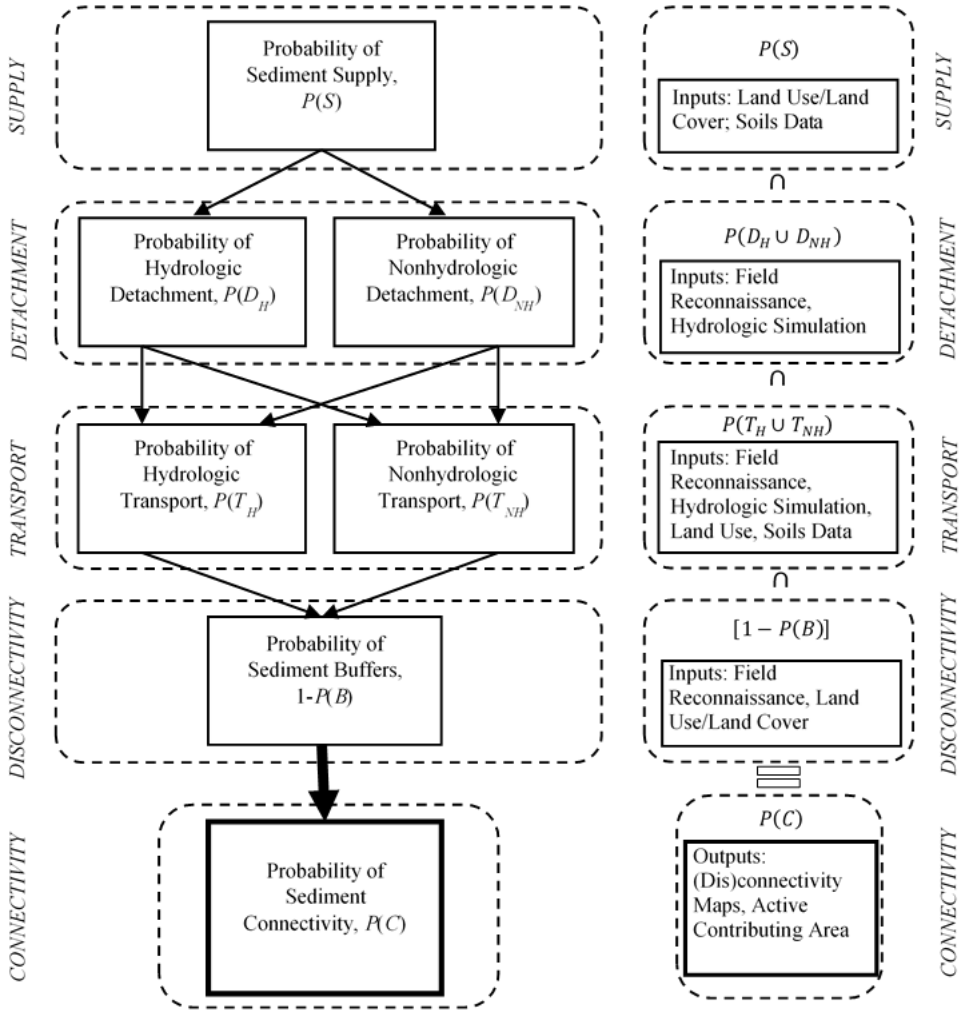

Figure 5.4. Sediment flux evaluation flowchart that considers sediment connectivity and erosion simulated *via* RUSLE.

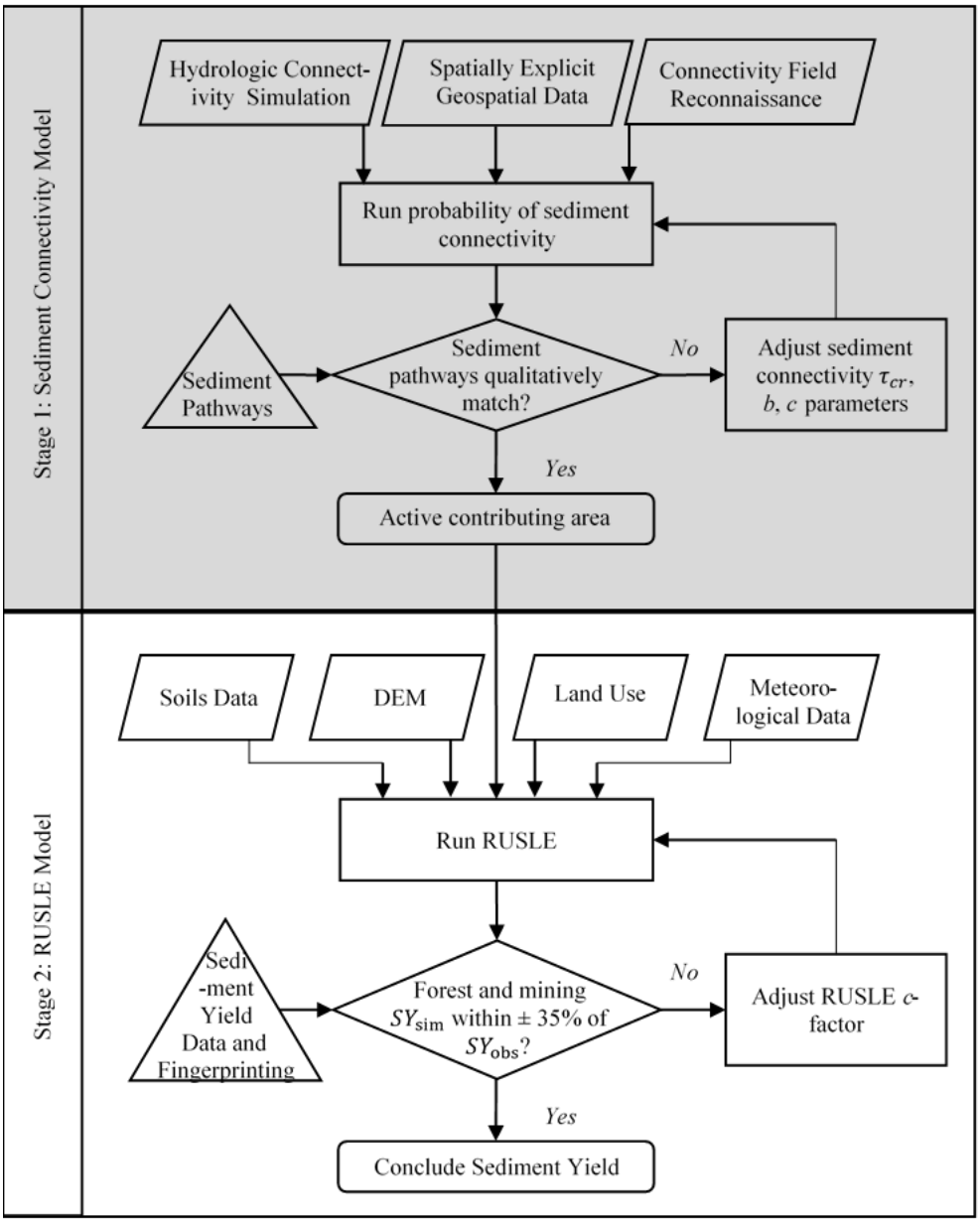

Figure 5.5. Spatial probability of connectivity results for four events of increasing hydrologic magnitude in the Whitaker Branch watershed including: (a) 3.0% connectivity during event 8 (July 24, 2007); (b) 9.3% connectivity during event 12 (October 24, 2007); (c) 18.8% connectivity during event 1 (March 1, 2007); and (d) 36.2% connectivity during event 5 (April 14, 2007). These events approximately represent the minimum (event 8), 25% quartile (event 12), 75% quartile (event 1), and maximum (event 5) $P(C)$ results.

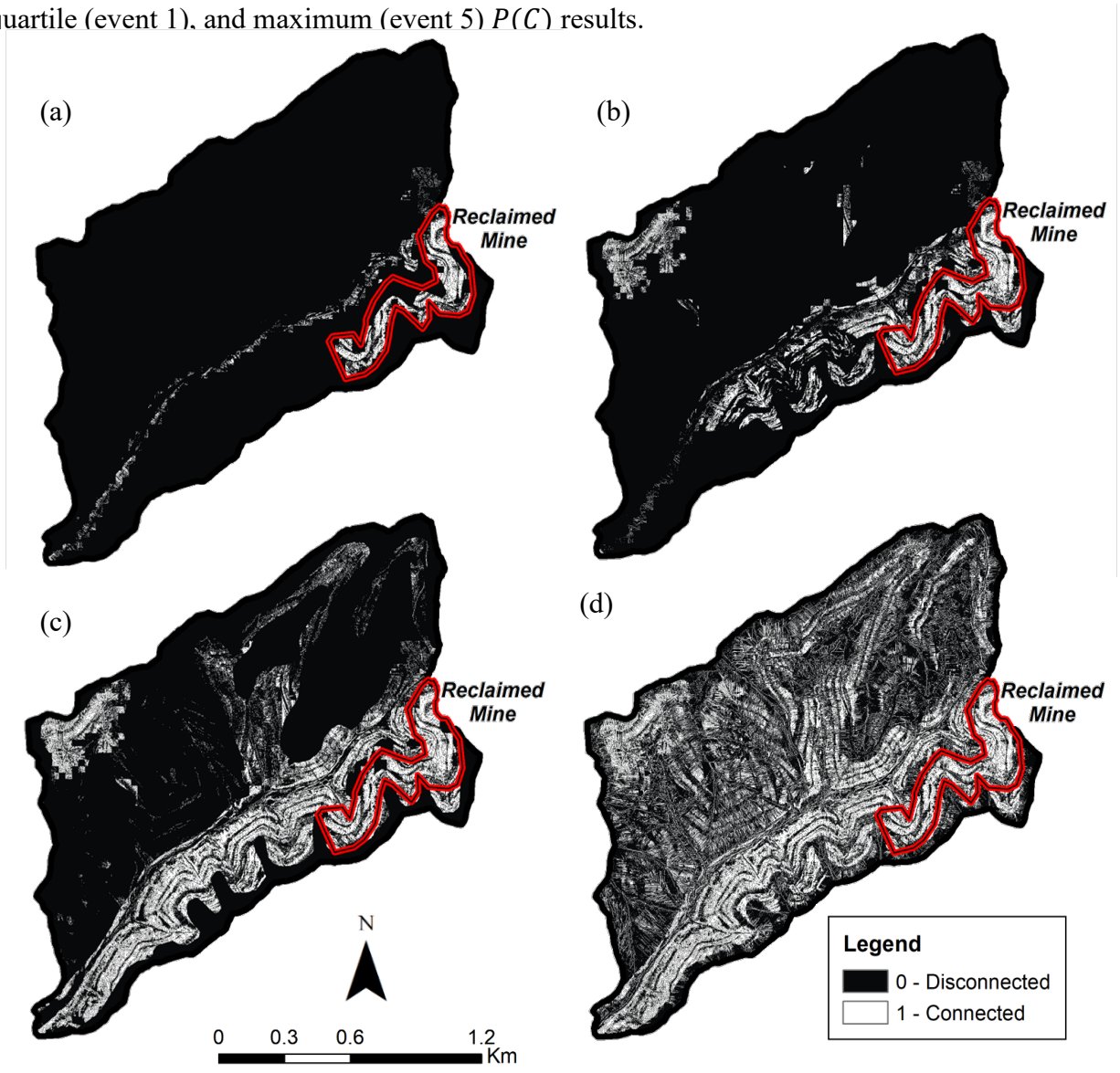

Figure 5.6. Probability of connectivity results reveals connected and disconnected morphologic features. Imagery, slope, and probability of connectivity results are shown for three locations within the Whitaker Branch watershed. (a) Connectivity from concentrated forest pathways on steep slopes and disconnectivity due to soil texture and fast drainage. (b) Connectivity caused by steep slopes and disconnectivity from historic terracing found throughout the watershed. (c) Connectivity within the reclaimed mine and disconnectivity on flat ridgelines created during reclamation

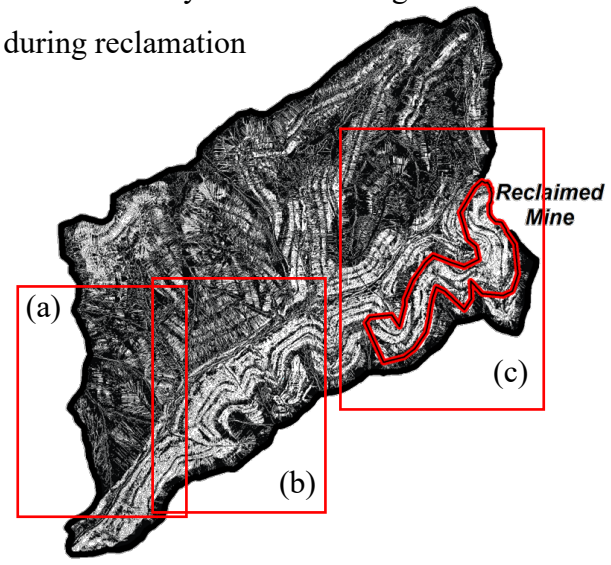

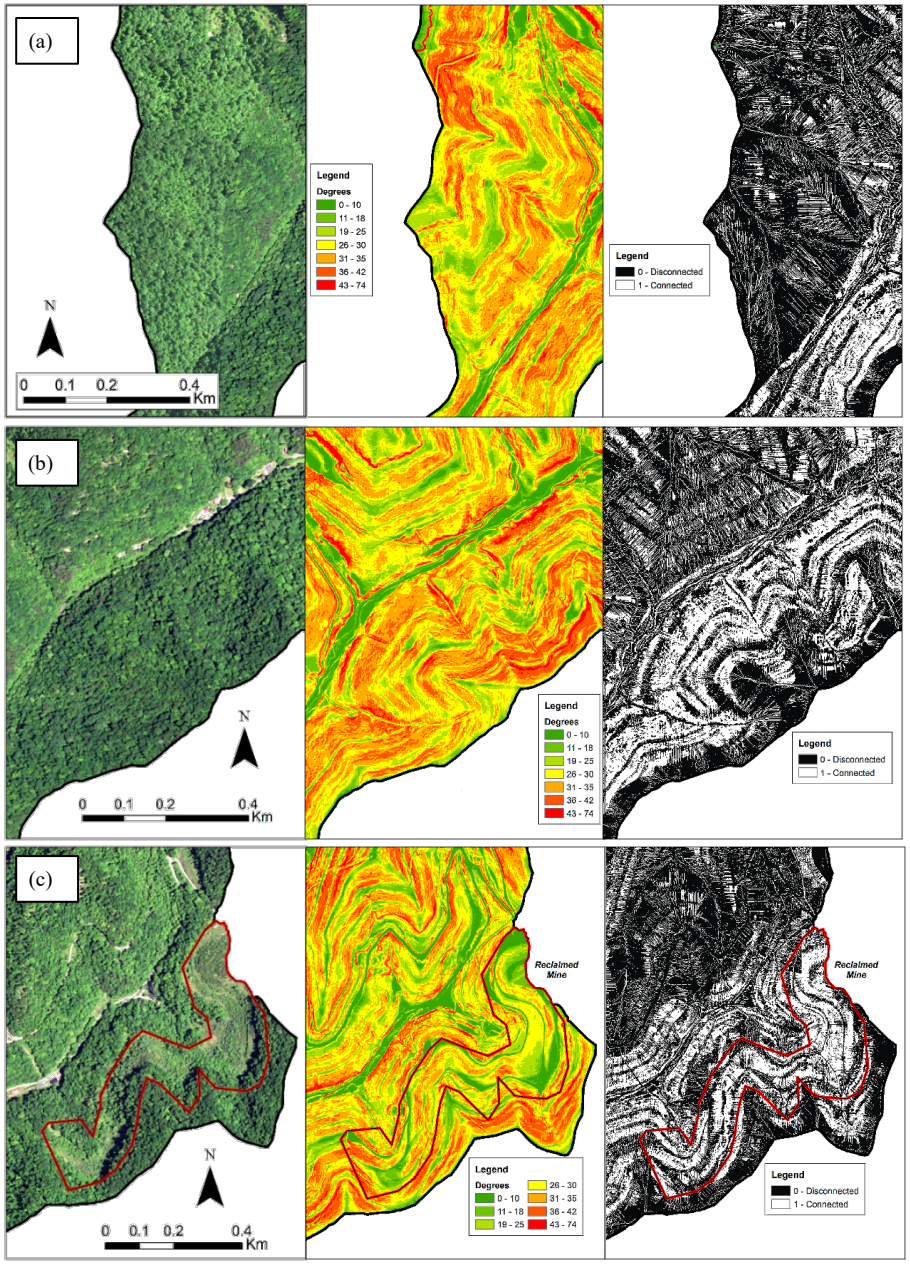

Figure 5.7. Variability of sediment connectivity probabilities, including the probability of sediment supply, P(S), probability of downstream hydrologic transport, P(TH-DWN), probability of upstream hydrologic transport, P(TH-UP), probability of hydrologic detachment, P(DH) and probability of connectivity, P(C). Probabilities are shown for selected events in (a) Whitaker Branch, (b) forested land uses, and (c) reclaimed mine land. These events approximately represent the minimum (event 8), 25% quartile (event 12), 75% quartile (event 1), and maximum (event 5) $\boldsymbol{P(C)}$ results.

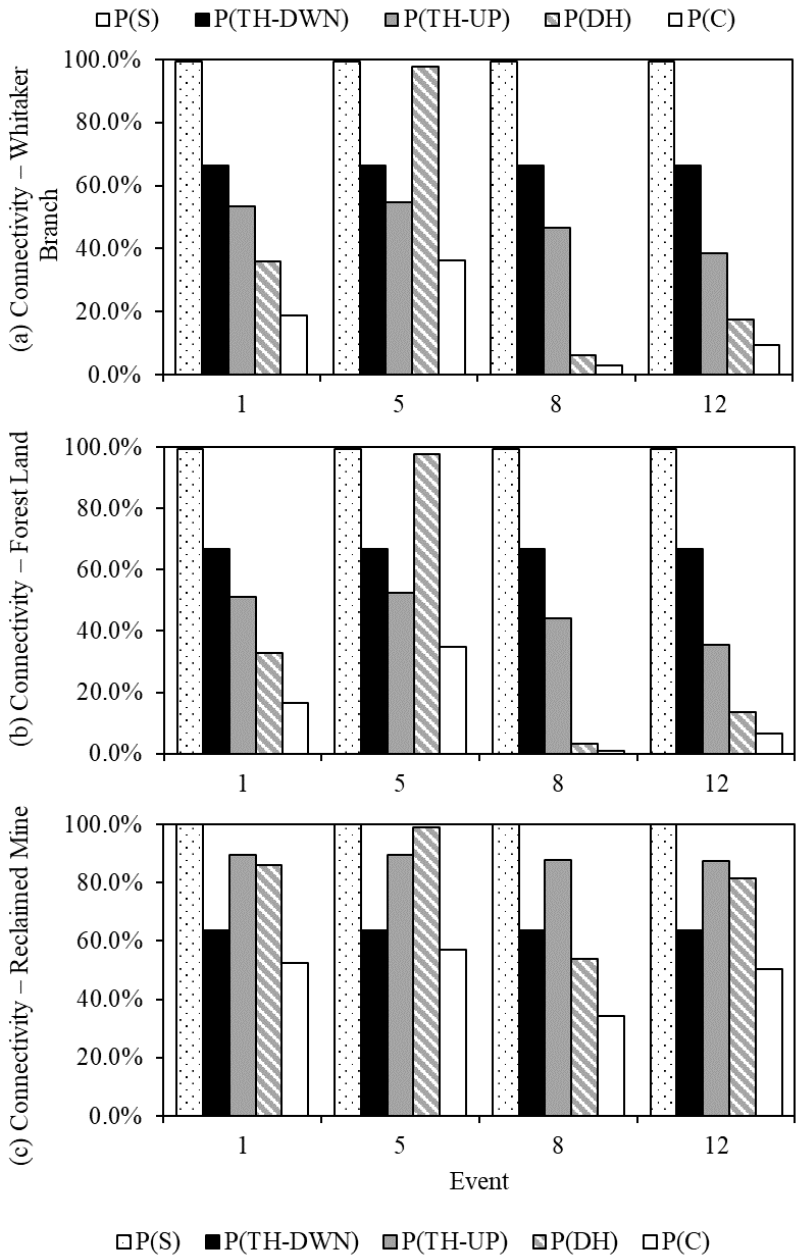

Figure 5.8. Results of (a) probability of connectivity, (b) probability of hydrologic detachment and (c) probability of hydrologic upstream transport for each of the 12 hydrologic events for forest and reclaimed mining surface cover.

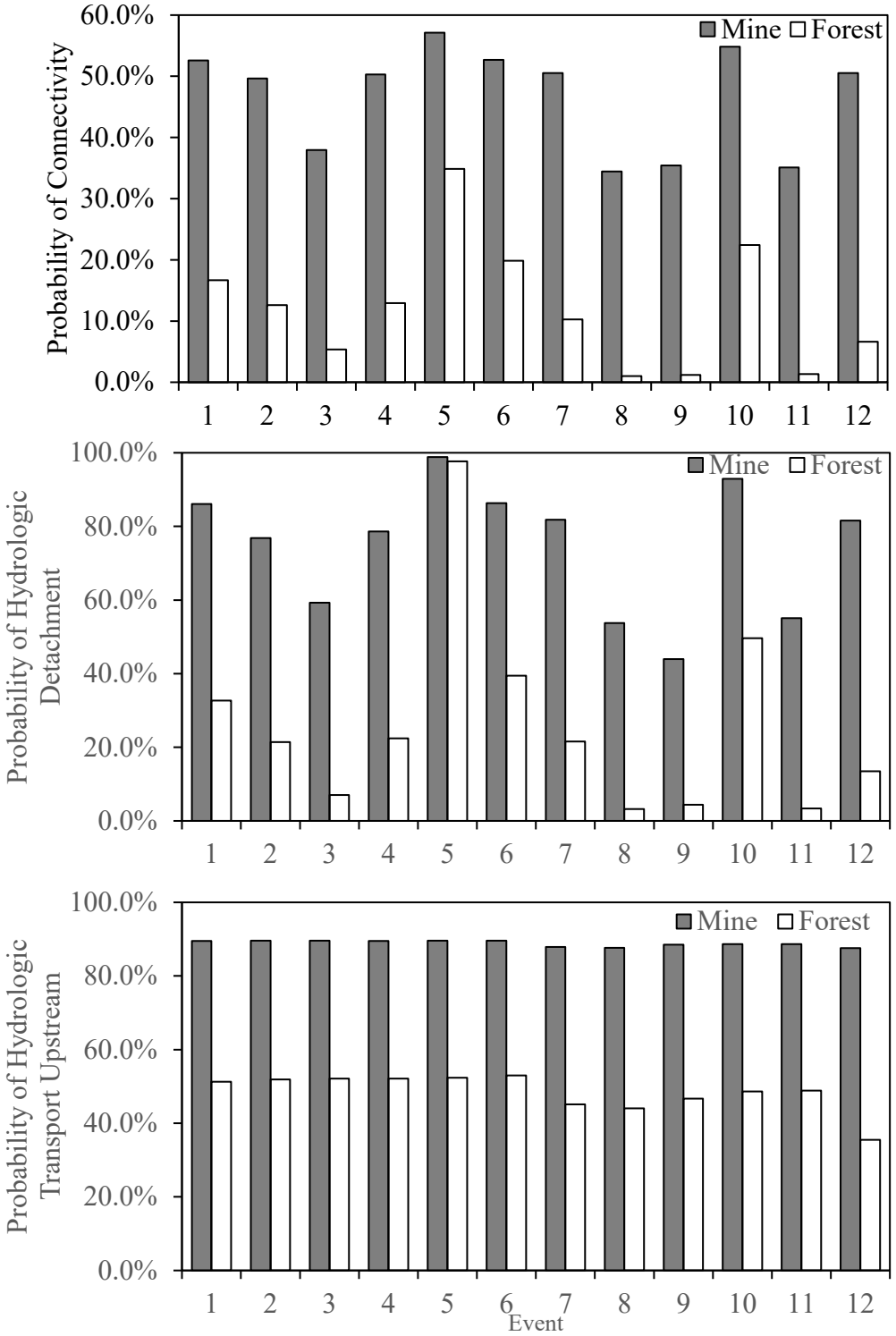

Figure 5.9. Spatially-distributed erosion and connectivity results. Distributed connectivity and RUSLE results for four events of increasing probability of connectivity in the Whitaker Branch watershed including: (a) event 8 (July 24, 2007) with 3.0% connectivity; (b) event 12 (October 24, 2007) with 9.3% connectivity; (c) event 1 (March 1, 2007) with 18.8% connectivity; and (d) event 5 (April 14, 2007) with 36.2% connectivity.

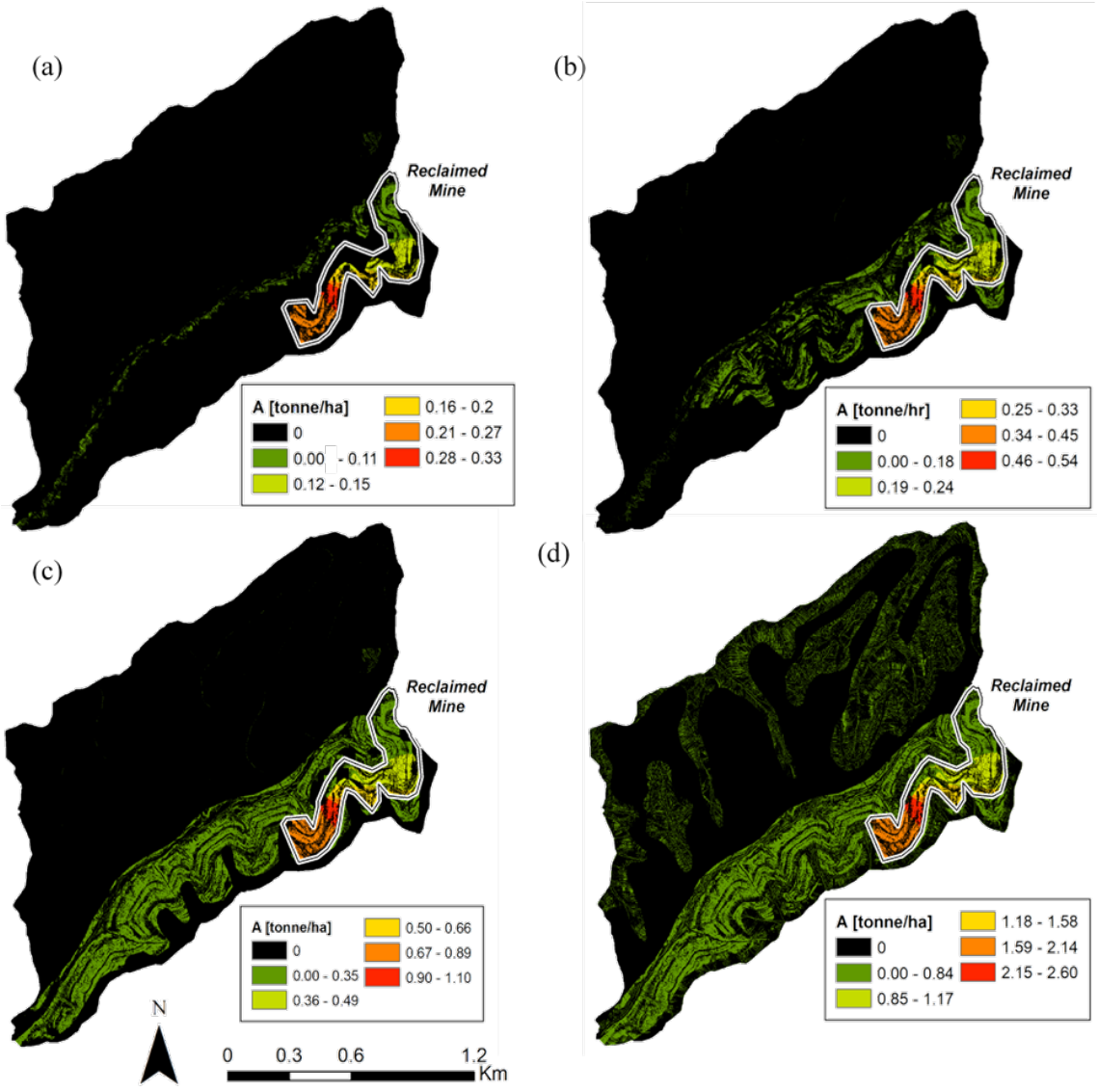

Figure 5.10. Soil loss for land uses versus probability of connectivity results.

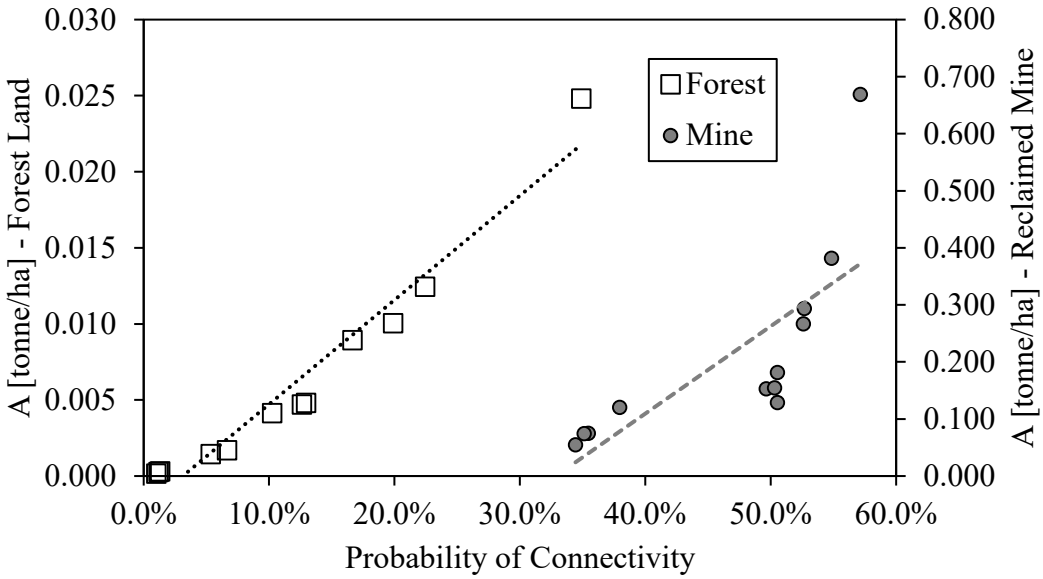

Chapter 6. Formulating the probability of connectivity within the sediment continuity equation shows lithological barriers control stream geometry and sediment (dis)connectivity in low gradient stream

6.0 ABSTRACT

Structural properties of stream networks are well-known to influence stream evolution, morphology, hydraulics, and sediment transport. However, impacts of structural barriers on longitudinal sediment transport are understudied with respect to quantitative perception of timescales and controls of instream erosion and deposition dynamics, especially in low-gradient systems. Herein, we couple field reconnaissance observations with instream numerical modeling to improve conceptual understanding of longitudinal connectivity in low-gradient systems and formulate instream connectivity equations coupled with sediment continuity. Our objective was to better understand timescales and thresholds associated with control of instream barriers on sediment connectivity and transport processes. We apply framework to the low-gradient, bedrock controlled Upper South Elkhorn watershed.

Field investigation suggests the stream profile is locally controlled by lithology for the low gradient bedrock system studied and specifically behave as barriers to sediment transport. Our results suggest morphologic control of the pool:riffle length ratio for the stream network is due to dissolution of fluviokarst landscape to create the hilly topography typical of karst terrain in this region. We develop a conceptual model of the behavior and timescales of barrier activity based on our field investigations.

Our numerical model represented the bedrock riffles as discontinuous barriers that can be breached, and sediment transport modelling results were found to agree well with our field investigation of sediment transport. We compared model results for spatially explicit consideration of riffle-morphology with implicit consideration and found that while both models adequately simulated sediment flux according to traditional watershed modeling objective functions, explicit simulation of riffle-pool morphology and variable stream gradient during hydraulic regimes better predicted event-to-event sediment flux and recession dynamics. Probability of connectivity and probability of continuity results

indicate that bedrock outcrops behave discontinuously with respect to erosion, deposition, and connectivity, supporting early geomorphologic frameworks of such systems.

6.1 INTRODUCTION

Structural properties of stream networks are well-known to influence stream evolution, morphology, hydraulics, and sediment transport (e.g., Schumm, 1954; Leopold et al., 1964; Henderson, 1966; Chorley and Kennedy, 1971; Chang, 1888; Fryirs et al., 2007; Fryirs, 2013). For example, lithology is well-established as a structural control of instream longitudinal profile, bed material, and particle size (Hack, 1957; Leopold et al., 1964; Wainwright et al., 2011) and plays important roles in resistance and non-uniformity in streams (Phillips, 2003; Toone et al., 2014). We find, however, that impacts of structural barriers on longitudinal sediment transport are understudied with respect to quantitative perception of timescales and controls of instream erosion and deposition dynamics, especially in low-gradient systems (e.g., Mahoney et al., 2018; Mahoney et al., 2019). An increasingly promising approach to view and quantify impacts of structural elements on streambed morphology and longitudinal sediment transport is through the lens of connectivity theory (see Fryirs, 2013; Bracken et al., 2015; Heckmann et al., 2018). Over the last two decades, quantification of sediment connectivity has been forded primarily using: (1) visual connectivity assessments and (2) numerical models and indices of connectivity (e.g., Borselli et al., 2008; Mahoney et al., 2018; Heckmann et al., 2018). Coupling connectivity measurements with watershed and sediment transport models has recently shown promise for improving sediment simulations and representing impacts of structural properties at quasi spatially and temporally-explicit resolutions (Vigiak et al., 2012; Heckmann et al., 2018; Mahoney et al., 2018). We find that coupled connectivity and sediment transport models have seldom been leveraged to quantify structural barriers in low-gradient stream networks.

Our motivation was to better understand structural watershed properties that control sediment transport and sediment connectivity in low-gradient stream networks by coupling the sediment continuity equation with longitudinal sediment connectivity simulations and field reconnaissance. We applied the model to a low-gradient, bedrock controlled stream network in the Inner Bluegrass region of Kentucky, USA. This paper served the motivations of: (1) formulating instream connectivity equations coupled with sediment

continuity for the first time, to our knowledge; (2) coupling field reconnaissance observations with instream numerical models to improve conceptual understanding of longitudinal connectivity in low-gradient systems; and (3) understanding timescales and thresholds associated with control of instream barriers on sediment connectivity and transport processes.

In this study, we seek to better understand lithological controls of stream morphology and sediment transport, and specifically quantify the timescales and thresholds associated with the activity and inactivity of such controls. One such example of lithological controls in stream networks includes bedrock outcrops which obtrude from streambanks, are locally resistant to erosion, and function as instream hydraulic controls (e.g., Chang et al., 1988; Toone et al., 2014, Wohl, 2015, Mahoney et al., 2018). In steep-gradient systems, bedrock controls have been observed to promote deposition through the formation of riffle-pool sequences that "filter" course grained sediment, thus winnowing suspended sediment loads. Instream bedrock sequencing has been identified by a number of researchers (e.g., Toone et al., 2014; Wohl, 2015) to importantly influence sediment dynamics in stream networks, and is recognized as an important feature of structural watershed properties (i.e., Wainwright et al., 2011; Heckmann et al., 2018).

In this study, we seek to better understand the control of lithology and bedrock outcrops on sediment transport within the context of low-gradient stream networks. We find that systems with low-gradient streams perhaps are understudied with respect to quantification of bedrock outcrop control on sediment transport. The upland morphology of low-gradient systems typically is considered as "gently rolling" with relatively stable land surfaces and ephemeral pathways (Jarrit and Lawrence, 2007; Ford and Fox, 2014) and contributes supply of sediment to the stream when hydrologic connectivity is established (Mahoney et al., 2018). The low-gradient nature of the stream network promotes instream deposition and sediment storage (McGrain, 1983). We find that previous study of lithological control of instream sediment transport has previously been investigated primarily in steep-gradient systems (e.g., Toone et al., 2014; Wohl, 2015), and that low-gradient systems are understudied.

To quantify impacts of lithological controls such as bedrock outcrops on longitudinal sediment transport, we suggest coupling traditional sediment continuity model

structures with sediment connectivity theory. We define sediment connectivity as an emergent system property that reflects the strength and continuity of sediment linkages between and within system compartments over a specified timescale (see Heckmann et al., 2018; Wohl et al., 2019). Utility of the sediment connectivity framework has been leveraged to qualitatively and quantitatively describe active and inactive sediment pathways in variable dimensions of the sediment cascade and for variable timescales (Fryirs et al., 2007; Fryirs, 2013; Ali et al., 2018). For example, recent sentiment has emphasized the conceptualization of connectivity in lateral, longitudinal, and vertical dimensions in order to better understand morphologic features that impede transport (Fryirs, 2013), termed as buffers, barriers, and blankets (Fryirs et al., 2007; Fryirs, 2013). We find usefulness in framing the control of instream lithology in terms of buffers, barriers, and blankets because, conceptually, lithology has been understood to control instream sediment transport processes for many years (e.g., Hack, 1957; Leopold et al., 1964). Conceptual frameworks to understand the timescales and thresholds of when barriers are active and inactive, and hence longitudinal connectivity, have been well developed over the past decade in the geomorphology and engineering communities (e.g., Hooke, 2003; Borselli et al., 2008; Fryirs, 2013; Bracken et al., 2015; Gran and Czuba, 2017; Ali et al., 2018; Mahoney et al., 2018). Recent developments to understand connectivity from both qualitative and quantitative perspectives include field assessments (e.g., Borselli et al., 2008; Wohl et al., 2017) and numerical models and indices (e.g., Borselli et al., 2008; Cavalli et al., 2013; Crema and Cavalli, 2018; Heckmann et al., 2018; Mahoney et al., 2018).

The value of field-based connectivity knowledge has been recognized by many researchers (e.g. Brierley et al., 2006; Fryirs et al., 2007; Borselli et al., 2008; Lexartza-Artza and Wainwright, 2009), and connectivity field assessments have thus become a cornerstone of sediment connectivity analyses (Bracken and Croke, 2007; Fryirs et al., 2007; Borselli et al., 2008; Lexartza-Artza and Wainwright, 2009; Messenzehl et al., 2014; Bracken et al., 2015; Marchamalo et al., 2016; Mahoney, 2017; Wohl et al., 2017). Examples of field assessments include field-based connectivity maps (Hooke 2003; Messenzehl et al., 2014); the field index of connectivity (FIC; Borselli et al., 2008), and field-based connectivity rankings (Wohl et al., 2017), which have been leveraged to infer

connectivity processes and validate connectivity assessments from geospatial analyses (Borselli et al., 2008; Wohl et al., 2017). We posit that similar visual-based strategies have promise to better understand the impact of lithology and bedrock outcrops on sediment transport and connectivity from a conceptual standpoint.

Indices and models have also been leveraged to gain qualitative and quantitative insight to connectivity processes and have been developed in tandem with field-based methods (Fryirs et al., 2007; Borselli et al., 2008; Heckman and Schwanghart, 2013; Gran and Czuba, 2017; Mahoney et al., 2018). Examples of such analyses include: (1) index-based assessments of connectivity (see Heckmann et al., 2018 for review); (2) effective catchment area simulations (Fryirs et al., 2007; Nicoll and Brierley, 2017); and (3) network-based connectivity simulations (Heckmann and Schwanghart, 2013; Czuba and Foufoula-Georgiou, 2014). Fryirs et al., (2007) and Nicoll and Brierley (2017) showed promising development of coupling effective catchment area estimates with field-based knowledge of buffers, barriers, and blankets to quantify sediment connectivity over long timescales.

One direction in which connectivity application is currently underdeveloped is consideration of functional connectivity (e.g., a system's processes dynamics due to hydrologic forcings; Wainwright et al., 2011; Heckmann et al., 2018) in model structures. Current frameworks, including the widely popular *Index of Connectivity* (see Borselli et al., 2008) and derivatives thereof (e.g., Cavalli et al., 2013), tend to capture structural tenets of connectivity well, but are generally dissociated from functional processes that limit connectivity at event and seasonal timescales (Bracken et al., 2015; Heckmann et al., 2018; Zingaro et al., 2019; Mahoney et al., 2020). Explicit consideration of structural and functional processes poses as one method to advance quantification of connectivity at high spatial and temporal resolutions and improve understanding of instream controls of sediment connectivity such as bedrock barriers (e.g., Bracken et al., 2015; Mahoney et al., 2018; Wohl et al., 2019). In this manner, we seek to improve structural and functional representation of longitudinal connectivity using field assessments and numerical models to quantify timescales when barriers are active and thresholds when barriers are deactivated in low-gradient systems (Ali et al., 2018; Keestra et al., 2018).

Another application of connectivity theory that is currently underdeveloped is incorporation of connectivity formulae within instream sediment transport model structures. Connectivity serves to improve the spatial and temporal resolution of instream sediment continuity simulations, as suggested by recent connectivity literature (e.g., Heckmann et al., 2018; Wohl et al., 2019) and successful demonstration in watershed uplands (Mahoney et al., 2018; Mahoney et al., 2020a; Mahoney et al., 2020b). However, we find a lack of consideration of connectivity theory in instream sediment transport modeling. Herein, we couple instream sediment continuity equations with probability of connectivity and probability of continuity theory from Mahoney et al., (2018; 2020a) and formulate equations for low-gradient instream networks. We hypothesize that such considerations might broaden our view of instream erosion and deposition processes in low-gradient systems in the light of being "continuous" or "discontinuous", where the former is defined as a process that occurs gradually or continuously, and the latter is defined as a process that occurs and ceases abruptly (Toone et al., 2014; Grant et al., 2017).

Objectives of this paper include: (1) formulating and conducting field assessments of sediment connectivity to gain conceptual understanding of the function of lithological controls related to sediment transport processes; (2) formulating the instream sediment continuity equation to explicitly include probability of connectivity theory; (3) utilizing the coupled model to predict sediment flux; and (4) identifying the timescales and thresholds associated with instream morphologic features to impart longitudinal and vertical (dis)connectivity, such as bedrock outcrops. We hope to further understand erosion and depositional processes in the light of continuity and discontinuity through this investigation.

6.2 THEORETICAL DEVELOPMENT

We extend the probability-based approach described in Mahoney et al., (2020a) to predict instream sediment flux and connectivity. We leverage probability theory to simulate flux given the stochastic nature of sediment transport and heterogeneity of instream sediment processes (Gessler, 1971; Hargrave and Burns, 1979; Wright and Webster, 1991; Borselli et al., 2008; Mahoney et al., 2018). Flux is formulated for stream reaches that have varying water and sediment variables as

$$\dot{m}_{ij} = G_{ij}\left[P(C)_{ij} \cdot P(\tau)_{ij} \cdot P(\gamma)_{ij}\right] \quad (1)$$

where m is sediment flux, G is the instream sediment generation rate, $P(C)$ is the probability of instream sediment connectivity representing the spatial extent (i.e., spatial patterns) of connectivity, $P(\tau)$ is the probability of sediment timing representing active time for eroded sediment to reach a specified stream location, $P(\gamma)$ is the probability of sediment (dis)continuity representing continuity of connectivity within the reach, i is the temporal step, and j is the spatial step. We expand Eq. 1 to formulate instream sediment flux and consider the sediment continuity equation as:

$$\frac{dm}{dt} = \left[E_{ij} + SS_{i-1\,j} + SS_{in_{ij}} - SS_{out_{ij}} + SS_{up_{ij}}\right]\left[P(C)_{ij} \cdot P(\tau)_{ij} \cdot P(\gamma)_{ij}\right] \quad (2)$$

where *SS* is suspended sediment load, *in* is sediment entering the reach, *out* is sediment exiting the reach, and *E* is the erosion rate from the bed. Considering sediment flux and integrating Eq. 2 in time yields the following:

$$SS_{ij} = \left\{SS_{i-1\,j} + E_{ij} + \Delta t\left[Qss_{in} - Qss_{out} + Qss_{up}\right]\right\}\left[P(C)_{ij} \cdot P(\tau)_{ij} \cdot P(\gamma)_{ij}\right] \quad (3)$$

We expand Eq. 3 using the distributed property as

$$SS_{ij} = \left[E_{ij}\right]\left[P(C)_{ij} \cdot P(\tau)_{ij} \cdot P(\gamma)_{ij}\right] + \left[SS_{i-1\,j}\right]\left[P(C)_{ij} \cdot P(\tau)_{ij} \cdot P(\gamma)_{ij}\right] + \Delta t[QSS_{in}]\left[P(C)_{ij} \cdot P(\tau)_{ij} \cdot P(\gamma)_{ij}\right] - \Delta t[QSS_{out}]\left[P(C)_{ij} \cdot P(\tau)_{ij} \cdot P(\gamma)_{ij}\right] + \Delta t\left[Qss_{up}\right]\left[P(C)_{ij} \cdot P(\tau)_{ij} \cdot P(\gamma)_{ij}\right] \quad (4)$$

Eq. 4 is the full representation of connectivity formulae and the sediment continuity equations. We make several simplifying assumptions regarding Eq. 4. First, we assume that the fine discretization of Eq. 4 allows for sediment transport and erosion to be simulated at the actual time scale in which sediment processes physically occur, and thus $P(\tau)_{ij}$ is unity for all reaches (Mahoney et al., 2020a). Second, we assume that erosion and deposition are mutually exclusive such that either erosion or deposition can occur during a single time step in a reach (Russo and Fox, 2012). Third, we consider that bed sediment eroded in a spatial step is fully continuous because a prerequisite of erosion is that transport capacity is greater than suspended sediment load and erosion and deposition are mutually exclusive. Fourth we note that at lack of deposition in a reach does not necessarily indicate that erosion occurs because erosion can be supply, detachment, or transport limited (Mahoney et al., 2019). Fifth, we assume that suspended sediments in the reach are fully connected since downstream transport has previously occurred for the sediment to enter or exit the reach. Sixth, we define continuity as the continuum from fully connected to fully

disconnected such that if discontinuity occurs, all suspended sediment is deposited. Likewise, we assume that for full continuity of suspended sediments to occur, no deposition occurs and all suspended sediment reaches the downstream cell. Finally, we assume the magnitude of the connections is reflected by both: (1) probability of continuity and (2) the mass of sediment in the reach. Thus, several probability components of Eq. 4 can be assumed as equal to unity and Eq. 4 is simplified as:

$$SS_{ij} = [E_{ij}][P(C)_{ij} \cdot 1 \cdot 1] + [SS_{i-1\,j}][1 \cdot 1 \cdot P(\gamma)_{ij}] + \Delta t[QSS_{in}][1 \cdot 1 \cdot 1] - \Delta t[QSS_{out}][1 \cdot 1 \cdot 1] + \Delta t[QSS_{up}][1 \cdot 1 \cdot 1] \quad (5)$$

When considering *k* different sediment sources, Eq. 5 becomes

$$SS_{ij} = [E_{ij}][P(C)_{ij}]_k + [SS_{i-1\,j}][P(\gamma)_{ij}] + \Delta t[Qss_{in}] - \Delta t[Qss_{out}] + \Delta t[Qss_{up}] \quad (6)$$

where *k* is the sediment source in the bed.

We formulate the probability of continuity for suspended sediments to represent instances when suspended sediments fall out of suspension due to deposition. Deposition is conceptualized to occur when the transport capacity of the fluid is less than the load of suspended sediment from the previous time step. If deposition of suspended sediment occurs, we define the probability of continuity as the fraction of suspended sediments that remain in suspension after deposition occurs as:

$$P(\gamma) = \begin{cases} 1, & T_c > SS \\ \left[1 - \frac{D_f}{G}\right], & T_c \leq SS \end{cases} \quad (7)$$

Where $P(\gamma) \in [0\ 1]$ and T_C is transport capacity of the fluid. We utilize intersecting probabilities of sediment supply, detachment, transport, and the absence of barriers to formulate the probability of instream connectivity for instream bed sediment of source *k* as

$$[P(C)_{ij}]_k = [P(S)_{ij} \cap P(D)_{ij} \cap P(T)_{ij} \cap [1 - P(B)_{ij}]]_k \quad (8)$$

where $P(S)_{ij}$ is the probability of sediment supply, $P(D)_{ij}$ is the probability of hydrologic detachment, $P(T)_{ij}$ is the probability of hydrologic transport, and $P(B)_{ij}$ is the probability that a barrier to sediment transport occurs in the reach. We assume that strictly hydrologic detachment and transport are possible within low-gradient stream networks and that each process is independent such that

$$\left[P(C)_{ij}\right]_k = \left[P(S)_{ij} \cdot P(D)_{ij} \cdot P(T)_{ij} \cdot \left[1 - P(B)_{ij}\right]\right]_k \quad (9)$$

We adopt a Boolean approach to parameterize probabilities shown in Eq. 8, as discussed in section 6.4.2

6.3 STUDY SITE AND MATERIALS

We applied the coupled connectivity and continuity model and field reconnaissance of sediment connectivity to the Upper South Elkhorn watershed (61.7 km^2) located in the Inner Bluegrass region of Kentucky, USA (see Fig. 1). The stream network is considered low-gradient and consists of deposited sediment pools atop limestone bedrock. Elevation of the catchment ranges between 837 and 1065 m asl (see Fig. 2a). Upland slopes are considered "gently rolling" which are generally low gradient with locally steep surfaces that dissect the land surface (see Fig. 2b; McGrain, 1983; Mahoney et al., 2019). Upland soils consist primarily of silt-loams and are generally well-drained. Land use in the watershed is approximately 55% agricultural forest and 45% urban land (Fig. 2c). Lithology of the watershed is primarily Middle Ordovician Lexington Limestone (see Fig. 2d; KGS, 2013), and karst potential throughout the watershed is considered high. The region's climate is humid subtropical. Temperatures range between 0.5°C and 24.5°C and average yearly precipitation equal to 1184 mm (Ulack et al., 1977). Long, flat floodplains are present on either side of the catchment and impede lateral sediment transport (Mahoney et al., 2018).

Materials used in this study include high-resolution geospatial data, high-temporal frequency sediment data, existing connectivity modeling, and software to carry out field reconnaissance and couple the probability of connectivity model with instream sediment continuity simulations. A summary of data used herein, data frequency, and data collection methods is recorded in Table 1. We used remote sensing and high-resolution geospatial data to assist with field reconnaissance and connectivity modeling. We collected total suspended solids samples (TSS) and turbidity data at the UK SENSE station (see Fig. 1) to assist with calibration and validation of the coupled connectivity and continuity sediment model. TSS sediments were collected using a Teledyne ISCO automated sampler at 7 hour frequency and were retrieved and processed weekly. Sampled TSS Values ranged between 0.5 and 214 mg l^{-1} and corresponded to turbidity between 0.6 and 245 NTU. The coefficient of determination for relating TSS samples and turbidity measurements was 0.86. We used

15-minute streamflow from USGS station 03289000, NOAA weather data at the Bluegrass Airport, and the *Soil and Water Assessment Tool* to quantify hydrology and hydraulics in the Upper South Elkhorn watershed. We used the modelling framework from Mahoney et al., (2020a, b) to simulate upland sediment connectivity and flux. Software used to simulate connectivity and process field reconnaissance included ArcGIS 10.4.1, ArcSWAT 2012.10.21, and Matlab R2019b.

6.4 METHODS

6.4.1 WAVES Field reconnaissance

We used the Watershed Assessment and Visualization of Erosion and Sedimentation (WAVES) protocol to conduct visual assessment of connectivity and sediment transport in the Upper South Elkhorn watershed (Mahoney, 2017). WAVES was developed by reviewing contemporary methods to visually assess watersheds and streams including: (1) the Stream Visual Assessment Protocol (SVAP) Version 2 (NRCS, 2009); (2) the Bank Erosion Hazard Index (BEHI) (Rosgen, 2001); (3) the Rapid Bioassessment Protocol (RBP) (USEPA, 1999); (4) visual assessments of stream networks from local consulting companies; and (5) connectivity literature (Fryirs et al., 2007).

Parameters assessed in the WAVES protocol for reaches include: (1) connectivity, (2) streambanks and floodplains, (3) streambed, (4) upland land use, and (5) miscellaneous qualities. Mahoney, (2017) explains the assessment methods for each parameter as follows:

> *"Connectivity is assessed by identifying source to sink pathways of sediment and impedances which may cause disconnectivity within the subreach. The condition of the streambanks and floodplains is assessed by observing the riparian buffer surrounding the stream, the structure of the banks, and human infrastructure which may impact sediment transport. The streambed is assessed through the determination of bed bathymetry, morphology, instream sediment storage, and the type of sediment stored. Upland land use conditions are assessed through identification of the type of land use, evidence of historic upland erosion, and upland human interferences that may accelerate sediment transport. Finally, miscellaneous aspects of the subreach that may further contribute to or yield evidence of sediment transport are assessed through the identification of karst features, water quality, and ecosystem quality."*

Prior to the visit, we mapped tributaries with contributing areas greater than 0.5 km^2 to identify stream access points and the assessment domain. Aerial imagery and DEM

analyses were used to validate delineation of stream networks. Information collected during field reconnaissance was later georeferenced to this tributary delineation. Materials used to conduct the field reconnaissance included a digital water proof camera with GPS capabilities, survey rods, rulers, field notebooks, and maps of the stream. We conducted preliminary visits to the field to delineate reaches within the stream network, which were defined as geomorphologically similar lengths of the stream. We noted the start and end of reaches using a GPS.

During site visits, a minimum of two researchers conducted the WAVES assessment due to safety purposes and to limit subjectivity from the assessors. An example of the WAVES protocol form is shown in Appendix I. We followed procedures described in Mahoney (2017) to then conduct the assessment, described as follows:

> "*Starting at the downstream end of each reach, researchers walked upstream and observed the qualities of the subreach, keeping in mind the five aforementioned parameters. While assessing each reach, geolocated photographs were taken of many features within the stream corridor. Images were taken of (1) the left bank and right bank angle and height at the downstream end, middle, and upstream end of the reach, or wherever significant alterations occurred; (2) hotspots of bank erosion throughout the reach, as well as in-stream sediment storage (i.e. by placing a surveying rod into the sediment); (3) bed material at the beginning, middle, and end of the storage zone; (4) any and all inflowing tributaries and outfalls. Where possible, researchers also walked tributaries and noted bank angles, heights, bed material, erosional hotspots, and upstream land use/land cover. Pictures were also taken of sources of (dis)connectivity within the stream: i.e. check dams, bed rock outcrops, point bars, depositional zones, armoring zones, connected hillslopes, floodplains, in-stream features (riffles, runs, and pools) as well as upland features (land use, human or livestock interference, erosion). At the end of the reach, researchers filled out the WAVES Protocol sheets. This was done individually to minimize subjectivity. While completing the assessment sheets, researchers noted the features separating one reach from another on the Intermediate Reach form. Unique features of the reach, weather, flow rate, and other conditions were noted on this form as well. This process was completed for each reach assessed during each site visit.*"

After the site visit, we processed and stored WAVES field sheets in an ArcGIS database. We applied qualitative erosion and deposition indices from Mahoney (2017) to visualize hotspots of erosion and deposition determined as:

$$OEI = \frac{\sum(avg\ extent + avg\ density) * (value\ weight)}{\sum(value\ weight)} \quad (10)$$

$$ODI = \sum\left(\frac{longitudinal\ extent}{10} * lateral\ extent * weight\right), \quad (11)$$

where *OEI* is the qualitative observed erosion index, *ODI* is the observed deposition index, *avg extent* is the average extent of erosion within the reach (rated subjectively from 1-10), *avg density* represents the severity of erosion in the reach (rated subjectively from 1-10), *value weight* is a qualitative weighting coefficient based on the type of erosion developed by Mahoney (2017), *longitudinal extent* is the longitudinal extent of deposition (rated subjectively from 1-10), *lateral extent* is the lateral extent of deposition per reach (rated subjectively from 1-10), *weight* is the qualitative weighting coefficient based on the type and severity of deposition according to Mahoney (2017), and 10 is a normalization parameter to relate longitudinal and lateral extents of deposition The average extent and density of erosion were calculated using the arithmetic means of the scores from the WAVES Protocol sheets. Averages of the researchers' scores were used to create the hotspot maps to limit subjectivity of the field assessment.

As a final note from Mahoney (2017):

> "*The main utility of the WAVES Protocol is to understand qualitatively where erosion, deposition, and (dis)connectivity are most pronounced to help infer the governing processes of watershed sedimentation prior to creating a model to assess connectivity and sediment flux. This can later serve as a qualitative validation to a connectivity model. Another utility of this Protocol is that disconnectivity features, such as floodplains, were geospatially mapped, and thus can be parameterized in a connectivity model with a high degree of certainty. Finally, the geospatial database of geo-located photographs serves as useful tool for performing other types of visual assessments without having to go into the field. For example, it was intended that the multitude of pictures taken should allow researchers to perform an analysis like the BEHI without having to go back into the field."*

6.4.2 Connectivity and Continuity Model Formulation

We route sediments from the watershed uplands through reaches and to the outlet following Russo and Fox (2012), Mahoney et al., (2018), and Mahoney et al., (2020b) and with the connectivity equations presented in Eq. 9 using the following equations:

$$SS^{j}_{i+\frac{1}{2}} = \left[SS^{j}_{i-\frac{1}{2}} \cdot P(\gamma)_{ij} + \left[P(C)_{ij}\right]_k \cdot \left[E_{ij}\right]_k + Q^{j}_{SS,in\,i}\,\Delta t + Q^{j}_{SS,up\,i}\,\Delta t - \right.$$

$$\left. kss\left(\frac{SS^{j}_{i-\frac{1}{2}}}{V^{j}_{i-\frac{1}{2}}}\right) Q^{j}_{out\,i-\frac{1}{2}} \Delta t \right] \left[1 + (1 - kss)\left(\frac{Q^{j}_{out\,i+\frac{1}{2}}}{V^{j}_{i+\frac{1}{2}}}\right)\Delta t \right]^{-1}, \quad (12)$$

$$Q^{j}_{SS,up\,i} = G \cdot \overline{\overline{P(C)}} a^{j} \sum_{i-\frac{1}{2}}^{i+\frac{1}{2}} A_{sed} f(t)_{sed}\,, \quad (13)$$

$$Q^{j}_{SS,in\,i} = k_{ss}\left(\frac{SS^{j-1}_{(i-1)-\frac{1}{2}}}{V^{j-1}_{(i-1)-\frac{1}{2}}}\right) Q^{j-1}_{out\,(i-1)-\frac{1}{2}} + (1 - k_{ss})\left(\frac{SS^{j-1}_{(i-1)+\frac{1}{2}}}{V^{j-1}_{(i-1)+\frac{1}{2}}}\right) Q^{j-1}_{out\,(i-1)+\frac{1}{2}}\,, \text{ and} \quad (14)$$

$$Q^{j}_{SS,out\,i} = k_{ss}\left(\frac{SS^{j}_{i-\frac{1}{2}}}{V^{j}_{i-\frac{1}{2}}}\right) Q^{j}_{out\,i-\frac{1}{2}} + (1 - k_{ss})\left(\frac{SS^{j}_{i+\frac{1}{2}}}{V^{j}_{i+\frac{1}{2}}}\right) Q^{j}_{out\,(i-1)+\frac{1}{2}}\,, \quad (15)$$

where SS is the mass of suspended sediment (kg); Q and Q_{ss} denote water and sediment discharge ($m^3\ s^{-1}$ and $kg\ s^{-1}$); *in* and *out* denote flux into or out of a model stream reach; k_{ss} is the sediment routing coefficient (dimensionless); V is the volume of water (m^3); A_{sed} is a sediment attenuation factor (dimensionless); G is the upland erosion generation rate ($kg\ cell^{-1}$), $\overline{\overline{P(C)}}$ is the spatially and temporally averaged upland probability of connectivity for an event; and a^j is the area of catchment *j*. Parameterization of Eq. 11 for upland sediment input to the stream network is presented in Mahoney et al., (2020b).

We parameterize the probability of connectivity $P(C)$ for instream sediments of variable source using a series of piecewise functions to represent sediment transport processes in reaches as:

$$\left[P(C)_{ij}\right]_k = \left[P(S)_{ij}\right]_k \cdot \left[P(D)_{ij}\right]_k \cdot \left[P(T)_{ij}\right]_k \cdot \left[P(B)_{ij}\right]_k \quad (16)$$

where

$$\left[P(S)_{ij}\right]_k = \begin{cases} 1, & \left[S_{ij}\right]_k > 0 \\ 0, & \left[S_{ij}\right]_k = 0 \end{cases} \quad (17)$$

$$\left[P(D)_{ij}\right]_k = \begin{cases} 1, & \tau_{f_{ij}} > \tau_{cr_k} \\ 0, & \tau_{f_{ij}} \leq \tau_{cr_k} \end{cases} \quad (18)$$

$$\left[P(T)_{ij}\right]_k = \begin{cases} 1, & T_{c\,residual_k} > 0 \\ 0, & T_{c\,residual_k} \leq 0 \end{cases} \quad (19)$$

$$\left[P(B)_{ij}\right]_k = \begin{cases} 1, & Q > \theta_k \\ 0, & Q \leq \theta_k \end{cases} \quad (20)$$

where $\left[S_{ij}\right]_k$ is the supply of sediment source k, τ_f is the fluid shear stress, τ_{cr_k} is the critical shear stress of sediment source k, $T_{c\,residual_k}$ is residual transport capacity available to transport source k, and θ_k is the threshold flowrate at which barriers become inactive. We parameterize $P(C)$ for three sediment types in the Upper South Elkhorn watershed based on field investigations including: (1) SFGL sediments which lie atop bed sediments, have low critical shear stress, and erode preferentially in the system (Droppo and Stone, 1994), (2) bed sediments, and (3) bank sediments. We parameterize stream gradient by assuming that stream gradient is equal to bed gradient until a flow threshold is breached, at which point an average stream gradient is used. We record specific equations used to calculate sediment transport parameters in Appendix II and is described in depth in Russo and Fox (2012). A list of symbols is included in Appendix III.

We discretized the watershed into 181 catchments and 362 reaches to parameterize the stream network for explicit simulation of instream sediment continuity and connectivity based on the location of bedrock outcrops identified by the WAVES protocol. Sediment transport was predicted at 15-minute time steps, which satisfied the CFL condition (Courant et al., 1967). We ran the connectivity and continuity simulations between September 2017 and February 2019. Inputs and parameter ranges used in the model are recorded in Table 2. Parameter ranges derived from existing literature are as follows: SFGL parameters were derived from studies of Stone and Droppo (1994) and Droppo and Amos (2001); transport capacity ranges were derived from Dou (1974), Ahmadi et al., (2006), Yan et al., (2008), Guy et al., (2009), and Madej et al., (2009); shear stress coefficient ranges were derived from Chang (1988); critical shear stress ranges were derived from Sandford and Maa (2001), Hanson and Simon (2001), and Simon and Thomas (2002). Settling velocity was based on study from Fox et al., (2010). Bathymetry was parameterized using 1.5 m digital elevation models and stream surveys (KYAPED, 2014).

Qualitative visual analyses of time series and sediment flux measurements using turbidity and TSS data were used to calibrate and validate the model. Calibration currently extends between September, 2017 until February, 2019. Validation of the model is ongoing. Turbidity measurements were collected using a YSI 6-series and YSI EXO optical

turbidity sensors. Quality assurance of data was performed using methods described in Mahoney et al., (2020b).

Evaluation of the model is shown in Fig. 3. Briefly, upland sediment connectivity simulations were conducted and coupled with erosion rates to simulate upland sediment entering the stream network. Instream probability of connectivity and sediment continuity equations were run simultaneously to simulate instream (dis)connectivity and sediment flux. If Nash Sutcliffe Efficiency of observed and simulated sediment flux was greater than 0.2 and instream connectivity and disconnectivity simulations agreed with our visual assessment results, we accepted the realization of the model, otherwise we adjusted instream and upland sediment parameters and slope threshold parameters until simulations were acceptable. Qualitative sensitivity analyses were performed to understand behavior of the model in response to input parameter values.

6.5 RESULTS AND DISCUSSION

6.5.1 Field investigation suggests lithological control on pool:riffle length ratio in fluviokarst

Field investigation suggests the stream profile is locally controlled by lithology for the low gradient bedrock system studied. Locally resistant limestone often extends as outcrops from banks. The limestone extends across the stream channel creating a barrier to flowing water and in turn sediment. The limestone outcrops, or barriers, function as downstream hydraulic controls that cause upstream pools with locally flat energy gradients during low flow conditions. These observations were consistent as we walked and mapped the approximately 30 km stream network during low flow conditions. Fig. 4 shows our field research results where we identified 181 bedrock-riffle (black sections in Fig. 4) and pool (grey sections in Fig. 4) sequences throughout the stream network.

As shown in the blow up map in Table 3 and Fig. 4, the lengths of the riffles and pools varied from sequence to sequence, but one distinct feature is the pools were almost always greater in length than the pools. The length of pools (mean $L:W$=32, n=181) was a half order of magnitude greater than length of bedrock 'riffles' (mean $L:W$=7, n=181). On average, the pool:riffle length for this low gradient bedrock system was 4.6. In-stream incision is less pronounced for the bedrock-riffles than limestone in pools just upstream

and downstream (see photos in Fig. 4) creating local concavity longitudinally for the streambed profile for the riffle-pool sequences. Further investigation shows the presence of the lithologic control and catchment morphology on controlling the pool:riffle length ratio for this system. As shown in the watershed map with the 181 catchments in Fig. 4, the bedrock-riffles always occur at the catchment divides with the pools being located in the catchment interior (see 'black' riffles at catchment divides in Fig. 4). In this way, the dissolution of fluviokarst landscape to create the hilly topography typical of karst terrain in this region (Phillips 2003, 2015; Phillips et al., 2004) helps control the morphology of the pool:riffle length ratio for the stream network.

The pool:riffle length for this low gradient bedrock system greatly contrasts pool:riffle geometry of alluvial systems. For example, one study of alluvial systems found the pool:riffle length equals 0.56 (1:1.8) for low gradient channels (Wohl et al., 1993), which is an order of magnitude lower than the pool:riffle length ratio equal to 4.6 found in this current study. In alluvial systems, pool:riffle depth and length ratios are attributed to internal energy of the system and specifically are suggested to reflect energy expenditure as a function of gradient and the fluid's ability to erode its channel boundaries (Richards, 1978; Wohl et al., 1993). In this fluviokarst region with bedrock streams, the pool:riffle geometry more likely is controlled by the development and maturity of the karst topography. The dissolution of limestone can remove softer limestone strata creating sinkholes, cover collapses and downcutting of the terrain. This action combined with fluvial action causes the landscape to evolve to a hilly terrain (Phillips 2003, 2015; Phillips et al., 2004) leaving behind more resistant rock creating the catchment divides and riffles. Ongoing work is currently being conducted to validate these results.

The field geomorphology results from this study extend the body of literature focused on lithologic control on stream networks. A number of studies have shown lithologic control on channel geometry and stream profile in steeper terrain (Duvall et al., 2004; Pike et al., 2010; Whitbread et al., 2015), but few studies, to our knowledge, have reported lithological control on pool:riffle ratios for low gradient streams in fluviokarst regions. The lithologic control on the stream profile in turn is expected to impact the present-day ecology and sediment dynamics of the low gradient bedrock stream, which is discussed next.

6.5.2 Field investigation of sediment transport provides a concept model for bedrock barriers and sediment (dis)connectivity

Field investigation of sediment connectivity accomplished with our *WAVES* protocol shows the resistant limestone features act as sediment barriers in the low gradient system. Our field research results showed observations of the pools trapping surficial fine grained laminae as well as relatively deep consolidated deposits over bedrock. The riffles on the other hand were generally scoured to bedrock with at times a thin film of loose deposited fluvial sediment. The field observations agrees with concept of the bedrock-riffles acting as a hydraulic controls and in turn sediment barriers during most flow conditions. The energy gradient upstream of the limestone controls is near zero for baseflow and moderate storm events due to the long length of the pools relative to riffles. This sediment disconnectivity causes deposition throughout the pools with observations showing surficial fine grained laminae as well as relatively deep consolidated deposits over bedrock in pools.

Our field research results of sediment erosion and deposition patterns in the pool:riffle sequences allowed us to arrive at a conceptual model of the fluid energy gradient and action of the bedrock-riffles as sediment barriers. This concept is shown in Fig. 5. In the figure, bedrock outcrops are highlighted in red. Three different hydraulic and sediment transport conditions are shown in Fig. 5. Fig. 5a shows stream profile during low-magnitude hydraulic regimes occurs when the bedrock outcrops function as downstream hydraulic controls that form upstream pools with locally flat gradients where erosion is limited and deposition is promoted. Riffles form downstream of bedrock outcrops with relatively high velocity and low depth. Generally, only erosion of the SFGL is possible due to low supply of bed sediment in riffles and low transport capacity in the pools. Bed and bank sediment are relatively immobile. Fig 5b shows the stream profile during medium-magnitude hydraulic regimes cause bedrock outcrops to continue to function as downstream hydraulic controls, however stream depth and surface gradient in pools is generally increased. Erosion of SFGL and bed sediment in both riffles and pools is possible. Fig. 5c shows stream profile during high-magnitude hydraulic regimes cause bedrock outcrops no function as barriers of sediment transport. Erosion of SFGL, bed, and

bank sediment is possible. Deposition can occur when suspended sediment is greater than stream transport capacity.

Consistent with connectivity theory of barriers (Fryirs et al., 2013), we hypothesized thresholds occur to breach disconnectivity in the riffle-pool model shown in Fig. 5. In this manner, we represent hydraulic and sediment transport conditions when the barrier is overcome and the energy gradient of the system increases to allow greater sediment transport carrying capacity through the pools. This result adds the limestone controls to the list of barriers in connectivity discussions such as check dams and bendway weirs, with the limestone controls perhaps being specific to low gradient limestone systems.

Our numerical modelling of hydraulics allowed us to estimate pool:riffle depth ratios for the system to accompany our estimates of pool:riffle length ratio equal to 4.6. The mean pool:riffle depth for our entire stream network was found to equal 1.9, 1.9, and 1.8 for low, moderate and high flow conditions. The mean pool:riffle depth of our low gradient bedrock system contrasts findings for low gradient alluvial systems; for example one study found that the mean pool:riffle depth was 6.2 for low gradient alluvial systems (Wohl et al., 1993). The differences are attributed to the lithologic versus fluvial controls discussed in section 5.2. In addition, the mean pool:riffle depth for our systems is shown to decrease as the hydrologic regime increases, which qualitatively agrees with our concept model in Fig. 5.

6.5.3 Validation of Numerical Modeling using Field Reconnaissance

Our numerical model of probability of connectivity formula within sediment continuity equations represented the bedrock riffles as discontinuous barriers that can be breached, and sediment transport modelling results were found to agree well with our field investigation of sediment transport. Results of the WAVES field assessment and values of the observed erosion index highlight hotspots of instream erosion observed in the Upper South Elkhorn watershed (see Fig. 6a). Hotspots of erosion were observed in localized reaches throughout the Upper South Elkhorn as shown by Fig. 6a. We qualitatively compared results of the observed erosion index (Fig. 6b) with results of long-term erosion estimates from our modelling (Fig. 6c) between representative reaches 275 and 292 and found that field reconnaissance results validated results from the coupled connectivity and

continuity sediment model. We determined normalized erosion in reaches by summing total simulated erosion (kg) in reaches over the course of the simulation period and normalized erosion rates by stream length. Generally, upstream reaches (275-284) were predicted to have less instream erosion than downstream reaches (285-292), which visually agrees with findings from WAVES field reconnaissance. Interestingly, we find stream gradient between reaches 285 and 292, where observed and simulated erosion are highest, is less than stream gradient between reaches 275 and 284 (see Table 4), which suggests that long term instream erosion is more than just a function of stream gradient. This results highlights the importance of conducting both field reconnaissance and spatially explicit sediment modeling when understanding long-term erosion patterns.

Hotspots of instream deposition were also identified throughout the Upper South Elkhorn watershed, as shown by Fig. 7a using the observed deposition index. Qualitative comparison of depositional patterns in the reaches using the observed deposition index and the numerical model generally agrees for reaches 275-280, however the instream sediment model predicts increased deposition between reaches 281 and 292 which was not observed during field reconnaissance. One potential reason for this is because field reconnaissance was conducted in 2017, a year that was not particularly wet or dry for the region, while 2018, which consisted of the majority of the simulation period for the sediment model, was uncharacteristically wet. Improved field-based understanding of deposition and erosion might be ascertained by repeated reconnaissance across multiple seasons and years.

As an independent source of comparison, we compared erosion and deposition results from field reconnaissance and numerical model with the *Index of Connectivity* from Borselli et al., (2008). We derived the *IC* using the SedInConnect toolbox from Crema and Cavalli (2018).

We find that *IC* results match relatively well with findings from the observed erosion index and long-term erosion patterns determined with the numerical modelling. This result indicates that perhaps instream simulations of connectivity and erosion over long time scales might be well simulated with the index of connectivity, which agrees with findings from Mahoney et al., (2020) that long term connectivity simulations matched relatively well with *IC* values when a thresholds was applied.

Ultimately, comparison of model and field reconnaissance results helped to visualize spatially explicit erosion and deposition patterns at the reach scale over seasonal to yearly timescales.

Long-term modeling of erosion and deposition in reaches and pools indicates that approximately 83% of eroded sediment is generated from pools and 17% is generated in riffles, while approximately 86% of deposition occurs pools and 14% of deposition occurs in riffles. Riffles comprise of approximately 20% of the Upper South Elkhorn stream length whereas pools generally comprise of approximately 80% of the stream network. The model simulated approximately 0.3 m of aggradation in the stream network throughout the simulation period, which is attributed to the uncharacteristically wet study year (2018; NOAA, 2020).

6.5.4 Coupled Sediment Connectivity and Continuity Model Evaluation

Qualitative and quantitative metrics were used to evaluate the coupled connectivity and sediment continuity model structure, and both indicate that the model adequately captures sediment connectivity and sediment transport processes. Qualitative metrics include visual comparison of simulated and observed sediment flux time series over the entire simulation period and during specific transport events. Fig. 9a and 9c show simulated and observed sediment flux at the outlet of the Upper South Elkhorn watershed. Generally, visual inspection of observed and simulated time series indicates that the model accurately predicts timing of peak sediment flux. Shape of serigraphs at the outlet of the watershed for both the rising limb and falling limb also tends to be well-simulated. We find that the model tends to under-predict peak sediment flux during events, which we generally attribute to under-prediction of upland sediment generation, as predicted by Mahoney et al., (2020b). Future iterations of the model parameterization might include physical representation of upland sediment erosion rate, which is currently simulated empirically.

Quantitative evaluation of the model includes optimization of the Nash-Sutcliffe efficiency (NSE) of simulated and observed sediment flux at the watershed outlet. We found that NSE was equal to 0.35 for the simulation period, which is considered to be satisfactory to excellent (see Moriasi et al., 2007); and the reason we argue NSE to be excellent is because we were using calculations with 15 minute observations and model results, which are well regarded to not be held at NSE criteria of daily simulations (Moriasi

et al., 2007). It is noteworthy, however, that optimized NSE alone did not necessarily improve simulation of sediment flux at the watershed outlet. Specifically, we found that by increasing transport capacity coefficients of the model we could further improve NSE, but doing so led to over-prediction of sediment flux during recession periods. This result is corroborated by work from Mahoney et al., (2020b), who found that when NSE was coupled with hysteresis analysis and the hysteresis index (see Sherriff et al., 2015; Clare, 2019), sediment simulations were improved at high-temporal frequencies. This result indicates that while NSE may be a mainstay of sediment transport and watershed model evaluation, additional metrics should be considered for the next generation of high-temporal frequency sediment simulations.

Optimal parameter values for the upland connectivity model and instream connectivity and continuity model are shown in Table 4, and all fall within permissible ranges as prescribed by the literature. Optimal transport capacity coefficients tend to be on the higher-end of the permissible range for low-gradient systems. Compared to results of Mahoney et al., (2019), we find that transport capacity coefficients are approximately an order of magnitude greater than optimal coefficients determined therein. One possible reason for this is due to the very fine spatial and temporal discretization of riffle-pool sequences considered in the model framework presented herein, which explicitly simulates hydraulics in the stream network at quasi-continuous temporal scales. Modeling from Mahoney et al., (2019) considered sediment flux at daily timescales and reaches on the order of 10 km, whereas modeling presented herein considers 15-minute sediment flux and reaches on the order of 10-200 m, which was important considering we find peak sediment flux and discharge occurs on the order of several hours in the 64.1 km^2 lowland watershed.

Sensitive parameters of sediment flux include instream transport capacity coefficients ($C_{tc\,(low)}, C_{tc\,(high)}$), instream deposition coefficients (k_p, ω_s), upland sediment generation (G_{upland}), and upland sediment attenuation (A_{sed}). We find that the upland sediment generation and sediment attenuation parameters affect the magnitude and shape of sediment flux entering the stream network, and thus sensitivity to these parameters is to be expected considering that upland sediment can consist of up to 50% of sediment yield for events of high-magnitude in low gradient systems like the Upper South Elkhorn (Mahoney et al., 2019). Insensitivity of the model to routing coefficients (k_{ss}) is likely

attributed to the fine spatial and temporal discretization of the stream network considered herein.

We investigated the importance of explicitly simulating bedrock out crops, riffles, and pools by comparing instream model results where 362 reaches and riffle-pool morphology were explicitly considered (Fig. 9a, 9c) with simulations where 181 reaches and average riffle-pool slope were considered (Fig. 9b, 9d). Generally, we found that both models adequately simulated sediment flux according to traditional watershed modeling objective functions (e.g., Moriasi et al., 2007) since both models have NSE values that fall within the "satisfactory" range. An important distinction between model results, however, is that explicit simulation of riffle-pool morphology and variable stream gradient during hydraulic regimes, as derived from our conceptual model and simulated in the parameterization with 362 reaches, increased simulated peak sediment flux during high-magnitude hydrologic events and decreased sediment flux on the falling limb of hydrographs, as evidenced by visual inspection of Fig. 9c and Fig. 9d. Visual observation of the time series in Fig. 9d indicates that formulation with 181 reaches and average riffle-pool slope tends to under-predict peak sediment flux during events of high hydrologic magnitude and over-predict sediment flux on the falling limb of the serigraphs compared to the formulation with 362 reaches and explicit slope consideration. One potential explanation for this is that an average stream gradient, as simulated with 181 reaches and average riffle-pool slope, under-predicts stream energy available to erode and transport sediment in riffles during high-magnitude hydraulic regimes and over-predicts stream energy available to erode and transport sediment in pools during low-magnitude hydraulic regimes. Explicit representation of stream gradient, as shown in the simulation with 362 reaches, seemed to rectify this problem. Interestingly, NSE of the simulation with 181 reaches and average riffle-pool slope was greater than NSE of the simulation with 362 reaches and explicit representation of riffle-pool sequences, reinforcing the earlier discussion that updated evaluation metrics should be considered for high-temporal frequency simulations of sediment flux. In summary, benefits of running the model with 362 reaches and explicit riffle-pool morphology include improved simulation of peak sediment flux and shape of the falling limb of the sedigraph, in addition to the added information afforded from improved explicit representation of the stream network.

One noteworthy matter regarding logistics of running both models is that computational time for the instream continuity model parameterized for 362 reaches is approximately two times as long as the computational time for the model parameterized for 181 reaches (approximately 150 s and 70 s, respectively), which is likely due to two times the number of spatial reaches being simulated in the parameterization with 362 reaches compared to 181 reaches. While unimportant for running the model for one realization, such considerations become important when running many model realizations required for robust sensitivity and uncertainty analyses. We note, however, that both models were parameterized using the same calibration values, perhaps indicating that optimal model parameterization for simplified model structures might be applicable to more discretized structures for the lowland, bedrock controlled system. This points to perhaps simplified and faster calibration strategies in future iterations of the modelling and warrants further investigation.

6.5.5 Spatial and temporal dynamics of sediment continuity and connectivity in pools and riffles

Our high-resolution simulations elucidate spatially and temporally explicit behavior of sediment continuity dynamics due to bedrock outcrops in riffles in pools over the course of hydrologic events. To highlight differences in continuity dynamics between riffles and pools, we observed changes in $P(\gamma)$ over the course of the sediment transport event occurring between May 5, 2018 and May 8, 2018 (see Fig. 10). The May 5, 2018 event approximately corresponds to an event with 6-month recurrence interval, and has been observed previously as an event that transports important amounts of sediment (Mahoney et al., 2020b). Fig. 10a shows $P(\gamma)$ results in four reaches prior to the start of the event. Pools (e.g., reaches 281 and 291) are generally disconnected during low-flow periods and this is reflected by the result that $P(\gamma) = 0$ during this time period. Bedrock outcrops were observed to control stream gradient in pools during such hydraulic regimes during WAVES field reconnaissance. $P(\gamma)$ in riffles (e.g., reaches 282 and 292) is equal to one, indicating that little deposition occurs in the reach during low-flow conditions, which is likely due to the steep stream gradient characteristic of the riffles and low sediment input due to deposition promoted in the analogous upstream pool. Discontinuity decreases in pools during the rising limb of the hydrograph (Fig. 10b) and interestingly increases in

riffles, reflected by $P(\gamma)$ greater than zero in pools, and $P(\gamma)$ less than one in riffles. One potential reason for increased discontinuity in the riffles during the rising limb of the hydrograph is that increased stream depth in pools (and hence increased transport capacity and bed shear) and onset of erosion of the low-critical shear stress SFGL increases sediment flux into the riffle, which is greater than transport capacity of the fluid when stream depth is still relatively small.

The differences in $P(\gamma)$ between riffle 282 and 292 can be explained by structural differences in each reach (see Table 4). Specifically, reach 292 has greater slope than reach 291, and thus fluid energy is greater in reach 292 during the rising limb of the hydrograph compared to reach 282. Another potential explanation is that reach 291 (pool upstream of reach 292) is flatter than reach 281 (pool upstream of reach 282), thus more deposition likely occurs in the reach compared to 281, thus limiting sediment flux into the reach and increasing transport capacity compared to 282.

During the peak of the hydrograph (Fig. 10c) continuity is maximum in both pools and riffles, which is reflected by $P(\gamma) = 1$ in all presented reaches. Control of the bedrock outcrop to limit stream gradient is reduced due to increased flow depth such that transport capacity of the fluid increases as well as stream gradient, thus explaining the increase in predicted $P(\gamma)$. During the receding limb of the hydrograph, continuity in pools is stifled due to reestablished control of the bedrock outcrop which promotes locally flat stream gradients in the upstream pool and low flow depth, where $P(\gamma)$ is less than unity. In summary, our result is that discontinuity is characteristic in pools upstream of bedrock outcrops, and only during the rising limb and peak of the hydrograph is discontinuity breached.

Time series analysis of $P(\gamma)$ and sediment flux gives indication of frequency and duration of continuity in pools and riffles. We plot time series of $P(\gamma)$, deposition, erosion, sediment flux, and stream depth in reach 281 (pool) and reach 282 (corresponding downstream riffle) for the May 5, 2018 event (see Fig. 11). We find that $P(\gamma)$ is less than one in reach 281 for the majority of the event, indicating that discontinuity up stream of the bedrock outcrop dominates. This result is notably different than $P(\gamma)$ in riffles, where discontinuity occurs very briefly during the rising limb of the hydrograph, as previously mentioned, and remains fully continuous for the remainder of the event. It is noteworthy

that continuity of the pool is relatively brief during the May 5, 2018 event, which is important because this event has a recurrence interval of approximately one in every sixth months. Further time series analysis of continuity in pool 281 indicates that during the approximately 1.5 year simulation period, discontinuity (e.g., $p(\gamma) = 0$) occurs approximately 93 % of the time and full continuity (e.g., $P(\gamma) = 1$) only occurs 1 % of the time. Conversely, discontinuity in riffles occurs approximately 0.1 % of the time and full continuity occurs 99 % of the time.

Our finding that pools upstream of bedrock outcrops are fully continuous for only 7 % of the year puts quantitative measurements on the timescales of (dis)continuity and (dis)connectivity in stream networks due to functioning of instream barriers such as bedrock outcrops (e.g., Fryirs, 2013; Ali et al., 2018), which adds to an ongoing discussion of the importance of buffers, barriers, and blankets to control sediment connectivity and transport in watersheds (Fryirs, 2013). Fryirs (2013) defines buffers, barriers, and blankets as morphologic features that impede sediment transport in lateral, longitudinal, and vertical directions, respectively. Seldom in the literature have quantitative metrics been used to describe periods when barriers are active, however work compares relatively with study from Ali et al., (2018), who use the T-TEL method to quantify the timescales of connectivity best corroborates our work.

The sharp increase in $P(\gamma)$ (Fig. 11a), sudden cessation of deposition (Fig. 11c) and abrupt increase of erosion (Fig. 11e) in reach 281 is indicative of rapid connectivity of the bed sediments in the pool (reach 281), and points towards the idea that erosion and deposition upstream of bedrock outcrops are discontinuous processes (e.g., Grant et al., 2017) as opposed to continuous processes. One reason for abrupt changes in continuity within the pool is related to the breaching of discontinuity thresholds related to the stream depth and stream gradient within the reach. Erosion occurs abruptly in the pool strictly when stream depth increases and is terminated when stream depth begins to decrease after the peak of the hydrograph (see Fig. 11i). This notion reflects the idea that a threshold breach of discontinuity suddenly permits contribution of bed sediments, and connection prior to the threshold breach is unlikely.

This finding is corroborated by researchers who present discontinuous, as opposed to continuous, frameworks for simulating sediment transport and connectivity (Grant et al.,

2017; Schumm, 1979). For example, the seminal work of Schumm (1979) points towards the concept of thresholds to control and influence long term landscape morphology. Our findings point to the idea that thresholds (discontinuous processes) as opposed to gradients (continuous processes) are representative of instream erosion and deposition in pools upstream of bedrock outcrops.

As a second discussion point, the method presented herein offers one approach to understanding timescales of disconnectivity and thresholds when barriers are deactivated. Specifically, we find that barriers are likely active until very large hydrologic events occur when the stream depth is increasing and reactivate at the falling limb of the hydrograph. Other frameworks that analyze timescales and thresholds of connectivity include the T-TEL method from Ali et al., (2018).

We find that connectivity results differ between riffles and pools and between sediment types in time (e.g., SFGL versus bed sediment). Fig. 12 presents time series of $P(C)$ results for SFGL and bed sediments for reach 281 (pool) and 282 (riffle) for the May 5, 2018 to May 9, 2018 event. In the pool, SFGL sediments are connected (e.g., $P(C) = 1$) only for a brief period during the event, which corresponds with times when discharge and flow depth increases in the reach (Fig. 12a). Inspection of sub-process probabilities of connectivity indicates that the probability of transport ($P(T)$) limits connectivity for the majority of the event, however there are instances when the probability of detachment ($P(D)$) is equal to zero, and thus also limits connectivity. $P(T)$ and $P(D)$ being equal to zero is attributed to the low stream gradient of the pool. This result is validated by previous modeling from Russo and Fox (2012) and Mahoney et al., (2019), who found that the system was transport limited. SFGL sediments typically remain connected throughout the simulated event in the riffle (reach 282), however connectivity briefly goes to zero (i.e., disconnectivity occurs, $P(C) = 0$) at the onset of the hydrologic event when the pool initially becomes connected (Fig. 12b). When $P(C)$ is equal to zero, we find that $P(T)$ for SFGL sediment is also equal to zero, indicating that transport capacity limits connectivity briefly in the riffle. This validates our aforementioned proposition that brief disconnectivity and deposition in reach 282 are likely due to the increase of sediment entering the reach from the upstream pool (reach 281). It is noteworthy that although riffles are connected for longer durations compared to pools with respect to SFGL sediment, the magnitude of bed

connectivity may be relatively weak in these reaches, which is evidenced in Fig. 11f, which shows that large amounts of erosion occur only during larger hydraulic regimes.

In the pool, we find that bed sediments are connected for less time than SFGL sediments, which is to be expected because SFGL sediments preferentially erode in the system given their low critical shear stress and since residual transport capacity is needed to erode bed sediment (Fig. 12c). We find that both $P(T)$ and $P(D)$ limit connectivity of bed sediments in the pool, which again is attributed to the low stream energy, low fluid shear stress, and low transport capacity needed to erode and transport bed sediment. We find peak erosion rates in the bed tend to coincide with the onset of connectivity of bed sediment, which perhaps indicates that the greatest amount of erosion in the low-gradient system occurs during rare high-magnitude hydrologic events when bed sediments become connected. Interestingly, this finding points to notion that bed sediments are primarily disconnected from the sediment cascade for the majority of time, highlighting the importance of the low-gradient system to store sediment in the bed for relatively long periods of time until connectivity is abruptly reestablished and large amounts of the bed are moved at one time in pulses. This work is corroborated by Toone et al (2014) who found that bedrock outcrops tended to cause upstream deposition of courser sediments and allow passage of fine grained sediments, thus acting as a filter of suspended sediments. We find that bedrock outcrops in this system behave similarly.

The presence of SFGL sediment atop bed sediments serves as one example of a blanket (sensu Fryirs, 2013) that impedes vertical sediment transport, which we find is seldom discussed in the literature. Because SFGL sediments preferentially erode in the stream network, residual transport capacity of the fluid must accommodate first the supply of SFGL sediments and second bed sediments. In this sense, SFGL sediments use up available transport capacity of the fluid that otherwise would be available to transport bed sediment and thus limit bed connectivity.

We find that bed sediments are disconnected throughout the entire event in the riffle, as shown in Fig. 12d. Probability of supply ($P(S)$) was found to limit bed connectivity during the event, which indicates that an available supply of bed sediment for erosion is not present in the reach. One explanation for this is that bed sediments typically are only transported during high-magnitude hydrologic events, and during these instances

transport capacity in the relatively higher-gradient riffle is larger than sediment load such that sediment remains in suspension. This finding is validated by results from our field reconnaissance, which indicated that very little stored sediment was observed in riffles.

This work adds to an ongoing discussion of structural and functional controls of sediment connectivity in fluvial systems. We find that both structural and functional elements of the stream network play important roles in controlling longitudinal sediment connectivity and sediment transport during different times. Specifically, we find that structural disconnectivity from the bedrock outcrops tends to control (limit) connectivity during low-magnitude hydraulic regimes. During high-magnitude hydraulic regimes, we find the control of structural elements of the stream network diminishes as control of bedrock outcrops becomes reduced, at which point the degree of connectivity is limited by the amount of energy generated from the storm event.

Controls of instream longitudinal connectivity tend to contrast structural and functional controls of sediment connectivity in upland networks. For example, several researchers have discussed that functional connectivity limits sediment transport in watershed uplands during the majority of hydrologic events (Heckann et al., 2018; Wohl et al., 2019; Mahoney et al., 2020a, b, c). Over time, however, and during large-magnitude hydrologic events, control of sediment connectivity shifts from functional connectivity to structural connectivity because structural elements tend to serve as an upper bound of potentially connected pathways (Mahoney et al., 2020a). One reason for this contrast is due to the perennial nature of flow in the low-gradient stream network compared to the upland network, in which hydrologic connectivity is established for only brief periods when runoff occurs which is requisite for sediment connectivity in low gradient and gently rolling systems (Bracken et al., 2015; Mahoney et al., 2018).

6.6 CONCLUSION

Conclusions of this paper are as follows:

1. Field reconnaissance shows the stream profile is locally controlled by lithology for the low-gradient bedrock system studied herein. Locally resistant limestone often extends as outcrops from banks, and instream incision is less pronounced compared to limestone in nearby upstream pools. This causes local longitudinal

concavity for the streambed analogous to riffle-pool sequences in alluvial systems, however with noteworthy differences in morphology. Length of pools is approximately a half order of magnitude greater than length of bedrock "riffles". This result adds to the discussion of lithological controls on river formation, and this highly localized morphology can impact ecology and sediment dynamics of the stream.

2. Field investigation of sediment connectivity accomplished with our *WAVES* protocol shows that the resistant limestone bedrock features act as barriers in the low gradient system. The energy gradient upstream of the limestone outcrops is near-zero for baseflow and moderate storm events due to the long length of the pools relative to the riffles. Longitudinal sediment disconnectivity emerges as a result of the bedrock outcrops and promotes deposition throughout the pools, as indicated from observations of surficial fine grained laminae and relatively deep consolidated deposits over bedrock in pools. Hypothesized thresholds are proposed representing breaches of disconnectivity. This result adds the limestone bedrock controls to the list of barriers impeding longitudinal sediment transport, and perhaps is unique to low gradient limestone systems.
3. Formulation of sediment continuity using connectivity formulae allows spatial representation of sediment dynamics in riffle-pool sequences. Comparison of sediment model results with field reconnaissance validates erosion-deposition simulations. Coupling model parameterization of ground-truthed field investigations improved model results.
4. Sediment connectivity and continuity formulae adequately predicted sediment discharge at the watershed outlet at quasi-continuous timescales during the simulation period. Model configurations that did not explicitly simulate riffle-pool sequences tended to under-estimate peak sediment flux during high-magnitude hydrologic events and over-estimate sediment transport on the falling limb of hydrographs.
5. Modelling results highlight dynamics of (dis)connectivity and (dis)continuity during hydrologic events in riffles and pools. Disconnectivity and discontinuity are predominant in pools upstream of bedrock outcrops for the majority of flow

conditions, and are only briefly connected during large-magnitude hydrologic events when thresholds are breached. Riffles downstream of bedrock outcrops typically remain connected during lower-magnitude hydraulic regimes, but are supply and transport capacity limited, and thus connectivity is weak. Instream sediment connectivity is controlled by both hydraulic regime (functional connectivity) and the presence of bedrock outcrops (structural connectivity). The conceptual model derived from field reconnaissance observations improved our understanding of spatial and temporal sediment connectivity upstream of bedrock outcrops and validated limitations of sediment connectivity in riffles downstream of bedrock outcrops.

Possible future work includes quantification of feedback propagation and instream morphologic changes which manifest from interactions between upland sediment generation and instream transport capacity. Specifically, such investigations might involve understanding the impact of upland sediment flux and connectivity on the function of barriers like bedrock outcrops. Additionally, future discussions include investigation of the appropriateness of sediment flux data collected at the watershed outlet to evaluate reach-scale erosion and deposition dynamics. We posit that more sophisticated data collection, such as high-temporal resolution sediment fingerprinting might improve evaluation of such simulations. Additionally, the coupled connectivity-continuity model structure affords information that might assist with long-term sediment budgeting for the watershed uplands and stream network at seasonal-yearly time scales. Specifically, long-term analyses of erosion and deposition in riffles and pools might give insight to long term system dynamics.

6.7 APPENDIX I: WAVES Protocol sheets

Reach: **Subreach:** **Subreach Length:**

Connectivity

Erosion Scars, Rills, Gullies, Banks

Type	Extent (1 = Few)	Density	Number of Hotspots
SCAR RL GUL BE OTHER	1 2 3 4 5 6 7 8 9 10	1 2 3 4 5 6 7 8 9 10	
SCAR RL GUL BE OTHER	1 2 3 4 5 6 7 8 9 10	1 2 3 4 5 6 7 8 9 10	
SCAR RL GUL BE OTHER	1 2 3 4 5 6 7 8 9 10	1 2 3 4 5 6 7 8 9 10	

Buffers, Barriers, Blankets

Type	Extent (1 = Few)	Disconnecting	Comments
CD TR FP SLUG BAR SFGL SS OT	1 2 3 4 5 6 7 8 9 10	Y N	
CD TR FP SLUG BAR SFGL SS OT	1 2 3 4 5 6 7 8 9 10	Y N	
CD TR FP SLUG BAR SFGL SS OT	1 2 3 4 5 6 7 8 9 10	Y N	

Stream Banks and Floodplains

Outfalls

Type	Active	Effluent	Diameter (inch)	Comments
CUL TD STRM P OTHER	Y N	Y N		
CUL TD STRM P OTHER	Y N	Y N		
CUL TD STRM P OTHER	Y N	Y N		

Vegetation/Riparian Buffer

Type	Root Depth (1 = Shallow Roots)	Density (1 = Few)	Extent	Comments
S T G BST FR	1 2 3 4 5 6 7 8 9 10	1 2 3 4 5 6 7 8 9 10		
S T G BST FR	1 2 3 4 5 6 7 8 9 10	1 2 3 4 5 6 7 8 9 10		
S T G BST FR	1 2 3 4 5 6 7 8 9 10	1 2 3 4 5 6 7 8 9 10		

Streambank Condition

Extent	Bank Angle	Bank Cover (1=bad)	Bank Stability	Incision	Comments
	< 15 30 45 60 75 > 90	1 2 3 4 5 6 7 8 9 10	1 2 3 4 5 6 7 8 9 10	Y N	
	< 15 30 45 60 75 > 90	1 2 3 4 5 6 7 8 9 10	1 2 3 4 5 6 7 8 9 10	Y N	
	< 15 30 45 60 75 > 90	1 2 3 4 5 6 7 8 9 10	1 2 3 4 5 6 7 8 9 10	Y N	

Restorative Measures

Type	Effectiveness (1 = Ineffective)	Extent (1=Sparse)	Comments
RIP GAB REST	1 2 3 4 5 6 7 8 9 10	1 2 3 4 5 6 7 8 9 10	
RIP GAB REST	1 2 3 4 5 6 7 8 9 10	1 2 3 4 5 6 7 8 9 10	

Shade/Coverage

Extent	Shade Coverage (1 = Poor)	Comments
	1 2 3 4 5 6 7 8 9 10	
	1 2 3 4 5 6 7 8 9 10	

Livestock in Stream Corridor

Interference	Coordinates	Livestock Type	Number	Comments
Y N		Cow Goat Horse Other		

Entering Tributaries

Tributary Bank Angle	Trib Incision	Bank Erosion	Comments
< 15 30 45 60 75 > 90	Y N	1 2 3 4 5 6 7 8 9 10	
< 15 30 45 60 75 > 90	Y N	1 2 3 4 5 6 7 8 9 10	
< 15 30 45 60 75 > 90	Y N	1 2 3 4 5 6 7 8 9 10	

Stream Bed

Sediment Storage in Streambed

Storage Type	Lateral Extent	Long Extent	Diversity	Depth (cm)
SFGL BAR THIN DEEP OTHER	1 2 3 4 5 6 7 8 9 10	1 2 3 4 5 6 7 8 9 10	1 2 3 4 5 6 7 8 9 10	
SFGL BAR THIN DEEP OTHER	1 2 3 4 5 6 7 8 9 10	1 2 3 4 5 6 7 8 9 10	1 2 3 4 5 6 7 8 9 10	
SFGL BAR THIN DEEP OTHER	1 2 3 4 5 6 7 8 9 10	1 2 3 4 5 6 7 8 9 10	1 2 3 4 5 6 7 8 9 10	

Stream Bed

Bed Material

Bed Material	Extent	Depth (1=thin)	Roughness (cm)	Comments
FINE SAND GRV COB BR HCM OTHER		1 2 3 4 5 6 7 8 9 10	< 1 2 4 6 8 > 10	
FINE SAND GRV COB BR HCM OTHER		1 2 3 4 5 6 7 8 9 10	< 1 2 4 6 8 > 10	
FINE SAND GRV COB BR HCM OTHER		1 2 3 4 5 6 7 8 9 10	< 1 2 4 6 8 > 10	

Channel Dimensions

Extent	Approx Width (m)	Approx Depth (m)	Comments

Algae

Type	Lateral Extent	Long Extent	Comments
Benthic Bloom Other	1 2 3 4 5 6 7 8 9 10	1 2 3 4 5 6 7 8 9 10	
Benthic Bloom Other	1 2 3 4 5 6 7 8 9 10	1 2 3 4 5 6 7 8 9 10	

Comments:

Leaves and Detritus

Lateral Coverage (%)	Longitudinal Coverage (%)	Type	Comments
10 20 30 40 50 60 70 80 90 100	10 20 30 40 50 60 70 80 90 100		

Morphology

Riffles	Runs	Pools	Diversity (1=Homogenous)	Comments
			1 2 3 4 5 6 7 8 9 10	

Upland Land Use

Noticed Upstream Erosion

Type	Extent (1 = Few)	Density	Land Use
SCAR RL GUL BE OTHER	1 2 3 4 5 6 7 8 9 10	1 2 3 4 5 6 7 8 9 10	UR UI UC AG PAST RC

Irrigation

Type	Coordinates	Comments
INT DIT		

Agriculture

Extent	Type	Management	Comments
	RC PAST OTHER	1 2 3 4 5 6 7 8 9 10	
	RC PAST OTHER	1 2 3 4 5 6 7 8 9 10	

Miscellaneous

Karst Features

Type	Coordinates	Comments
SP SW SI OTHER SP SW SI OTHER SP SW SI OTHER		

Habitat/Ecosystem

Available Cover (1= Bad Cover)	Aquatic Life (1 = None)	Extent	Comments
1 2 3 4 5 6 7 8 9 10	1 2 3 4 5 6 7 8 9 10		
1 2 3 4 5 6 7 8 9 10	1 2 3 4 5 6 7 8 9 10		

Water Quality

Appearance (1 = Poor)	Turbidity (1 = Turbid)	Comments
1 2 3 4 5 6 7 8 9 10	1 2 3 4 5 6 7 8 9 10	

Misc.

Item	Location	Comments

Downstream Controls

Reach:	Intermitten Reach:	Length:	
Bed Rock Outcrop			
Longitudinally Connected	Approx Lenth (m)	Approx Width (m)	Comments
Y N			*Get up and downstream coordinates
Debris			
Longitudinally Connected	Approx Lenth (m)	Extent (1 = Few Debris)	Comments
Y N		1 2 3 4 5 6 7 8 9 10	*Get coordins.
Check Dam			
Longitudinally Connected	Dam Type	Sed. Buildup (1 = Little Sed)	Comments
Y N		1 2 3 4 5 6 7 8 9 10	*Get coord
Misc. Downstream Control			
Longitudinally Connected	Comments		
Y N	*Get Coordinates		

Notes: (i.e. Weather, flow rate, etc.)

List of Acronyms

Connectivity	Erosion	SCAR	Erosion Scar
		RL	Rill Erosion
		GL	Gully Erosion
		BE	Bank Erosion
	Buffers, Barriers, Blankets	CD	Check Dam
		TR	Terrace
		FP	Disconnected Floodplain
		SLUG	Sediment Slug
		BAR	Sand/Sediment Bar
		SFGL	Surface Fine Grain Laminae
		OT	Limestone Outcrop
		SS	Sediment Sheet
Streambanks and Floodplains	Outfalls	CUL	Culvert
		STRM	Stormwater Outlet
		TD	Tile Drain
		P	Misc. Pipe
	Restorative Measures	RIP	Rip Rap
		GAB	Gabion Baskets
		REST	Other Restoritive Methods
	Vegetation/Riparian Buffer	S	Shrubs
		T	Trees
		G	Grasses
		BST	Buffer Strip
		FR	Forrest
Streambed	Sediment Storage in Streambed	SFGL	Surface Fine Grain Laminae
		BAR	Sand/Sediment Bar
		THIN	Thin Sediment Layer on Channel Bottom
		DEEP	Deep Bed Deposit
	Bed Material	FINE	Fine Material (Clay, Silt)
		SAND	Sandy Material
		GRV	Gravel Material
		COB	Cobble Material
		HCM	Hard Consolidated Material
		BR	Bed Rock
Watershed Land Use	Noticed Upstream Erosion & Agriculture	UR	Urban - Resdiential
		UI	Urban - Industrial
		UC	Urban - Commercial
		AG	Agriculture
		PAST	Pasture
		RC	Row Crop
	Irrigation	IN	Intake
		DIT	Irrigation Ditch/canal
Misc.	Karst Features	SP	Spring
		SW	Swallet
		SI	Sink hole

6.8 APPENDIX II: EQUATIONS OF THE INSTREAM SEDIMENT TRANSPORT MODEL

$$Q_i^j = \frac{1}{n_j}\frac{(A_i^j)^{5/3}}{(P_i^j)^{2/3}}(S_j)^{1/2} \quad \text{(A.1)}$$

$$B_i^j = B_{i-1}^j + Ed_i^j \quad \text{(A.2)}$$

$$SS_i^j = SS_{i-1}^j + \sum_{k=1}^{N} E_{i\,(k)}^j - D_i^j + Q_{ssin_i}^j\,\Delta t - Q_{ssout_i}^j\,\Delta t \quad \text{(A.3)}$$

$$Tc_i^j = C_{Tc}\,(\tau_{f_i}^j)^{1.5}\,L_{reach_j}\,\Delta t \quad \text{(A.4)}$$

$$Tc_i^j > SS_{i-1}^j, \quad \text{(A.5)}$$

$$Tc_i^j < SS_{i-1}^j \quad \text{(A.6)}$$

$$Tc_{(k)_i}^j = Tc_{(k-1)_i}^j - E_{(k)_i}^j \quad \text{(A.7)}$$

$$E_{(k)_i}^j = \min[a_{(k)}\left(\tau_{f_i}^j - \tau_{cr_{(k)_i}}^j\right)^b SA_{(k)_i}^j\,\Delta t, Tc_{(k)_i}^j, S_{(k)_i}^j] \quad \text{(A.8)}$$

$$\tau_{f_i}^j = C_{\tau(1)}(\rho g R_i^j S_j + C_{\tau(2)}\rho\left(\frac{u_i^j - u_{i-1}^j}{\Delta t}\right)R_i^j) \quad \text{(A.9)}$$

$$C_{\tau(bed)} = 4.05 * 10^{-6}\left(\frac{B_i^j}{H_i^j}\right)^6 + 2.1201 * 10^{-4}\left(\frac{B_i^j}{H_i^j}\right)^5 - 4.37492 * 10^{-3}\left(\frac{B_i^j}{H_i^j}\right)^4 + 0.04505583\left(\frac{B_i^j}{H_i^j}\right)^3 - 0.241185\left(\frac{B_i^j}{H_i^j}\right)^2 + 0.58925899\left(\frac{B_i^j}{H_i^j}\right)^1 + 1.00975426$$

$$if\ C_{\tau(bed)} > 1.5, then\ C_{\tau(bed)} = 1.5 \quad \text{(A.10)}$$

$$C_{\tau(bank)} = 2.4825 * 10^{-3}\left(\frac{B_i^j}{H_i^j}\right)^2 - 0.0773109\left(\frac{B_i^j}{H_i^j}\right)^1 + 1.6$$

$$if\ C_{\tau(bank)} > 1.5, then\ C_{\tau(bank)} = 1.5 \quad \text{(A.11)}$$

$$E_{SFGL_i}^j = \min[a_{SFGL}\left(\tau_{f_i}^j - \tau_{cr_{SFGL_i}}^j\right)^b SA_{SFGL_i}^j\,\Delta t, Tc_{SFGL_i}^j, S_{SFGL_i}^j] \quad \text{(A.12)}$$

$$S_{SFGL_i}^j = S_{SFGL\,sediment_i}^j - S_{SFGL\,biology_i}^j \quad \text{(A.13)}$$

$$S_{SFGL\,sediment_i}^j = \min[\left(S_{SFGL\,sediment_{i-1}}^j - E_{SFGL\,sediment_i}^j + D_{SFGL\,sediment_i}^j\right), S_{SFGL\,sediment\ max}] \quad \text{(A.14)}$$

$$S_{SFGL\,biology_i}^j = \min[\left(S_{SFGL\,biology_{i-1}}^j - E_{SFGL\,biology_i}^j + D_{SFGL\,biology_i}^j + G_{SFGL\,sediment}\right),\ S_{SFGL\,biology\ max}] \quad \text{(A.15)}$$

$$E_{Bed_i}^j = \min[a_{Bed}\left(\tau_{f_i}^j - \tau_{cr_{Bed_i}}^j\right)^b SA_{Bed_i}^j\,\Delta t, Tc_{Bed_i}^j, S_{Bed_i}^j] \quad \text{(A.16)}$$

$$S_{bed_i}^j = S_{bed_{i-1}}^j + D_{bed_{i-1}}^j - E_{bed_{i-1}}^j \quad \text{(A.17)}$$

$$E_{Bank_i}^j = \min[a_{Bank}\left(\tau_{f_i}^j - \tau_{cr_{Bank_i}}^j\right)^b SA_{Bank_i}^j\,\Delta t, Tc_{Bank_i}^j] \quad \text{(A.18)}$$

$$D_i^j = \frac{\omega_s\,\Delta t}{K p_i^j H_i^j}\,(SS_{i-1}^j - Tc_i^j) \quad \text{(A.19)}$$

$$z^{*}{}_i^j = \frac{ws}{K\,U_{*_i}^j} \quad \text{(A.21)}$$

$$U_{*_i}^j = \left(g\,H_i^j\,S_j\right)^{0.5} \quad \text{(A.22)}$$

$$P_{Upland}{}_i^j = \frac{(Qssup_i^j + Qssup_i^{j-1}) * \Delta t}{\sum_{k=1}^{N}(E_i{}_{(k)}^j + E_i{}_{(k)}^{j-1})} * (1 - Exf) \quad \text{(A.23)}$$

$$P_{Bed}{}_i^j = 1 - P_{Upland}{}_i^j \quad \text{(A.24)}$$

6.9 APPENDIX III: LIST OF SYMBOLS

ρ_w	=	density of fluid
$\rho bank$	=	density of bank sediment
ρ_{SFGL}	=	density of SFGL sediment
P_i^j	=	wetted peremeter
B_i^j	=	channel width
Ed_i^j	=	erosion/deposition from/to the banks
Exf	=	sediment exchange factor
j	=	a particular stream-reach
i	=	a particular time step
k	=	the sediment source
N	=	number of sediment sources
SS	=	mass of sediment
E	=	erosion
D	=	deposition
$Q_{ss\ in}$	=	sediment flow rate in the reach
$Q_{ss\ up}$	=	sediment flow rate in the reach from the uplands
$Q_{ss\ out}$	=	sediment flow rate out of the reach
S_{bed}	=	mass of bed sediments
Δt	=	the time step
T_c	=	transport capacity
C_{Tc}	=	transport capacity coefficient
L_{reach}	=	length of the spatial step
k	=	a particular sediment source
a_k	=	erodibility of the source
SA	=	surface area of the sediment source
S	=	supply of a sediment source
$C_{\tau(1)}$	=	coefficient accounting for the difference between bed and banks erosion
H	=	flow depth
R	=	hydraulic radius
u	=	flow velocity
S_{SFGL}	=	supply to the SFGL layer
$S_{SFGL\ sediment}$	=	supply to the SFGL sediment layer
$S_{SFGL\ biology}$	=	supply to the SFGL biofilm layer
S_{bed}	=	supply to the bed layer
z^*	=	rouse number
U_*	=	friction velocity

P_{Upland}	=	percent of exported sediment from the uplands
P_{Bed}	=	percent of exported sediment from the bed
$C_{\tau(2)}$	=	shear stress coefficient for unsteady flow
$C_{tc(low)}$	=	transport capacity coefficient for low flows
$C_{tc(high)}$	=	transport capacity coefficient for high flows
ω_s	=	mean settling velocity of suspended material
κ	=	von Karmen coefficient
$D_{SFGL,\ max}$	=	maximum depth of SFGL
t_d	=	development time of the SFGL layer
$G_{SFGL,\ Bio}$	=	generation rate of SFGL biofilm
$\tau_{cr(sfgl)}$	=	critical shear of the SFGL source
$\tau_{cr(bed)}$	=	critical shear of the bed source
$\tau_{cr(bank)}$	=	critical shear of the bank source
$a_{(sfgl)}$	=	erodibility of the SFGL source
$a_{(bed)}$	=	erodibility of the bed source
$a_{(bank)}$	=	erodibility of bank source
k_{ss}	=	sediment routing coefficient
k_s	=	flood wave coefficient
N_{reach}	=	number of reaches in the stream segment
Θ	=	bank sideslope
B_{upper}	=	channel bottom width, upper catchment
B_{lower}	=	channel bottom width, lower catchment
n_{upper}	=	manning's coefficient, upper catchment
n_{lower}	=	manning's coefficient, lower catchment
S_{upper}	=	channel slope, upper catchment
S_{lower}	=	channel slope, lower catchment
$L_{reach,\ upper}$	=	channel length, upper catchment
$L_{reach,\ lower}$	=	channel length, lower catchment
$H_{bank,\ upper}$	=	bankfull depth, upper catchment
$H_{bank,\ lower}$	=	bankfull depth, lower catchment
$Q_{boundary,\ upper}$	=	boundary flow, upper catchment
$Q_{boundary,\ lower}$	=	boundary flow, upper catchment
K_p	=	settling depth coefficient

Table 6.1. High-resolution data used to simulate instream connectivity, continuity, and sediment flux.

Data Type	Resolution	Collection Method
Digital Elevation Model	1.5 m by 1.5 m	LiDAR (KYAPED, 2014)
Total Suspended Solids Samples	7 hours	Teledyne ISCO Sampler
Turbidity	15 minutes	YSI 6-Series Optical Sensor; YSI EXO Series Optical Sensor
Upland Flux Simulation	15 minutes	Connectivity model (see Mahoney et al., 2020a,b)
Upland Connectivity Simulation	15 minutes	Connectivity model (see Mahoney et al., 2020)
Stream Bathymetry	Reach	Field reconnaissance, remote sensing
Discharge	15 minutes	USGS Gage 03289000
Precipitation	Hourly	NOAA Lexington Bluegrass Airport Station

Table 6.2. Connectivity and continuity model inputs and parameters.

Parameter	Description	Value/Parameter Range	Units
ρ_w	Density of fluid	1000	kg m^{-3}
ρ_{bank}	Density of bank sediment	1500	kg m^{-3}
ρ_{SFGL}	Density of SFGL sediment	1,000	kg m^{-3}
$C_{\tau(2)}$	Shear stress coefficient for unsteady flow	1-100	Unitless
$C_{tc(low)}$	Transport capacity coefficient for low flows	6.0 x 10^{-7}- 4.0 x 10^{-6}	$m^{1/2}$ s^2 $kg^{-1/2}$
$C_{tc(high)}$	Transport capacity coefficient for high flows	6.0 x 10^{-7}- 4.0 x 10^{-6}	$m^{1/2}$ s^2 $kg^{-1/2}$
ω_s	Mean settling velocity of suspended material	0.00036-0.00240	m s^{-1}
κ	Von Karmen coefficient	0.4	Unitless
$D_{SFGL,\ max}$	Maximum depth of SFGL	0.001-0.010	m
t_d	Development time of the SFGL layer	300-3000	s
$G_{SFGL,Bio}$	Generation rate of SFGL biofilm	1.81 x 10^{-9}	kg m^{-2} s^{-1}
$\tau_{cr(sfgl)}$	Critical shear of the SFGL source	0.024-1.20	Pa
$\tau_{cr(bed)}$	Critical shear of the bed source	1.0-10.0	Pa
$\tau_{cr(bank)}$	Critical shear of the bank source	10.0-93.0	Pa
$a_{(sfgl)}$	Erodibility of the SFGL source	1.0 x 10^{-4}-1.0 x 10^{-2}	kg Pa^{-2} m^{-2} s^{-1}
$a_{(bed)}$	Erodibility of the bed source	1.0 x 10^{-5}-1.0 x 10^{-3}	kg Pa^{-2} m^{-2} s^{-1}
$a_{(bank)}$	Erodibility of bank source	1.0 x 10^{-6}-2.0 x 10^{-4}	kg Pa^{-2} m^{-2} s^{-1}
k_{ss}	Sediment routing coefficient	0.00-0.50	Unitless
N_{reach}	Number of reaches in the stream segment	181, 362	Unitless
K_p	Settling depth coefficient	0.10-1.0	Unitless
Θ	Bank sideslope	16.9	°
B	Channel bottom width	Varies	m
n	Manning's coefficient	0.03	Unitless
S	Channel slope	Varies	m m^{-1}
L_{reach}	Channel length	Varies	m
$H_{bank,\ upper}$	Bankfull depth	Varies	m
$Q_{boundary}$	Boundary flow	Varies	m^3 s^{-1}
A_{sed}	Upland sediment attenuation coefficient	0.0-10.0	Unitless
β_{SFGL}	SFGL barrier threshold coefficient	0.0-1.0	Unitless
β_{Bed}	Bed barrier threshold coefficient	0.0-1.0	Unitless
β_{Bank}	Bank barrier threshold coefficient	0.0-1.0	Unitless
λ_{Slope}	Slope threshold coefficient	Varies	m^3 s^{-1} m^{-2}

Table 6.3. Representative reach structural properties.

Reach Number	Slope ($m\ m^{-1}$)	Width (m)	Length (m)	Sinuosity ($m\ m^{-1}$)	L:W ($m\ m^{-1}$)	Morphology
275	0.0026	10	167	1.09	16.66	Pool
276	0.0035	10	17	1.09	1.71	Riffle
277	0.0075	10	44	1.08	4.40	Pool
278	0.0165	10	20	1.08	1.95	Riffle
279	0.0033	10	20	1.06	2.02	Pool
280	0.0088	10	10	1.06	0.95	Riffle
281	0.0006	10	185	1.22	18.48	Pool
282	0.0105	10	54	1.22	5.43	Riffle
283	0.0028	10	198	1.19	19.82	Pool
284	0.0028	10	26	1.19	2.64	Riffle
285	0.0020	10	139	1.16	13.92	Pool
286	0.0046	10	29	1.16	2.95	Riffle
287	0.0001	10	48	1.09	4.82	Pool
288	0.0020	10	18	1.09	1.84	Riffle
289	0.0001	10	63	1.13	6.32	Pool
290	0.0115	10	18	1.13	1.81	Riffle
291	0.0002	13	369	1.20	28.39	Pool
292	0.0170	13	16	1.20	1.22	Riffle

Table 6.4. Optimal parameter values for upland connectivity model and instream connectivity and continuity model.

Parameter	Description	Value/Parameter Range	Units
$C_{\tau(2)}$	Shear stress coefficient for unsteady flow	85	Unitless
$C_{tc(low)}$	Transport capacity coefficient for low flows	4×10^{-6}	$m^{1/2} s^2 kg^{-1/2}$
$C_{tc(high)}$	Transport capacity coefficient for high flows	4×10^{-6}	$m^{1/2} s^2 kg^{-1/2}$
ω_s	Mean settling velocity of suspended material	0.00079	$m\ s^{-1}$
κ	Von Karmen coefficient	0.4	Unitless
$D_{SFGL,\ max}$	Maximum depth of SFGL	0.002	m
t_d	Development time of the SFGL layer	1010	s
$G_{SFGL,Bio}$	Generation rate of SFGL biofilm	1.81×10^{-9}	$kg\ m^{-2}\ s^{-1}$
$\tau_{cr(sfgl)}$	Critical shear of the SFGL source	0.11	Pa
$\tau_{cr(bed)}$	Critical shear of the bed source	5.68	Pa
$\tau_{cr(bank)}$	Critical shear of the bank source	12.69	Pa
$a_{(sfgl)}$	Erodibility of the SFGL source	7.54×10^{-3}	$kg\ Pa^{-2}\ m^{-2}\ s^{-1}$
$a_{(bed)}$	Erodibility of the bed source	5.84×10^{-4}	$kg\ Pa^{-2}\ m^{-2}\ s^{-1}$
$a_{(bank)}$	Erodibility of bank source	1.64×10^{-4}	$kg\ Pa^{-2}\ m^{-2}\ s^{-1}$
k_{ss}	Sediment routing coefficient	0.35	Unitless
K_p	Settling depth coefficient	0.98	Unitless
A_{sed}	Upland sediment attenuation coefficient	5	Unitless
β_{SFGL}	SFGL barrier threshold coefficient	0	Unitless
β_{Bed}	Bed barrier threshold coefficient	0.02	Unitless
β_{Bank}	Bank barrier threshold coefficient	0.25	Unitless
λ_{Slope}	Slope threshold coefficient	$\overline{Q_{norm,\ j}} + 4 \cdot \sigma_{norm\,j}$	$m^3\ s^{-1}\ m^{-2}$

Figure 6.1. Upper South Elkhorn watershed. The Upper South Elkhorn watershed (61.4 km^2) is located in the Kentucky River Basin of Kentucky, USA. We discretized the watershed into 181 catchments based on the location of bedrock outcrops. USGS gage 0328900 and the University of Kentucky SENSE station monitor water quality and discharge at the watershed outlet.

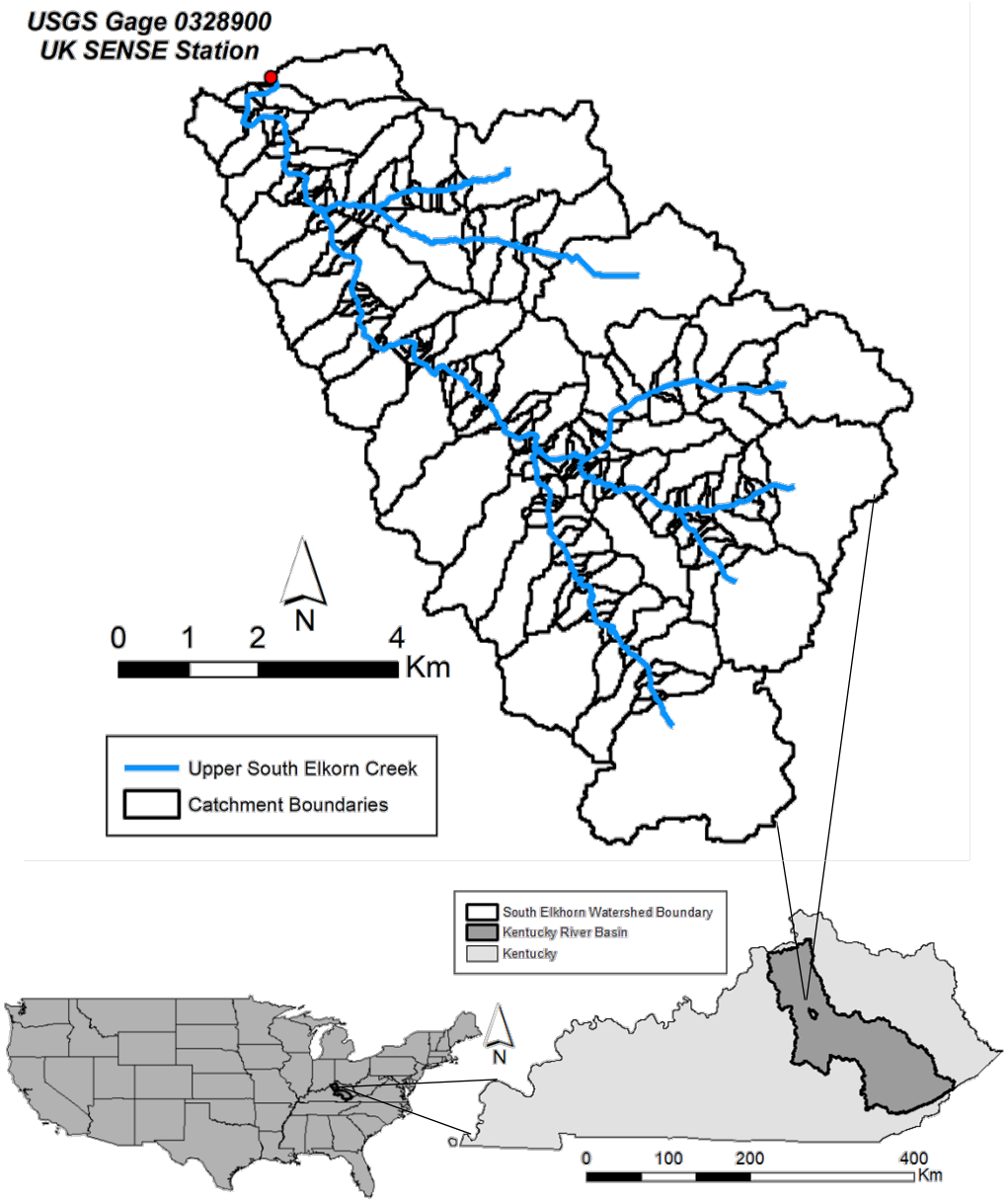

Figure 6.2. Upper South Elkhorn geospatial data including: (a) elevation (KYAPED, 2014); (b) slope (m m^{-1}); (c) land cover and land use (NLCD, 2007); and (d) lithology. Bedrock consists primarily fossiliferous limestone with interbedded shale. Land use is approximately 55% agriculture and forest and 45% urban land.

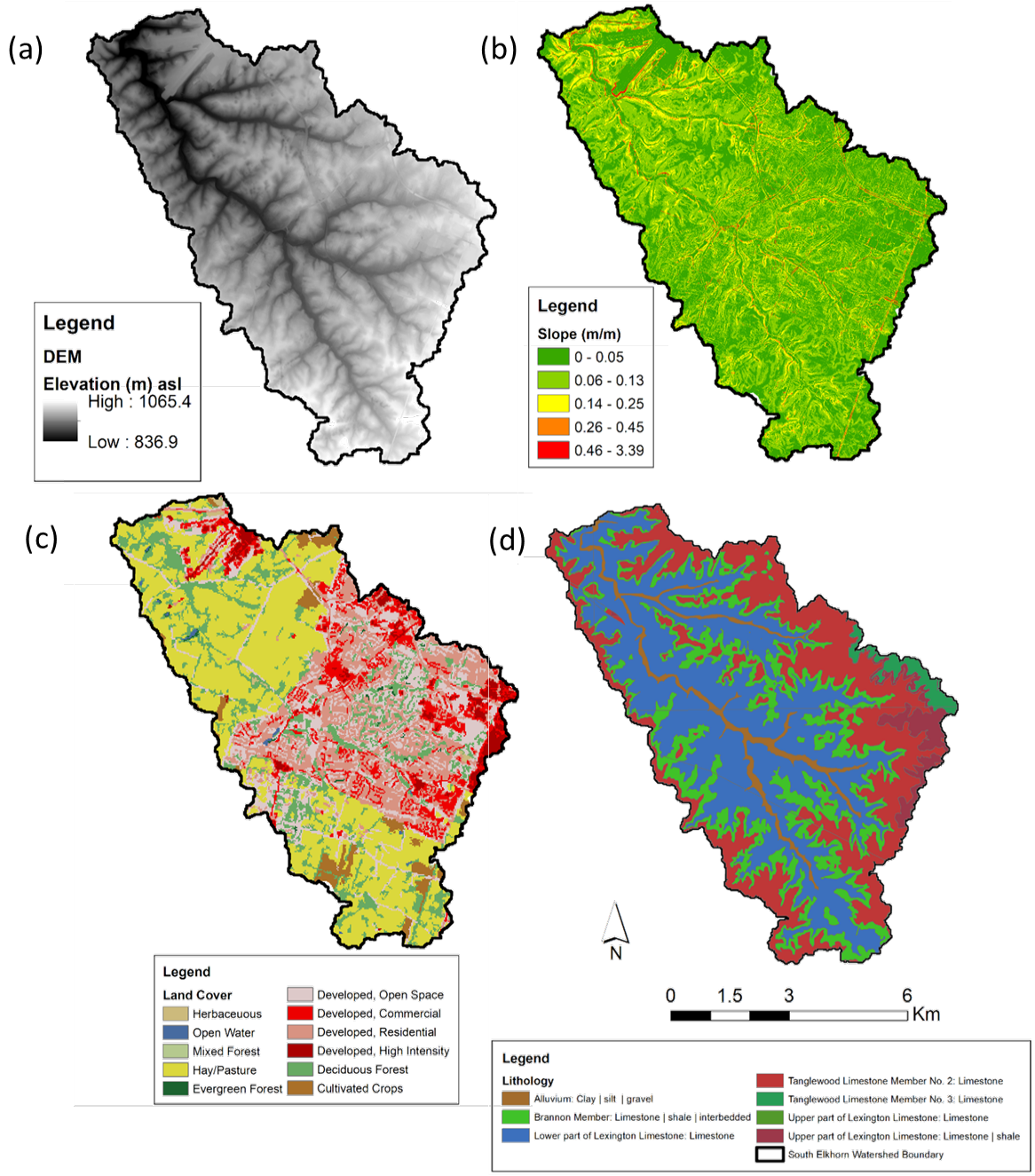

Figure 6.3. Model evaluation procedure. Upland sediment erosion and connectivity is predicted following methods presented in Mahoney et al., (2020).

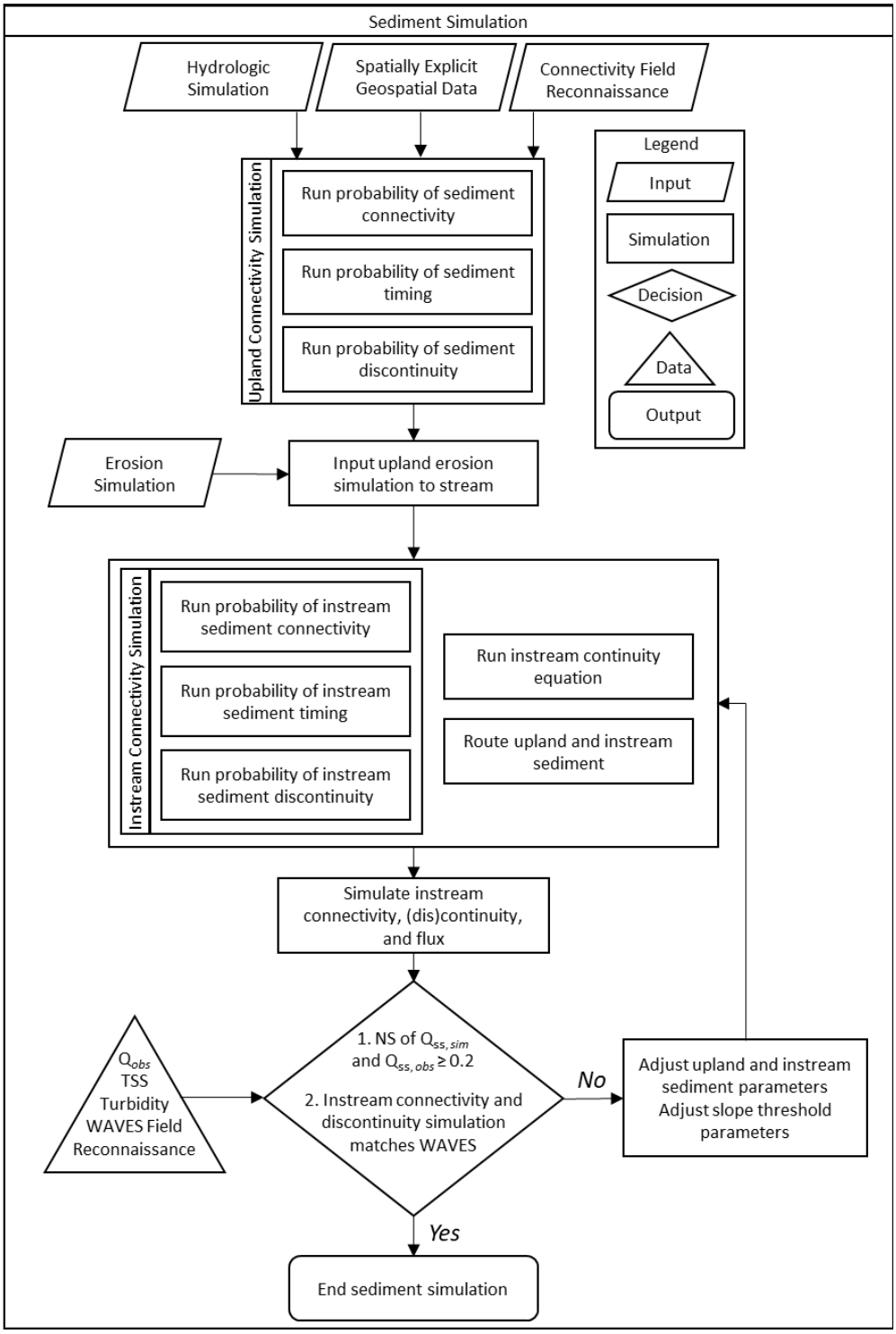

Figure 6.4. Identification of bedrock outcrops, pools and riffles in the Upper South Elkhorn watershed from *WAVES* visual assessment. 181 catchments and 362 reaches were identified in the Upper South Elkhorn watershed based on the location of bedrock outcrops that form pools (odd numbered reaches) and riffles (even numbered reaches) using the *WAVES* protocol. Each catchment consists of one pool and one riffle, which were explicitly represented during instream sediment modeling. We show several representative reaches in the watershed and a bedrock outcrop, as identified during field reconnaissance.

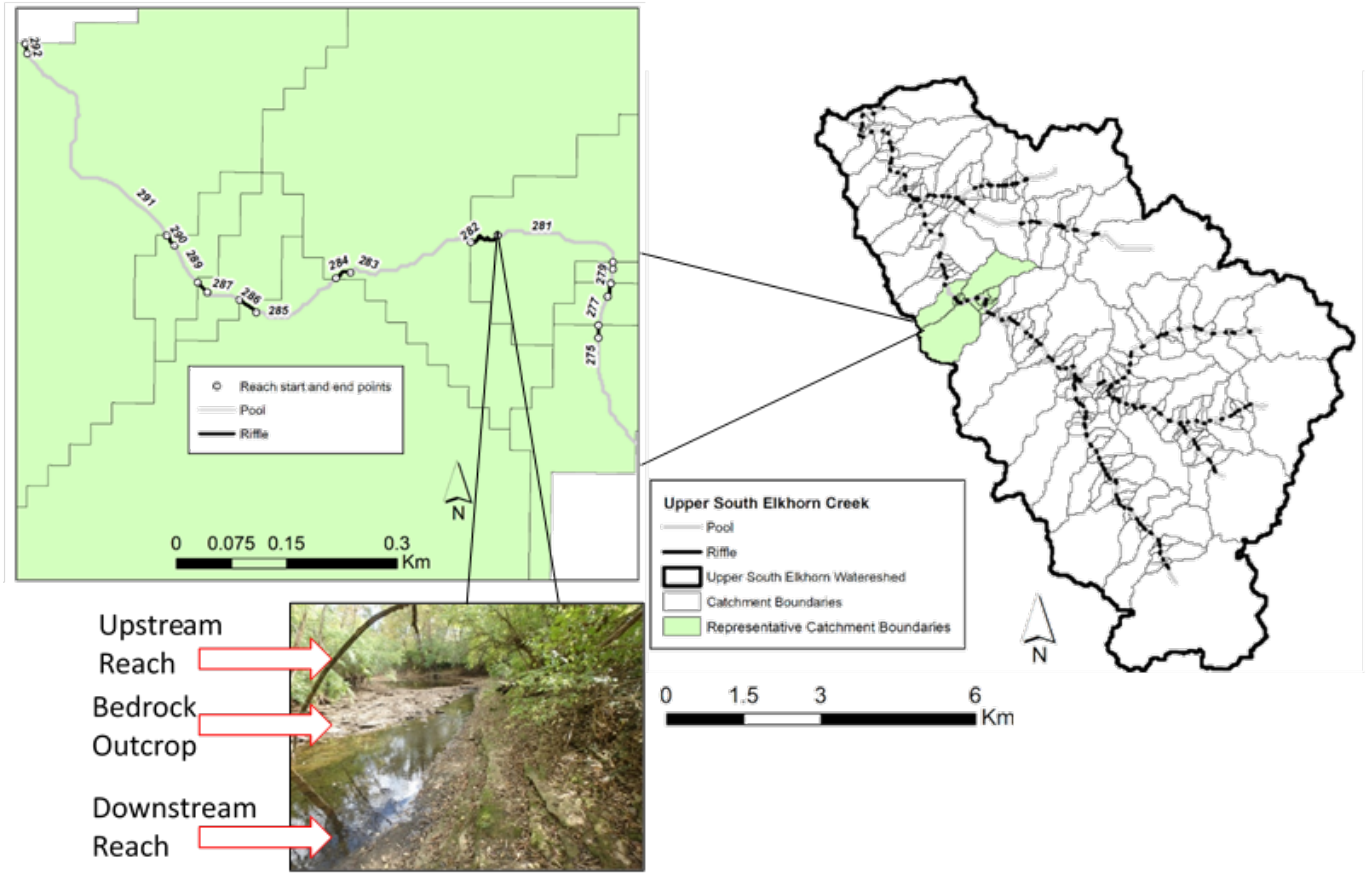

Figure 6.5. Conceptual model of stream hydraulics and sediment transport controlled by bedrock outcrops derived from *WAVES* field assessment. Bedrock outcrops are highlighted in red. *WAVES* assessment identified greater amounts of stored SFGL and bed sediments in pools upstream of bedrock outcrops compared to riffles downstream of bedrock outcrops, which is reflected in the figure. (a) Stream profile during low-magnitude hydraulic regimes. Bedrock outcrops function as downstream hydraulic controls that form upstream pools with locally flat gradients where erosion is limited and deposition is promoted. Riffles form downstream of bedrock outcrops with relatively high velocity and low depth. Generally, only erosion of the SFGL is possible due to low supply of bed sediment in riffles and low transport capacity in the pools. Bed and bank sediment are relatively immobile. (b) Stream profile during medium-magnitude hydraulic regimes. Bedrock outcrops continue to function as downstream hydraulic controls, however stream depth and surface gradient in pools is generally increased. Erosion of SFGL and bed sediment in both riffles and pools is possible. (c) Stream profile during high-magnitude hydraulic regimes. Bedrock outcrops no function as barriers of sediment transport. Erosion of SFGL, bed, and bank sediment is possible. Deposition can occur when suspended sediment is greater than stream transport capacity.

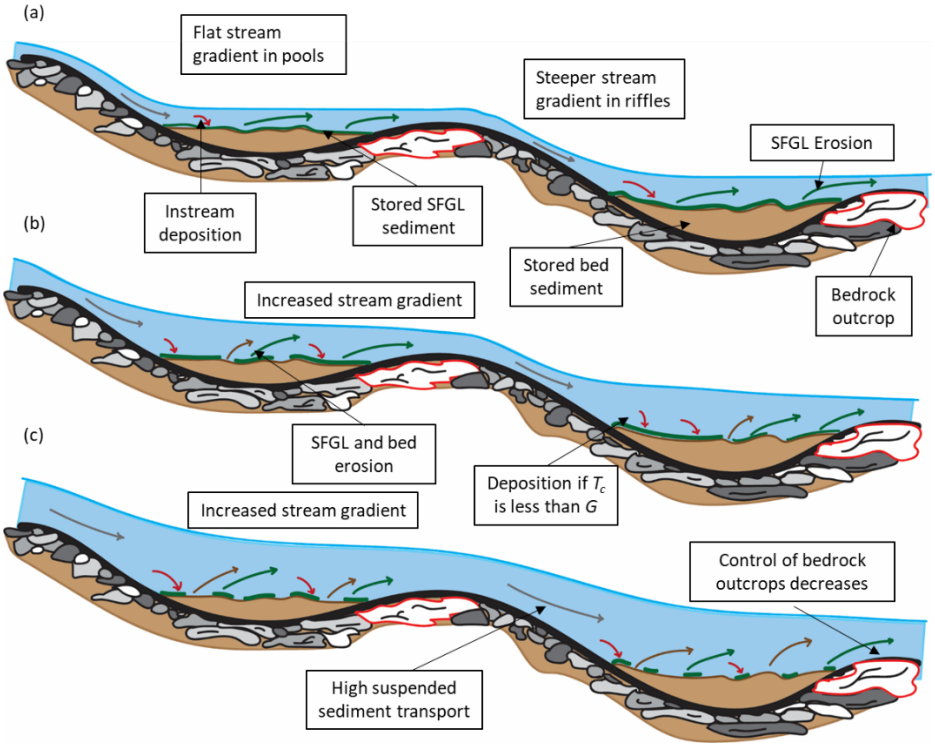

Figure 6.6. Comparison of observed erosion identified during *WAVES* field reconnaissance with total erosion simulated over the entire study period. Hotspots of instream erosion are shown in red. (a) Observed erosion index determined using the *WAVES* protocol for the entire Upper South Elkhorn watershed. (b) Observed erosion index for representative reaches in the Upper South Elkhorn. (c) Total simulated erosion (kg m^{-1}) normalized by reach length in representative reaches throughout the simulation period.

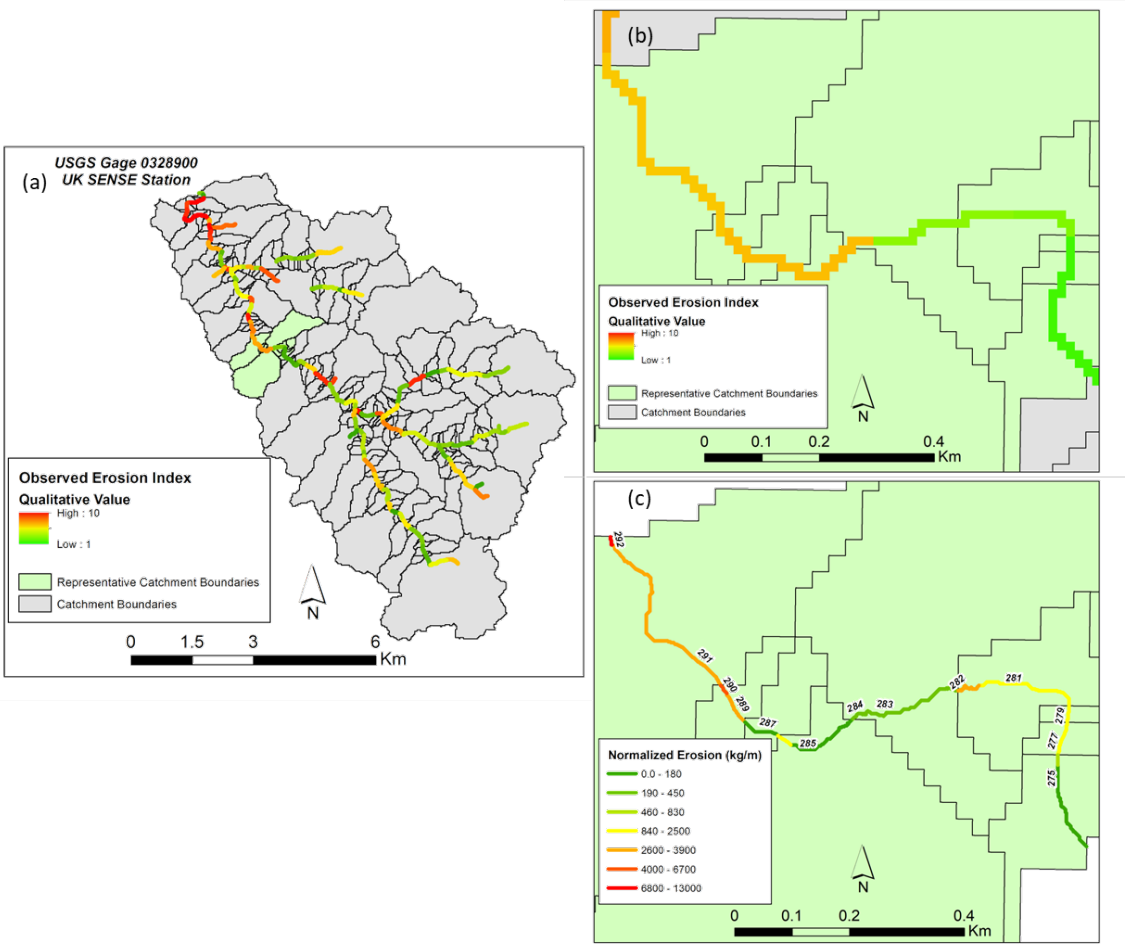

Figure 6.7. Comparison of observed deposition identified during *WAVES* field reconnaissance with total deposition simulated over the entire study period. Hotspots of instream deposition are shown in red. (a) Observed deposition index determined using the *WAVES* protocol for the entire Upper South Elkhorn watershed. (b) Observed deposition index for representative reaches in the Upper South Elkhorn. (c) Total simulated deposition (kg m^{-1}) normalized by reach length in representative reaches throughout the simulation period.

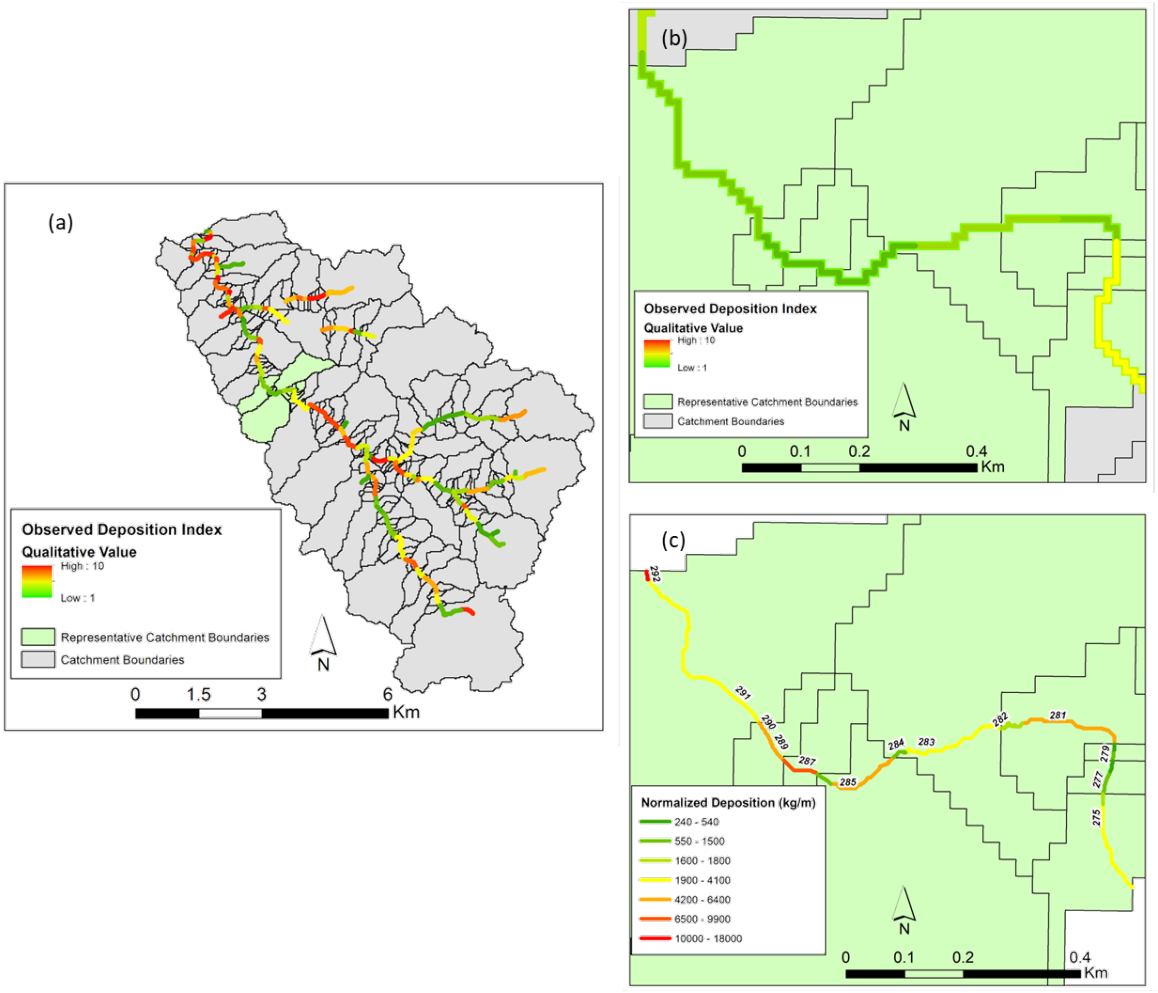

Figure 6.8. (a) Index of connectivity (Borselli et al., 2008; Crema and Cavalli, 2018) results for the Upper South Elkhorn watershed. (b) Instream *IC* results for the representative study reaches.

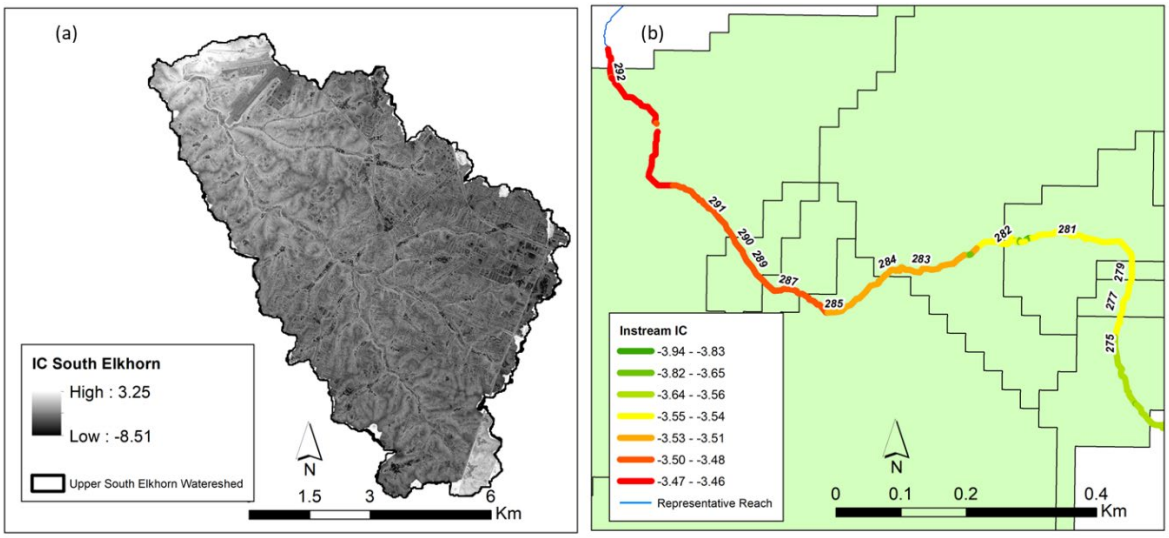

Figure 6.9. Simulated and observed sediment flux at the outlet of the Upper South Elkhorn watershed. (a) Observed and simulated results using 362 reaches with explicit representation of riffles and pools for the entire simulation period between August 2017 and February 2019. (b) Observed and simulated results using 181 reaches with implicit representation of riffles and pools for the entire simulation period between August 2017 and February 2019. (c) Observed and simulated results for the period between May and July 2018 for the simulation with 362 reaches. (d) Observed and simulated results for the period between May, 2018 and July 2018 for the simulation with 181 reaches.

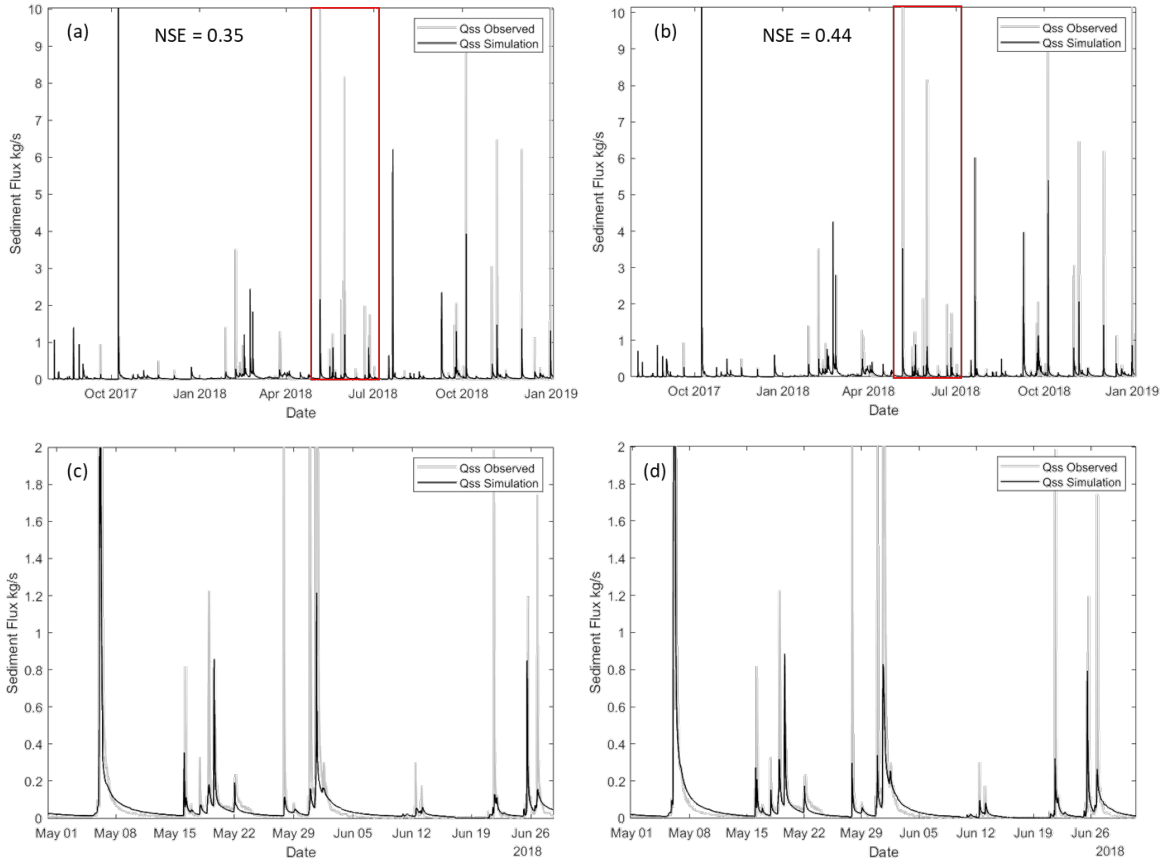

Figure 6.10. $P(\gamma)$ results at multiple representative reaches during the May, 2018 event including two pools and two riffles. Reach locations are shown in Fig. 4. (a) $P(\gamma)$ prior to the event. (b) $P(\gamma)$ during the rising limb of the event. (c) $P(\gamma)$ during the peak of the event. (d) $P(\gamma)$ during the falling limb of the event.

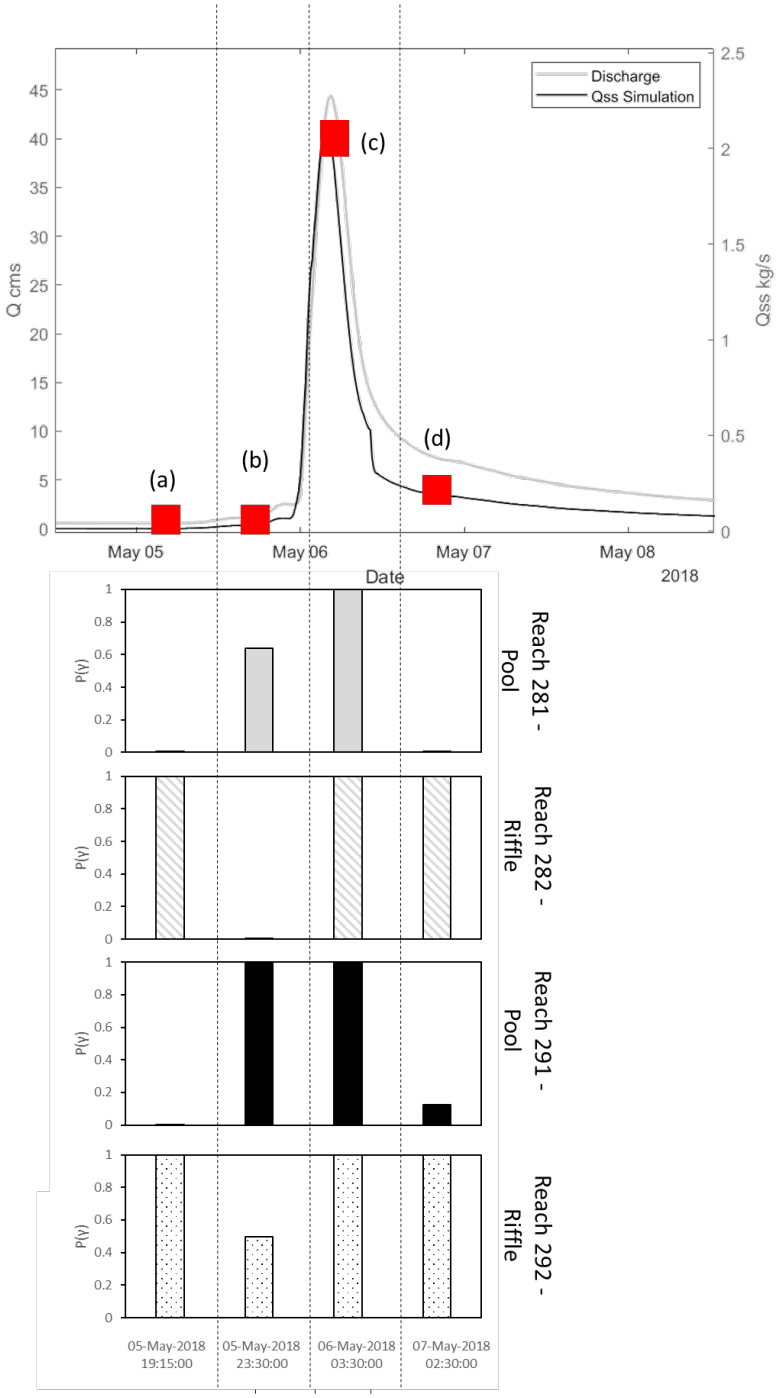

Figure 6.11. Time series of sediment flux, $P(\gamma)$, erosion, and deposition for representative reaches 281 (pool) and 282 (riffle) during the event occurring between May 5 and May 9. A bedrock outcrop, as shown in Fig. 4 separates reaches 281 and 282. (a) $P(\gamma)$ for reach 281. (b) $P(\gamma)$ for reach 282. (c) Deposition in reach 281. (d) Deposition in reach 282. (e) Erosion in reach 281. (f) Erosion in reach 282. (g) Sediment flux in reach 281. (h) Sediment flux in reach 282. (i) Flow depth in reach 281. (j) Flow depth in reach 282.

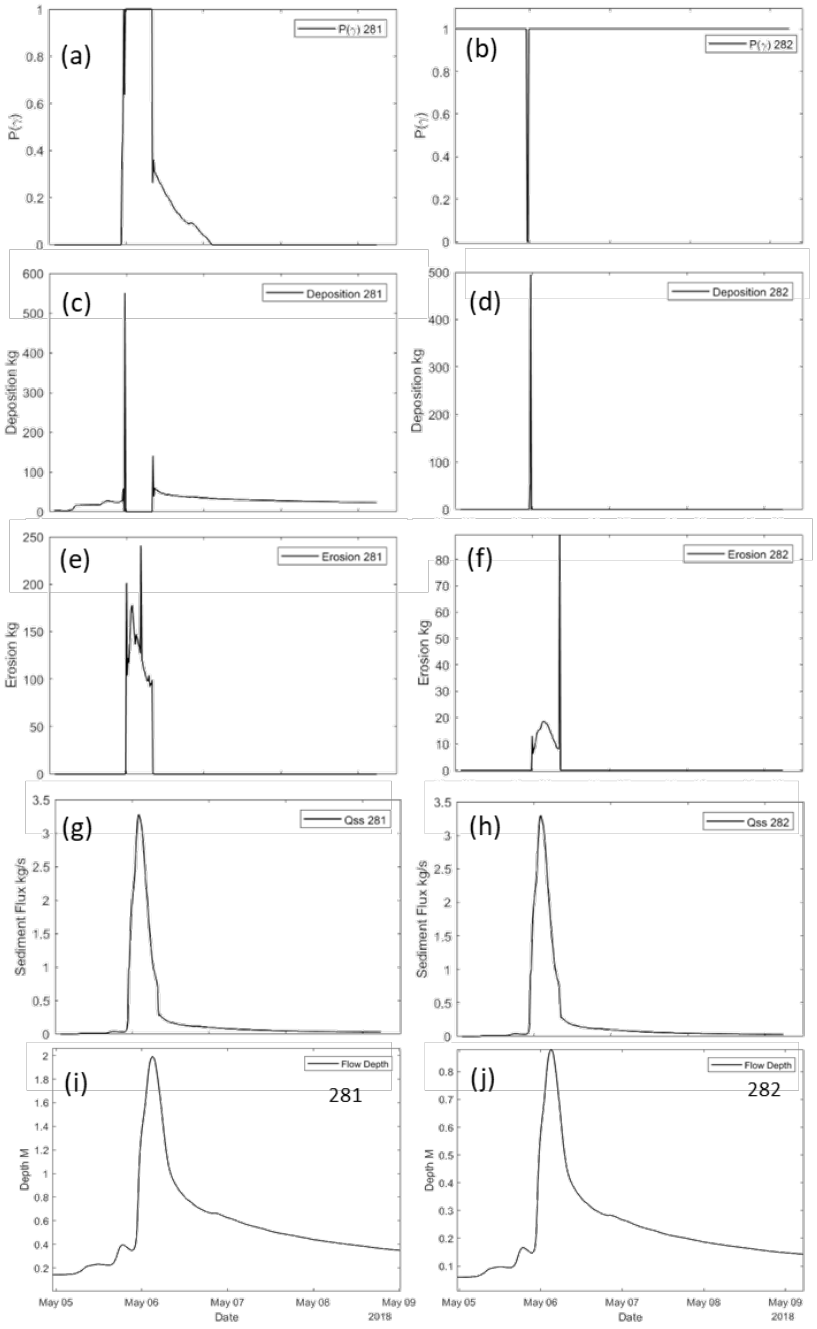

Figure 6.12. Probability of connectivity results during the May 5 to May 9, 2018 event for bed sediments. (a) $P(C)$ results for reach 281 for SFGL sediment. (b) $P(C)$ results for reach 282 for SFGL sediment. (c) $P(C)$ results for reach 281 for bed sediment. (d) $P(C)$ results for reach 282 for bed sediment.

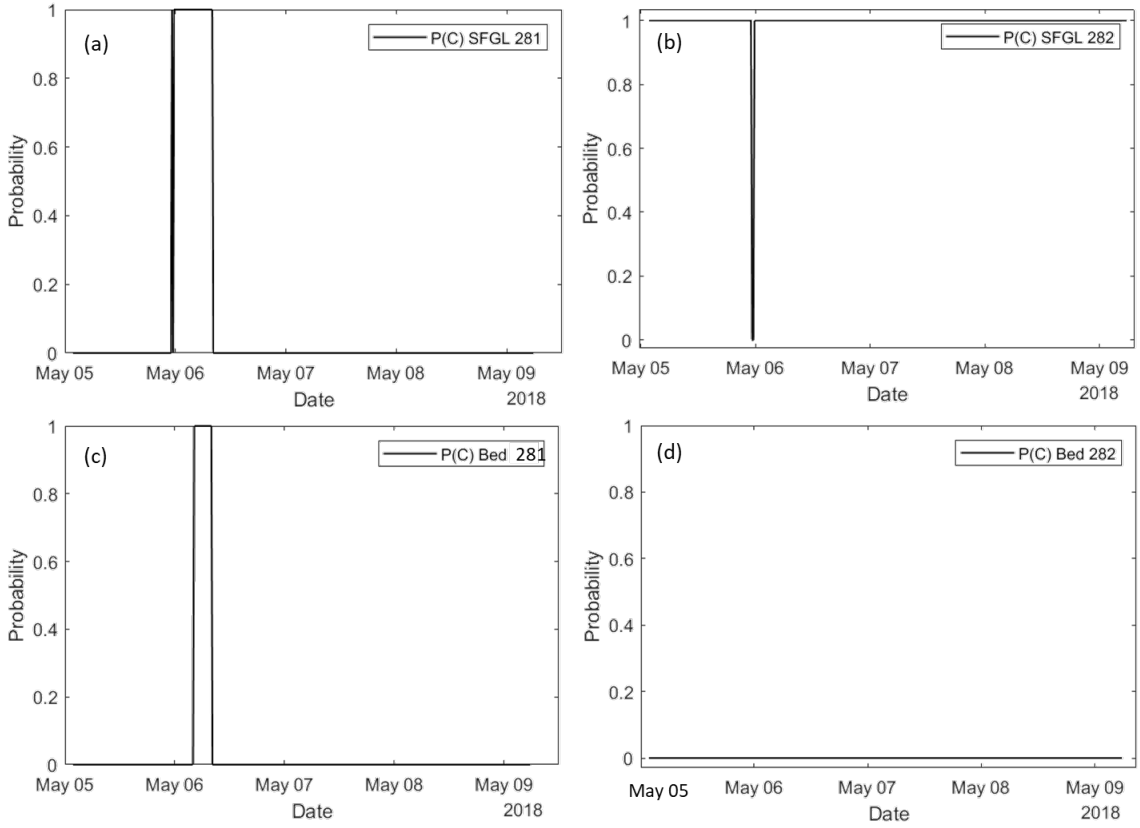

REFERENCES

Abbaspour, K. C., Yang, J., Maximov, I., Siber, R., Bogner, K., Mieleitner, J., ... & Srinivasan, R. (2007). Modelling hydrology and water quality in the pre-alpine/alpine Thur watershed using SWAT. Journal of hydrology, 333(2), 413-430.

Acton, P.M., Fox, J.F., Campbell, J.E., Jones, A.L., Rowe, H., Martin, D. and Bryson, S. 2011. The role of soil health in maintaining environmental sustainability of surface coal mining. Environmental Science and Technology, 45, 10265-10272.

Aguilera, R., Melack, J.M., 2018. Concentration-Discharge Responses to Storm Events in Coastal California Watersheds. Water Resour. Res. 54, 407–424. https://doi.org/10.1002/2017WR021578

Ahmadi, S.H., Amin, S., Keshavarzi, A.R. and Mirzamostafa, N., 2006. Simulating watershed outlet sediment concentration using the ANSWERS model by applying two sediment transport capacity equations. Biosystems engineering, 94(4), 615-626.

Al Aamery, N., Fox, J.F., Snyder, M., 2016. Evaluation of climate modeling factors impacting the variance of streamflow. J. Hydrol. 542, 125–142. https://doi.org/10.1016/j.jhydrol.2016.08.054

Alberts EE, Nearing MA, Weltz MA, Risse LM, Pierson FB, Zhang XC, Laflen JM, Simanton JR (1995) Chapter 7 soil component. In: Flanagan DC, Nearing MA, USDA. Water erosion and prediction project hillslope profile and watershed model documentation, NSERL Report No. 10 USDA-ARS National Soil Erosion Research Laboratory, West Lafayette, pp 7.1-7.47

Ali, G., Oswald, C., Spence, C., Wellen, C., 2018. The T-TEL Method for Assessing Water, Sediment, and Chemical Connectivity. Water Resour. Res. 54, 634–662. https://doi.org/10.1002/2017WR020707

Ambroise, B., 2004. Variable‘active’ versus‘contributing’ areas or periods: a necessary distinction. Hydrol. Process. 18, 1149–1155. https://doi.org/10.1002/hyp.5536

Angel, P. et al., 2005. The Appalachian Regional Reforestation Initiative. The Appalachian Regional Reforestation Initiative, Forest Reclamation Advisory No. 1.

Arnold JG, Allen PM (1999) Automated methods for estimating baseflow and ground water recharge from streamflow records. J Am Water Resour As 35(2):411-424

Arnold JG, Allen PM, Muttiah R, Bernhardt G (1995) Automated base flow separation and recession analysis techniques. Ground Water 33(6):1010-1018

Arnold, J. G., Kiniry, J. R., Srinivasan, R., Williams, J. R., Haney, E. B., & Neitsch, S. L. (2011). Soil and Water Assessment Tool input/output file documentation: Version 2009. Texas Water resources institute technical report, 365.

Arnold, J. G., Moriasi, D. N., Gassman, P. W., Abbaspour, K. C., White, M. J., Srinivasan, R., ... & Kannan, N. (2012). SWAT: Model use, calibration, and validation. Transactions of the ASABE, 55(4), 1491-1508.

Arnold, J.G., Srinivasan, R., Muttiah, R.S., Williams, J.R., 1998. Large area hydrologic modeling and assessment part I: model development. JAWRA J. Am. Water Resour. Assoc. 34 (1), 73–89.

Ashkar, F., Mahdi, S., 2006. Fitting the log-logistic distribution by generalized moments. J. Hydrol. 328, 694–703. https://doi.org/10.1016/j.jhydrol.2006.01.014

Baartman, J.E.M., Masselink, R., Keesstra, S.D., Temme, A.J.A.M., 2013. Linking landscape morphological complexity and sediment connectivity. Earth Surf. Process. Landforms 38, 1457–1471. https://doi.org/10.1002/esp.3434

Batista, P.V.G., Davies, J., Silva, M.L.N., Quinton, J.N., 2019. On the evaluation of soil erosion models: Are we doing enough? Earth-Science Rev. 197, 102898. https://doi.org/10.1016/j.earscirev.2019.102898

Bellanger B, Huon S, Velasquez F, Valles V, Girardin C, Mariotti A (2004) Monitoring soil organic carbon erosion with δ13C and δ15N on experimental field plots in the Venezuelan Andes. Catena 58(2):125-150

Bingner, R.L. and Theurer, F.D. 2001. AGNPS 98: A Suite of water quality models for watershed use. In Proceedings of the Sediment: Monitoring, Modeling, and Managing, 7th Federal Interagency Sedimentation Conference, Reno, NV, 25-29 March 2001: Subcommittee on Sedimentation of the Interagency Advisory Committee on Water Data, p. VII-1 - VII-8.

Blake WH, Ficken KJ, Taylor P, Russell MA, Walling DE (2012) Tracing crop-specific sediment sources in agricultural catchments. Geomorphology 139:322-329

Bonn BA, Rounds SA (2010) Use of stable isotopes of carbon and nitrogen to identify sources of organic matter to bed sediments of the Tualatin River, Oregon (No. 2010-5154). US Geological Survey

Bonta, J. V. (2000). Impact of coal surface mining and reclamation on suspended sediment in three Ohio watersheds. Jounral of the American Water Resources Association , 36 (4), 869-887.

Borselli, L., Cassi, P., Torri, D., 2008. Prolegomena to sediment and flow connectivity in the landscape: A GIS and field numerical assessment. Catena 75, 268–277. https://doi.org/10.1016/j.catena.2008.07.006

Bracken, L.J. and Croke, J., 2007. The concept of hydrological connectivity and its contribution to understanding runoff-dominated geomorphic systems. Hydrological Processes: An International Journal, 21(13), pp.1749-1763.

Bracken, L.J., Turnbull, L., Wainwright, J., Bogaart, P., 2015. Sediment connectivity: A framework for understanding sediment transfer at multiple scales. Earth Surf. Process. Landforms 40, 177–188. https://doi.org/10.1002/esp.3635

Bracken, L.J., Wainwright, J., Ali, G.A., Tetzlaff, D., Smith, M.W., Reaney, S.M., Roy, A.G., 2013. Concepts of hydrological connectivity: Research approaches, Pathways and future agendas. Earth-Science Rev. 119, 17–34. https://doi.org/10.1016/j.earscirev.2013.02.001

Brierley, G., Fryirs, K., Jain, V., 2006. Landscape connectivity: The geographic basis of geomorphic applications. Area 38, 165–174. https://doi.org/10.1111/j.1475-4762.2006.00671.x

Brunsden, D. (1993). Barriers to geomorphological change. Landscape sensitivity, 675.

Cambardella CA, Elliott ET (1992) Particulate soil organic-matter changes across a grassland cultivation sequence. Soil Sci Soc Am J 56:777-783

Campbell, J.E., Fox, J.F., Davis, C.M., Rowe, H.D. and Thompson, N. 2009. Carbon and nitrogen isotopic measurements from southern Appalachian soils: assessing soil carbon sequestration under climate and land use variation. Journal of Environmental Engineering, ASCE, Vol. 135, No. 6, 439-448.

Cantreul, V., Bielders, C., Calsamiglia, A., Degré, A., 2018. How pixel size affects a sediment connectivity index in central Belgium. Earth Surf. Process. Landforms 43, 884–893. https://doi.org/10.1002/esp.4295

Cavalli, M., Tarolli, P., Dalla Fontana, G., Marchi, L., 2016. Multi-temporal analysis of sediment source areas and sediment connectivity in the Rio Cordon catchment (Dolomites). Rendiconti Online Della Soc. Geol. Ital. 39, 27–30. doi:10.3301/ROL.2016.39

Cavalli, M., Trevisani, S., Comiti, F., Marchi, L., 2013. Geomorphometric assessment of spatial sediment connectivity in small Alpine catchments. Geomorphology 188, 31–41. https://doi.org/10.1016/j.geomorph.2012.05.007

Cavalli, M., Vericat, D., Pereira, P., 2019. Mapping water and sediment connectivity. Sci. Total Environ. 673, 763–767. https://doi.org/10.1016/j.scitotenv.2019.04.071

Cellino, M., Lemmin, U., 2004. Influence of Coherent Flow Structures on the Dynamics of Suspended Sediment Transport in Open-Channel Flow. J. Hydraul. Eng. 130, 1077–1088. https://doi.org/10.1061/(ASCE)0733-9429(2004)130

Chang, H., 1988. Fluvial Processes in River Engineering. Krieger Publishing Company Malabar, Florida

Chartin, C., Evrard, O., Laceby, J.P., Onda, Y., Ottlé, C., Lefèvre, I., Cerdan, O., 2017. The impact of typhoons on sediment connectivity: Lessons learnt from contaminated coastal catchments of the Fukushima Prefecture (Japan). Earth Surf. Process. Landf. 42, 306–317. https://doi.org/10.1002/esp.4056.

Chen J. The simulation of runoff using a time-area graph derived from DTM. ITC Journal 1998;1998–2:113–7.

Chorley, R.J., Kennedy, B.A., 1971. Physical geography: a systems approach. Prentice Hall.

Chow, V. T., Maidment, D. R., and Mays, L. W. (1988). Applied hydrology, McGraw-Hill, New York.

Clare, E, 2019. Decomposing a watershed's nitrate signal using spatial sampling and continuous sensor data. Theses and Dissertations--Civil Engineering. 87. https://uknowledge.uky.edu/ce_etds/87

Collins AL, Walling DE, Leeks GJL (1997) Source type ascription for fluvial suspended sediment based on a quantitative composite fingerprinting technique. Catena 29(1):1-27

Cooper RJ, Pedentchouk N, Hiscock KM, Disdle P, Krueger T, Rawlins BG (2015) Apportioning sources of organic matter in streambed sediments: an integrated molecular and compound-specific stable isotope approach. Sci Total Environ 520:187-197

Coulthard, T.J., 2001. Landscape evolution models: a software review. Hydrol. Process. 15, 165–173. https://doi.org/10.1007/BF02110219

Courant, R., Friedrichs, K., Lewy, H., 1967. On the partial difference equations of mathematical physics. *IBM journal of Research and Development*, *11*(2), 215-234.

Crema, S., Cavalli, M., 2018. SedInConnect: a stand-alone, free and open source tool for the assessment of sediment connectivity. Comput. Geosci. 111, 39–45. https://doi.org/10.1016/j.cageo.2017.10.009

Croke, J., Fryirs, K., & Thompson, C. (2013). Channel–floodplain connectivity during an extreme flood event: implications for sediment erosion, deposition, and delivery. Earth Surface Processes and Landforms, 38(12), 1444-1456.

Currens J. C., Paylor R. L., and Ray J. A. (2002). Mapped karst groundwater basins in the Lexington 30 x 60 minute quadrangle. Kentucky Geological Survey, University of Kentucky, Lexington, KY USA.

Curtis, W. R., 1978. Effects of surface mining on hydrology, erosion, and sedimentation in eastern Kentucky. Fourth Kentucky Coal Refuse Disposal and Utilization Seminar, Lexington, KY, 17–19.

Czuba, J.A., Foufoula-Georgiou, E., 2014. A network-based framework for identifying potential synchronizations and amplifications of sediment delivery in river basins. Water Resour. Res. 50, 3826–2851.

D'Haen, K., Dusar, B., Verstraeten, G., Degryse, P., De Brue, H., 2013. A sediment fingerprinting approach to understand the geomorphic coupling in an eastern Mediterranean mountainous river catchment. Geomorphology 197, 64–75.

Dalzell BJ, Filley TR, Harbor JM (2007) The role of hydrology in annual organic carbon loads and terrestrial organic matter export from a midwestern agricultural watershed. Geochim Cosmochim Ac 71(6):1448-1462

Davis C (2008) Sediment fingerprinting using organic matter tracers to study streambank erosion and streambed sediment storage processes in the South Elkhorn watershed. MSc Thesis, University of Kentucky

Davis CM, Fox JF (2009) Sediment fingerprinting: review of the method and future improvements for allocating sediment non-point source pollution. J Environ Eng, ASCE 135(7):490-504

De Vente, J., Poesen, J., & Verstraeten, G. (2005). The application of semi-quantitative methods and reservoir sedimentation rates for the prediction of basin sediment yield in Spain. Journal of Hydrology, 305(1), 63-86.

De Vente, J., Poesen, J., Verstraeten, G., Govers, G., Vanmaercke, M., Van Rompaey, A., Arabkhedri, M., Boix-Fayos, C., 2013. Predicting soil erosion and sediment yield at regional scales: Where do we stand? Earth-Science Rev. 127, 16–29. https://doi.org/10.1016/j.earscirev.2013.08.014

Dou, G.R., 1974. Similarity theory and its application to the design of total sediment transport model. Research Bulletin of Nanjing Hydraulic Research Institute.

Douglas-Mankin, K.R., Srinivasan, R., Arnold, J.G., 2010. Soil and water assessment tool (SWAT) model: current developmens and applications. Trans. Am. Soc. Agric. Biol. Eng. 53, 1423–1431.

Droppo, I.G. and Amos, C.L., 2001. Structure, stability, and transformation of contaminated lacustrine surface fine-grained laminae. Journal of Sedimentary Research, 71(5), 717-726.

Droppo, I.G. and Stone, M., 1994. In-channel surficial fine-grained sediment laminae. Part I: Physical characteristics and formational processes. Hydrological Processes, 8(2), pp.101-111.

Duvall, A., Kirby, E. and Burbank, D., 2004. Tectonic and lithologic controls on bedrock channel profiles and processes in coastal California. Journal of Geophysical Research: Earth Surface, 109(F3).

Eagleson, P. S. (1970). Dynamic hydrology, McGraw-Hill, New York.

Einstein, H. A. (1950). The bed-load function for sediment transportation in open channel flows (Vol. 1026). Washington DC: US Department of Agriculture.

Entekhabi, D., Njoku, E.G., Neill, P.E.O., Kellogg, K.H., Crow, W.T., Edelstein, W.N., Entin, J.K., Goodman, S.D., Jackson, T.J., Johnson, J., Kimball, J., Piepmeier, J.R., Koster, R.D., Martin, N., Mcdonald, K.C., Moghaddam, M., Moran, S., Reichle, R., Shi, J.C., Spencer, M.W., Thurman, S.W., Tsang, L., Zyl, J. Van, 2010. The Soil Moisture Active Passive (SMAP) Mission. Proc. IEEE 98.

ESR-Equine Survey Report, 2013. 2012 Kentucky Equine Survey. University of Kentucky Agriculture Equine Program, Lexington, Kentucky.

Evans, C., Davies, T.D., 1998. Causes of concentration/discharge hysteresis and its potential as a tool for analysis of episode hydrochemistry. Water Resour. Res. 34, 129–137. https://doi.org/10.1029/97WR01881

Evans, S. Personal Communication. March 20, 2017.

Evrard, O., Navratil, O., Ayrault, S., Ahmadi, M., Némery, J., Legout, C., Lefèvre, I., Poirel, A., Bonté, P., Esteves, M., 2011. Combining suspended sediment monitoring and fingerprinting to determine the spatial origin of fine sediment in a mountainous river catchment. Earth Surf. Process. Landforms 36, 1072–1089. https://doi.org/10.1002/esp.2133

Ferguson, R.I., 1981. Channel form and channel changes. British Rivers 90, 125

Florsheim, J. L., Mount, J. F., & Constantine, C. R. (2006). A geomorphic monitoring and adaptive assessment framework to assess the effect of lowland floodplain river restoration on channel–floodplain sediment continuity. River Research and Applications, 22(3), 353-375.

Ford WI, Fox JF (2017) Stabilization of benthic algal biomass in a temperate stream draining agroecosystems. Water Res 108:432-443

Ford WI, Fox JF, Pollock E, Rowe H, Chakraborty S (2015b) Testing assumptions for nitrogen transformations in a low gradient agricultural stream. J Hydrol 527(2015): 908–922

Ford WI, Fox JF, Rowe, H (2015a) Impact of extreme hydrologic disturbance upon the sediment carbon quality in agriculturally-impacted temperate stream. Ecohydrology 8(3):438-449

Ford, W. I., & Fox, J. F. (2014). Model of particulate organic carbon transport in an agriculturally impacted stream. Hydrological Processes, 28(3), 662-675.

Ford, W.I., Fox, J.F., 2014. Model of particulate organic carbon transport in an agriculturally impacted stream. Hydrol. Process. 28, 662–675. https://doi.org/10.1002/hyp.9569

Ford, William Isaac III. (2011). Particulate organic carbon fate and transport in a lowland, temperate watershed. *University of Kentucky Master's Theses*. 647. http://uknowledge.uky.edu/gradschool_theses/647

Foster, G. R., Flanagan, D. C., Nearing, M. A., Lane, L. J., Risse, L. M., & Finkner, S. C., 1995. Hillslope erosion component. WEPP: USDA-Water Erosion Prediction Project, 11-1.

Fovet, O., Humbert, G., Dupas, R., Gascuel-Odoux, C., Gruau, G., Jaffrezic, A., Thelusma, G., Faucheux, M., Gilliet, N., Hamon, Y., Grimaldi, C., 2018. Seasonal variability of stream water quality response to storm events captured using high-frequency and multi-parameter data. J. Hydrol. 559, 282–293. https://doi.org/10.1016/j.jhydrol.2018.02.040

Fox JF (2006) Fingerprinting using biogeochemical tracers to investigate watershed processes. PhD Dissertation, University of Iowa

Fox JF (2009) Identification of sediment sources in forested watersheds with surface coal mining disturbance using carbon and nitrogen isotopes. J Am Water Resour As 45(5):1273-1289

Fox JF, Ford WI, Strom K, Villarini G., Meehan M (2014) Benthic control upon the morphology of transported fine sediments in a low-gradient stream. Hydrol Process 28(11):3776–3788

Fox JF, Martin DK (2015) Sediment fingerprinting for calibrating a soil erosion and sediment-yield model in mixed land-use watersheds. J Hydrol Eng 20(6):C4014002

Fox JF, Papanicolaou AN (2007) The use of carbon and nitrogen isotopes to study watershed erosion processes. J Am Water Resour As 43(4):1047-1064

Fox JF, Papanicolaou AN (2008a) An un-mixing model to study watershed erosion processes. Adv Water Resour 31(1):96-108

Fox JF, Papanicolaou AN (2008b) Application of the spatial distribution of nitrogen stable isotopes for sediment tracing at the watershed scale. J Hydrol 358(1-2):46-55

Fox, G. A., Sabbagh, G. J., Chen, W., & Russell, M. H. (2006). Uncalibrated modelling of conservative tracer and pesticide leaching to groundwater: Comparison of potential Tier II exposure assessment models. Pest management science, 62(6), 537-550.

Fox, J.F., 2009 Measurements of sediment transport processes in forested watersheds with surface coal mining disturbance using carbon and nitrogen isotopes. Journal of the American Water Resources Association, 45(5): 1273-1289.

Fox, J.F., Davis, C.M., Martin, D.K., 2010. Sediment Source Assessment in a Lowland Watershed Using Nitrogen Stable Isotopes. J. Am. Water Resour. Assoc. 46, 1192–1204. https://doi.org/10.1111/j.1752-1688.2010.00485.x

Fox, J.F., Martin, D.K., 2015. Sediment fingerprinting for calibrating a soil erosion and sediment-yield model in mixed land-use watersheds. J. Hydrol. Eng. 20. https://doi.org/10.1061/(ASCE)HE.1943-5584.0001011

Fry, J., Xian, G., Jin, S., Dewitz, J., Homer, C., Yang, L., Barnes, C., Herold, N., and Wickham, J., 2011. Completion of the 2006 National Land Cover Database for the Conterminous United States, PE&RS, Vol. 77(9):858-864.

Fryirs KA, Brierley GJ, Preston NJ, Kasai M (2007a) Buffers, barriers and blankets: the (dis) connectivity of catchment-scale sediment cascades. Catena 70(1):49-67

Fryirs, K., 2013. (Dis)Connectivity in catchment sediment cascades: A fresh look at the sediment delivery problem. Earth Surf. Process. Landforms 38, 30–46. https://doi.org/10.1002/esp.3242

Fryirs, K.A., Brierley, G.J., Preston, N.J., Spencer, J., 2007. Catchment-scale (dis)connectivity in sediment flux in the upper Hunter catchment, New South Wales, Australia. Geomorphology 84, 297–316. https://doi.org/10.1016/j.geomorph.2006.01.044

G.R. Foster, D.C. Flanagan, M.A. Nearing, L.J. Lane, L.M. Risse and S.C. Finkner, 1995, Chapter 11. Hillslope erosion component, In: D. C. Flanagan and M. A. Nearing, USDA – Water erosion and prediction project hillslope profile and watershed model documentation, NSERL Report No. 10 USDA-ARS National Soil Erosion Research Laboratory, West Lafayette, Indiana 47907.

Gay, A., Cerdan, O., Mardhel, V., Desmet, M., 2015. Application of an index of sediment connectivity in a lowland area. J. Soils Sediments 1–14. doi:10.1007/s11368-015-1235-y

Gellis AC, Hupp CR, Pavich MJ, Landwehr JM, Banks WS, Hubbard BE, Langland MJ, Ritchie JC, Reuter JM (2009) Sources, transport, and storage of sediment at selected sites in the Chesapeake Bay Watershed. U. S. Geological Survey Scientific Investigations Report 2008-5186, 95 p.

Gessler, J. (1971) Aggradation and Degradation. Ins.H. W. Shen (Editor) River Mechanics Vol. 1, Ch. 8, Publisher H. W. Shen, Fort Collins, Colorado.

Gibbs MM (2008) Identifying source soils in contemporary estuarine sediments: a new compound-specific isotope method. Estuar Coasts 31(2):344-359

Glymph, L. M. (1954). Studies of sediment yields from watersheds. International Association of Hydrological Sciences Publication, 36, 261-268.

Gomez B, Trustrum NA, Hicks DM, Rogers KM, Page MJ, Tate KR (2003) Production, storage, and output of particulate organic carbon: Waipaoa River basin, New Zealand. Water Resour Res 39(6). doi: 10.1029/2002WR001619

Goudie, A. (Ed.). (2004). Encyclopedia of geomorphology(Vol. 2). Psychology Press.

Gourdin E, Huon S, Evrard O, Ribolzi O, Bariac T, Sengtaheuanghoung O, Ayrault S (2015) Sources and export of particle-borne organic matter during a monsoon flood in a catchment of northern Laos. Biogeosciences 12(4):1073-1089

Gran, K.B., Czuba, J.A., 2017. Sediment pulse evolution and the role of network structure. Geomorphology 277, 17–30. https://doi.org/10.1016/j.geomorph.2015.12.015

Grant, G.E., O'Connor, J., Safran, E., 2017. Excursions in fluvial (dis)continuity. Geomorphology 277, 145–153. https://doi.org/10.1016/j.geomorph.2016.08.033

Grimaldi, S., Petroselli, A., Alonso, G., Nardi, F., 2010. Flow time estimation with spatially variable hillslope velocity in ungauged basins. Adv. Water Resour. 33, 1216–1223. https://doi.org/10.1016/j.advwatres.2010.06.003

Guebert, M.D., Gardner, T.W., 2001. Macropore flow on a reclaimed surface mine: Infiltration and hillslope hydrology. Geomorphology 39, 151–169. https://doi.org/10.1016/S0169-555X(00)00107-0

Gumbert, A. Personal Communication. February 21, 2017.

Gupta, RS., 2016. Hydrology and hydraulic systems. Waveland Press, Long Grove.

Guy, B.T., Rudra, R.P., Dickenson, W.T. and Sohrabi, T.M., 2009. Empirical model for calculating sediment-transport capacity in shallow overland flows: Model development. Biosystems engineering, 103(1), pp.105-115.

Haan, C. T., Barfield, B. J., & Hayes, J. C. (1994). Design hydrology and sedimentology for small catchments. Elsevier.

Hack, J.T., 1957. Studies of longitudinal stream profiles in Virginia and Maryland (Vol. 294). US Government Printing Office.

Hamel, P., Chaplin-Kramer, R., Sim, S., Mueller, C., 2015. A new approach to modeling the sediment retention service (InVEST 3.0): Case study of the Cape Fear catchment, North Carolina, USA. Sci. Total Environ. 524–525, 166–177. https://doi.org/10.1016/j.scitotenv.2015.04.027

Hancock GJ, Revill AT (2013) Erosion source discrimination in a rural Australian catchment using compound-specific isotope analysis (CSIA). Hydrol Process 27(6):923-932

Hanson, G.J., Simon, A., 2001. Erodibility of cohesive streambeds in the loess area of the Midwestern USA. Hydrol. Process. 15, 23–38. https://doi.org/10.1002/hyp.149

Harden, C.P. and Scruggs, P.D., 2003. Infiltration on mountain slopes: a comparison of three environments. Geomorphology, 55(1-4), pp.5-24.

Hargrave, B. T., & Burns, N. M., 1979. Assessment of sediment trap collection efficiency. Limnology and Oceanography, 24(6), 1124-1136.

Harvey, A.M., 1996. Holocene hillslope gully systems in the Howgill Fells, Cumbria. Adv. Hillslope Process. 2, 731–752.

Harvey, A.M., 2002. Effective timescales of coupling within fluvial systems. Geomorphology 44, 175–201. https://doi.org/10.1016/S0169-555X(01)00174-X

Hawkins RH, Ward TJ, Woodward DE, van Mullem JA (eds). 2009. Curve Number Hydrology: State of the Practice; ASCE: Reston, VA.

Heckmann, T., Cavalli, M., Cerdan, O., Foerster, S., Javaux, M., Lode, E., Smetanová, A., Vericat, D., Brardinoni, F., 2018. Indices of sediment connectivity:

opportunities, challenges and limitations. Earth-Science Rev. 187, 77–108. https://doi.org/10.1016/j.earscirev.2018.08.004

Heckmann, T., Schwanghart, W., 2013. Geomorphic coupling and sediment connectivity in an alpine catchment - Exploring sediment cascades using graph theory. Geomorphology 182, 89–103. https://doi.org/10.1016/j.geomorph.2012.10.033

Henderson, F.M., 1966. *Open channel flow* (No. 532 H4).

Hessel, R., Jetten, V., Guanghui, Z., 2003. Estimating Manning's n for steep slopes. Catena 54, 77–91. https://doi.org/10.1016/S0341-8162(03)00058-4

Hewlett, J.D. and Hibbert, A.R., 1965. Response of small watersheds to precipitation. In International symposium on forest hydrology. Pergamon Press, New York.

Hoffmann, T., 2015. Sediment residence time and connectivity in non-equilibrium and transient geomorphic systems. Earth-Science Rev. 150, 609–627. https://doi.org/10.1016/j.earscirev.2015.07.008

Hooghoudt SB (1940) General consideration of the problem of field drainage by parallel drains, ditches, watercourses, and channels. Publ. No.7 in the series Contribution to the knowledge of some physical parameters of the soil (titles translated from Dutch). Bodemkundig Instituut, Groningen, The Netherlands

Hooke JM, Sandercock P, Cammeraat LH, Lesschen JP, Borselli L, Torri D, Meerkerk A, van Wesemael B, Marchamalo M, Gonzalo B, Boix-Fayos C, Castillo V, Navarro-Cano JA. 2017. Mechanisms of Degradation and Identification of Connectivity and Erosion Hotspots. In Combating Desertification and Land Degradation, Hooke J, Sandercock P (eds). Springer International Publishing: Cham; 13–37.

Hooke, J., 2003. Coarse sediment connectivity in river channel systems: A conceptual framework and methodology. Geomorphology 56, 79–94. https://doi.org/10.1016/S0169-555X(03)00047-3

Hupp, C. R. (2000). Hydrology, geomorphology and vegetation of Coastal Plain rivers in the south-eastern USA. Hydrological processes, 14(16-17), 2991-3010.

Husic, A., Fox, J., Agouridis, C., Currens, J., Ford, W., & Taylor, C. (2017). Sediment carbon fate in phreatic karst (Part 1): Conceptual model development. Journal of Hydrology, 549, 179-193.

Jacinthe PA, Lal R, Owens LB (2009) Application of stable isotope analysis to quantify the retention of eroded carbon in grass filters at the North Appalachian experimental watersheds. Geoderma 148(3-4):405-412

Jaeger KL, Olden JD., 2012. Electrical resistance sensor arrays as a means to quantify longitudinal connectivity of rivers. River Research and Applications 28: 1843–1852.

Jaeger, K. L., Sutfin, N. A., Tooth, S., Michaelides, K., & Singer, M. (2017). Geomorphology and Sediment Regimes of Intermittent Rivers and Ephemeral Streams. In Intermittent Rivers and Ephemeral Streams (pp. 21-49).

Jain, S.C., 2001. Open-channel flow. John Wiley & Sons, pp. 58.

Jain, V., & Tandon, S. K. (2010). Conceptual assessment of (dis) connectivity and its application to the Ganga River dispersal system. Geomorphology, 118(3), 349-358.

James, A. L., & Roulet, N. T. (2009). Antecedent moisture conditions and catchment morphology as controls on spatial patterns of runoff generation in small forest catchments. Journal of Hydrology, 377(3), 351-366.

Jamshidi, R., Dragovich, D., Webb, A.A., 2014. Distributed empirical algorithms to estimate catchment scale sediment connectivity and yield in a subtropical region. Hydrol. Process. 28, 2671–2684. https://doi.org/10.1002/hyp.9805

Jarritt, N.P. and Lawrence, D.S.L., 2007. Fine sediment delivery and transfer in lowland catchments: modelling suspended sediment concentrations in response to hydrological forcing. Hydrological Processes: An International Journal, 21(20), 2729-2744.

Jencso, K. G., McGlynn, B. L., Gooseff, M. N., Wondzell, S. M., Bencala, K. E., & Marshall, L. A. (2009). Hydrologic connectivity between landscapes and streams: Transferring reach-and plot-scale understanding to the catchment scale. Water Resources Research, 45(4).

Jin, C.X., Dabney, S.M., Romkens, M.J.M., 2002. Trapped mulch increases sediment removal by vegetative filter strips: A flume study. Trans. ASAE 45, 929-939.

Jin, C.X., Romkens, M.J.M., 2001. Experimental studies of factors in determining sediment trapping in vegetative filter strips. Trans. ASAE 44, 277-288.

Joe S, Kuo FY (2003) Remark on algorithm 659: Implementing Sobol's quasirandom sequence generator. ACM T Math Software 29(1):49-57

Julien PY, Simons DB (1985) Sediment transport capacity of overland flow. T ASAE 28(3):755-0762

Jung BJ, Lee HJ, Jeong JJ, Owen J, Kim B, Meusburger K, Alewell C, Gebauer G, Shope C, Park JH (2012) Storm pulses and varying sources of hydrologic carbon export from a mountainous watershed. J Hydrol 440:90-101

Kalantari, Z., Cavalli, M., Cantone, C., Crema, S., Destouni, G., 2017. Flood probability quantification for road infrastructure: Data-driven spatial-statistical approach and case study applications. Sci. Total Environ. 581–582, 386–398. doi:10.1016/j.scitotenv.2016.12.147

Kalisz, Paul J. 1986. Soil Properties of Steep Appalachian Old Fields, Ecology, Vol. 67, No. 4 (Aug., 1986), pp. 1011-1023.

Katz, D.M., Watts, F.J., Burroughs, E.R., 1995. Effects of surface roughness and rainfall impact on overland flow. J. Hydraul. Eng. 121, 546–553. https://doi.org/10.1061/(ASCE)0733-9429(1995)121:7(546)

Keesstra, S., Nunes, J.P., Saco, P., Parsons, T., Poeppl, R., Masselink, R., Cerdà, A., 2018. The way forward: Can connectivity be useful to design better measuring and modelling schemes for water and sediment dynamics? Sci. Total Environ. 644, 1557–1572. https://doi.org/10.1016/j.scitotenv.2018.06.342

Kentucky Geologic Survey, 2017. Kentucky LiDAR sinkholes. Kentucky Geological Survey, University of Kentucky, KY USA.

Kentucky Geological Survey, 2013. "US-KY_KGS_24K_Lithology". Retrieved from: https://kgs.uky.edu/usgin/rest/services/OneGeology/KYGS_Kentucky_Geology_24K/MapServer/2. Accessed 4/15/2020

Khan A. and Ormsbee L. 1989. A COMPARISON OF TWO HYDROLOGIC MODELS FOR STEEPLY SLOPING FORESTED WATERSHEDS, Journal of Hydrology, 109 (1989) 325-349

Knighton, A. D. (1989). River adjustment to changes in sediment load: the effects of tin mining on the Ringarooma River, Tasmania, 1875–1984. Earth Surface Processes and Landforms, 14(4), 333-359.

Koiter, A.J., Lobb, D.A., Owens, P.N., Petticrew, E.L., Tiessen, K.H.D., Li, S., 2013. Investigating the role of connectivity and scale in assessing the sources of sediment in an agricultural watershed in the Canadian prairies using sediment source fingerprinting. J. Soils Sediments 13, 1676–1691. https://doi.org/10.1007/s11368-013-0762-7

Kouhpeima A, Feiznia S, Ahmadi H, Hashemi SA, Zareiee AR (2010) Application of quantitative composite fingerprinting technique to identify the main sediment sources in two small catchments of Iran. Hydrol Earth Syst Sc Discussions (5):6677-6698

Kronvang, B., Andersen, I. K., Hoffmann, C. C., Pedersen, M. L., Ovesen, N. B., & Andersen, H. E. (2007). Water exchange and deposition of sediment and phosphorus during inundation of natural and restored lowland floodplains. Water, Air, and Soil Pollution, 181(1-4), 115-121.

KYAPED, 2014. Kentucky Aerial Photography and Elevation Data Program. Accessed: 01/30/19. http://kygeonet.ky.gov/kyfromabove/.

Laceby JP, Huon S, Onda Y, Vaury V, Evrard O (2016) Do forests represent a long-term source of contaminated particulate matter in the Fukushima Prefecture? J Environ Manage 183:742-753

Laceby JP, Olley J, Pietsch TJ, Sheldon F, Bunn SE (2015) Identifying subsoil sediment sources with carbon and nitrogen stable isotope ratios. Hydrol Process 29(8):1956-1971

Laflen, J. M., Lane, L. J., & Foster, G. R., 1991. WEPP: A new generation of erosion prediction technology. *Journal of soil and water conservation*, *46*(1), 34-38.

Lal, R. (1999). Soil management and restoration for C sequestration to mitigate the accelerated greenhouse effect. Progress in Environmental Science, 1(4), 307-326.

Lambert CP, Walling DE (1988) Measurement of channel storage of suspended sediment in a gravel-bed river. Catena 15(1):65-80

Latocha, A., 2014. Geomorphic connectivity within abandoned small catchments (Stołowe Mts, SW Poland). Geomorphology 212, 4–15. https://doi.org/10.1016/j.geomorph.2013.04.030

Le Bissonnais, Y., Lecomte, V., Cerdan, O., 2004. Grass strip effects on runoff and soil loss. Agronomie 24, 129-136.

Leibowitz, S.G., Wigington, P.J., Rains, M.C., Downing, D.M., 2008. Non-navigable streams and adjacent wetlands: Addressing science needs following the Supreme Court's Rapanos decision. Front. Ecol. Environ. 6, 364–371. https://doi.org/10.1890/070068

Lenhart, T., A. Van Rompaey, A. Steegen, N. Fohrer, H.-G. Frede,and G. Govers. 2005. Considering spatial distribution anddeposition of sediment in lumped and semi-distributed models.Hydrol. Process. 19(3): 785-794.

Leopold, L.B., Wolman, M.G., Miller, J.P., 1964. Fluvial Processes in Geomorphology. W.H. Freeman, New York.

Lexartza-Artza, I., Wainwright, J., 2009. Hydrological connectivity: Linking concepts with practical implications. Catena 79, 146–152. https://doi.org/10.1016/j.catena.2009.07.001

Liu, X.M., Mang, X.Y., Zhang, M.H., 2008. Major factors influencing the efficacy of vegetated buffers on sediment trapping: A review and analysis. J. Environ. Qual. 37, 1667-1674.

Liu, Y., & Fu, B. (2016). Assessing sedimentological connectivity using WATEM/SEDEM model in a hilly and gully watershed of the Loess Plateau, China. Ecological indicators, 66, 259-268.

Lloyd, C. E. M., Freer, J. E., Johnes, P. J., & Collins, A. L., 2016. Using hysteresis analysis of high-resolution water quality monitoring data, including uncertainty, to infer controls on nutrient and sediment transfer in catchments. *Science of the Total Environment*, *543*, 388-404.

López-Vicente M., X. Sun, Y. Onda, H. Kato, T. Gomi, and M. Hiraoka (2017). Effect of tree thinning and skidding trails on hydrological connectivity in two Japanese forest catchments. Geomorphology, 292: 104-114.

López-Vicente, M., Álvarez, S., 2018. Influence of DEM resolution on modelling hydrological connectivity in a complex agricultural catchment with woody crops. Earth Surf. Process. Landforms 43, 1403–1415. https://doi.org/10.1002/esp.4321

López-Vicente, M., Nadal-Romero, E., Cammeraat, E.L.H., 2016. Hydrological Connectivity Does Change Over 70 Years of Abandonment and Afforestation in the Spanish Pyrenees. Land Degrad. Dev. n/a- n/a. doi:10.1002/ldr.2531

López-Vicente, M., Poesen, J., Navas, A., & Gaspar, L. (2013). Predicting runoff and sediment connectivity and soil erosion by water for different land use scenarios in the Spanish Pre-Pyrenees. Catena, 102, 62-73.

López-Vicente, M., Quijano, L., Palazón, L., Gaspar, L., Navas, A., 2015. Assessment of Soil Redistribution at Catchment Scale by Coupling a Soil Erosion Model and a Sediment Connectivity Index (Central Spanish Pre-Pyrenees). Cuad. Investig. Geogr. 41, 127–147. https://doi.org/10.18172/cig.2649

Lu, H., Moran, C.J., Prosser, I.P., 2006. Modelling sediment delivery ratio over the Murray Darling Basin. Environ. Model. Softw. 21, 1297–1308. https://doi.org/10.1016/j.envsoft.2005.04.021

Madej, M.A., Sutherland, D.G., Lisle, T.E. and Pryor, B., 2009. Channel responses to varying sediment input: A flume experiment modeled after Redwood Creek, California. Geomorphology, 103(4), 507-519.

Mahoney DT, Fox JF, Al Aamery N (2018) Watershed erosion modeling using the probability of sediment connectivity in a gently rolling system. J Hydrol 561:862-883

Mahoney, D.T., Al Aamery, N., Fox, J.F., Riddle, B., Ford, W., Wang, Y.T., 2019. Equilibrium sediment exchange in the earth's critical zone: evidence from sediment fingerprinting with stable isotopes and watershed modeling. J. Soils Sediments 19, 3332–3356. https://doi.org/10.1007/s11368-018-2208-8

Mahoney, D.T., Blandford, B., Fox, J.F., 2020c. Coupling the probability of connectivity and RUSLE reveals pathways of sediment transport and soil loss rates for forest and reclaimed mine landscapes. *In preparation.*

Mahoney, D.T., Fox, J.F., Al Aamery, N., 2018. Watershed erosion modeling using the probability of sediment connectivity in a gently rolling system. J. Hydrol. 561, 862–883. https://doi.org/10.1016/j.jhydrol.2018.04.034

Mahoney, D.T., Fox, J.F., Al Aamery, N., Clare, E.C., 2020a. Integrating connectivity theory within watershed modelling part II: Application and evaluating structural and functional connectivity. Sci. Total Environ. *In press.*

Mahoney, D.T., Fox, J.F., Al Aamery, N., Clare, E.C., 2020b. Integrating connectivity theory within watershed modelling part I: model formulation and investigating the timing of sediment connectivity. Sci. Total Environ. *In press.*

Mahoney, David Tyler, 2017. Sediment transport modelling using dynamic (dis)connectivity prediction for a bedrock controlled catchment. Theses and Dissertations—Civil Engineering. 55. https://uknowledge.uky.edu/ce_etds/55

Maidment, D. R. (2002). Arc Hydro: GIS for water resources (Vol. 1). ESRI, Inc.

Maidment, D.R., Olivera, F., Calver, A., Eatherall, A., Fraczek, W., 1996. Unit hydrograph derived from a spatially distributed velocity field. Hydrol. Process. 10, 831–844. https://doi.org/10.1002/(SICI)1099-1085(199606)10:6<831::AID-HYP374>3.0.CO;2-N

Maner, S.B., 1958. Factors affecting sediment delivery rates in the red hills physiographic area. Eos, Trans. Am. Geophys. Union 39, 669–675. https://doi.org/10.1029/TR039i004p00669

Maner, Sam B., and L. H. Barnes. (1953). Suggested criteria for estimating gross sheet erosion and sediment delivery rates for the blackland prairies problem area in soil conservation, U. S. Dept. Agr., Soil Cons. Serv., Fort Worth, 17.

Marchamalo, M., Hooke, J.M., Sandercock, P.J., 2016. Flow and Sediment Connectivity in Semi-arid Landscapes in SE Spain: Patterns and Controls. L. Degrad. Dev. 27, 1032–1044. https://doi.org/10.1002/ldr.2352

Masselink, R.J.H., Keesstra, S.D., Temme, A.J.A.M., Seeger, M., Giménez, R., Casalí, J., 2016. Modelling Discharge and Sediment Yield at Catchment Scale Using Connectivity Components. L. Degrad. Dev. 27, 933–945. https://doi.org/10.1002/ldr.2512

McCarney-Castle K, Childress TM, Heaton CR (2017) Sediment source identification and load prediction in a mixed-use Piedmont watershed, South Carolina. J Environ Manage 185:60-69

McConnachie JL, Petticrew EL (2006) Tracing organic matter sources in riverine suspended sediment: implications for fine sediment transfers. Geomorphology 79(1-2):13-26

McCool, D.K., Renard, K.G. and Foster, G.R. 1993. The Revised Universal Soil Loss Equation. Proc. Int'l. Workshop on Soil Erosion, Moscow, Russia. (Larionov & Nearing, eds). p.45-59. Center for Techn. Transfer and Pollution Prevention, Purdue Univ., USA.

McCorkle EP, Berhe AA, Hunsaker CT, Johnson DW, McFarlane KJ, Fogel ML, Hart SC (2016) Tracing the source of soil organic matter eroded from temperate forest catchments using carbon and nitrogen isotopes. Chem Geol 445:172-184

McCuen RH. Hydrologic design and analysis. New Jersey: Prentice Hall; 1998.

McGrain P, 1983. The geologic story of Kentucky. Kentucky Geological Survey, University of Kentucky Special Publication 8: Series XI, Lexington

Meade, R. H., Yuzyk, T. R., & Day, T. J. (1990). Movement and storage of sediment in rivers of the United States and Canada. IN: Surface Water Hydrology. Geological Society of America, Boulder, Colorado. 1990. p 255-280, 21 fig, 3 tab, 185 ref.

Merritt, W. S., Letcher, R. A., & Jakeman, A. J. (2003). A review of erosion and sediment transport models. Environmental Modelling & Software, 18(8), 761-799.

Messenzehl, K., Hoffmann, T., Dikau, R., 2014. Sediment connectivity in the high-alpine valley of Val Müschauns, Swiss National Park - linking geomorphic field mapping with geomorphometric modelling. Geomorphology 221, 215–229. https://doi.org/10.1016/j.geomorph.2014.05.033

Michaelides, K., & Wainwright, J. (2002). Modelling the effects of hillslope–channel coupling on catchment hydrological response. Earth Surface Processes and Landforms, 27(13), 1441-1457.

Millar, R. G., & Quick, M. C. (1998). Stable width and depth of gravel-bed rivers with cohesive banks. Journal of Hydraulic Engineering, 124(10), 1005-1013.

Minella JPG, Merten GH, Clarke RT (2004) Identification of sediment sources in a small rural drainage basin. IAHS P 288:44-51

Mishra, K., Sinha, R., Jain, V., Nepal, S., Uddin, K., 2019. Towards the assessment of sediment connectivity in a large Himalayan river basin. Sci. Total Environ. 661, 251–265. https://doi.org/10.1016/j.scitotenv.2019.01.118

Mockus, V. 1961. Watershed lag. U.S. Dept. of Agriculture, Soil Conservation Service, ES–1015, Washington, DC.

Montgomery, D.R. and Dietrich, W.E. (1994). Landscape dissection and drainage area-slope thresholds. In: M.J. Kirkby (Editor), Process Models and Theoretical Geomorphology. Wiley, Chichester, pp. 221-246.

Moriasi, D.N., Arnold, J.G., Van Liew, M.W., Bingner, R.L., Harmel, R.D., Veith, T.L., 2007. Model evaluation guidelines for systematic quantification of accuracy in watershed simulations. Trans. ASABE 50 (3), 885–900.

Morris, G. L., & Fan, J. (1998). Reservoir sedimentation handbook: design and management of dams, reservoirs, and watersheds for sustainable use. McGraw Hill Professional.

Morris, G.L. and Fan, J. (2009). Reservoir Sedimentation Handbook. Design and Management of Dams, Reservoirs, and Watersheds for Sustainable Use. McGraw-Hill.

Mukundan R, Radcliffe DE, Ritchie JC (2011) Channel stability and sediment source assessment in streams draining a Piedmont watershed in Georgia, USA. Hydrol Process 25(8):1243-1253

Mukundan R, Radcliffe DE, Ritchie JC, Risse LM, McKinley RA (2010) Sediment fingerprinting to determine the source of suspended sediment in a Southern Piedmont stream. J Environ Qual 39(4):1328-1337

Nachtergaele J, Poesen J, Sidorchuk A, Torri D (2002) Prediction of concentrated flow width in ephemeral gully channels. Hydrol Process 16(10):1935-1953

Nadelhoffer KF, Fry B (1988) Controls on natural 15N and 13C abundances in forest soil organic matter. Soil Sci Soc Am J 52:1633-1640

National Oceanic and Atmospheric Administration, 2012. Climatology – Lexington, Ky. https://www.weather.gov/lmk/clilex Accessed: 12/12/2019

National Oceanic and Atmospheric Administration, 2019. Climatology – Lexington, Ky. https://www.weather.gov/lmk/clilex Accessed: 12/12/2019

Natural Resource Conservation Service NRCS, 2009. Web soil survey. URL http://www. websoilsurvey.ncsc. usda. gov/app/[verified October 29, 2009].

Natural Resource Conservation Service NRCS. (2010). Time of Concentration. Part 630 Hydrology National Engineering Handbook. Accessed 5/4/2017.

Natural Resource Conservation Service NRCS. 1972. “Hydrology.” National engineering handbook, Sec. 4, U.S. Department of Agriculture, Washington, D.C.

Nazari Samani A, Wasson RJ, Malekian A (2011) Application of multiple sediment fingerprinting techniques to determine the sediment source contribution of gully erosion: Review and case study from Boushehr province, southwestern Iran. Prog Phys Geog 35(3):375-391

Neitsch SL, Arnold JG, Kiniry JEA, Srinivasan R, Williams JR (2002) Soil and water assessment tool user’s manual version 2000. GSWRL Report 202:02-06

Neitsch SL, Arnold JG, Kiniry JR, Williams JR (2011) Soil and water assessment tool theoretical documentation version 2009. Texas Water Resources Institute, College Station, Texas

Neugirg, F., Kaiser, A., Huber, A., Heckmann, T., Schindewolf, M., Schmidt, J., Becht, M., Haas, F., 2016. Using terrestrial LiDAR data to analyse morphodynamics on steep unvegetated slopes driven by different geomorphic processes. Catena 142, 269–280.

Nezu I, Nakagawa H (1993) Turbulence in open channel flows. In: Technology and Engineering. Taylor & Francis, Abingdon

Nicholls DJ (2001) The source and behaviour of fine sediment deposits in the River Torridge Devon and their implications for salmon spawning. Unpublished PhD thesis, University of Exeter

Nicoll, T., Brierley, G., 2017. Within-catchment variability in landscape connectivity measures in the Garang catchment, upper Yellow River. Geomorphology 277, 197–209. https://doi.org/10.1016/j.geomorph.2016.03.014

Noto, L. V., La Loggia, G., 2007. Derivation of a distributed unit hydrograph integrating GIS and remote sensing. J. Hydrol. Eng. 12, 639–650. https://doi.org/10.1061/(ASCE)1084-0699(2007)12:6(639)

Nunes, J.P., Wainwright, J., Bielders, C.L., Darboux, F., Fiener, P., Finger, D., Turnbull, L., 2017. Better models are more effectively connected models. Earth Surf. Process. Landforms 43, 1355–1360. https://doi.org/10.1002/esp.4323

Owens, P.N., Duzant, J.H., Deeks, L.K., Wood, G.A., Morgan, R.P.C., Collins, A.J. (2007). Evaluation of contrasting buffer features within an agricultural landscape

for reducing sediment and sediment-associated phosphorus delivery to surface waters. Soil Use and Management 23, 165-175.

Palanisamy, B. and Workman, S.R., 2014. Hydrologic modeling of flow through sinkholes located in streambeds of Cane Run Stream, Kentucky. Journal of Hydrologic Engineering, 20(5), p.04014066.

Papanicolaou AN, Fox JF, Marshall J (2003) Soil fingerprinting in the Palouse Basin, USA, using stable carbon and nitrogen isotopes. Int J Sediment Res 18(2):278-284

Papanicolaou, A.N., Elhakeem, M., Krallis, G., Prakash, S., Edinger, J., 2008. Sediment transport modeling review - Current and future developments. J. Hydraul. Eng. 134, 1–14. https://doi.org/10.1061/(ASCE)0733-9429(2008)134:1(1).

Parsons, A.J., Bracken, L., Poeppl, R.E., Wainwright, J., Keesstra, S.D., 2015. Introduction to special issue on connectivity in water and sediment dynamics. Earth Surf. Process. Landforms 40, 1275–1277. https://doi.org/10.1002/esp.3714

Partheniades E (1965) Erosion and deposition of cohesive soils. J Hydr Div 91(1):105-139

Passalacqua, P, Belmont, P, Staley, D et al. 2015. Analyzing high resolution topography for advancing the understanding of mass and energy transfer through landscapes: a review. Earth Science Reviews 148, 174–193.

Pellerin, B.A., Stauffer, B.A., Young, D.A., Sullivan, D.J., Bricker, S.B., Walbridge, M.R., Clyde, G.A., Shaw, D.M., 2016. Emerging Tools for Continuous Nutrient Monitoring Networks: Sensors Advancing Science and Water Resources Protection. J. Am. Water Resour. Assoc. 52, 993–1008. https://doi.org/10.1111/1752-1688.12386

Phillips JM, Russell MA, Walling DE (2000) Time-integrated sampling of fluvial suspended sediment: a simple methodology for small catchments. Hydrol Process 14:2589-2602

Phillips, J. D., Šamonil, P., Pawlik, Ł., Trochta, J., & Daněk, P. (2017). Domination of hillslope denudation by tree uprooting in an old-growth forest. Geomorphology, 276, 27-36.

Phillips, J.D., 2003. Sources of nonlinearity and complexity in geomorphic systems. Prog. Phys. Geogr. 27 (1), 1–23.

Phillips, J.D., 2015. Badass geomorphology. Earth Surf. Process. Landforms 40, 22–33. https://doi.org/10.1002/esp.3682

Phillips, J.D., Martin, L.L., Nordberg, V.G., Andrews, W.A., 2004. Divergent evolution in fluviokarsts landscapes of Central Kentucky. Earth Surf. Proc. Land. 29, 799–819.

Phillips, J.D., Šamonil, P., Pawlik, Ł., Trochta, J., Daněk, P., 2017. Domination of hillslope denudation by tree uprooting in an old-growth forest. Geomorphology 276, 27–36.

Piest, R. F., Kramer, L. A., & Heinemann, H. G. (1975). Sediment movement from loessial watersheds. Present and prospective technology for predicting sediment yields and sources, 40, 30-141.

Pike, A.S., Scatena, F.N. and Wohl, E.E., 2010. Lithological and fluvial controls on the geomorphology of tropical montane stream channels in Puerto Rico. Earth Surface Processes and Landforms, 35(12), pp.1402-1417.Richards, K.S., 1978. Channel geometry in the riffle-pool sequence. *Geografiska Annaler: Series A, Physical Geography*, *60*(1-2),.23-27.

Pilgrim, D.H., 1976. Travel times and nonlinearity of flood runoff from tracer measurements on a small watershed. Water Resour. Res. 12, 487–496. https://doi.org/10.1029/WR012i003p00487

Ponce, V. M. (1989). *Engineering hydrology: Principles and practices* (Vol. 640). Englewood Cliffs, NJ: Prentice Hall.

Pringle, C., 2003. What is hydrologic connectivity and why is it ecologically important? Hydrol. Process. 17, 2685–2689. https://doi.org/10.1002/hyp.5145

Reed, T. M., McFarland, J. T., Fryar, A. E., Fogle, A. W., & Taraba, J. L. (2010). Sediment discharges during storm flow from proximal urban and rural karst springs, central Kentucky, USA. Journal of hydrology, 383(3-4), 280-290.

Renard, K., Foster, G., Weesies, G., McCool, D., & Yoder, D. (1997). Predicting soil erosion by water: A guide to conservation planning with the Revised Universal Soil Loss Equation (RUSLE). Washington D.C.: United States Department of Agriculture.

Rhoton FE, Emmerich WE, DiCarlo DA, McChesney DS, Nearing MA, Ritchie JC (2008) Identification of suspended sediment sources using soil characteristics in a semiarid watershed. Soil Sci Soc Am J 72(4):1102-1112

Ricci, G.F., De Girolamo, A.M., Abdelwahab, O.M.M., Gentile, F., 2018. Identifying sediment source areas in a Mediterranean watershed using the SWAT model. L. Degrad. Dev. 29, 1233–1248. https://doi.org/10.1002/ldr.2889

Rienzi, E. A., Fox, J. F., Grove, J. H., & Matocha, C. J. (2018). Experimental results and temporal surrogate modeling of particulate organic carbon released during interrill erosion. CATENA, 163, 1-12.

Roberts, R. G., & Church, M. (1986). The sediment budget in severely disturbed watersheds, Queen Charlotte Ranges, British Columbia. Canadian Journal of Forest Research, 16(5), 1092-1106.

Roehl, J. W. (1962). Sediment source areas, delivery ratios and influencing morphological factors. International Association of Scientific Hydrology, 59, 202-213.

Roering, J. J., Kirchner, J. W., & Dietrich, W. E. (1999). Evidence for nonlinear, diffusive sediment transport on hillslopes and implications for landscape morphology. Water Resources Research, 35(3), 853-870.

Rose LA, Karwan DL, Aufdenkampe AK (2018) Sediment fingerprinting suggests differential suspended particulate matter formation and transport processes across hydrologic regimes. J Geophys Res-Biogeo123:1213-1229

Rosgen, D. L., 2001. A practical method of computing streambank erosion rate. In *Proceedings of the Seventh Federal Interagency Sedimentation Conference* (Vol. 1).

Russell MA, Walling DE, Hodgkinson RA (2001) Suspended sediment sources in two small lowland agricultural catchments in the UK. J Hydrol 252(1-4):1-24

Russo JP (2009) Investigation of surface fine grained laminae, streambed, and streambank processes using a watershed scale hydrologic and sediment transport model. MSc Thesis, University of Kentucky

Russo, J., Fox, J., 2012. The role of the surface fine-grained laminae in low-gradient streams: A model approach. Geomorphology 171–172, 127–138. https://doi.org/10.1016/j.geomorph.2012.05.012

Russo, Joseph Paul. (2009). Investigation of surface fine grained laminae, streambed, and streambank processes using a watershed scale hydrologic and sediment transport model. *University of Kentucky Doctoral Dissertations*. 750.

Saltelli A, Ratto M, Andres T, Campolongo F, Cariboni J, Gatelli D, Saisana M, Tarantola S (2008) Global sensitivity analysis: the primer. Wiley, New York

Sanford, L.P. and Maa, J.P.Y., 2001. A unified erosion formulation for fine sediments. Marine Geology, 179(1-2), 9-23.

Schindler Wildhaber Y, Liechti R, Alewell C (2012) Organic matter dynamics and stable isotope signature as tracers of the sources of suspended sediment. Biogeosciences 9(6):1985-1996

Schumm, S. A. (1977). The fluvial system, 338 pp. New York, NY: Willey.

Schumm, S.A., 1979. Geomorphic thresholds: the concept and its applications. Trans. Inst. Br. Geogr. 4 (4), 485–515.

Schumm, Stanley A. (1954). The relation of drainage basin relief to sediment loss, Internat. Assn. Hydrology, IUGG, Tenth Gen. Assembly, Rome, 1,216-219.

Sear, D. A. (1996). Sediment transport processes in pool–riffle sequences. Earth Surface Processes and Landforms, 21(3), 241-262.

Sherriff, S.C., Rowan, J.S., Fenton, O., Jordan, P., Melland, A.R., Mellander, P.E., Huallacháin, D., 2016. Storm Event Suspended Sediment-Discharge Hysteresis and Controls in Agricultural Watersheds: Implications for Watershed Scale Sediment Management. Environ. Sci. Technol. 50, 1769–1778. https://doi.org/10.1021/acs.est.5b04573

Sherriff, S.C., Rowan, J.S., Fenton, O., Jordan, P., Melland, A.R., Mellander, P.E., Huallacháin, D., 2015. Storm Event Suspended Sediment-Discharge Hysteresis and Controls in Agricultural Watersheds: Implications for Watershed Scale Sediment Management. Environ. Sci. Technol. 50, 1769–1778. https://doi.org/10.1021/acs.est.5b04573

Shoda, M. E., Lathrop, T. R., Risch, M. R., 2015. Real-time, continuous water quality monitoring in Indiana and Kentucky. US Geological Survey Fact Sheet, 3041.

Shoukri, M.M., Mian, I.U.H., Tracy, D.S., 1988. Sampling properties of estimators of the log-logistic distribution with application to Canadian precipitation data. Can. J. Stat. 16, 223–236. https://doi.org/10.2307/3314729

Shrestha, R. K.; Lal, R. Ecosystem carbon budgeting and soil carbon sequestration in reclaimed mine soil. Environ. Int. 2006, 32, 781–796.

Shukla M.K., R. Lal, and M. Ebinger. 2004. SOIL QUALITY INDICATORS FOR RECLAIMED MINESOILS IN SOUTHEASTERN OHIO, 0038-075X/04/16902-133–142 February 2004, Soil Science Vol. 169, No. 2

Simon, A. and Thomas, R.E., 2002. Processes and forms of an unstable alluvial system with resistant, cohesive streambeds. Earth Surface Processes and Landforms: The Journal of the British Geomorphological Research Group, 27(7), pp.699-718.

Sims R.P., D.G. Preston, A.J. Richardon, J.H. Newton, D. Isgrig and R.L. Blevins. (1968). Soil survey of Fayette county, Kentucky. USDA Soil Conservation Service, U.S. Government Printing Office, Washington D.C.

Skousen, J., Zipper, C.E. Post-mining policies and practices in the Eastern USA coal region. Int J Coal Sci Technol 1, 135–151 (2014). https://doi.org/10.1007/s40789-014-0021-6

Slimane AB, Raclot D, Evrard O, Sanaa M, Lefèvre I, Ahmadi M, Le Bissonnais Y (2013) Fingerprinting sediment sources in the outlet reservoir of a hilly cultivated catchment in Tunisia. J Soils Sediments 13(4):801-815

Sloan, P. G., Moore, I. D., Coltharp, G. B., and Eigel, J. D. 1983. "Modeling surface and subsurface stormflow on steeply-sloping forested watersheds." Research Rep., Univ. of Kentucky, Lexington, KY.

Smallwood, R. Personal Communication. February 16, 2017.

Smith HG, Blake WH (2014) Sediment fingerprinting in agricultural catchments: a critical re-examination of source discrimination and data corrections. Geomorphology 204:177-191

Smith, M.W., Vericat, D., 2015. From experimental plots to experimental landscapes: Topography, erosion and deposition in sub-humid badlands from Structure-from-Motion photogrammetry. Earth Surf. Process. Landforms 40, 1656–1671. https://doi.org/10.1002/esp.3747

Souza, J. O., Correa, A. C., & Brierley, G. J. (2016). An approach to assess the impact of landscape connectivity and effective catchment area upon bedload sediment flux in Saco Creek Watershed, Semiarid Brazil. Catena, 138, 13-29.

Stewart HA, Massoudieh A, Gellis A (2015) Sediment source apportionment in Laurel Hill Creek, PA, using Bayesian chemical mass balance and isotope fingerprinting. Hydrol Process 29(11):2545-2560

Stewart RL, Fox JF (2015) Role of macroturbulence to sustain turbulent energy in decelerating flows over a gravel bed. Geomorphology 248(2015):147–160

Stewart, Bruce E. 2003. When Darkness Reigns Then is the Hour to Strike: Moonshining, Federal Liquor Taxation, and Klan Violence in Western North Carolina, 1868–1872. North Carolina Historical Review. 80 (4): 453–474. JSTOR 23522839.

Stone M, Droppo IG (1994) In-channel surficial fine-grained sediment laminae. Part II: Chemical characteristics and implications for contaminant transport in fluvial systems. Hydrol Process 8(2):113-124

SWAT (2012). SWAT: Model use, calibration, and validation. Transactions of the ASABE, 55(4), 1491-1508.

Taylor, C. J., & Nelson, H. L. (2008). A compilation of provisional karst geospatial data for the Interior Low Plateaus physiographic region, central United States (No. 339). Geological Survey (US).

Taylor, C.J., 1992. Ground-water Occurrence and Movement Associated with Sinkhole Alignments in the Inner Bluegrass Karst Region of central Kentucky MS Thesis. University of Kentucky, Lexington, Kentucky.

Taylor, P. D., Fahrig, L., Henein, K., & Merriam, G. (1993). Connectivity is a vital element of landscape structure. Oikos, 571-573.

Taylor, T. J., Agouridis, C. T., Warner, R. C., & Barton, C. D. (2009). Runoff Curve Numbers for Losse-dumped Spoil in the Cumberland Plateau. International Journal of Mining, Reclamation and Environment , 23, 103-120.

Third Rock Consulting. LFUCG Stormwater Stakeholder Advisory Committee. Accessed 2/18/2016. http://www.lexingtonky.gov/Modules/ShowDocument.aspx?documentid=27603

Thrailkill, J., 1974. Pipe flow models of a Kentucky limestone aquifer. Groundwater, 12 (4), 202–205.

Thrailkill, J., Sullivan, S.B., Gouzie, D.R., 1991. Flow parameters in a shallow conduit flow carbonate aquifer, Inner Bluegrass Karst Region, Kentucky, USA. Journal of Hydrology, 129 (1), 87–108.

Tisdall, J. M., & Oades, J. (1982). Organic matter and water-stable aggregates in soils. Journal of soil science, 33(2), 141-163.

Toone, J., Rice, S.P., Piégay, H., 2014. Spatial discontinuity and temporal evolution of channel morphology along a mixed bedrock-alluvial river, upper DrÔme River, southeast France: Contingent responses to external and internal controls. Geomorphology 205, 5–16. https://doi.org/10.1016/j.geomorph.2012.05.033

Torri, D., Poesen, J., 2014. A review of topographic threshold conditions for gully head development in different environments. Earth-Science Rev. 130, 73–85. https://doi.org/10.1016/j.earscirev.2013.12.006

Toy, T. J., Foster, G. R., & Renard, K. G. (2002). *Soil erosion: processes, prediction, measurement, and control*. John Wiley & Sons.

Trimble, S. W., 1993, The distributed sediment budget model and watershed management in the Paleozoic plateau of the upper midwestern United States: Physical Geography, v. 14, p. 285–303.

Trimble, S.W., 1997. Contribution of stream channel erosion to sediment yield from an urbanizing watershed. Science (80-.). 278, 1442–1444. https://doi.org/10.1126/science.278.5342.1442

U.S. Environmental Protection Agency, 1999. *Protocol for Developing Sediment TMDLs*. EPA 841-B-99-004. Office of Water (4503F), United States Environmental Protection Agency, Washington D.C. 132 pp.

Ulack, R., Raitz, K., & Pauer, G., 1977. *Atlas of Kentucky*. University Press of Kentucky.

USDA Soil Science Division Staff (2017) Soil survey manual. In: Ditzler C, Scheffe K, Monger HC. USDA Handbook 18. Government Printing Office, Washington, D.C.

USEPA, 2004. The Incidence and Severity of Sediment Contamination in Surface Waters of the United States, EPA 823-R-04-007. http://www.epa.gov/waterscience/cs/report/2004/nsqs2ed-complete.pdf

Vandaele, K. (1993). Assessment of factors affecting ephemeral gully erosion in cultivated catchments of the Belgian Loam Belt. In: S. Wicherek (Editor), Farm Land Erosion in Temperate

Vandaele, K., Poesen, J., Govers, G., vanWesemael, B. (1996) Geomorphic threshold conditions for ephemeral gully incision. Geomorphology 16, 161–173.

Vigiak, O., Borselli, L., Newham, L. T. H., McInnes, J., & Roberts, A. M. (2012). Comparison of conceptual landscape metrics to define hillslope-scale sediment delivery ratio. Geomorphology, 138(1), 74-88.

Wainwright, J., Turnbull, L., Ibrahim, T.G., Lexartza-Artza, I., Thornton, S.F., Brazier, R.E., 2011. Linking environmental régimes, space and time: Interpretations of structural and functional connectivity. Geomorphology 126, 387–404. https://doi.org/10.1016/j.geomorph.2010.07.027

Walling DE (2005) Tracing suspended sediment sources in catchments and river systems. Sci Total Environ 344(1-3):159-184

Walling DE, Collins AL, Sichingabula HM, Leeks GJL (2001) Integrated assessment of catchment suspended sediment budgets: a Zambian example. Land Degrad Dev 12(5):387-415

Walling DE, Owens PN, Leeks GJ (1999) Fingerprinting suspended sediment sources in the catchment of the River Ouse, Yorkshire, UK. Hydrol Process 13(7):955-975

Walling DE, Woodward JC (1995) Tracing sources of suspended sediment in river basins: a case study of the River Culm, Devon, UK. Mar Freshwater Res 46(1):327-336

Walling DE, Woodward JC, Nicholas AP (1993) A multi-parameter approach to fingerprinting suspended-sediment sources. IAHS P (215):329-338

Walling, D. E., Collins, A. L., Jones, P. A., Leeks, G. J. L., & Old, G. (2006). Establishing fine-grained sediment budgets for the Pang and Lambourn LOCAR catchments, UK. Journal of Hydrology, 330(1), 126-141.

Walling, D.E., 1983. The sediment delivery problem. J. Hydrol. https://doi.org/10.1016/0022-1694(83)90217-2

Wanielista, M., Kersten, R., & Eaglin, R. (1997). Hydrology: Water quantity and quality control. John Wiley and Sons.

Warner, R. C., Agouridis, C. T., Vingralek, P. T., & Fogle, A. W. (2010). Reclaimed Mineland Curve Number Response to Temporal Distribution of Rainfall. Journal of the Americal Water Resources Association , 46, 724 - 732.

Whitbread, K., Jansen, J., Bishop, P. and Attal, M., 2015. Substrate, sediment, and slope controls on bedrock channel geometry in postglacial streams. Journal of Geophysical Research: Earth Surface, 120(5), pp.779-798.Wohl, E.E., Vincent, K.R. and Merritts, D.J., 1993. Pool and riffle characteristics in relation to channel gradient. Geomorphology, 6(2), 99-110.

Wickham, J. D.; Riitters, K. H.; Wade, T. G.; Coan, M.; Homer, C. The effect of Appalachian mountaintop mining on interior forest. Landscape Ecol. 2007, 22, 179–187.

Williams, G., 1989. Sediment Concentration Versus Water Discharge During Single Event in rivers. J. Hydrol. 111, 89–106.

Winterwerp JC, Van Kesteren WG (2004) Introduction to the physics of cohesive sediment dynamics in the marine environment (Vol. 56). Elsevier

Wischmeier, W. H., & Smith, D. D. (1978). Predicting rainfall erosion losses-a guide to conservation planning. *Predicting rainfall erosion losses-a guide to conservation planning.*

Wohl, E., 2015. Particle dynamics: The continuum of bedrock to alluvial river segments. Geomorphology, 241, 192-208.

Wohl, E., 2017. Connectivity in rivers. Prog. Phys. Geogr. 41, 345–362. https://doi.org/10.1177/0309133317714972

Wohl, E., Brierley, G., Cadol, D., Coulthard, T.J., Covino, T., Fryirs, K.A., Grant, G., Hilton, R.G., Lane, S.N., Magilligan, F.J., Meitzen, K.M., Passalacqua, P., Poeppl, R.E., Rathburn, S.L., Sklar, L.S., 2019. Connectivity as an emergent property of geomorphic systems. Earth Surf. Process. Landforms 44, 4–26. https://doi.org/10.1002/esp.4434

Wohl, E., Magilligan, F.J., Rathburn, S.L., 2017. Introduction to the special issue: Connectivity in Geomorphology. Geomorphology 277, 1–5. https://doi.org/10.1016/j.geomorph.2016.11.005

Wohl, E., Rathburn, S., Chignell, S., Garrett, K., Laurel, D.A., Livers, B., Patton, A., Records, R., Richards, M., Schook, D.M., Sutfin, N.A., Wegener, P., 2017. Mapping longitudinal stream connectivity in the North St. Vrain Creek watershed of Colorado. Geomorphology 277, 171–181. https://doi.org/10.1016/j.geomorph.2016.05.004

Wood, P.J., Armitage, P.D., 1997. Biological effects of fine sediment in the lotic environment. Environ. Manage. 21, 203–217. https://doi.org/10.1007/s002679900019

Wright, A. C., & Webster, R., 1991. A stochastic distributed model of soil erosion by overland flow. Earth Surface Processes and Landforms, 16(3), 207-226.

Yan, L.J., Yu, X.X., Lei, T.W., Zhang, Q.W. and Qu, L.Q., 2008. Effects of transport capacity and erodibility on rill erosion processes: a model study using the Finite Element method. *Geoderma*, *146*(1-2), pp.114-120.

Zhang Y, Collins AL, McMillan S, Dixon ER, Cancer-Berroya E, Poiret C, Stringfellow A (2017) Fingerprinting source contributions to bed sediment-associated organic matter in the headwater subcatchments of the River Itchen SAC, Hampshire, UK. River Res Appl 33(10):1515-1526

Zhu, J., Taylor, T. P., Currens, J. C., & Crawford, M. M. (2014). Improved karst sinkhole mapping in Kentucky using LIDAR techniques: a pilot study in Floyds Fork Watershed. Journal of Cave and Karst Studies, 76(3), 207.

Zingaro, M., Refice, A., Giachetta, E., D'Addabbo, A., Lovergine, F., De Pasquale, V., Pepe, G., Brandolini, P., Cevasco, A., Capolongo, D., 2019. Sediment mobility and connectivity in a catchment: A new mapping approach. Sci. Total Environ. 672, 763–775. https://doi.org/10.1016/j.scitotenv.2019.03.461

VITA

David Tyler Mahoney

EDUCATION

Master of Science, Civil Engineering — Aug. 2017

Thesis Title: Sediment transport modelling using dynamic (dis)connectivity prediction for a bedrock controlled catchment; Advisor: Dr. James F. Fox.

University of Kentucky, Lexington, KY

Bachelor of Science, Civil Engineering — Dec. 2015

University of Kentucky, Lexington, KY

RESEARCH EXPERIENCE & APPOINTMENTS

Graduate Research Assistant — 2016 – Present
Hydrosystems Lab at the University of Kentucky, Lexington, KY

Graduate Teaching — 2016 – Present
College of Engineering at the University of Kentucky, Lexington KY

Graduate Mentoring and Advising — 2016 – Present
Department of Civil Engineering at the University of Kentucky, Lexington KY

Undergraduate Researcher – Research Advisor: Dr. Scott Yost, P.E. — 2014 - 2016
Hydrosystems Lab at the University of Kentucky, Lexington, KY

AWARDS & HONORS

1. KentuckyView Graduate Fellowship Award ($600) — 2019
   KentuckyView (facet of AmericaView)
2. NSF SENSE Fellowship Award (tuition and stipend) — 2018 - 2019
   Department of Civil Engineering, University of Kentucky
3. University of Kentucky Research Travel Award ($1,800 total) — 2017 - 2019
   The Graduate School, University of Kentucky
4. Raymond Fellowship Award ($700 total) — 2017 – 2019
   Department of Civil Engineering, University of Kentucky
5. Kentucky/Tennessee Section Scholarship Award ($2,000) — 2018

Water Environmental Association (WEA) and American Water Works Association (AWWA)

6. Robert A. and Maywin S. Lauderdale Fellowship Award (tuition and stipend) 2016 – 2017
   Department of Civil Engineering, University of Kentucky

7. Outstanding University Scholar Award 2016
   Chi Epsilon Chapter, University of Kentucky

8. Highest GPA Scholarship ($1,500 total) 2014 - 2016
   Phi Gamma Delta, Upsilon Kappa Chapter

9. Frank Warren Endowed Scholarship ($1,000) 2015
   Department of Civil Engineering, University of Kentucky

10. Outstanding Senior Award 2015
    Phi Gamma Delta, Upsilon Kappa Chapter

11. George M. Binder Scholarship ($2,500) 2015
    Kentucky Society of Professional Engineers

12. University Scholar 2015
    The Graduate School, University of Kentucky

13. Kentucky Governor's Scholar Presidential Scholarship (tuition) 2011 - 2015
    University of Kentucky

14. Thurston H. Strunk Engineering Scholarship ($12,000 total) 2011 - 2015
    College of Engineering, University of Kentucky

15. Kentucky Educational Excellence Scholarship ($10,000 total) 2011 - 2015
    Kentucky Higher Education Assistance Authority

16. HMB Professional Engineers Inc. Civil Engineering Scholarship ($500) 2011
    HMB Professional Engineers Inc.

17. Governor's Scholar 2010
    Kentucky Governor's Scholars Program

PROFESSIONAL & SCHOLARLY AFFILIATIONS

1. University of Kentucky Water Professionals Student Chapter (WPSC) 2017 - Present

2. University of Kentucky American Water Works Association (AWWA-SC) 2017 - Present
3. University of Kentucky Environmental Water Resources Institute (EWRI-SC) 2017 - Present
4. ASCE Environmental Water Resources Institute (EWRI) 2017 - Present
5. American Water Works Association (AWWA) 2017 - Present
6. American Water Resources Association (AWRA) 2017 - Present
7. Tau Beta Pi (National Engineering Honor Society) 2014 - Present
8. American Society of Civil Engineers (ASCE) 2014 - Present
9. Kentucky Society of Professional Engineers Student Chapter (KSPE) 2014 - 2015
10. Chi Epsilon (National Civil Engineering Honor Society) 2013 - Present

PUBLICATIONS

Journal Papers in Review

1. Husic, A., Fox, J.F., **Mahoney, D.T.**, Gerlitz, M., Pollock, E., & Backus, J. Optimal transport for assessing nitrate source-pathway connectivity. *Water Resources Research, in review*.
2. **Mahoney, D.T.**, Al-Aamery, N., Fox, J.F & Clare, E.C. Connectivity formula for watershed sediment modeling part I: model formulation and investigating the timing of sediment connectivity. *STOTEN, in review.*
3. **Mahoney, D.T.**, Al-Aamery, N., Fox, J.F & Clare, E.C. Connectivity formula for watershed sediment modeling part II: application and evaluating structural and functional connectivity. *STOTEN, in review.*
4. Al-Aamery, N., Fox, J.F., & **Mahoney, D.T.** Variance decomposition of forecasted sediment transport in a lowland watershed using global climate model ensembles. *Journal of Hydrology, in review.*

Published Journal Papers

5. Ford, W.I., Fox, J.F., **Mahoney, D.T.**, Erhardt, A., Degraves, G., & Jensen, A. Backwater confluences of the Ohio River: organic and inorganic fingerprints explain sediment dynamics in wetlands and marinas. *Journal of the American Water Resources Association, in review.*

6. **Mahoney, D. T.**, Fox, J. F., & Al-Aamery, N. (2018). Watershed erosion modeling using the probability of sediment connectivity in a gently rolling system. *Journal of Hydrology,* 561, 862-883. *Impact Factor: 4.405 (2018)*
7. **Mahoney, D. T.**, Al Aamery, N., Fox, J. F., Riddle, B., Ford, W., & Wang, Y. T. (2019). Equilibrium sediment exchange in the earth's critical zone: evidence from sediment fingerprinting with stable isotopes and watershed modeling. Journal of Soils and Sediments, 19(9), 3332-3356. *Impact Factor: 2.669 (2018)*

Journal Papers in Preparation

8. **Mahoney, D.T.**, Al-Aamery, N., Fox, J.F., & Husic, A. (*approximately* 2020). Coupling three-dimensional probability of connectivity with sediment continuity reveals influence of barriers in low gradient bedrock streams. *In preparation for Hydrological Processes.*
9. **Mahoney, D.T.**, Clare, E.C., Fox, J.F., Al-Aamery, N., & Ford, W.I. (*approximately* 2020). Non-stationary nitrate source and transport identified with the probability of connectivity theory, watershed modelling, high-resolution sensors, and data optimization. *In preparation for Hydrologic Processes.*
10. **Mahoney, D.T.**, Blandford, B., & Fox, J.F. (*approximately* 2020). Erosion modelling using the probability of sediment connectivity and RUSLE reveal pathways and buffers in Appalachian catchments. *In preparation for Journal of Hydrologic Engineering.*
11. **Mahoney, D.T.**, Fox, J.F., Husic, A., Al-Aamery, N., & Ford, W.I. (*approximately* 2020). Connectivity modelling, hysteresis, and sediment fingerprinting: a review of state-of-the-art tools for connectivity quantification and view for moving forward. *In preparation for Earth Surface Land Processes.*

Other Writings

12. **Mahoney, D.T.** (2017). Sediment transport modelling using dynamic (dis)connectivity prediction for a bedrock controlled catchment. M.S.C.E. Thesis, University of Kentucky Department of Civil Engineering, Lexington, KY, USA.
13. **Mahoney D.T.**, Agouridis C.T., & Warner R.C. (2016). Hydrologic Modeling. University of Kentucky Cooperative Extension Service: AEN-127

CONFERENCE PRESENTATIONS

1. Husic, A., Fox, J.F., **Mahoney, D.T.,** & Clare, E.C. (2020). High-frequency sensing of nitrate to improve numerical model performance: insights from an extensively modeled karst spring, 2020 World Environmental & Water Resources Congress, EWRI, ASCE, Henderson, NV, May 17-21, 2020.
2. Husic, A., Fox, J.F., **Mahoney, D.T.**, Gerlitz, M., Pollock, E., & Backus, J. (2019). Optimal Transport for Assessing Nitrate Source and Pathway Connectivity in a Human-Disturbed Watershed, American Geophysical Union Fall 2019 Meeting, San Francisco, CA, December 9-13, 2019.
3. Ford, W.I., Fox, J.F., **Mahoney, D.T.**, Erhardt, A., DeGraves, G., & Jensen, A. (2019). Sediment fingerprinting in lowland confluences of the Ohio River estimates sediment source provenance from river backwaters versus tributary sediment, 2019 World Environmental & Water Resources Congress, EWRI, ASCE, Pittsburgh, PA, May 19-23, 2019.
4. **Mahoney, D.T.**, Al-Aamery, N., Fox, J.F., Clare, E.C., & Husic, A. (2019). Formulation of the probability of connected timing and sediment connectivity prediction to advance watershed models, 2019 World Environmental & Water Resources Congress, EWRI, ASCE, Pittsburgh, PA, May 19-23, 2019. *Oral Presentation.*
5. Clare, E.C., **Mahoney, D.T.**, Fox, J.F., Al-Aamery, N., & Ford, W.I. (2019). Nitrate modelling using the probability of connectivity and signal decomposition, 2019 World Environmental & Water Resources Congress, EWRI, ASCE, Pittsburgh, PA, May 19-23, 2019. *Oral Presentation.*
6. Clare, E.C., **Mahoney, D.T.**, Fox, J.F., Dunlop, T., Day, S., & Pike, J. (2019). Continuous nutrient and turbidity sensors reveal the response of watershed sources connected during storm events, Kentucky Water Resources Annual Symposium, Lexington, KY, March 25, 2019.
7. Al-Aamery, N., **Mahoney, D.T.**, & Fox, J.F. (2019). Climate change impacts on sediment transport in a lowland watershed system: controlling processes and projection, Kentucky Water Resources Annual Symposium, Lexington, KY, March 25, 2019.
8. **Mahoney, D.T.**, Al-Aamery, N., Fox, J.F., Clare, E.C., Dunlop, T., Day, S., & Pike, J. (2019). Probability of connected timing and sediment connectivity prediction advances watershed modelling, Kentucky Water Resources Annual Symposium, Lexington, KY, March 25, 2019. *Oral Presentation*.
9. Gerlitz, M., Adams, E., Al-Aamery, N., Clare, E., **Mahoney, D.T.**, Fox, J.F., & Husic, A. (2018). Measuring and Modeling Morphologic Processes in Karst to Sustain Water Resources in the Future, UK Sustainability Student Poster Contest, Tracy Farmer Institute for Sustainability and the Environment, Lexington, KY, December 6, 2018.
10. Clare, E.C., **Mahoney, D.T.**, & Fox, J.F. (2018). Spatial and temporal variations of in-stream nutrient concentrations in similar mixed-use watersheds, Kentucky Water Resources Annual Symposium, Lexington, KY, March 19, 2018.

11. **Mahoney, D.T.**, Fox, J.F., Al-Aamery N., & Husic, A. (2018). Advancement in watershed and sediment transport modeling using dynamic lateral, longitudinal, and vertical sediment (dis)connectivity prediction, Kentucky Water Resources Annual Symposium, Lexington, KY, March 19, 2018. *Oral Presentation*
12. Al-Aamery, N., **Mahoney, D.T.**, & Fox, J.F. (2018). Climate change impacts on sediment transport in a lowland watershed system: controlling processes and projection, Kentucky Water Resources Annual Symposium, Lexington, KY, March 19, 2018.
13. Riddle, B., Fox, J.F., and **Mahoney, D.T.** (2018). Sediment fingerprinting with non-conservative stable isotopes in a lowland catchment to assess nutrient pollution impacts on water supply, Kentucky Water Resources Annual Symposium, Lexington, KY, March 19, 2018.
14. **Mahoney, D.T.**, Fox, J.F. & Al-Aamery N. (2017). Advancement in watershed modelling using dynamic lateral and longitudinal sediment (dis)connectivity prediction, American Geophysical Union Fall 2017 Meeting, New Orleans, LA, December 11-15, 2017. *Poster Presentation.*
15. Al-Aamery, N., Fox, J.F., **Mahoney, D.T.**, & Husic, A. (2017). Climate change impacts on sediment transport in a lowland watershed system: controlling connectivity processes and projection, American Geophysical Union Fall 2017 Meeting, New Orleans, LA, December 11-15, 2017. *Poster Presentation*.
16. **Mahoney, D.T.,** Fox J.F. & Al-Aamery N. (2017). Sediment transport modelling using dynamic (dis)connectivity prediction for a bedrock controlled catchment, 2017 World Environmental & Water Resources Congress, EWRI, ASCE, Sacramento, CA, May 21-25, 2017. *Oral Presentation*.
17. **Mahoney, D.T.**, Fox, J.F., Clare, E.C., Kendig, R., & Cambron, A. (2017). WAVES: A comprehensive visual assessment of watershed sedimentation processes, Kentucky Water Resources Annual Symposium, Lexington, KY, March 20, 2017. *Poster Presentation*.
18. **Mahoney, D.T.**, Fox J.F., and Al-Aamery N. (2017). Sediment transport modeling using dynamic (dis)connectivity to assess sediment impacts on water supply, Kentucky Water Resources Annual Symposium, Lexington, KY, March 20, 2017. *Oral Presentation*.

TEACHING EXPERIENCE & ADVISING

University of Kentucky Teaching

Co-instructor and Teaching Associate: Department of Civil Engineering 2018 - Present

Course Taught: *Watershed Sedimentation* (CE 547/BAE 547)

Guest Lecturer: Department of Civil Engineering

Course: Water Quality in Surface Waters (CE 653/BAE 653) 2019

Course: Water Resources Engineering (CE 461G) 2016, 2017

Graduate Teaching Assistant: First-Year Engineering Program 2017

Courses Taught: *Fundamentals of Engineering Computing* and *Introduction to Engineering for Graduate Students* (EGR 102-002, EGR 102-003, EGR 102-004, EGR 102-010, EGR 102-011, EGR 102-012, EGR 112-001)

Graduate Teaching Assistant: Department of Civil Engineering 2017

Courses Taught: *Watershed Sedimentation* and *Introduction to Fluid Mechanics* (CE547/BAE 547, CE 341)

Invited Lectures

Organization: University of Kentucky Department of Plant and Soil Sciences Nov. 2019

Presentation Title: Modelling and Monitoring Instream Nitrate Cycling

Organization: University of Kansas Department of Civil, Environmental, and Architectural Engineering Oct. 2019

Presentation Title: Assessing Sediment Connectivity at the Watershed Scale

NSF-Funded Research Experience for Undergraduates SENSE Program Teaching

Graduate Teaching Associate 2018, 2019

Mentoring and Advising

1. Leonie Bettel June 2019 - Present
   Study of nutrient transport and fate in karstic watersheds using stable isotopes and high-resolution nitrate sensing. *Student continued on to pursue PhD in CE at the University of Kentucky.*
2. Noah Smith Jan. 2019 - Present
   Study of sediment sources *via* stable carbon and nitrogen isotopes at the watershed scale in Kentucky, USA. *Student continued on to pursue MBA at the University of Kentucky.*
3. John Pike Jan. 2018 - Present
   Study of water quality and sensor maintenance and data analysis for agricultural watersheds in Kentucky, USA. *Student continued on to pursue MSCE at the University of Kentucky.*
4. Frank England May 2018 - Aug. 2018
   Study of water quality and total suspended solids at the watershed scale; implementation of mobile sensor platform in agricultural watersheds in Kentucky, USA.
5. Thomas Dunlop Jan. 2018 - May 2019

Study of total suspended solids and water quality using high-resolution sensors in the agro-karstic watersheds. *Student continued on to pursue MSCE at the University of Kentucky.*

6. Stephen Day Jan. 2018 - May 2019
   Fabrication of platform for advanced sensors in agricultural watersheds and study of data quality assurance. *Student continued on to pursue MSCE at the University of Kentucky.*
7. Isaac Weddington Jan. 2017 - Dec. 2017
   Study of water quality using advanced sensors and grab sampling in agro-karstic watersheds in Kentucky, USA.
8. Gabriel Draughon Aug. 2016 - May 2017
   Study of water quality and sensor network implementation in agro-karstic watersheds in Kentucky, USA. *Student continued on to purse PhD in CE at University of Michigan.*
9. Evan Clare Aug. 2016 - May 2017
   Study of water quality and nutrient dynamics in agro-karstic watersheds using stable isotopes, water quality sensors, and grab sampling. *Student continued on to pursue MSCE at the University of Kentucky.*
10. Rachel Kendig Aug. 2016 - May 2017
    Study of water quality using field reconnaissance in the agricultural watersheds in Kentucky, USA.
11. Aaron Cambron Aug. 2016 - May 2017
    Study of sediment transport in agricultural watersheds using field reconnaissance and GIS. *Student continued on to pursue MSCE at the University of Kentucky.*

SERVICE AND PROFESSIONAL ACTIVITIES

Professional Service

1. Peer Reviewer 2020 – Present
   Journal of Hydraulic Engineering reviewer.

UK College of Engineering Service

2. Discover What's Wildly Possible: Pathways in Civil Engineering 2019 - Present

Seminar committee member; organized seminar series to highlight career journeys of civil engineers and civil engineering faculty.

3. University of Kentucky Environmental & Water Resources Institute 2019 - Present
   President; led and organized meetings, served as chapter liaison, etc.
4. University of Kentucky American Water Works Association (AWWA) 2019 - Present
   President; led and organized meetings, served as chapter liaison, etc.
5. University of Kentucky Design Week 2019
   Jury member; helped judge *UK Design Week* competition for landscape architecture and civil engineering students. Students presented stream restoration design for local development.
6. University of Kentucky Wildcat Cage 2019
   Presenter; pitched the idea of a water-resources outreach "Water Wagon" to local engineering firms in University-wide competition. Project was funded $1,500.
7. University of Kentucky Water Week 2018 - 2019
   Volunteer; assisted with University of Kentucky Water Week planning and preparation for the 2018 and 2019 terms.
8. University of Kentucky Environmental & Water Resources Institute2017 - 2019
   Secretary; recorded chapter minutes and photographed events, assisted with yearly reports.
9. University of Kentucky American Water Works Association (AWWA) 2017 - 2019
   Secretary; recorded chapter minutes and photographed events, assisted with yearly reports.
10. University of Kentucky Engineering Day (E-Day) 2016 - 2019
    Volunteer; helped set up and run Engineering Day activities at the University of Kentucky for young students interested in engineering.
11. Excellence in Teaching (Lutes) Award 2018
    Award Selection Committee Member; served as graduate student representative for the selection committee of the highest award the College of Engineering bestows on a faculty.
12. University of Kentucky Graduate Student Congress 2017 - 2018
    Department of Civil Engineering Representative; represented civil engineering department at meetings and promoted interests of graduate students in civil engineering.
13. University of Kentucky Graduate Student Congress 2017 - 2018
    Internal Affairs Committee Member; assisted in financial analysis and co-authored report highlighting graduate student salaries.
14. Water for Life 2017
    Volunteer; assisted with public outreach regarding water quality and ecosystem health.
15. Kentucky Society of Professional Engineers Student Chapter 2014 - 2015

Treasurer; maintained budget for the KSPE student chapter during the school year.

University of Kentucky Service

16. Upsilon Kappa Chapter Phi Gamma Delta Board of Chapter Advisors 2016 - 2018
    Member; advised undergraduate fraternity members in regard to philanthropy and service at the University of Kentucky.
17. University of Kentucky Bluegrass Ensemble 2014 - 2016
    Mandolinist; performed with the University of Kentucky Bluegrass Ensemble. Performed at UK's world music concerts and various campus functions.
18. Upsilon Kappa Phi Gamma Delta Chapter 2014 - 2015
    President; served as chief liaison for the undergraduate chapter of Phi Gamma Delta at the University of Kentucky.
19. Upsilon Kappa Phi Gamma Delta Chapter 2013 - 2014
    Historian; maintained minutes and chapter history for the undergraduate chapter of Phi Gamma Delta at the University of Kentucky.
20. University of Kentucky K-Week 2012 - 2013
    K-Crew Leader; led/mentored incoming freshmen for the University of Kentucky's K-Week orientation and throughout the school year. Recognized as one of the top three K-Week groups.
21. Upsilon Kappa Phi Gamma Delta Chapter 2012 - 2015
    House Manager; served as liaison between house members and the house corporation; conducted house maintenance and upkeep.

Non-University Public Service

22. Habitat for Humanity 2012 – 2018
    Volunteer; organized groups and volunteered for Habitat for Humanity projects in Lexington, KY.
23. Kentucky Educational Television (KET) telethon 2012 – 2015
    Volunteer; assisted with answering phone calls during telethon to raise money for KET.
24. Relay for Life
    2013, 2015*Participant*; raised $200 for *Relay for Life*, a fundraiser for cancer research.
25. *BonnaMu* Philanthropy Event 2014

Organizer and judge; a "battle of the bands" competition that raised nearly $5,000 in support of the American Red Cross and Children's Miracle Network.

26. *DanceBlue* 2012
Participant; raised $350 for the University of Kentucky dance marathon funding pediatric oncology research.

INDUSTRY EXPERIENCE

Project Engineer Intern, Stantec INC. 2015 - 2016
- Assisted in modelling a hydraulic network to de-water coal residual landfills in Tennessee and Alabama.
- Developed scour and erosion protection alternatives for river embankments.

Project Engineer Intern, HMB Professional Engineers INC. 2011 - 2012
- Assisted in roadway design; determined cut and fill volumes.
- Reviewed and edited plan sheets and specifications.